CHARACTERIZATION OF MUTANT HUMAN BRAIN SODIUM CHANNELS ASSOCIATED WITH FAMILIAL EPILEPSY

By

Sunita N. Misra

Dissertation
Submitted to the Faculty of the
Graduate School of Vanderbilt University
in partial fulfillment of the requirements
for the degree of

DOCTOR OF PHILOSOPHY

in

Pharmacology

August, 2008
Nashville, Tennessee

Approved:
P. Jeffrey Conn
Vsevolod V. Gurevich
Robert L. Macdonald
Danny G. Winder
Gregory C. Mathews
Alfred L. George, Jr.

To my loving, supportive family

and

To my boyfriend Reuben

for unending patience and support through the hard times.

ACKNOWLEDGMENTS

I would like to start by thanking my mentor Al George. My four years in the lab has flown by and left me with many unforgettable memories. I have grown both personally and professionally during my time in the lab. I appreciate the guidance and opportunities I was given during my tenure in the lab. I would also like to thank the other members of my committee for their patience and critical evaluations of my work. My committee chairman, Jeff Conn and Danny Winder both asked me to consider how what I studied fit into the bigger picture. Seva Gurevich sat patiently through the numerous electrophysiological experiments before any biochemical experiments were presented. Greg Mathews always made himself available to discuss careers, data, and directions of specific aims. Greg and several people in his lab including Misty Cook and Molly Fricke taught me the how to do the hippocampal dissections. And Bob Macdonald always challenged and encouraged me to improve my project and learn more from it. His expertise and suggestions were always incredibly valuable in shaping the direction of my projects.

I also want to thank the George lab and members of the Genetic Medicine administrative staff. The George lab was always an interesting place to work with many different people coming together from varied backgrounds. I learned many scientific and life lessons from people in the lab. Christoph Lossin, Carlos Vanoye, and Dao Wang all gave me help at the beginning of my electrophysiological experiments. Kris Kahlig became my unofficial mentor and collaborator within the lab. Most of my best ideas came from discussions with Kris and I wish him the best of luck with his career in academia. Nila Gillani has been an excellent friend and was always willing to lend a supportive shoulder or a helping hand when needed. Reshma Desai taught me much of what I know about molecular biology of sodium channels which was no simple task. The former and present graduate students in the George lab always made things more enjoyable. I had a lot of fun at our payday lunches, Starbucks runs, Biophysics meetings, and in hindsight working on the pharmacology retreat video together.

Jennifer Kearney came to Vanderbilt towards of the end of my graduate career, but I feel very fortunate to have become friends with her and to have learned from her scientifically. I appreciated that Jennifer unofficially adopted me into her lab instead of just being a scientific collaborator. I really value the advice and quiet understanding that she gave me. Additionally Jennifer, Elizabeth Rutter, and Rebecca Somershoe have collectively taught me most of what I know about working with mice.

I must acknowledge that many friends and family also contributed to my success in graduate school. I was fortunate to have support from my medical school, MSTP, graduate school, and non-Vanderbilt friends, each contributed by providing a sense of balance to my life. I would especially like to thank Rekha Mody, Cindy Wilson, Cindy Chin, and Christina Speirs from my medical school class. Will Oldham always kept me informed about the next steps in pharmacology and medical school. Megan Rothney and Lindsey Tambora were so important for keeping me balanced and helping me through a few rough patches. Rich Gustin and Brett English made graduate school far more fun than it would have been without them. As for my family, I want to thank them for not considering me to be completely crazy for pursuing this and supporting me throughout the endless unsuccessful experiments. My sister Vinita has always been proud and supportive. My parents were my inspiration early on and always find ways to encourage me along. And finally I must thank my boyfriend Reuben for being my biggest supporter throughout. I would never have made it this far without his patient love and belief in me.

TABLE OF CONTENTS

Page

Appendix

LIST OF TABLES

LIST OF FIGURES

LIST OF ABBREVIATIONS

General abbreviations

α subunit = the major pore forming subunit of the voltage-gated sodium channel

β subunit = the auxiliary subunit of the voltage-gated sodium channel

B6.Q54 = congenic C57BL/6J transgenic mouse carrying the Q54 transgene

BCA = bicinchoninic acid, an assay used to determine protein concentrations

bp = base pairs

$CaCl_2$ = calcium chloride

CHO-K1 = chinese hamster ovary cells

CNS = central nervous system

CsCl = cesium chloride

CsF = cesium fluoride

C terminus = carboxy terminus (COOH)

DI = domain 1, 1st homologous domain in sodium channel α subunit topology

DII = domain 2, 2nd homologous domain in sodium channel α subunit topology

DIII = domain 3, 3rd homologous domain in sodium channel α subunit topology

DIV = domain 4, 4th homologous domain in sodium channel α subunit topology

DEKA = residues in each domain contributing to selectivity filter

DMEM = Dulbecco’s Modified Eagle’s Medium

EDTA = ethylenediaminetetraacetic acid

EEG = electroencephalogram

eGFP = enhanced green fluorescent protein

EGTA = ethylene glycol tetraacetic acid

F1.Q54 = transgenic mouse from C57BL/6J cross with SJL/J carrying the Q54 transgene

FBS = fetal bovine serum

FHM = familial hemigplegic migraine

GFP = green fluorescent protein

HEK293 = human embryonic kidney 293 cells

HEPES = 4-(2-hydroxyethyl)-1-piperazineethanesulfonic acid

HH = Hodgkin-Huxley mechanism of independent gating processes

Ig = immunoglobulin fold

IGEPAL CA-630 = Octylphenyl-polyethylene glycol

IRES = internal ribosome entry site

KCl = potassium chloride

LQTS = long QT syndrome

$MgCl_2$ = magnesium chloride

mM = millimolar, 10^{-3} molar, a measure of concentration

MRI = magnetic resonance imaging

mRNA = messenger ribonucleic acid

N terminus = amino terminus (NH_2)

nA = nanoamp, 10^{-9} Amperes, a measure of current

Na^+ = sodium ion

nAChR = nicotinic acetylcholine receptor

NaCl = sodium chloride

NaF = sodium fluoride

$Na_V1.1$ = the α1 voltage-gated sodium channel, encoded by the gene *SCN1A*

$Na_V1.2$ = the α2 voltage-gated sodium channel, encoded by the gene *SCN2A*

$Na_V1.3$ = the α3 voltage-gated sodium channel, encoded by the gene *SCN3A*

$Na_V1.4$ = the α4 voltage-gated sodium channel, encoded by the gene *SCN4A*

$Na_V1.5$ = the α5 voltage-gated sodium channel, encoded by the gene *SCN5A*

$Na_V1.8$ = the α6 voltage-gated sodium channel, encoded by the gene *SCN6A*

NSE = neuronal specific enolase, promoter used to drive the Q54 transgene

ORF = open reading frame

P = postnatal day, number of days after birth

pA = picoamp, 10^{-12} amperes, a measure of current

PBS = phosphate buffered saline

PCR = polymerase chain reaction

PLO = poly-l-ornithine

P-loop = pore loop formed by reentrant loop between S5 and S6 segments

PNS = peripheral nervous system

PV = parvalbumin, refers to a specific subset of inhibitory interneurons

Q54 = transgenic mouse overexpressing GAL879-881QQQ mutation in rat *Scn2a*

RFLP = restriction fragment length polymorphism

RX = R1407X SMEI mutation in $Na_V1.1$

S1 = transmembrane segment 1

S2 = transmembrane segment 2

S3 = transmembrane segment 3

S4 = transmembrane segment 4

S5 = transmembrane segment 5

S6 = transmembrane segment 6

SCN1A = the gene encoding the protein $Na_V1.1$

SCN2A = the gene encoding the protein $Na_V1.2$

SCN3A = the gene encoding the protein $Na_V1.3$

SCN4A = the gene encoding the protein $Na_V1.4$

SCN5A = the gene encoding the protein $Na_V1.5$

SCN8A = the gene encoding the protein $Na_V1.6$

SDS = sodium dodecyl sulfate

SIDS = sudden infant death syndrome

SNP = single nucleotide polymorphism

TEVC = two-electrode voltage clamp, electrophysiological method employed on *Xenopus* oocytes

TTX = tetrodotoxin, sodium channel pore blocker

UTR = untranslated region

WT = wild-type, the normal or control used for electrophysiology experiments

Epilepsy syndrome abbreviations

ADLTLE = autosomal dominant lateral temporal lobe epilepsy

ADNFLE = autosomal dominant nocturnal frontal lobe epilepsy

ARX = Aristaless-related homeobox

BFIS = benign familial infantile seizures

BFNC = benign familial neonatal convulsions

BFNIS = benign familial neonatal-infantile seizures

BRD2 = bromodomain containing protein 2

CAE = childhood absence epilepsy

CNTNAP2 = contactin-associated protein-like 2

EFHC1 = EF-hand domain containing protein

FS = febrile seizures

FS+ = complex febrile seizures

GEFS+ = generalized epilepsy with febrile seizures plus

HS = hippocampal sclerosis

ICEGTC = intractable childhood epilepsy with generalized tonic-clonic seizures

IGE = idiopathic generalized epilepsy

IS = infantile spasms

JME = juvenile myoclonic epilepsy

LGI1 = leucine-rich glioma 1

MASS1 = monogenic audiogenic seizure susceptibility

ME2 = malic enzyme 2

MOE1, MOE2 = modifier of epilepsy 1 and 2 identified with Q54 mouse model of TLE

MTLE = mesial temporal lobe epilepsy

PTZ = pentylenetetrazole, chemical that induces epilepsy in animal models

SMEI = severe myoclonic epilepsy of infancy, also called Dravet syndrome

stg = stargazer, spontaneous animal model of epilepsy

swe = slow-wave epilepsy, spontaneous animal model of epilepsy

TLE = temporal lobe epilepsy

Amino acid abbreviations

A = alanine
C = cysteine
D = aspartic acid
E = glutamic acid
F = phenylalanine
G = glycine
H = histidine
I = isoleucine
K = lysine
L = leucine
M = methionine
N = asparagine
P = proline
Q = glutamine
R = arginine
S = serine
T = threonine
V = valine
W = tryptophan
Y = tyrosine

CHAPTER I

VOLTAGE-GATED SODIUM CHANNELS ASSOCIATED WITH EPILEPSY

Introduction

Epilepsy is a widespread and complex brain disease characterized by abnormal neuronal signaling. To help clinicians diagnose and treat patients, the epilepsies have been divided into epilepsy syndromes based on age of onset, types of seizures, duration of symptoms, severity, and etiology. These groupings allow clinicians to utilize the most effective treatment plan for a particular epilepsy. Channelopathies encompass a subset of genetic epilepsy syndromes with associated mutations in genes encoding various voltage-gated and ligand-gated ion channels such as potassium and sodium channels (George, Jr., 2005). Commonly used anticonvulsant agents including phenytoin, carbamazepine, valproate, lamotrigine and topiramate target voltage-gated sodium channels (Ragsdale and Avoli, 1998). Investigating the molecular basis underlying inherited epilepsy disorders is essential for proper identification and treatment.

Epidemiology of genetic forms of epilepsy

The prevalence of epilepsy in the general population is 0.5% with a lifetime prevalence of 3%. Over 2.7 million Americans suffer from epilepsy (Centers for Disease Control). Epidemiological studies of Western populations have revealed that 5% of first-degree relatives of patients with epilepsy also have epilepsy, suggesting a moderate genetic component (Beaussart and Loiseau, 1969; Bianchi et al., 2003; Vestergaard et al., 2007). Although inherited epilepsy syndromes represent a small subset of all epilepsy, genetic risk factors have been increasingly identified and implicated in forms of epilepsy not initially labeled as genetic.

In the 1930s, William Lennox became the first to apply the scientific method to inherited seizure disorders through examining twin cohorts. Monozygotic twins showed a high concordance (40-50%) whereas dizygotic twins had a moderate concordance (10-15%) suggesting a strong genetic component in epilepsy (Lennox, 1951; Berkovic et al., 1998; Kjeldsen et al., 2003). Subsequent twin studies have not always resulted in reproducible genetic risk factors for specific genetic epilepsy phenotypes. Instead most of the advances in the molecular mechanisms underlying epilepsy were discovered through multiplex family or family aggregation studies (Helbig et al., 2008).

In the late 1980s to 1990s, attempts to isolate epilepsy-associated mutations identified large candidate chromosomal regions through linkage analysis in large families with a single epilepsy syndrome. The positional cloning technique was employed to narrow down the candidate region by isolating overlapping DNA fragments until discrete genes associated with the phenotype were identified (Frankel, 1999). Candidate genes typically encode proteins thought to be important in neuronal excitability. The candidate gene is then directly sequenced in affected family members to search for a rare mutation or a single nucleotide polymorphism (SNP). Once identified, nonsense, frameshift, or splice site mutations can easily be postulated to have deleterious effects on the protein, but missense mutations often require functional data to be distinguished from common benign SNPs (George, Jr., 2004).

Genetics of inherited epilepsy

Idiopathic and symptomatic epilepsies are two broad categories into which epilepsy syndromes can be divided. Idiopathic epilepsies are those occurring in the absence of brain lesions or neurological deficits, and without any known external causes. Most cases of Idiopathic generalized epilepsy (IGE) are thought to have polygenic inheritance but this is the category of epilepsy disorders most commonly thought to be caused by mutations in a single gene. In contrast to IGE, symptomatic epilepsies have underlying brain abnormalities or neurological insults. A subset of symptomatic epilepsies is caused by complex genetic syndromes. As genetic factors are increasingly implicated in all types of epilepsy, divisions between the categories are becoming less distinct. Now epilepsy is more commonly postulated to be a spectrum of disorders with those entirely caused by a mutation in a single gene at one end and those with no identifiable genetic susceptibility at the other (Figure 1) (Berkovic et al., 2006; Helbig et al., 2008).

Studying rare monogenetic epilepsy syndromes increases understanding of general epilepsy pathophysiology. Monogenic epilepsies are easier to study than those with polygenic inheritance, a combination of acquired and genetic factors, or no known genetic risk factors (Figure 1). Often the genes affected in Mendelian epilepsies have altered function in more common epilepsy syndromes. By understanding how dysfunction of these genes modulates neuronal excitability, we may be able to better understand more genetically complex forms of epilepsy. Rare monogenetic epilepsies may also contribute to our understanding of genes involved in normal brain function and the diversity of mechanisms contributing to altered excitability. Also studying Mendelian epilepsies can aid with discovery of avenues for novel therapeutic treatments.

Most of the genes known to be mutated in genetic epilepsies encode for voltage-gated or ligand-gated ion channels, though there are recent examples of non-ion channel proteins increasing susceptibility for or causing certain forms of epilepsy. Examples of mutations identified in monogenetic epilepsy syndromes are described below: first the epilepsy syndromes related to defective ion channels will be explored and secondly a few novel genes will be discussed (Table 1).

Figure 1. Neurobiological spectrum of epilepsy. Idiopathic epilepsies are commonly associated with monogenetic mutations in ion channels. Mutant ion channels can lead to altered neuronal excitability. Some epilepsy syndromes result from polygenic inheritance or from the interplay between genetic and acquired factors. These syndromes may be the result of differential gene regulation or post-transcriptional modifications to ion channels. Symptomatic epilepsies result from congenital malformations, stroke, trauma, or neoplasia. Rarely, symptomatic epilepsies may be caused by genetic syndromes. Increasing evidence also shows that symptomatic epilepsies, especially those without an identifiable brain lesion, have underlying alterations of ion channel function. Epilepsies used to be easily categorized as genetic or acquired, but the distinctions between these have now become less distinct. Adapted from (Berkovic et al., 2006; Helbig et al., 2008).

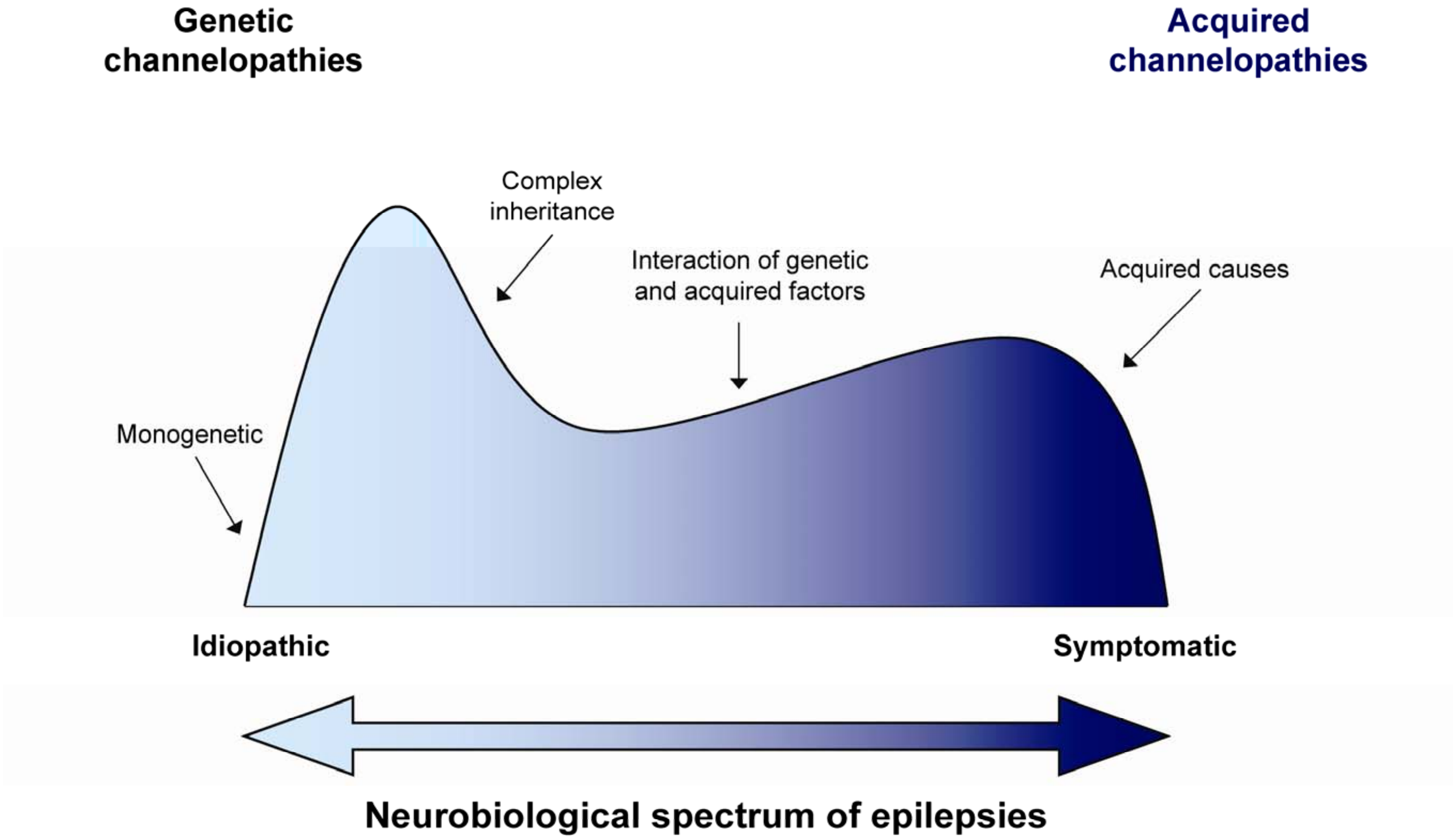
Genetic channelopathies
Acquired channelopathies
Complex inheritance
Interaction of genetic and acquired factors
Acquired causes
Monogenetic
Idiopathic
Symptomatic
Neurobiological spectrum of epilepsies

Table 1. Genes involved in inherited forms of epilepsy

Genes	**Syndrome**§	**Chromosome**
Sodium channel		
SCN1A	GEFS+ type 2	2q24.3
	ICEGTC	
	SMEI	
	IS (West Syndrome)	
	TLE	
SCN2A	BFNIS	2q23-q24
	BFIS	
	GEFS+	
	SMEI	
SCN3A	Cryptogenic pediatric partial epilepsy	2q24
SCN1B	GEFS+ type 1	19q13.1
Potassium channel		
KCNQ2	BFNC type 1	20q13.3
KCNQ3	BFNC type 2	8q24
KCNA1	Partial epilepsy / Episodic ataxia	12p13.32
Calcium channel		
CACNA1A	IGE / Episodic ataxia type 2	19p13.2-p13.1
CACNA1H	CAE	16p13.3
CACNB4	IGE / JME	2q22-q23

Chloride channel		
CLCN2	CAE / juvenile absence epilepsy/ JME / Epilepsy with grand mal seizure on wakening	3q27-q28
GABA Receptor		
GABRA1	JME / CAE type 4	5q34-q35
GABRG2	GEFS+ type 3 / CAE type 2/ SMEI	5q31.1-q33.1
GABRD	GEFS+	1p36.3
Acetylcholine Receptor		
CHRNA4	ADNFLE type 1	20q13.2-q13.3
CHRNB2	ADNFLE type 3	1q21.3
Novel genes		
LGI1	TLE	10q24
MASS1/VLGR1/GPR98	FS with afebrile seizures	5q13
EFHC1	JME	6p12.3
BRD2	JME	6p21.3
ME2	IGE	18q21
CNTNAP2	Focal epilepsy/ developmental delay / cortical migration abnormalities	7q35-q36
ARX	X-linked West Syndrome (IS)	Xp21
ATP1A2	BFIS	1q21-q23

[§] GEFS+ – generalized epilepsy with febrile seizures plus, ICEGTC – intractable childhood epilepsy with generalized tonic-clonic seizures, SMEI – severe myoclonic epilepsy of infancy, IS – infantile spasms, TLE – temporal lobe epilepsy, BFNIS – benign familial neonatal-infantile seizures, BFIS – benign familial infantile seizures, BFNC – benign familial neonatal convulsions, IGE – idiopathic generalized epilepsy, CAE – childhood absence epilepsy, JME – juvenile myoclonic epilepsy, ADNFLE – autosomal dominant nocturnal frontal lobe epilepsy, FS – febrile seizures

In 1995, a large Australian family was identified with several members affected by autosomal dominant nocturnal frontal lobe epilepsy (ADNFLE). Onset of ADNFLE is in middle childhood and is characterized by clustered seizures at night during dozing or before awakening (Berkovic and Scheffer, 1997). The ADNFLE phenotype was linked to 20q13.2 (Phillips et al., 1995), and further studies found the putative disease causing missense mutation in the α_4 neuronal nicotinic acetylcholine receptor (nAChR) encoded by *CHRNA4* (Steinlein et al., 1995). Additional ADNFLE mutations were identified several years later in the β_2 nAChR subunit encoded by *CHRNB2* (De et al., 2000).

Next defects in voltage-gated potassium channels were associated with a Mendelian form of epilepsy. In 1998, mutations in the *KCNQ2* and *KCNQ3* genes encoding $K_V7.2$ and $K_V7.3$ were linked to benign familial neonatal convulsions (BFNC) (Singh et al., 1998; Charlier et al., 1998). BFNC is an autosomal dominant disorder that causes seizures in the neonatal period that spontaneously remit within the first few months of life (Singh et al., 1998). BFNC mutations in $K_V7.2$ and $K_V7.3$ lead to aberrant neuronal M current, a slowly activating and deactivating current responsible for regulating neuronal excitability.

Generalized epilepsy with febrile seizures plus (GEFS+) is a mild epilepsy syndrome that has autosomal dominant inheritance. Patients initially experience febrile seizures (FS), seizures that are provoked by fever. Typical FS occur in children younger than six years old, and are relatively common affecting about 3% of children (Wallace et al., 2001), but are not necessarily predictive of future seizures or development of epilepsy. In GEFS+ patients, the seizures progress to febrile seizures plus (FS+). FS+ is characterized by febrile seizures after the age of six with or without the presence of afebrile seizures (Scheffer and Berkovic, 1997) and has been thought to be a predisposing factor for later development of epilepsy. A diagnosis of GEFS+ is made when patients experience generalized convulsions as well as FS+. The first mutation identified in a GEFS+ family was found in the *SCN1B* gene that encodes the auxiliary voltage-gated sodium channel β_1 subunit (Wallace et al., 1998). The β_1 mutation C121W was the first time a voltage-gated sodium channel mutation was implicated in epilepsy. Now there are a total of four mutations in *SCN1B* associated with GEFS+ type 1 and there is functional data for three of the four mutations (Meadows et al., 2002; Audenaert et al., 2003; Scheffer et al., 2007; Xu et al., 2007a). Next a new locus for GEFS+ was mapped to 2q21-q33 (Baulac et al., 1999). This locus was refined revealing mutations in *SCN1A*, the α_1 voltage-gated sodium channel that became known as GEFS+ type 2 and will be further discussed below with other neuronal epilepsy sodium channel mutations.

$GABA_A$ receptors are another ion channel that is mutated in several genetic forms of epilepsy. In 2001, the first evidence for dysfunctional $GABA_A$ receptors in epilepsy was elucidated when another GEFS+ locus was narrowed down to the $GABA_A$ receptor γ_2 subunit encoded by *GABRG2* (Baulac et al., 2001a). GEFS+ type 3 refers to cases where *GABRG2* receptor mutations are identified. Variants in the $GABA_A$ receptor δ subunit have also been implicated to increase susceptibility to GEFS+ (Dibbens et al., 2004; Macdonald et al., 2004). Mutations in *GABRG2* were also found in patients with childhood absence epilepsy (CAE) type 2 and febrile convulsions (Kananura et al., 2002; Marini et al., 2003). An early truncation of the *GABRG2* subunit has been implicated as a rare cause of severe myoclonic epilepsy of infancy (SMEI) (Macdonald et al., 2004). *GABRA1* encodes the α_1 subunit of $GABA_A$ receptors. Mutations in *GABRA1* were identified in autosomal dominant juvenile myoclonic epilepsy (JME) (Cossette et al., 2002) and also in CAE type 4 (Maljevic et al., 2006).

Other forms of absence and myoclonic epilepsy are also associated with disturbances in other ion channels. CAE type 1 has been mapped to 8q24 but no specific gene has been identified (Fong et al., 1998). And a variety of IGE phenotypes including CAE type 3, juvenile absence epilepsy, and JME are associated with mutations in the voltage-gated chloride channel encoded by *CLCN2* (Haug et al., 2003), though epilepsy-associated mutations are rarely identified in this gene. Mutations in *CACNA1H* encoding the $Ca_V3.2$ T-type voltage-gated calcium channel are also associated with CAE (Chen et al., 2003). Variants in the α_{1a} subunit of the P/Q type voltage-gated calcium channel, encoded by *CACNA1A*, result in increased susceptibility for IGE (Chioza et al., 2001). Mutations in *CACNB4* encoding the β_4 subunit of the P/Q type voltage-gated calcium channel are associated with JME and IGE with episodic ataxia (Escayg et al., 2000a). Many of the epilepsy-associated mutations in ion channels have been functionally characterized to elucidate mechanisms of altered neuronal excitability.

Now non-ion channel proteins have been implicated in the pathogenesis of certain forms of epilepsy, but how mutations in these proteins alter neuronal excitability is largely unknown. For example, autosomal dominant lateral temporal lobe epilepsy (ADLTLE) is associated with mutations in leucine-rich glioma inactivated 1 (*LGI1l*) (Kalachikov et al., 2002; Morante-Redolat et al., 2002). Recent evidence showed that LGI1 complexes with presynaptic K_V1 channels and modifies the N-type inactivation caused by $K_V\beta1$ (Schulte et al., 2006), but how this relates to epilepsy has still not been explored. Monogenic audiogenic seizure susceptibility (*MASS1*) is part of a larger gene called *VLGR1* which contains a structural motif similar to *LGI1*. The *MASS1/VLGR1* gene product resides within the FEB4 FS locus, but no mutations have been positively linked to FS. There have been heterozygous mutations in *MASS1/VLGR1* reported in Japanese families with febrile and afebrile seizures (Nakayama et al., 2002).

Studies now indicate that mutations in proteins as varied as EF-hand domain containing protein (*EFHC1*), malic enzyme 2 (*ME2*), bromodomain containing protein 2 (*BRD2*), and contactin-associated protein-like 2 (*CNTNAP2*) are associated with various epilepsy syndromes (George, Jr., 2004; Gurnett and Hedera, 2007). Rarely infantile spasms (IS) are associated with an X-linked form of West Syndrome due to mutant

Aristaless-related homeobox (*ARX*) (Stromme et al., 2002). Determining the function of these proteins and the continual search for other novel proteins involved in epilepsy pathogenesis will provide new avenues for studying the genetics of epilepsy. An additional direction this field is moving towards is to understand the role of susceptibility genes that contribute to complex inheritance of epilepsy when multiple proteins are involved in producing a seizure phenotype. Overall studying the dysfunctional proteins implicated in epilepsy helps to better define normal brain excitability and identify specific perturbations underlying epilepsy that may be better targeted with a different therapeutic approach.

Structure and function of voltage-gated sodium channels

Neuronal voltage-gated sodium channels are responsible for the rapid membrane depolarization that characterizes the initial “upstroke” of the action potential. Although no crystal structure exists, mammalian neuronal sodium channels have been well characterized. Channels consist of multiple interacting subunits: a large (~ 260 kDa) α subunit, which forms the channel pore, and smaller (~ 33-36 kDA) β accessory subunits that appear to modulate the activity, expression, and localization of the α subunit (Isom et al., 1994; Kazen-Gillespie et al., 2000; Malhotra et al., 2000). The human pore-forming α subunits exist in nine isoforms with varying degrees of amino acid conservation as shown in Figure 2 (Plummer and Meisler, 1999). Structurally, α subunits consist of four homologous domains (DI-DIV). The membrane topology of a typical α subunit is depicted in Figure 3. Each domain has six putative transmembrane-spanning segments (S1-S6) along with a reentrant hydrophobic pore loop (P-loop) between S5 and S6. Ion selectivity through the pore is conferred by the selectivity filter located in the P-loop. For voltage-gated sodium channels, the DEKA residues in each domains P-loop

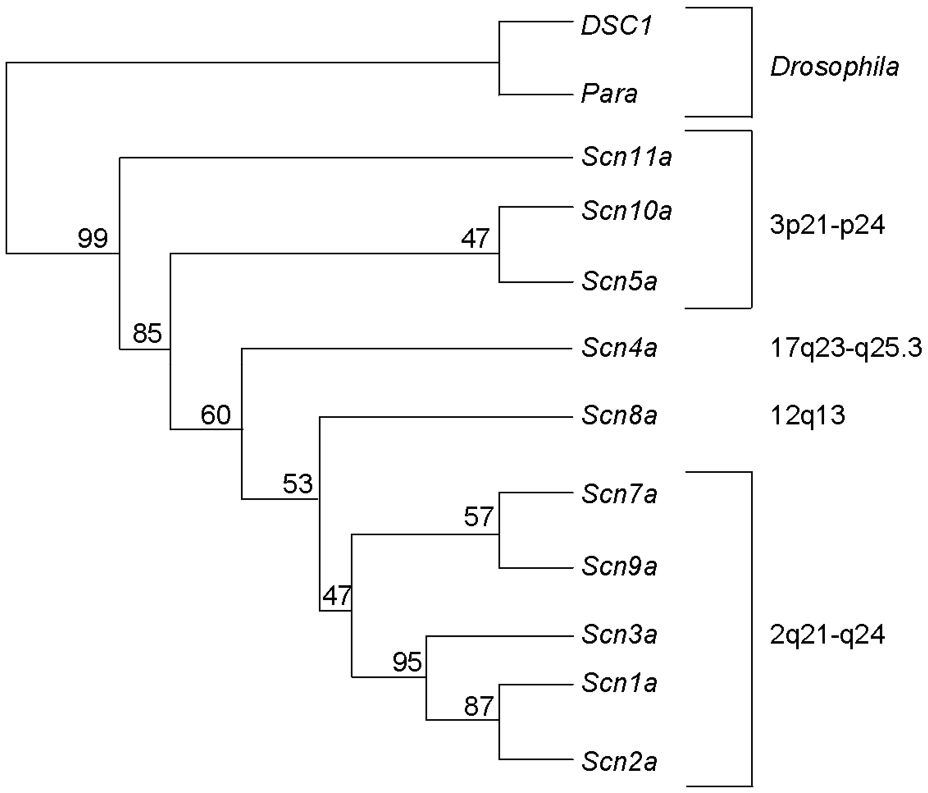

Figure 2. Evolutionary diversity of voltage-gated sodium channels. Adapted from (Plummer and Meisler, 1999) showing phylogenetic relationships of the rodent and drosophila voltage-gated sodium channel α isoforms. The percentage conservation between protein sequences is shown as is the chromosomal location for the human orthologs.

Figure 3. Schematic of a voltage-gated sodium channel. One sodium channel α isoform is shown with key structural elements including the intracellular amino (N) and carboxy (C) termini. The main pore-forming α subunit has four domains (D1-D4) that have homologous elements and are comprised of six transmembrane-spanning segments (S1-S6) each. The S4 segment contains positively charged residues that allow it to act as the voltage sensor by moving through the lipid bilayer in response to changes in voltage. The reentrant loop between each S5 and S6 are pore loops (P-loop) with the selectivity filter to determine what ion species can pass. For voltage-gated sodium channels, the important selectivity filter residues are the DEKA residues. The fast inactivation gate is on the D3-D4 linker with critical IFM residues. On either side of the α subunit are the β_1 and β_2 subunits which are single transmembrane domain proteins. The extracellular amino terminus has an immunoglobulin (Ig) fold and the intracellular carboxy terminus has several important regulatory sites.

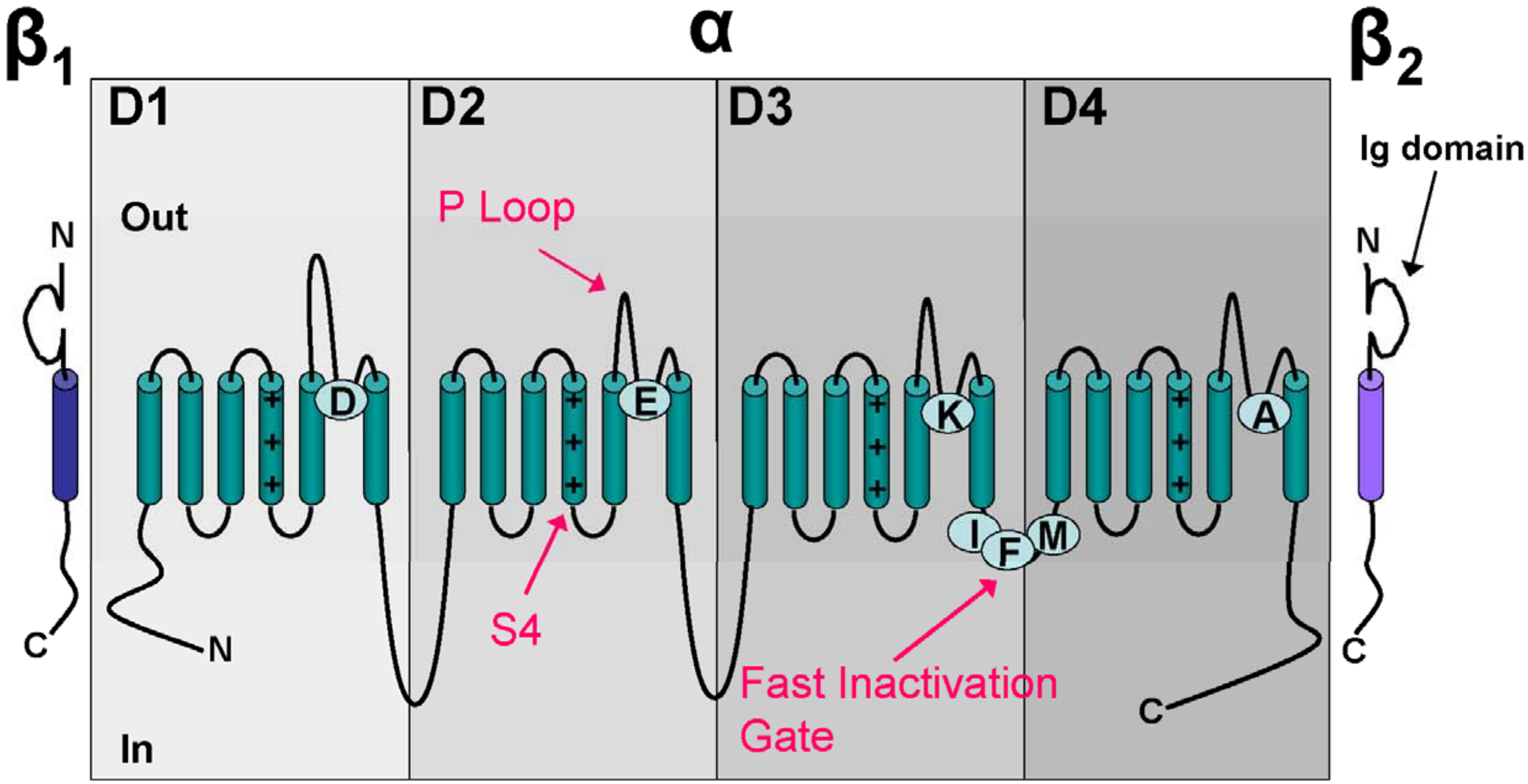
β1
α
β2
D1
D2
D3
D4
Ig domain
Out
P Loop
N
N
D
E
K
A
+
+
+
I
F
M
S4
C
N
C
Fast Inactivation Gate
C
In

are important for preferential Na^+ conductance through the channel pore (Figure 3). The voltage sensor of the sodium channel is comprised of the four S4 helices, which contain arginine (R) or lysine (K) residues (basic amino acids) at every third position (Figure 3). These positively charged residues are thought to move through the lipid bilayer in response to voltage changes allowing the sodium channel to change conformations (Stühmer et al., 1989).

Neuronal sodium channels are thought to be formed by one α subunit along with the β_1 and β_2 subunits as shown in Figure 3 (Catterall, 2000). The role of voltage-gated sodium channel complexes with β_3 and β_4 *in vivo* is still largely undetermined. The β subunit structure consists of a large extracellular amino-terminal domain, one transmembrane domain, and a small cytoplasmic carboxy-terminal domain (Figure 3) (Hanlon and Wallace, 2002). The amino terminus has a large immunoglobulin (Ig) domain with critical cysteine residues. The carboxy terminus has many regulatory sites. There are four known β subunits encoded by the genes *SCN1B-SCN4B*. In heterologous expression systems, co-expression of the β_1 subunit increases current density and accelerates both activation and inactivation (Isom et al., 1992). Similarly, co-expression of the β_2 subunit increases current amplitude and modulates gating (Isom et al., 1995). The β_1 and β_2 subunits also regulate localization of α subunits through interactions with cytoskeletal proteins (Malhotra et al., 2000; McEwen et al., 2004). The β_3 and β_4 subunits are less well characterized than the originally identified β_1 and β_2 isoforms leading to a largely unknown role for these subunits in the brain (Morgan et al., 2000; Yu et al., 2003).

Voltage-gated sodium channels open and close in response to changes in membrane potential. According to the classical model developed by Hodgkin and Huxley (Hodgkin and Huxley, 1952b; Hodgkin and Huxley, 1952c; Hodgkin and Huxley, 1952d; Hodgkin and Huxley, 1952a), two kinetic processes control changes in ionic permeability in excitable membranes: activation and inactivation. Membrane depolarization that opens (activates) sodium channels will result in a rapid, localized rise in sodium permeability. The increased sodium permeability is short-lived due to a rapid inactivation process, which is thought to be coupled to activation. Fast inactivation serves to limit the total amount of Na^+ that enters the cell and is critical for action potential repolarization at nodes of Ranvier (Ulbricht, 2005). A cytoplasmic linker between domains III and IV with the critical IFM residues acts as a hinge, docking to the S4-S5 loops of domains III and IV to mediate fast inactivation (Figure 3) (Stühmer et al., 1989; West et al., 1992). Upon repolarization, sodium channels enter the closed state and release the fast inactivation gate in preparation for the next cycle of depolarization and action potential initiation. A distinct slower form of inactivation has been described, but this mechanism remains less clear than fast inactivation (Ruben et al., 1992; Vilin et al., 1999). Slow inactivation is likely important *in vivo* because it has been observed in mammalian neurons. Channel availability following prolonged depolarization or repetitive stimulation and regulation of excitability are thought to be determined by slow inactivation (Ulbricht, 2005).

Localization of neuronal voltage-gated sodium channels

The nine isoforms of voltage-gated sodium channel α subunits have distinct expression patterns within the brain, peripheral nerves, ganglia, heart, skeletal muscle, glia, and certain neuroendocrine tissues shown in Table 2 (Noda et al., 1986) (Trimmer et al., 1989; Gautron et al., 1992; George, Jr. et al., 1992; Klugbauer et al., 1995). Mutations in many of the human voltage-gated sodium channel α isoforms have been identified in a wide variety of diseases (Table 2). SCN1A, SCN2A, SCN3A, and SCN8A encoding $Na_V1.1$, $Na_V1.2$, $Na_V1.3$, and $Na_V1.6$ respectively, are found at high levels in the central nervous system (CNS). Several groups have used antibodies directed against the four brain isoforms to determine the cellular and subcellular localization in both rodent and human brains. Subtype specific antibodies have also been employed to study the developmental expression patterns of neuronal voltage-gated sodium channels. Regarding the primarily neuronal subunits, several genetic epilepsy syndromes are associated with mutations in human SCN1A and SCN2A. There were recently reported epilepsy mutations in human SCN3A but currently there are no known mutations in human SCN8A that are associated with genetic epilepsy. The epilepsy phenotypes associated with neuronal voltage-gated sodium channels will be explored below in detail. SCN1A and SCN2A share 87% amino acid identity (Plummer and Meisler, 1999), have distinct expression patterns in the CNS, and most likely have different functional roles within neurons. The goal of this thesis research is to understand the molecular basis of inherited epilepsy disorders through studying SCN1A and SCN2A mutations in multiple model systems.

In rodent and human brains, $\mathrm{Na_V}1.1$ is generally found on the soma or dendritic trees of neurons, whereas $\mathrm{Na_V}1.2$ mostly localizes to axons and fiber tracts. $\mathrm{Na_V}1.1$ is expressed at moderate levels in the hippocampus. Dentate granule cells and interneurons in the dentate hilus show strong immunoreactivity to $\mathrm{Na_V}1.1$. Somatic and proximal dendrites of pyramidal cells within the CA1, CA2, and CA3 subregions of the hippocampus also express $\mathrm{Na_V}1.1$ (Gong et al., 1999; Whitaker et al., 1999; Whitaker et al., 2000; Whitaker et al., 2001). Recent studies also show $\mathrm{Na_V}1.1$ at the axon initial segment of parvalbumin (PV) interneurons in the developing mouse cortex and at the somata and axon initial segment of PV interneurons in the developing hippocampus (Ogiwara et al., 2007).

Early in development $\mathrm{Na_V}1.2$ is highly expressed in areas destined to become nodes of Ranvier but are developmentally replaced by $\mathrm{Na_V}1.6$ in adult rat brains (Kaplan et al., 2001). $\mathrm{Na_V}1.2$ is enriched at axon initial segments in developing neurons and

Table 2. Mammalian voltage-gated sodium channel genes

Gene	**Protein**	**Major expression**	**Minor expression**	**Disorders**
SCN1A	$Na_V1.1$	CNS, PNS	Cardiac muscle	Epilepsy, FHM
SCN2A	$Na_V1.2$	CNS, PNS		Epilepsy
SCN3A	$Na_V1.3$	CNS, PNS		Epilepsy
SCN4A	$Na_V1.4$	Skeletal muscle		Myotonia, periodic paralysis
SCN5A	$Na_V1.5$	Cardiac muscle	Skeletal muscle, brain	LQTS, Brugada syndrome, SIDS
SCN8A	$Na_V1.6$	CNS, PNS	Cardiac muscle	
SCN9A	$Na_V1.7$	PNS		Primary erythermalgia
SCN10A	$Na_V1.8$	PNS		
SCN11A	$Na_V1.9$	PNS		
SCN1B	β_1	CNS	Skeletal muscle, cardiac muscle	Epilepsy
SCN2B	β_2	CNS		
SCN3B	β_3	CNS		
SCN4B	β_4	CNS		

Abbreviations as follows: CNS – central nervous system, PNS – peripheral nervous system, FHM – familial hemiplegic migraine, LQTS – long QT syndrome, SIDS – sudden infant death syndrome.

unmyelinated axons in the adult brain (Boiko et al., 2003; Garrido et al., 2003b; Garrido et al., 2003a; Westenbroek et al., 1989; Westenbroek et al., 1992). In contrast to $Na_V1.1$, $Na_V1.2$ is located on axons and terminals of many hippocampal pathways including the perforant path that arises from the entorhinal cortex and projects through the middle third of the molecular layer of the dentate gyrus. $Na_V1.2$ is associated with dentate granule cell axons called mossy fibers located just above the pyramidal neurons in region CA3. Additionally, $Na_V1.2$ is expressed near the termination of the Schaffer collaterals, which are projections from CA3 to CA1. An exception to the usual expression pattern of $Na_V1.2$ is the somatodendritic expression of $Na_V1.2$ on CA1 pyramidal neurons (Gong et al., 1999; Whitaker et al., 1999; Whitaker et al., 2000; Whitaker et al., 2001).

In the cerebellum, $Na_V1.1$ is moderately expressed somatodendritically in granule cells, Purkinje cells, other cells within the molecular layer, and cells of the deep cerebellar nuclei. Surprisingly, $Na_V1.1$ was also expressed along distal axons of developing mouse cerebellar fibers (Ogiwara et al., 2007). Unlike $Na_V1.1$, $Na_V1.2$ immunoreactivity is diffusely seen throughout the molecular layer of the cerebellum probably associated with terminals and axons such as the parallel fibers of granule cells (Gong et al., 1999; Whitaker et al., 1999; Whitaker et al., 2000; Whitaker et al., 2001).

Northern blot and in situ hybridization experiments examining the distribution of β subunit mRNAs have shown distinct regional expression patterns within human and rodent brains. In the hippocampus, both β_1 and β_2 are highly expressed in the CA regions and dentate gyrus and are weakly expressed in hilar neurons. In the cerebellum, the β_1 subunit is highly expressed in the granular layer, in Purkinje cells, and deep cerebellar nuclei and moderately expressed in the molecular layer. The β_2 subunit is also strongly expressed in the granular layer and in Purkinje cells, but is only weakly associated with the molecular layer and deep cerebellar nuclei (Whitaker et al., 1999; Whitaker et al., 2000). In contrast to β_1, the β_3 subunit expression begins early in development and is maintained at a high level of expression in the adult brain (Shah et al., 2001). The β_3 subunit in the adult rat brain is highly expressed in forebrain structures of the olfactory system, layers II and III of the neocortex, and CA subfields of the hippocampus (Morgan et al., 2000). β_4 is expressed in pyramidal neurons of the cortex and hippocampus, a subset of hilar neurons, and highly expressed in dorsal root ganglia (DRG), Purkinje cells and deep cerebellar nuclei (Yu et al., 2003).

Neuronal voltage-gated sodium channels associated with epilepsy

Throughout the central nervous system, voltage-gated sodium channels are critical for the initiation and propagation of action potentials. Voltage-gated sodium channels are important pharmacological targets for anticonvulsant therapeutics (Macdonald and Greenfield, Jr., 1997; Catterall, 1999) and over 300 mutations have been linked to some forms of genetic epilepsy (Mulley et al., 2005; Meisler and Kearney, 2005; Harkin et al., 2007; Herlenius et al., 2007; Holland et al., 2008; Zucca et al., 2008). One genetic epilepsy syndrome with encephalopathic features is SMEI, formerly known as Dravet Syndrome. SMEI causes FS during the first year of life followed by progression to intractable epilepsy, impaired psychomotor development, and ataxia (Scheffer et al., 2001). In this rare convulsive disorder, the seizures are typically resistant to anticonvulsant therapeutics. Greater than 70% of SMEI patients have a mutation in *SCN1A* in some populations (Zucca et al., 2008), whereas other studies have identified $Na_V1.1$ mutations in only one-third of SMEI cases (Wallace et al., 2003). Over 180 heterozygous mutations in *SCN1A* have been reported in SMEI patients. Many of the SMEI mutations are nonsense mutations leading to premature truncation, or insertions or deletions that shift the open reading frame. Many of the nonsense or frameshift mutations would encode non-functional sodium channels. Other SMEI alleles are missense mutations that more likely are functional and may exhibit a mix of gain- or loss-of-function (Mulley et al., 2005; Harkin et al., 2007; Zucca et al., 2008).

GEFS+ is a less severe form of genetic epilepsy. GEFS+ patients experience FS and other types of afebrile seizures beyond six years of age. The inheritance of GEFS+ is autosomal dominant with incomplete penetrance and a high rate of phenocopy. Mutations in genes encoding voltage-gated sodium channel α (*SCN1A*, *SCN2A*) (Escayg et al., 2000b; Sugawara et al., 2001) or β_1 (*SCN1B*) (Wallace et al., 1998) and the $GABA_A$ receptor subunit (*GABRG2*) (Baulac et al., 2001a; Wallace et al., 2001) have been associated with GEFS+. In many cases of GEFS+ there is no identifiable mutation in one of the four genes listed above. It is thought that about 17% of all GEFS+ cases are due to mutations in a voltage-gated sodium channel gene (Nakayama and Arinami, 2006). Common clinical characteristics and similar genetic etiologies suggest that GEFS+ and SMEI, may represent a spectrum of the same disease (Singh et al., 2001).

Intractable childhood epilepsy with generalized tonic-clonic seizures (ICEGTC) is an epilepsy syndrome that is also hypothesized to reside in the GEFS+ and SMEI spectrum with an intermediate severity (Stafstrom, 2003). The seizures begin prior to one year of age often during fever and are accompanied with mental decline. Another distinguishing feature of ICEGTC is the presence of diffuse theta waves on electroencephalogram (EEG). Mutations in *SCN1A* are the only known cause of ICEGTC (Fujiwara et al., 2003; Osaka et al., 2007).

Other epilepsy phenotypes are uncommonly linked to alterations in *SCN1A*. The triad of symptoms associated with West Syndrome include IS, hypsarrythmia and developmental regression. West Syndrome is often found in the presence of metabolic or structural brain abnormalities. About one-third of cases have a positive family history of FS or idiopathic epilepsy. Two missense point mutations in *SCN1A* were identified in

IS patients with West Syndrome, but only one alters a highly conserved residue (Wallace et al., 2003). Temporal lobe epilepsy (TLE), one of the most common forms of partial epilepsy, initially was primarily considered to be an acquired disorder with little known about its inheritance (Baulac et al., 2001b). Now there are two reports in the literature of *SCN1A* mutations in either FS or GEFS+ families and one *SCN1B* mutation in a GEFS+ family that had a few family members who subsequently developed TLE (Abou-Khalil et al., 2001; Colosimo et al., 2007; Scheffer et al., 2007). Recently, mutations in *SCN1A* have also been identified in cryptogenic epilepsy syndromes (Zucca et al., 2008). Interestingly, a few mutations in $Na_V1.1$ have also been identified in familial hemiplegic migraine (FHM), a rare headache disorder with concomitant epilepsy in some family members. The relationship between migraine and epilepsy is a novel source for investigation (Dichgans et al., 2005; Thomsen et al., 2007; Vanmolkot et al., 2007; Gargus and Tournay, 2007).

Rarely dysfunction of $Na_V1.2$ is found in severe epilepsy cases. There has been one report of a GEFS+ phenotype segregating with a mutation in *SCN2A* (Sugawara et al., 2001). A nonsense mutation in *SCN2A* that disables channel function has been associated with an unclassified, malignant epilepsy similar to SMEI (Kamiya et al., 2004). Epilepsy syndromes linked to neuronal sodium channel mutations may also have benign phenotypes causing seizures only during infancy and early childhood before spontaneous remission. Rarely a mutation in $Na_V1.2$ has resulted in benign familial infantile seizures (BFIS) (Striano et al., 2006a). BFIS is an epilepsy syndrome that affects children in the first few months of life but resolves within one year. BFIS is more commonly associated with dysfunction of the *ATP1A2* gene (Striano et al., 2006b). Eight missense mutations in *SCN2A* are associated with a mild form of epilepsy known as benign familial neonatal-infantile seizures (BFNIS). The clinical characteristics of BFNIS are slightly distinct from BFNC but may share some overlapping features with BFIS

(Striano et al., 2006b). BFNIS is an autosomal dominant disorder with onset during early infancy that remits by one year of age and has no known long-term neurological sequelae. Afebrile secondarily generalized partial seizures and rare febrile seizures characterize BFNIS (Kaplan and Lacey, 1983; Heron et al., 2002; Berkovic et al., 2004; Herlenius et al., 2007). The factors that distinguish benign from malignant epilepsy syndromes caused by sodium channel mutations are currently unknown. One important goal of this thesis research is to understand the functional consequences of *SCN2A* mutations in the mild BFNIS phenotype for comparison with other brain sodium channel defects associated with more severe epilepsy phenotypes.

Screening *SCN1A* and *SCN2A* for genetic mutations in familial epilepsy syndromes has become more common, but the other sodium channels predominantly expressed in brain, *SCN3A* and *SCN8A*, had not been as widely investigated or implicated in inherited epilepsies. Recently children with pharmacoresistant cryptogenic pediatric partial epilepsy were screened for mutations in *SCN3A*. The diagnosis was made when partial epilepsy was confirmed and was labeled cryptogenic when other structural abnormalities, neurological disorders, or idiopathic epilepsy syndromes were ruled out. One mutation and 12 novel SNPs in *SCN3A* were identified thereby implicating $Na_V1.3$ dysfunction as a cause of epilepsy (Holland et al., 2008).

Functional studies of epilepsy-associated voltage-gated sodium channel mutants

The fastest approach to obtain functional data from epilepsy mutations has been through electrophysiological experiments of heterologously expressed mutant sodium channel. Functional studies of epilepsy mutations in voltage-gated sodium channels primarily make use of heterologous expression in a transformed mammalian cell line, commonly tsA201 or CHO-K1 cells. The recombinant sodium channel may be transiently transfected alone or in combination with auxiliary β subunits. Earlier studies introduced the mutation into a non-neuronal voltage-gated sodium channel isoform or a rodent ortholog of *SCN1A* or *SCN2A* that is more amenable to site-directed mutagenesis. The transfected cells are subjected to whole-cell voltage clamp recording with relatively standard protocols to assess current-voltage (I-V) relationship, voltage dependence of activation, fast inactivation, and other parameters. Another heterologous expression model system that some researchers utilized was two-electrode voltage clamp (TEVC) in *Xenopus* oocytes injected with cRNA encoding the wild-type (WT) or mutant sodium channel. One major goal of heterologous expression studies is to make genotype-phenotype correlations where multiple mutations linked to one epilepsy syndrome may cause similar disturbances in sodium current explaining the common disease phenotype.

To date functional studies of $Na_V1.1$ mutations associated with GEFS+, SMEI, ICEGTC, TLE and $Na_V1.2$ mutations associated with GEFS+, SMEI, and BFNIS have been performed (Alekov et al., 2000; Sugawara et al., 2001; Lossin et al., 2002; Lossin et al., 2003; Rhodes et al., 2004; Spampanato et al., 2004b; Kamiya et al., 2004; Rhodes et al., 2005; Mantegazza et al., 2005; Ohmori et al., 2006; Barela et al., 2006; Scalmani et al., 2006; Xu et al., 2007b). The biophysical function of each mutation differs slightly based on which heterologous expression system was used. Biophysical phenotypes run a large range from nonfunctional sodium currents to small differences in comparison to WT. Below biophysical defects affecting different parameters identified by experiments using heterologous expression systems are highlighted (Table 3).

Perturbations in the voltage dependence of activation lead to a change in the magnitude of depolarization needed for the channel to open and conduct sodium ions. A few GEFS+ mutations, including I1656M and R1657C, caused positive shifts in the voltage dependence of activation in comparison to WT-$Na_V1.1$. These two mutations disrupt conserved residues in the D4/S4 segment and may alter neuronal excitability by requiring a greater membrane depolarization for the channel to activate (Lossin et al., 2003). A different *SCN1A* GEFS+ mutation, W1204R caused a negative shift in activation allowing the channel to open at more negative membrane potentials (Lossin et al., 2002; Spampanato et al., 2003). Opposing shifts in the voltage dependence of activation by GEFS+ mutations exemplifies the difficulty with making generalizations about how biophysical defects are causing disease.

Whole-cell current decay, voltage dependence of fast inactivation and recovery from fast inactivation are important for determining the duration of sodium conductance and the ability of the channel to reset for subsequent depolarizations. The GEFS+ mutation in $Na_V1.2$, R188W, delayed whole-cell current decay. R188W also caused a negative shift in the voltage dependence of fast inactivation. The impairments in fast inactivation caused by R188W predict an increased sodium conductance that could cause hyperexcitability (Sugawara et al., 2001). The T875M mutation in $Na_V1.1$ was identified in GEFS+ patients and exhibited a delayed recovery in fast inactivation. Alternatively, the $Na_V1.1$ mutations R1648H, R1648C, and F1661S all accelerated recovery from fast inactivation (Lossin et al., 2002; Lossin et al., 2003). The recovery from fast inactivation findings are another example of one parameter that is altered in opposing ways by mutations associated with the same Mendelian epilepsy.

Slow inactivation is thought to regulate channel availability following prolonged depolarization or repetitive stimulation. The *SCN1A* GEFS+ mutation R1657C accelerated recovery from slow inactivation (Lossin et al., 2003). On the other hand, the $Na_V1.1$ mutations F1661S and R859C delayed recovery from slow inactivation (Rhodes et al., 2004; Barela et al., 2006). Thus deficits in slow inactivation appear to cause dysfunctional sodium channels leading to alterations in neuronal excitability.

Many other defects in sodium channel function have been linked to the pathogenesis of monogenetic epilepsies. GEFS+ and SMEI $Na_V1.1$ mutations, including R1648H and R1648C, exhibited increased persistent sodium current that can be

Table 3. Biophysical defects from heterologous expression systems

Biophysical abnormality	**Mutation**	**Syndrome**
Depolarized voltage dependence of activation (h*SCN1A*, tsA201 cells) (r*Scn1a*, *Xenopus* oocytes)	I1656M, R1657C R859C	GEFS+
Hyperpolarized voltage dependence of activation (r*Scn1a*, *Xenopus* oocytes / h*SCN1A*, tsA201 cells)	W1204R	GEFS+
Delayed whole-cell current decay / Hyperpolarized voltage dependence of fast inactivation (r*Scn2a*, HEK293 cells)	R188W*	GEFS+
Delayed recovery from fast inactivation (h*SCN1A*, tsA201 cells)	T875M	GEFS+
Accelerated recovery from fast inactivation (h*SCN1A*, tsA201 cells)	R1648H R1648C, F1661S	GEFS+ SMEI
Delayed recovery from slow inactivation (h*SCN1A*, tsA201 cells) (r*Scn1a*, *Xenopus* oocytes)	F1661S R859C	SMEI, GEFS+
Accelerated recovery from slow inactivation (h*SCN1A*, tsA201 cells)	R1657C	GEFS+
Increased persistent current (h*SCN1A*, tsA201 cells)	R1648H R1648C F1808L	GEFS+ SMEI ICEGTC
Increased late openings, longer mean open time by single channel analysis (h*SCN1A*, tsA201 cells)	R1648H	GEFS+

Decreased interaction with β_1 (r*Scn1a*, *Xenopus* oocytes)	D1866Y	GEFS+
Decreased use-dependent channel behavior (h*SCN1A*, tsA201 cells)	V893A, F1808L	ICEGTC
Decreased current density (h*SCN1A*, tsA201 cells) (h*SCN1A*, HEK293 cells)	G1749E R712X, G979R	SMEI
Dominant negative effect on WT channel (h*SCN2A*, HEK293 cells)	R102X*	SMEI
Nonfunctional sodium channels (h*SCN1A*, tsA201 cells)	A1685V, V1353L T1902I L986F, F902C, G1647R	GEFS+ ICEGTC SMEI

* denotes mutation in *SCN2A*. All other mutations were identified in *SCN1A*. The heterologous expression system used is in parentheses. The h denotes human and r denotes rat for the sodium channel α isoform characterized in the study.

observed during the end of a depolarizing voltage step. Increased late sodium current is hypothesized to increase sodium conductance leading to a more depolarized resting membrane potential (Lossin et al., 2002; Lossin et al., 2003). Single channel recordings have rarely been performed on WT or mutant $Na_V1.1$, but can provide information that is unattainable through whole-cell methods. The R1648H GEFS+ mutation was found to have increased late openings and longer mean open time compared to WT-$Na_V1.1$. These findings are thought to explain the increase in persistent current seen at the whole-cell level (Vanoye et al., 2006). A weakened interaction between α and β_1 subunits leading to a less hyperpolarized voltage dependence of inactivation in the presence of β_1 was observed for D1866Y, a GEFS+ mutation in *SCN1A* (Spampanato et al., 2004b). Interaction with β subunits is critical for proper sodium channel function, localization, and expression levels so loss of this interaction could result in epilepsy (Isom et al., 1995; Malhotra et al., 2000; McEwen et al., 2004).

Many SMEI mutations encode nonsense or frameshift mutations that are predicted to encode nonfunctional sodium channels. However, some SMEI, ICEGTC, and GEFS+ missense mutations also result in nonfunctional sodium channels (Table 3). Two possible explanations for nonfunctional sodium channels are that the proteins have aberrant trafficking or that the channel is unable to conduct Na^+ (Lossin et al., 2003; Rhodes et al., 2004; Rhodes et al., 2005; Ohmori et al., 2006). Other SMEI mutations result in significantly reduced sodium current but are not entirely nonfunctional (Sugawara et al., 2003; Ohmori et al., 2006). One interesting $Na_V1.2$ mutation identified in a SMEI patient encodes a premature stop codon before the first transmembrane segment and is nonfunctional when expressed alone. When R102X is coexpressed with WT-$Na_V1.2$, it acts in a dominant negative fashion to decrease sodium current (Kamiya et al., 2004).

Recently there has been recognition that overexpression in non-neuronal cell lines may not be providing enough information to determine mechanisms underlying the epilepsy pathology or to reconcile the varied biophysical defects with clinical phenotype. Some groups have been trying to transfect acutely isolated neurons with recombinant sodium channels in the hope that the neuronal background will more closely resemble the physiological state (Scalmani et al., 2006). Unfortunately homogenous populations of neurons are difficult to isolate, transfect, maintain, and use in whole-cell voltage clamp experiments. Distinguishing mutant sodium current from the endogenous current can also be difficult depending on what electrophysiological methods are employed. Also overexpression of the sodium channel may overwhelm the endogenous interacting proteins that would regulate expression under normal physiological conditions. Below two other avenues of investigation for mutant voltage-gated sodium channels are discussed.

Computational models of voltage-gated sodium channels

Initial attempts to utilize computational modeling to simulate WT and mutant sodium channel function have followed the Hodgkin-Huxley (HH) mechanism of independent gating processes (Hodgkin and Huxley, 1952a). These computational models have been able to approximate some aspects of sodium channel function, especially the activation properties of the channel. $Na_V1.1$ channel models were created to hypothesize the effect of epilepsy-associated mutations on neuronal excitability parameters including action potential threshold and firing patterns (Spampanato et al., 2004a; Spampanato et al., 2004b; Barela et al., 2006). But the HH type models do not adequately recapitulate the fast inactivation and slow inactivation properties in part because activation and fast inactivation processes are coupled (Cha et al., 1999; Kuhn and Greeff, 1999). This makes it difficult to evaluate conclusions about neuronal excitability derived from HH $Na_V1.1$ models. Empirical and thermodynamic models have also been made to try and generate sodium channel behavior, but these models are also unable to simulate all aspects of sodium current (Patlak, 1991).

A newer approach to computational investigation of voltage-gated sodium channels utilizes Markov chain models. Markov chain models are based upon the idea of stochastic processes such that transitioning from one state to the next depends upon a probabilistic transition. The Markov chain models are better suited for replicating the sodium channel properties and for examining the contribution of the sodium channel to neuronal excitability (Vedantham and Cannon, 1998; Irvine et al., 1999). Computational models of $Na_V1.1$ using the Markov chain model more accurately emulate biophysical data and will hopefully suggest mechanisms for altered sodium current causing epilepsy (Clancy and Kass, 2004; Kahlig et al., 2006b). The sodium channel models should be validated by comparing the model to empirically derived biophysical data of many sodium channel parameters including activation, fast inactivation, slow inactivation, and persistent current.

Once accurate channel models exist, they can be inserted into different sized modeling environments including a simple cylindrical unit, singular cells, or complex neuronal networks. A simple cylindrical unit would allow one to refine the sodium channel model and test channel function or mutation effects without competing ion channel conductances. Inserting the $Na_V1.1$ model into a single neuron or neuronal network would provide a more realistic representation of how the model functions *in vivo* (Xu and Clancy, 2008). Freely accessible databases contain models of multiple neuron types that have incorporated data from morphology and physiology experiments. In addition to simulating a neuronal environment, another avenue for investigation is *in silico* pharmacology where the channel models can be tested against theoretical drugs to aid in rational drug design.

The major downside to computational modeling is the large amount of user control over a wide array of parameters. Some of these parameters have no supporting data so the user must make decisions about what values to use. A few of these parameters that are difficult to determine include sodium channel expression levels, subcellular localization of sodium channels, effects of auxiliary subunits, and similar considerations for other ion channels within the same compartment. Single neuron or neuronal network modeling environments are improving constantly, but cannot yet compete with using a biological model system derived from animal brain. Even with these potential disadvantages, computational modeling provides a robust way for us to better understand empirically derived data as well as guide future experiments.

Animal models of epilepsy with defective sodium channels

One way to obtain relevant physiological and behavioral data on sodium channel mutations is through the use of animal models of epilepsy. Early models involved inducing seizures through chemical or electrical means as in the case of kindling. Other models were obtained through spontaneous random mutations in inbred rat or mouse strains. As techniques for engineering genetically altered animals have become refined, several mouse models focused on sodium channel dysfunction have been developed (Table 4). Here we will discuss in detail only those mouse models that are relevant to later chapters.

In 2000, a characterization of mice with targeted disruption of *SCN2A* was published. The homozygous knockout mice exhibited perinatal lethality, or death by postnatal day (P) 2. The sodium currents from cultured hippocampal pyramidal cells showed a dramatic reduction in maximum conductance for the homozygous knockout and a modest reduction in maximum conductance for the hemizygous mice. No seizure activity was measured in either the homozygous knockout or hemizygous animals. The

Table 4. Mouse models of sodium channel mutations with neurological disorders

Gene	Channel	Mutation	Disorder
SCN1A	$Na_V1.1$	Targeted null	Homozygous lethal at P15, seizures and ataxia
		R1407X	Homozygous lethal after P18, seizures and ataxia
SCN2A	$Na_V1.2$	Q54 Transgene (GAL879-881QQQ)	Dominantly inherited TLE
		Targeted null	Homozygous lethal at P2
SCN8A	$Na_V1.6$	Spontaneous null	Paralysis, lethal
		Null heterozygote	Learning deficits
		A1071T	Ataxia, tremor
		Hypomorph (medJ)	Dystonia
		Conditional null	CRE-dependent lethal
SCN9A	$Na_V1.7$	Targeted null	Lethal
		Conditional null	Pain resistant
SCN10A	$Na_V1.8$	Targeted null	Pain resistant
SCN1B	β_1	Targeted null	Homozygous lethal by P26, seizures
		Conditional null	Not lethal
SCN2B	β_2	Targeted null	Homozygote susceptible to seizures

homozygous knockout animals lost weight during the first two days of life and appeared to have hypoxia that was presumed to be the cause of death. Homozygous knockout animals had normal neuroanatomy, but at the ultrastructural level mitochondrial disruptions and increased vacuolization were visualized. The heterozygous animals had normal life spans and no difficulty breeding (Planells-Cases et al., 2000).

The next mouse model was developed prior to identification of human mutations in voltage-gated sodium channels. A mutation in rat *Scn2a*, GAL879-881QQQ, caused impaired fast inactivation and increased persistent current when examined by TEVC in *Xenopus* oocytes. The GAL879-881QQQ mutation was inserted as a transgene into the mouse genome. The transgenic mice called Q54 exhibited spontaneous seizures of hippocampal origin similar to a dominantly inherited TLE within the first two months of life. Hippocampal CA1 pyramidal neurons isolated from the Q54 mice had significantly increased persistent sodium current compared with WT littermates and transgenic mice overexpressing WT *Scn2a* (Kearney et al., 2001).

Mice with targeted knockout of the auxiliary β_1 and β_2 subunits have also been characterized. Knockout of the β_2 subunit resulted in decreased sodium current density and a negatively shifted voltage dependence of inactivation in acutely isolated hippocampal neurons. Additionally the *SCN2B* null mice displayed an increase in seizure susceptibility by pilocarpine induction (Chen et al., 2002). Knockout of the β_1 subunit resulted in decreased $Na_V1.1$ and increased $Na_V1.3$ expression in a subset of pyramidal neurons in the CA2/CA3 regions of the hippocampus despite normal sodium currents. These mice had spontaneous generalized seizures and appeared ataxic (Chen et al., 2004). Recently mice with a floxed allele of *Scn1b* were made to study conditional inactivation of the β_1 subunit to allow for more specific investigation of the mechanism underlying the epilepsy phenotype (Chen et al., 2007).

In 2006, a study was published characterizing knockout of *Scn1a* in mice by disrupting the last coding exon (exon 26). Mice with only one $Na_V1.1$ allele were predicted to be a model for SMEI because many SMEI mutations lead to nonfunctional channels causing a haploinsufficiency. Hemizygous mice had spontaneous behavioral seizures and sporadic death beginning between P21 and P27. The hemizygous mice were often found dead from a presumed status epilepticus episode. EEG recordings showed the hemizygous mice having both clonic and tonic-clonic seizures. Homozygous knockout mice developed spontaneous seizures and ataxia around P9. Initially homozygous knockout animals lost postural control but by P15 had spontaneous generalized clonic and forelimb convulsive seizures. The null animals died on P15 from starvation or dehydration. Both hemizygous and homozygous null mice had decreased sodium currents specifically in acutely isolated bipolar neurons of the hippocampus and altered action potential amplitude and width. Acutely isolated hippocampal pyramidal neurons had normal sodium current leading to the hypothesis that the SMEI phenotype was the result of dysfunctional GABAergic interneurons (Yu et al., 2006).

Another mouse model of SMEI was made by targeted insertion of R1407X (RX) into *Scn1a*. The RX mutation was identified in multiple unrelated SMEI patients (Sugawara et al., 2002; Fujiwara et al., 2003; Fukuma et al., 2004) and was nonfunctional when heterologously expressed in HEK293 cells (Sugawara et al., 2003). The RX/RX mice became ataxic by P10 with increased difficulty for feeding and developed spontaneous, recurring clonic and tonic-clonic seizures between P12 to P16. Homozygous animals all died within the first three weeks of life. The heterozygous mice began having spontaneous recurring seizures and sporadic death after P18. Neurons from heterozygous mice showed increased spike amplitude decrement and an I-V relationship with more rectification at negative potentials (Ogiwara et al., 2007).

Now that mouse models with varying severity of epilepsy syndromes exist, and more are being developed including conditional and tissue-specific targeted insertions, physiologically relevant mechanistic data are on the horizon. Experiments with the mouse models should provide better genotype-phenotype correlations than heterologous expression experiments have given. The mouse models may also provide a new way to investigate therapeutic strategies for the pharmacoresistant severe epilepsy syndromes.

The disadvantages of using animal models include the difficulty and expense associated with making and maintaining the models. The result is that only a few distinct animal lines for each epilepsy syndrome are created and some benign forms of epilepsy may never be investigated with an animal model. Also there are differences between rodents and humans leading to difficulty discerning what the differences are and how they affect the conclusions. In all likelihood, multiple experimental paradigms with the animal models will provide the most useful data to guide alterations therapeutic management of patients.

Research goals

Mutations in neuronal voltage-gated sodium channels lead to several genetic epilepsy syndromes. These genetic forms of epilepsy differ in phenotype with regards to age of onset, severity, presence of seizures in adulthood, and responsiveness to anticonvulsant therapeutics. This suggests that inter-individual genetic differences causing changes in the properties of the neuronal voltage-gated sodium channels may modulate epilepsy severity or determine the epilepsy syndrome. We pursued a series of experiments designed to understand the functional effects of epilepsy-associated mutations in brain voltage-gated sodium channels and the relationship with epilepsy severity. In order to try and form better genotype-phenotype correlations, the three model systems described above were utilized. Thus the primary goal of this dissertation research has been to examine epilepsy-associated voltage-gated sodium channel mutations in multiple model systems to gain a deeper understanding of the molecular mechanism underlying these disorders.

Specific Aims

As described above, there is a lot known about the structure-function relationship of large structural regions of voltage-gated sodium channels. However, there still remain many avenues of discovery because we cannot predict the functional outcomes of a particular disease-associated mutation. Additionally, we do not know why some missense mutations cause benign epilepsy syndromes while others cause severe or intractable forms of epilepsy.

One of the main ways to study epilepsy-associated mutations in voltage-gated sodium channels has been to overexpress the mutation in a heterologous expression system and perform whole-cell patch clamp studies. These studies have provided a large amount of information about kinetic and voltage dependent alterations in channel function. Problems with these studies include that the mutations are overexpressed in cells of non-neuronal origin and may not be associating with proper auxiliary subunits. Recent studies from mutations overexpressed in neurons or studies from animal models have shown that mutant channels may have different functional consequences in each model system. Future experiments will have to reconcile data from different experimental paradigms in order to move the field forward. Here we describe investigation of epilepsy-associated mutations in $Na_V1.1$ and $Na_V1.2$ using multiple model systems to gain a deeper understanding of the molecular mechanism underlying these disorders through the following specific aims:

Specific Aim I: Prediction of the impact of a neuronal sodium channel biophysical defect on neuronal excitability

Specific Aim II: Functional characterization of neuronal sodium channel mutations associated with genetic epilepsy syndromes

Specific Aim III: Characterization of neuronal sodium channels in cultured neurons from mutant Scn2a transgenic mice with differing seizure susceptibility

In Specific Aim I, we utilized previously recorded data from tsA201 cells heterologously expressing WT-Na$_V$1.1 to construct a model Na$_V$1.1. We hypothesized that the biophysical parameters of WT sodium channels could be generated *in silico* to create an accurate model of WT-Na$_V$1.1. Once a WT-Na$_V$1.1 model was created, we constructed a model of the well characterized GEFS+ mutant R1648H. Disruption of a highly conserved arginine residue in Na$_V$1.1 caused increased persistent sodium current when R1648H is heterologously expressed. We hypothesized that our computational models could be used to predict how the persistent sodium current caused by R1648H might alter neuronal excitability. The results of these experiments are described in more detail in Chapter Two.

In Specific Aim II, we sought to determine genotype-phenotype correlations for the benign epilepsy syndrome BFNIS associated with missense mutations in Na$_V$1.2 and for a novel MTLE mutation identified in *SCN1A*. We hypothesized that we would be able to identify biophysical parameters that differed between WT and mutant neuronal sodium channels. We predicted that mutant sodium channels would be functional but could cause alterations in peak sodium current density. We hypothesized that peak current density disturbances could be due to altered cell surface expression or channel trafficking. Experiments examining WT and BFNIS-associated Na$_V$1.2 mutations are described in Chapters Three and Four. Descriptions of experiments performed with the novel MTLE mutation in Na$_V$1.1 are in Chapter Five.

In Specific Aim III we moved out of heterologous expression systems and into a previously established mouse model of epilepsy. We utilized the Q54 transgenic mice on two different background strains that had significantly different seizure susceptibilities. Our collaborator had performed a genome wide scan and identified two modifier loci within the mouse genome that accounted for the majority of the differing seizure susceptibility. Although our collaborator has identified candidate genes in the modifier loci, the final modifier genes and corresponding functions are not yet known. Our hypothesis was that one of the modifier genes would directly affect the sodium channel transgene function. We performed whole-cell voltage clamp recordings on acutely isolated neurons to identify differences in voltage-gated sodium channel properties. We also used western blot analysis of membrane preparations isolated from whole brain of mice from the two different background strains to examine expression levels. Chapter Six describes the optimization steps and preliminary results from utilizing a mouse model of epilepsy studies.

CHAPTER II

IMPAIRED INACTIVATION GATE STABILIZATION PREDICTS INCREASED PERSISTENT CURRENT FOR AN EPILEPSY-ASSOCIATED *SCN1A* MUTATION

Introduction

Mutations in genes encoding voltage-gated sodium channel subunits have been linked to several inherited disorders of membrane excitability including defects in skeletal muscle contraction, cardiac arrhythmias and epilepsies (George, Jr., 2005). Currently, more than 300 *SCN1A* mutations have been associated with various genetic epilepsies (Mulley et al., 2005; Meisler and Kearney, 2005; Harkin et al., 2007; Herlenius et al., 2007; Holland et al., 2008; Zucca et al., 2008). Functional studies of these *SCN1A* mutants in heterologous systems have revealed an array of biophysical abnormalities that are difficult to fully reconcile with the observed clinical phenotype. *In vivo* $Na_V1.1$ generates and propagates action potentials within an integrative environment consisting of multiple ionic conductances, thus establishing correlations between genotypes and biophysical phenotypes will likely require examination of $Na_V1.1$ mutant behavior within such a context using either animal or computational models.

The majority of efforts to simulate sodium channel behavior using computational models (including $Na_V1.1$ (Spampanato et al., 2004b; Spampanato et al., 2004a; Barela et al., 2006)) have utilized the classic Hodgkin-Huxley (HH) formalism (Hodgkin and Huxley, 1952b). These equations define sodium permeability in terms of multiple identical gates operating independently. However, this approach is unable to account for all channel behaviors (Hille, 2001). For instance, although voltage-gated sodium channels are constructed of four homologous domains (DI-DIV), each domain does not contribute identically to channel gating (Hille, 2001). In addition, inactivation and activation are coupled because channel inactivation preferentially immobilizes the DIII and DIV associated activation gating movements (Cha et al., 1999; Kuhn and Greeff, 1999). Additional discrepancies between HH-predicted and experimentally observed sodium channel behavior have also been described including gating currents, current fluctuation analysis, single channel activity and activation kinetics (Baranauskas and Martina, 2006; Patlak, 1991; Hille, 2001; Naundorf et al., 2006).

Attempts to reconcile the experimental voltage-gated sodium channel behavior to a mathematical description of channel activity have produced numerous thermodynamic and empirical models (see reviews by Patlak (Patlak, 1991) and Hille (Hille, 2001)). More recently, Markov chain models have been developed for excitability simulation studies that more faithfully approximate the biophysical activity of sodium channels (Irvine et al., 1999; Clancy and Rudy, 1999; Clancy and Rudy, 2002; Vedantham and Cannon, 1998; Clancy and Kass, 2004). Computational investigations with accurate sodium channel models promise to guide empirical experimentation and to predict novel mechanisms of abnormal excitability (Clancy and Kass, 2003).

In this chapter we utilize an expanded Markov model for $Na_V1.1$ to better define molecular mechanisms for an epilepsy-associated mutation. The model accurately reproduces all the measured whole-cell biophysical characteristics of the human wild-type (WT) channel co-expressed with the human β_1 and β_2 accessory subunits, and can be modified to simulate the behavior observed for the GEFS+ mutant R1648H. Moreover, both models provide theoretical insight into $Na_V1.1$ gating. Our models predict that $Na_V1.1$ open state inactivation occurs by a biphasic mechanism that can be conceptualized by docking of the inactivation gate to the cytoplasmic face of the pore followed immediately by gate stabilization (“latching”). Importantly, the increased persistent current exhibited by R1648H can be predicted by introducing a selective impairment of the latching mechanism, a heretofore unrecognized molecular mechanism for sodium channel dysfunction in epilepsy.

Materials and Methods

Electrophysiology

All heterologously expressed WT-$Na_V1.1$ and R1648H data used for the generation of the computational models has been previously reported by our laboratory (Lossin et al., 2002; Rhodes et al., 2004; Rhodes et al., 2005; Vanoye et al., 2006). Briefly, biophysical characterization of WT-$Na_V1.1$ and R1648H was performed using human tsA201 cells (HEK293 cells stably expressing the SV40 large T antigen). Cells transiently co-expressed human WT-*SCN1A* or R1648H cDNA as well as the human β_1 and β_2 accessory subunits. Specific voltage-clamp protocols assessing channel activation, inactivation and recovery from inactivation were employed. Representations of all voltage protocols are included as figure insets and all recordings were performed at room temperature. The average current recorded from multiple cells was used as a calibration standard to guide optimization of an accurate computational model response. $Na_V1.1$ persistent current measurements were obtained by digital subtraction of currents recorded in the presence and absence of 10 μM tetrodotoxin (TTX, Sigma, St. Louis, MO, USA). Heterologously expressed $Na_V1.1$ data is presented as mean ± SEM (Lossin et al., 2002; Rhodes et al., 2004; Rhodes et al., 2005; Vanoye et al., 2006).

Computational Modeling

The computational modeling was done as a collaborative project with Kristopher M. Kahlig, a postdoctoral fellow in the laboratory. The computational model reported here for $Na_V1.1$ is based on voltage-gated sodium channel modeling efforts by Clancy and Kass (Clancy and Kass, 2004), Clancy and Rudy (Clancy and Rudy, 2002; Clancy and Rudy, 1999) and Horn and Vandenberg (Vandenberg and Horn, 1984; Horn and Vandenberg, 1984). Figure 4 illustrates the Markov model for $Na_V1.1$ that includes states for the conditions: closed (***C***), open (***O***, conducting; ***Ø***, non-conducting), fast inactivated (***F***) and slow inactivated (***S***). Transitions between states are reversible and described by continuous equations whose instantaneous solution depends on the membrane voltage. In response to a voltage change, the channel distribution shifts to a new equilibrium over a time course determined by the new values of the rate constants. Alteration of a single transition effects channel occupancy for each state. During $Na_V1.1$ model optimization, the rate equations were constrained by the average whole-cell current recorded from heterologously expressed $Na_V1.1$.

Voltage-gated ion channels do not exist at thermodynamic equilibrium at membrane voltages other than 0 mV (i.e., the imposed voltage gradient influences channel conformation) (Colquhoun et al., 2004; Finkelstein and Peskin, 1984). Violations of the thermodynamic principle of detailed balance (microscopic reversibility) have been described previously for ion channels due to the influence of outside energies (ion electrochemical gradient or voltage gradient) on channel gating (Finkelstein and Peskin, 1984; Richard and Miller, 1990; Schneggenburger and Ascher, 1997; Wyllie et al., 1996). Thus, detailed balance was not imposed on the model for $Na_V1.1$ for the following reasons: 1) non thermodynamic equilibrium of $Na_V1.1$ resulting from membrane voltage (Colquhoun et al., 2004; Finkelstein and Peskin, 1984; Lauger, 1995); 2) microscopic reversibility has not been demonstrated for $Na_V1.1$; 3) the absorbing nature of $Na_V1.1$ inactivated states (low number of channel re-openings) limits the available information for assessing detailed balance (Vanoye et al., 2006); and 4) statistical tests for detailed balance lack sufficient power to test our complex and highly cyclic $Na_V1.1$ model

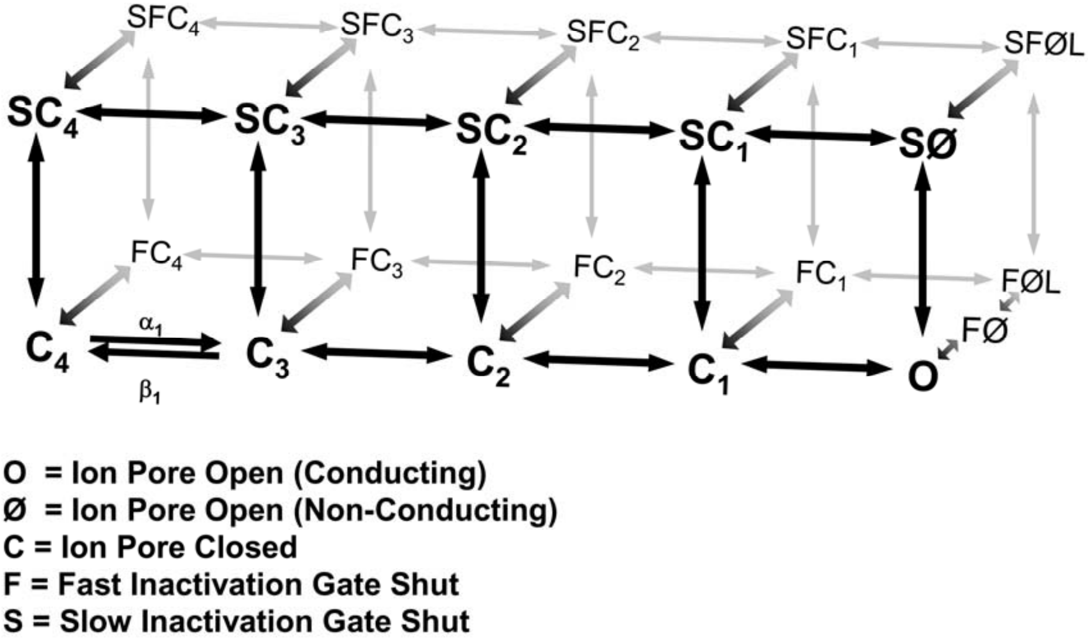

Figure 4. Diagram of Na_V1.1 Markov model. The Na_V1.1 Markov model consists of 21 states connected by 37 reversible transitions. The model includes states for the conditions: closed (***C***), open (***O***), fast inactivated (***F***) and slow inactivated (***S***). The only ion conducting state is ***O*** (***Ø*** states are non-conducting due to inactivation gate closure). Table 5 includes a complete list of the voltage-dependent rate equations.

(Rothberg and Magleby, 2001; The et al., 2002). Rate equations for all transitions are reported in Table 5.

The state ***O*** represents the conducting state and the occupancy of ***O*** determines the sodium current by: $I_{Na} = G_{Na\_bar} * O * (V - E_{Na})$, where I_{Na} is the sodium current, G_{Na_bar} is the maximum sodium current density, ***O*** is the fractional occupancy of the open state, V is the membrane voltage and E_{Na} is the sodium reversal potential. For whole-cell simulations, the computational $Na_V1.1$ model was expressed at a G_{Na_bar} of 0.02 S/cm^2. This corresponds to previously utilized sodium channel G_{Na_bar} values of between 0.01 and 0.2 S/cm^2 (Clancy and Kass, 2004; Spampanato et al., 2004b; Spampanato et al., 2004a; Barela et al., 2006). For single channel simulations, a single model $Na_V1.1$ channel was expressed with a conductance (G_{Na}) of 17 pS. This value corresponds to the single channel conductance previously reported for WT-$Na_V1.1$ (17.2 ± 0.5 pS, *n* = 10) and R1648H (16.9 ± 0.9 pS, *n* = 7) (Vanoye et al., 2006). The average empirically calculated reversal potential observed for $Na_V1.1$ was used for all simulations (E_{Na} = 71.3 ± 1.5 mV, *N* = 14) (Rhodes et al., 2005).

Computational modeling was performed using NEURON (www.neuron.yale.edu; (Hines and Carnevale, 2001). All simulations were performed using the default integration strategy (Backward Euler) with an implicit fixed time step of 25 μs to maintain temporal accuracy and efficiency. Simulations were implemented on either a PC workstation employing two parallel Intel Xeon dual-core 2.8 GHz processors or a PC desktop employing an Intel Pentium 4, 3.0 GHz processor. All simulations were performed in Windows XP.

For whole-cell simulations we constructed an *in silico* single compartment model of a tsA201 cell with a length of 20.0 μm, diameter of 12.1 μm and membrane capacitance of 1 μf/cm^2. The resulting computational surface area is equivalent to the

Table 5. Transition rates for Na$_V$1.1 models

	Transition	Forward Rate: α (ms^{-1})	Reverse Rate: β (ms^{-1})
(1)	$C_4 \leftrightarrow C_3$	77.149 * exp(v / 16.056) + 1.3181	5.63 * exp(-v / 47.619) + 2.6
(2)	$C_3 \leftrightarrow C_2$	48.115 * exp(v / 16.12) + 0.8	6.3137 * exp(-v / 73.692)
(3)	$C_2 \leftrightarrow C_1$	39.634 * exp(v / 44.236) + 5.3197	6.4559 * exp(-v / 28.947)
(4)	$C_1 \leftrightarrow O$	4.25 * exp(v / 43.478) + 0.76	3.8617 * exp(-v / 44.028)
(5)	$O \leftrightarrow F\text{Ø}$	5.2639 * exp(v / 31.779) + 3.8922e-4	0.033189 * exp(v / 11.34) + 0.22802
(6)	$F\text{Ø} \leftrightarrow F\text{Ø}L$	0.4437 * exp(v / 48.1)	0.007 * exp(v / 5e4)
(7)	$C_4 \leftrightarrow FC_4$	3.0e-8 * exp(-v / 5e5)	4.592e-4 * exp(-v / 25.873) + 0.01957
(8)	$C_3 \leftrightarrow FC_3$	0.003 * exp(-v / 52.632)	5.8e-10 * exp(-v / 6.41) + 8.87e-4
(9)	$C_2 \leftrightarrow FC_2$	0.1888 * exp(-v / 50.582)	3.642e-4 * exp(-v / 16.276)
(10)	$C_1 \leftrightarrow FC_1$	0.8635 * exp(-v / 121.181)	3.1e-6 * exp(-v / 10.101)
(11)	$FC_4 \leftrightarrow FC_3$	0.02 * exp(v / 5e4)	0.0186 * exp(-v / 36.456)
(12)	$FC_3 \leftrightarrow FC_2$	0.0098053 * exp(v / 10.258) + 0.03	0.00546 * exp(-v / 33.445)
(13)	$FC_2 \leftrightarrow FC_1$	0.24 * exp(v / 9.09)	0.0082 * exp(-v / 20.92)
(14)	$FC_1 \leftrightarrow F\text{Ø}L$	0.19 * exp(v / 15.151)	0.022 * exp(-v / 25.641)
(15)	$C_4 \leftrightarrow SC_4$	1.23285e-6 * exp(v / 47.772)	4.70479e-8 * exp(-v / 13.263)
(16)	$C_3 \leftrightarrow SC_3$	1.23285e-6 * exp(v / 47.772)	5.01079e-8 * exp(-v / 14.472)
(17)	$C_2 \leftrightarrow SC_2$	1.23285e-6 * exp(v / 47.772)	5.3367e-8 * exp(-v / 15.924)
(18)	$C_1 \leftrightarrow SC_1$	1.23285e-6 * exp(v / 47.772)	5.3367e-8 * exp(-v / 15.924)
(19)	$O \leftrightarrow S\text{Ø}$	1.23285e-6 * exp(v / 47.772)	5.3367e-8 * exp(-v / 15.924)
(20)	$FC_4 \leftrightarrow SFC_4$	1.23285e-6 * exp(v / 47.772)	3.51119e-8 * exp(-v / 9.555)
(21)	$FC_3 \leftrightarrow SFC_3$	1.23285e-6 * exp(v / 47.772)	4.32876e-8 * exp(-v / 11.943)
(22)	$FC_2 \leftrightarrow SFC_2$	5.49e-4 * exp(v / 104.932)	3.65143e-8 * exp(-v / 9.926)
(23)	$FC_1 \leftrightarrow SFC_1$	1.23285e-6 * exp(v / 47.772)	9.38931e-8 * exp(-v / 158.697)
(24)	$F\text{Ø}L \leftrightarrow SF\text{Ø}L$	5e-4 * exp(v / 74.627)	5.97425e-5 * exp(-v / 63.111)
(25)	$SC_4 \leftrightarrow SC_3$	0.385745 *exp(v / 16.056) + 0.00659	0.02815 * exp(-v / 47.619) + 0.013
(26)	$SC_3 \leftrightarrow SC_2$	0.240575 * exp(v / 16.12) + 0.004	0.0315685 * exp(-v / 73.692)
(27)	$SC_2 \leftrightarrow SC_1$	0.19817 * exp(v / 44.236) + 0.026599	0.0322795 * exp(-v / 28.947)
(28)	$SC_1 \leftrightarrow S\text{Ø}$	0.02125 * exp(v / 43.478) + 0.0038	0.0193085 * exp(-v / 44.028)
(29)	$S\text{Ø} \leftrightarrow SF\text{Ø}L$	0.026769 * exp(v / 32.146)	2.6567e-4 * exp(v / 50) + 8.8025e-4
(30)	$SC_4 \leftrightarrow SFC_4$	1.5e-10 * exp(-v / 5e5)	2.296e-6 * exp(-v / 25.873) + 9.785e-5
(31)	$SC_3 \leftrightarrow SFC_3$	1.5e-5 * exp(-v / 52.632)	2.9e-12 * exp(-v / 6.41) + 4.435e-6
(32)	$SC_2 \leftrightarrow SFC_2$	9.44e-4 * exp(-v / 50.582)	1.821e-6 * exp(-v / 16.276)
(33)	$SC_1 \leftrightarrow SFC_1$	0.0043175 * exp(-v / 121.181)	1.55e-8 * exp(-v / 10.101)
(34)	$SFC_4 \leftrightarrow SFC_3$	1e-4 * exp(v / 5e4)	9.3e-5 * exp(-v / 36.456)
(35)	$SFC_3 \leftrightarrow SFC_2$	4.90265e-5 * exp(v / 10.258) + 1.5e-4	2.73e-5 * exp(-v / 33.445)
(36)	$SFC_2 \leftrightarrow SFC_1$	1.2e-3 * exp(v / 9.091)	4.1e-5 * exp(-v / 20.921)
(37)	$FSC_1 \leftrightarrow SF\text{Ø}L$	9.5e-4 * exp(v / 15.152)	1.1e-4 * exp(-v / 25.641)

Modifications for R1648H Model

(6)	$F\text{Ø} \leftrightarrow F\text{Ø}L$		0.043 * exp(v / 5e4)

Modifications for WT-Na$_V$1.1 Model Without FO state (omit rate 6)

(5)	$O \leftrightarrow F\text{Ø}L$	5.2 *exp(v / 31.25)	0.006013 *exp(v / 23.952)

average surface area measured for WT-$Na_V1.1$ expressing tsA201 cells (7.6×10^{-6} cm^2, $n = 15$) (Rhodes et al., 2005). For single channel simulations we constructed an *in silico* single compartment model of an outside-out membrane patch with a length of 0.5 μm, diameter of 0.5 μm and membrane capacitance of 1 $\mu f/cm^2$. The resulting computational surface area corresponds to a pipette tip diameter of 1 μm.

To minimize artifacts due to voltage protocol discrepancies, simulation protocols were identical to those used to experimentally characterize WT-$Na_V1.1$ and R1648H (Lossin et al., 2002; Lossin et al., 2003; Rhodes et al., 2004; Rhodes et al., 2005; Vanoye et al., 2006). This includes test voltage sequence as well as relaxation time. After the entire protocol had been recorded the model was re-initialized to steady-state (–120 mV) prior to the next simulation. Therefore, non-specific protocol effects (e.g. accumulation of inactivation) should be identical between the model and the heterologously expressed channel.

The four previously reported $Na_V1.1$ computational models were constructed using the published parameters (Barela et al., 2006; Clancy and Kass, 2004; Spampanato et al., 2004b; Spampanato et al., 2004a). For simulation purposes, the G_{Na_bar} of each model was reset to 0.02 S/cm^2, the value used with our WT-$Na_V1.1$ model. Due to the arbitrary nature of G_{Na_bar}, all comparisons between the previously reported $Na_V1.1$ computational models and the empirically recorded $Na_V1.1$ biophysical data are performed using normalized data (with the exception of Figure 9A in the online supplement). The four previously reported $Na_V1.1$ models include one Markov (Model A) (Clancy and Kass, 2004) and three Hodgkin-Huxley style models (Models B-D) (Barela et al., 2006; Spampanato et al., 2004b; Spampanato et al., 2004a). The discrepancies between the previously reported activity of Model A and our simulations most likely reflect differences in simulation environment differences. These considerations are not applicable to Models B-D as these were previously constructed and reported using the NEURON simulation environment.

Data Analysis

Data analysis was performed using Clampfit 9.2, OriginPro 7.0 and GraphPad Prism 4.0. Channel inactivation was evaluated by fitting the decay phase of the whole-cell current with the two exponential function, $I/I_{max} = A_1 \times \exp(-t/\tau_1) + A_2 \times \exp(-t/\tau_2) + I_r$, where τ_1 and τ_2 denote the time constants (fast and slow components, respectively), A represents a fractional amplitude and I_r is the level of non-inactivating current. Whole-cell conductance was calculated by $G_{Na} = I_{Na} / (V-E_{Na})$ and normalized to the maximum conductance between –80 and +20 mV. Conductance-voltage and steady-state availability curves were fit with Boltzmann functions to determine the voltage for half-maximal activation/inactivation ($V_{1/2}$) and the slope factor (k). The time-dependent entry into and the recovery from inactivation was evaluated by fitting the peak current with the two exponential function $I/I_{max} = A_1 \times [1 - \exp(-t/\tau_1)] + A_2 \times [1 - \exp(-t/\tau_2)]$. Persistent current was measured during the final 10 ms of a 200 ms depolarization to –10 mV and expressed as a percentage of peak current.

Using the same model parameters, sequential whole-cell simulations generate the identical model response. In contrast, single channel simulations are stochastic and sequential runs generate unique data. Thus, whole-cell results are reported as the value of the measured activity and single channel results are presented as mean ± SEM for independent simulation sequences. To allow direct comparison of the single channel simulations with previously reported empirical data (Vanoye et al., 2006), single channel events less than 0.1 ms were excluded from analysis.

Results

The majority of ion channel computational models rely on the quantitative descriptions of axonal ionic currents first introduced in 1952 by Hodgkin and Huxley (Hodgkin and Huxley, 1952b). Subsequent work has shown that HH-style equations can only approximate neuronal voltage-gated sodium channel behavior (Hille, 2001; Patlak, 1991; Baranauskas and Martina, 2006; Naundorf et al., 2006). We developed enhanced Markov chain models for WT-Na$_V$1.1 and the GEFS+ mutant R1648H that very accurately reproduce the observed biophysical characteristics of the corresponding heterologously expressed channels.

Na$_V$1.1 Markov model

Figure 4 illustrates our Markov model for Na$_V$1.1. The model is composed of two interconnected layers of states: 1) a bottom layer containing the closed (***C***), open (***O***, conducting; ***Ø***, open but non-conducting) and fast inactivated states (***F***), and 2) a parallel upper layer containing the slow inactivated states (***S***). Only the ***O*** state conducts ions as ***Ø*** states have undergone inactivation. Each state approximates a theoretical conformation Na$_V$1.1 adopts during activation and inactivation. However, any direct correlation between a state within the diagram and a particular protein conformation is not possible. It is likely that many transient Na$_V$1.1 protein conformations are grouped and represented as a single state within the model.

This scheme integrates many features of previous sodium channel models including multiple closed states, a single conducting state, closed state inactivation and silent recovery from inactivation (Horn and Vandenberg, 1984; Vandenberg and Horn, 1984; Hille, 2001; Patlak, 1991). We positioned slow inactivation as a second upper layer due to the experimental observations that fast and slow inactivation are discrete, although not entirely autonomous, mechanisms (Featherstone et al., 1996; Vedantham and Cannon, 1998). Featherstone and colleagues reported that removing fast inactivation increased the rate of entry into slow inactivation (Featherstone et al., 1996). As a result, the state of one inactivation gate (open versus closed) impacts the kinetics of the other and parallel transitions in the model for Na_V1.1 are not modeled with identical kinetics (e.g. ***C_1*** to ***SC_1*** compared to ***FC_1*** to ***SFC_1***). In the model, fast and slow inactivation mechanisms are able to independently terminate current flow through the pore (transitions out of ***O***). The transitions ***O*** to ***FØ*** and ***O*** to ***SØ*** represent closure of the fast and slow inactivation gates, respectively. Both gates can be closed simultaneously (states labeled ***SF***), but this requires two independent and sequential steps (e.g. closure of the fast gate followed by closure of the slow gate).

Transitions are described by rate equations that are instantaneously voltage-dependent and were adjusted using previously recorded Na_V1.1 whole-cell recordings as a calibration standard (Rhodes et al., 2005). The model reproduces many key features of voltage-gated sodium channel behavior. At the holding potential of –120 mV (under steady-state conditions) 97% of channels are located in ***C_4***. Upon depolarization, channels move through the 4 closed states (***C_4-C_1***) before entering the ion conducting ***O*** state. Channels can enter fast inactivation (***F*** states) from either open or closed states. For a depolarization to –10 mV, a transient equilibrium is established after 20 ms with 69% of channels occupying ***FØL*** and 24% in ***FC_1***. Long lasting depolarizations drive channels from the ***F*** states into the upper layer of slow inactivated states (***S*** states). After 10 s at –10 mV, channels predominately occupy the upper states (44% ***FSØ***, 32% ***FSC_1***, and 6% ***FSC_2***). After repolarization, channels return to the lower layer reestablishing the steady-state equilibrium (either transitioning though the ***F*** states or moving directly into ***C*** states).

Open State Inactivation

The whole-cell current carried by human $Na_V1.1$ inactivates following a double exponential time course (Lossin et al., 2002; Rhodes et al., 2004; Rhodes et al., 2005; Vanoye et al., 2006; Lossin et al., 2003). Figure 5 illustrates theoretical investigations into possible mechanisms for generating this behavior. We first attempted to model open state inactivation with a single step (***O*** to ***FØL***, Figure 5A). The resulting simulated whole-cell current ("Model") decayed too quickly and followed a single exponential time course. For comparison with the current generated by heterologously expressed $Na_V1.1$, the average $Na_V1.1$ whole-cell current recorded from multiple independent cells is depicted as "Actual" in Figure 5A (Rhodes et al., 2005). Integrating the Model and Actual current traces between the peak and 10 ms reveals that a single step inactivation pathway conducts only 65.4% of the actual sodium influx. We next adjusted the rate constants for the ***O*** to ***FØL*** transition in an effort to introduce a second component to the whole-cell current inactivation. Slowing the ***O*** to ***FØL*** transition significantly increased the peak current amplitude and slowed the overall current decay without introducing a second time component (data not shown). Slowing inactivation by allowing channel reopening (increasing the ***FØL*** to ***O*** transition in Figure 5A) increased the peak current and induced a significant persistent current without introducing a second inactivation component (data not shown).

We next attempted to model the biphasic whole-cell current decay with two, parallel fast inactivation transitions (two transitions leading from ***O*** to the ***F*** states). Preliminary experiments with these models were unable to generate a whole-cell current decay that was well fit by a two-exponential equation (data not shown). Moreover, the mechanism of fast inactivation for voltage-gated sodium channels has been described in great detail and consists of pore occlusion by the DIII-DIV intracellular loop (Catterall et al., 2005; Vassilev et al., 1989). Introduction of a second fast inactivation pathway from

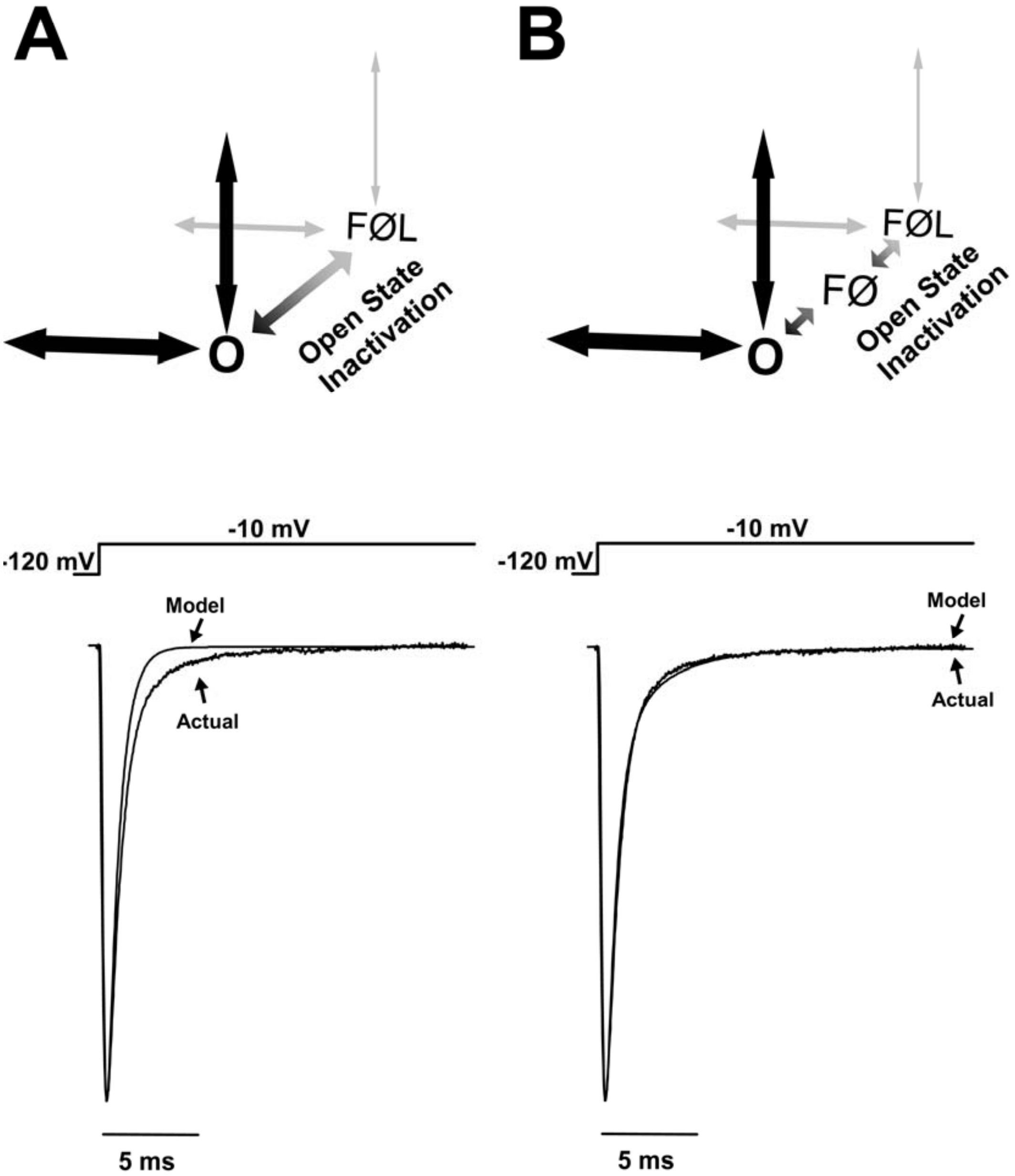

Figure 5. Secondary stabilization is essential for open state inactivation. $Na_V1.1$ open state inactivation was explored by modeling different inactivation mechanisms. **(A)** An open state inactivation pathway consisting of a single step (***O*** to ***FØL***) was unable to reproduce the biphasic whole-cell current characteristic of $Na_V1.1$. **(B)** A two step inactivation pathway reproduces the $Na_V1.1$ biphasic whole-cell current decay. The modeled inactivation pathway includes an unstable intermediate state ***FØ*** between the open state ***O*** and the stabilized “latched” inactivated state ***FØL***.

O would imply a second fast inactivation gate that is not supported by the experimental data.

An alternative approach to reproduce the biphasic whole-cell current decay is to add an intermediate state in the open state inactivation pathway. Figure 5B illustrates an inactivation mechanism for $Na_V1.1$ that consists of 2 states in series (***FØ*** and ***FØL***). In this design, channels leaving ***O*** first enter the less stable fast inactivated state ***FØ***. Most channels quickly transition into the absorbing fast inactivated locked state ***FØL***. A small fraction of ***FØ*** channels transiently return to ***O*** thereby re-opening before inactivating again to ***FØ*** and finally arriving in ***FØL***. The sodium current generated by this model overlay the current recorded for heterologously expressed $Na_V1.1$ (Figure 5B). Integrating the Model current trace between the peak and 10 ms reveals that a two step open state inactivation pathway conducts 98.5% of the actual sodium influx. All subsequent simulations were performed with models including the ***FØ*** state.

Model WT-$Na_V1.1$ generates accurate whole-cell currents

To verify that the WT-$Na_V1.1$ model reproduces the fundamental characteristics of $Na_V1.1$ activity, we characterized the whole-cell sodium currents generated by the model and compared these results to those previously reported for $Na_V1.1$ (Rhodes et al., 2005). Figure 6 illustrates a representative family of sodium current traces elicited by voltage steps to various potentials for (A) a tsA201 cell heterologously expressing WT-$Na_V1.1$ and (B) model WT-$Na_V1.1$. In both cases, the measured currents were inward and transient due to the rapid activation and inactivation of sodium influx. Overlaying the –10 mV current trace from panels A and B verifies that the model WT-$Na_V1.1$ activates and inactivates with kinetics similar to those actual measured for WT-$Na_V1.1$ (Figure 6C). Figure 6D illustrates normalized current traces generated by the previously reported

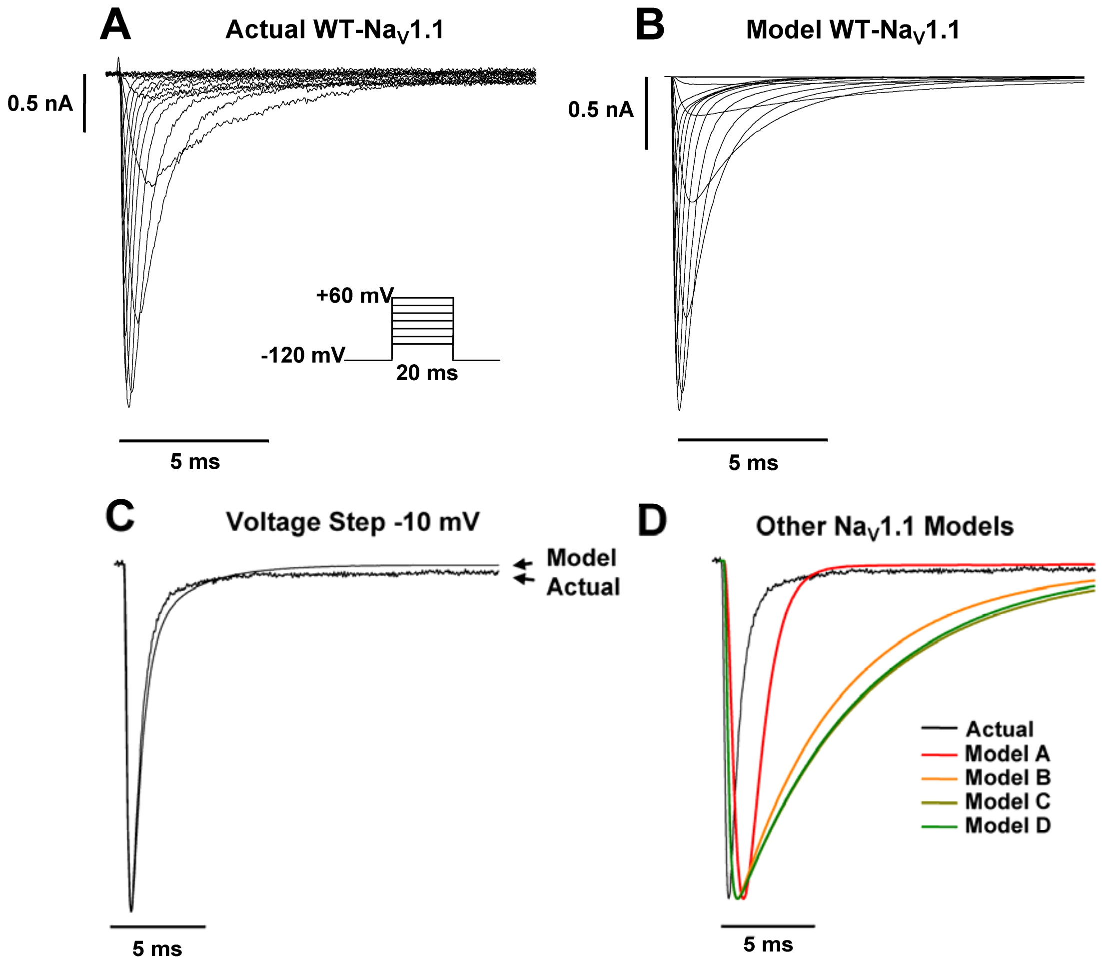

Figure 6. WT-Na$_V$1.1 model generates accurate whole-cell currents. (A) Representative whole-cell currents recorded from a tsA201 cell co-expressing the human wild-type *SCN1A* and the human β_1 and β_2 accessory subunits. Currents were elicited by voltage steps to potentials between –80 and +60 mV from a holding potential of –120 mV shown as panel inset. **(B)** Model WT-Na$_V$1.1 whole-cell currents recorded in response to the stimulation protocol in panel A. **(C)** Comparison of actual and model WT-Na$_V$1.1 current traces for the –10 mV voltage step from panels **A** and **B**, respectively. **(D)** Comparison of actual WT-Na$_V$1.1 and all previously reported Na$_V$1.1 computational models (Barela et al., 2006; Clancy and Kass, 2004; Spampanato et al., 2004b; Spampanato et al., 2004a) in response to the -10 mV voltage step.

$Na_V1.1$ models in response to a voltage step to –10 mV (Barela et al., 2006; Clancy and Kass, 2004; Spampanato et al., 2004b; Spampanato et al., 2004a). In our simulation environment, each model displayed altered current kinetics compared to those actually measured for WT-$Na_V1.1$. Figure 7 illustrates the whole-cell current generated by the previously reported WT-$Na_V1.1$ models in response to the voltage protocol in Figure 6A.

To further demonstrate the accuracy of the whole-cell currents generated by model WT-$Na_V1.1$, we characterized their activation and inactivation kinetics. Figure 8A illustrates the peak current-voltage relationship for the whole-cell currents shown in Figure 6. There is minimal difference between the peak current generated by the WT-$Na_V1.1$ model (open symbols) and actual $Na_V1.1$ (filled symbols). At 0 mV, the model generates a peak current of –307 pA/pF compared to –305 ± 38 pA/pF (*n* = 14) for actual WT-$Na_V1.1$ (Rhodes et al., 2005). We measured time to peak current for each voltage as an estimation of the rate of channel activation. Plotting the time to peak current for simulated and actual WT-$Na_V1.1$ demonstrates that our model activates with a similar time course (Figure 8B). At –10 mV, the time to peak current for model WT-$Na_V1.1$ was 0.35 ms compared to 0.38 ± 0.03 ms (*n* = 14) for actual WT-$Na_V1.1$. Figure 8C illustrates that the voltage-dependence of activation obtained from the normalized conductance values for simulated WT-$Na_V1.1$ is similar to that directly measured for the heterologously expressed channel (fit parameters are listed in Table 6) (Rhodes et al., 2005). To quantitatively evaluate $Na_V1.1$ current inactivation, the decay of the whole-cell current trace was fit with a two exponential equation (Table 7). Figure 8D demonstrates that the fast and slow inactivation components (τ_1 and τ_2, respectively) for model WT-$Na_V1.1$ are comparable to those previously reported. The differences in τ_s most likely reflect the contribution (5 ms after voltage step) of non-specific whole-cell currents in the heterologous recording system that are absent *in silico* (Figure 6A). These results

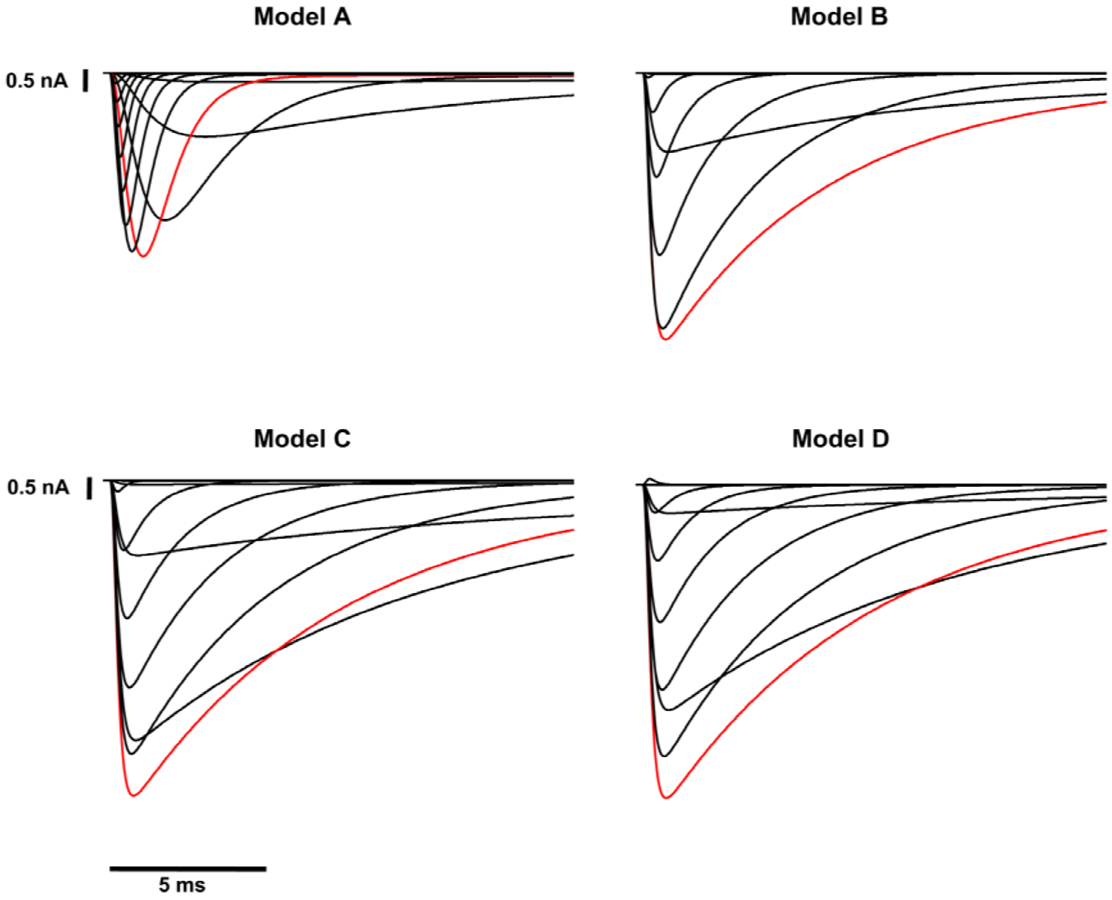

Figure 7. Whole-cell currents generated by previously reported Na$_V$1.1 models. Simulated whole-cell currents generated by previously reported computational models for Na$_V$1.1 (Barela et al., 2006; Clancy and Kass, 2004; Spampanato et al., 2004b; Spampanato et al., 2004a). The stimulation protocol was identical to that used in Figure 6A and the red trace highlights the voltage step to –10 mV.

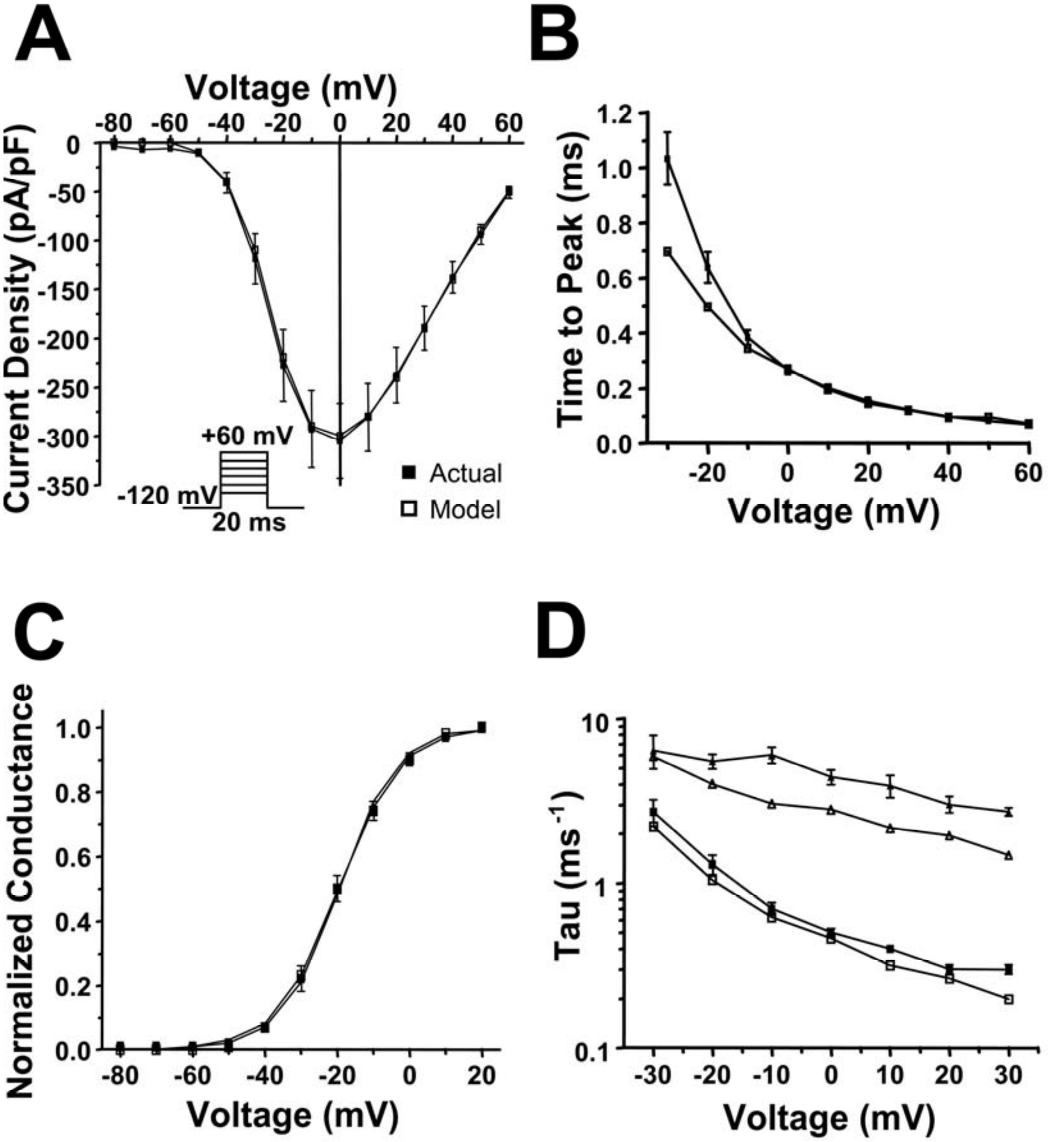

Figure 8. Analysis of simulated WT-Na$_V$1.1 whole-cell current. The WT-Na$_V$1.1 computational model (open symbols) reproduces the whole-cell biophysical characteristics of WT-Na$_V$1.1 heterologously expressed in tsA201 cells (*n* = 14, filled symbols). Whole-cell currents were elicited by the voltage protocol in panel **A** inset. **(A-B)** Peak current amplitude and time to peak current were plotted for each potential, respectively. **(C)** The voltage dependence of channel activation was calculated from the normalized conductance values. Data were fit using a Boltzmann equation and fit parameters are provided in Table 6. **(D)** Inactivation time constants were estimated by fitting the decay phase of the whole-cell current with a two exponential function. Fit parameters are provided in Table 7 and the fast and slow inactivation time constants are plotted for each potential.

Table 6. Biophysical parameters for activation and fast inactivation for $Na_V1.1$ models

		Activation			Voltage dependence of fast inactivation			Recovery from fast inactivation[§]		
		$V_{1/2}$ (mV)	k (mV)	*n*	$V_{1/2}$ (mV)	k (mV)	*n*	τ_1 (ms)	τ_2 (ms)	*n*
Actual	**WT-Na_V1.1**	-19.4 ± 1.4	7.9 ± 0.2	13	-62.7 ± 1.7	-6.9 ± 0.2	14	2.4 ± 0.3 (85 ± 1%)	41.0 ± 6.0 (15 ± 1%)	14
Model	**WT-Na_V1.1**	-19.9	8.5		-61.3	-7.7		2.2 (82 %)	26.6 (18 %)	
Model	**R1648H**	-19.9	8.5		-61.3	-7.8		2.1 (81%)	23.0 (19 %)	

§ values in parentheses represent amplitude.

Table 7. Whole-cell current inactivation time constants for Na$_V$1.1 models

	Fast Component[§]			Slow Component[§]		
	Actual WT-Na$_V$1.1	Model WT-Na$_V$1.1	Model R1648H	Actual WT-Na$_V$1.1	Model WT-Na$_V$1.1	Model R1648H
-30 mV	2.73 ± 0.49 (69 ± 18%)	2.20 (81 %)	2.22 (86 %)	6.4 ± 1.5 (31 ± 18%)	5.9 (19 %)	7.0 (14 %)
-20 mV	1.34 ± 0.18 (86 ± 5%)	1.04 (81 %)	1.03 (83 %)	5.5 ± 0.6 (14 ± 5%)	4.0 (19 %)	3.8 (17 %)
-10 mV	0.72 ± 0.06 (93 ± 1%)	0.62 (82 %)	0.68 (87 %)	6.0 ± 0.7 (7 ± 0.8%)	3.0 (18 %)	3.3 (13 %)
0 mV	0.47 ± 0.03 (94 ± 1%)	0.46 (87 %)	0.46 (89 %)	4.4 ± 0.5 (6 ± 0.7%)	2.8 (13 %)	2.6 (11 %)
10 mV	0.37 ± 0.02 (94 ± 1%)	0.32 (87 %)	0.33 (89 %)	3.9 ± 0.6 (6 ± 0.6%)	2.2 (13 %)	2.2 (11 %)
20 mV	0.31 ± 0.02 (92 ± 1%)	0.26 (89 %)	0.23 (85 %)	3.0 ± 0.3 (8 ± 1.2%)	1.9 (11 %)	1.6 (15 %)
30 mV	0.28 ± 0.02 (90 ± 1%)	0.20 (84 %)	0.19 (83 %)	2.7 ± 0.2 (10 ± 1.3%)	1.5 (16 %)	1.4 (17 %)

§ values in parentheses represent fractional amplitude.

demonstrate that our WT-$Na_V1.1$ model reproduces the fundamental properties of the whole-cell current (activation and inactivation) recorded from heterologously expressed $Na_V1.1$ (Rhodes et al., 2005). For comparisons with our model, Figures 9-11 illustrate properties of the whole-cell currents generated by other previously reported WT-$Na_V1.1$ models (Barela et al., 2006; Clancy and Kass, 2004; Spampanato et al., 2004b; Spampanato et al., 2004a).

Model WT-$Na_V1.1$ replicates fast and slow inactivation

Sodium channel fast inactivation is critical for limiting sodium influx during excitation and an accurate computational model should reproduce the fast inactivation properties of $Na_V1.1$. We examined both entry into (Figure 12A) and recovery from (Figure 12B) fast inactivation for our WT-$Na_V1.1$ model using standard two-pulse voltage protocols. The results were compared to the parameters measured for WT-$Na_V1.1$ (Table 6) (Rhodes et al., 2005). Figure 12A illustrates that our WT-$Na_V1.1$ model (open symbols) simulates currents that entered fast inactivation with the same voltage dependence as actual WT-$Na_V1.1$ (filled symbols). Similar to heterologously expressed WT-$Na_V1.1$, the model also exhibited recovery from fast inactivation that is well fit with a two exponential equation.

Slow inactivation has been proposed to regulate channel availability and may play a significant role during periods of prolonged depolarization or repetitive stimulation. We used two-pulse voltage protocols to test the ability of our WT-$Na_V1.1$ model to accurately emulate the time and voltage dependence of slow inactivation. The results were compared to the parameters actually measured for WT-$Na_V1.1$ (Table 8) (Rhodes et al., 2005). Model WT-$Na_V1.1$ (open symbols) exhibits the same time dependence of entry into slow inactivation as actual WT-$Na_V1.1$ (filled symbols, Figure 13A). Figure 13B shows that simulated WT-$Na_V1.1$ enters slow inactivation with an equivalent voltage

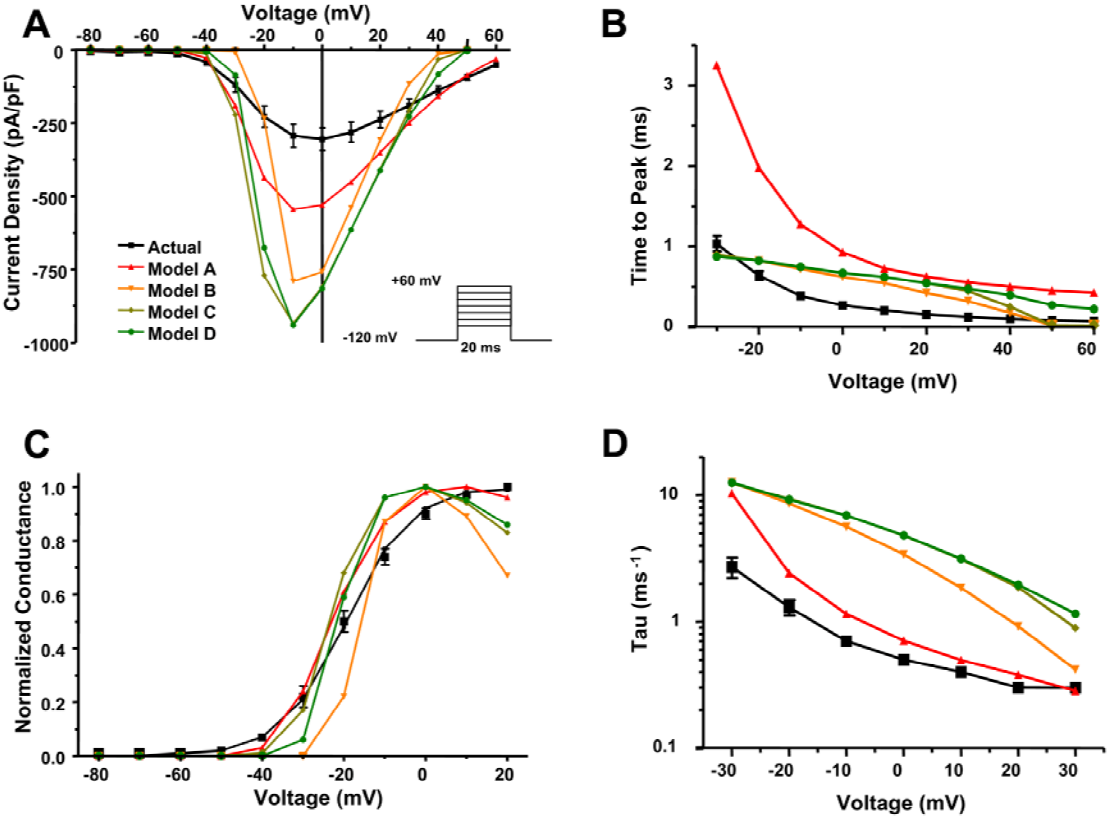

Figure 9. Analysis of whole-cell currents generated by other Na$_V$1.1 models. Comparison of the whole-cell current measured from heterologously expressed WT-Na$_V$1.1 (black symbols) and those generated by the previously reported Na$_V$1.1 computational models (colored symbols). Whole-cell currents were elicited by voltage steps to potentials between –80 and +60 mV from a holding potential of –120 mV (stimulation protocol used in Figures 8A). **(A-B)** Peak current amplitude and time to peak current plotted for each potential, respectively. **(C)** The voltage dependence of channel activation was plotted using the normalized conductance values. **(D)** Inactivation time constants were estimated by fitting the decay phase of the whole-cell currents in Figure 7 with a single exponential function. Fitting the current decay with a double exponential equation failed to reveal a second inactivation time component. For comparison with actual Na$_V$1.1 inactivation, the fast inactivation time constants are plotted for each potential (data from Figure 8D).

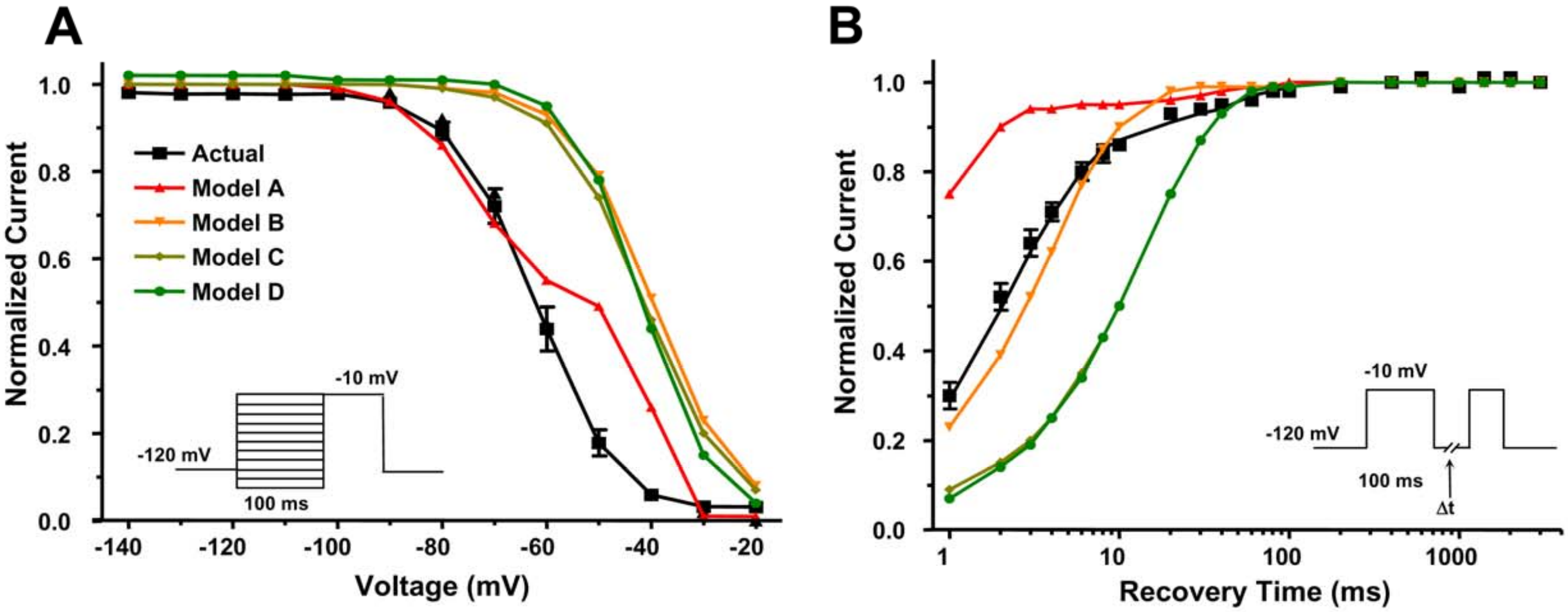

Figure 10. Fast inactivation exhibited by other Na$_V$1.1 models. Comparison of fast inactivation exhibited by heterologously expressed WT-Na$_V$1.1 (black symbols) and the previously reported Na$_V$1.1 computational models (colored symbols). **(A)** Voltage dependent entry into fast inactivation was examined using a two-pulse protocol consisting of a 100 ms conditioning pulse at various potentials followed by a test pulse at –10 mV. **(B)** Time dependent recovery from fast inactivation was examined using a two-pulse protocol consisting of a 100 ms inactivation pulse at –10 mV followed by a variable length return to –120 mV and a second test pulse to –10 mV.

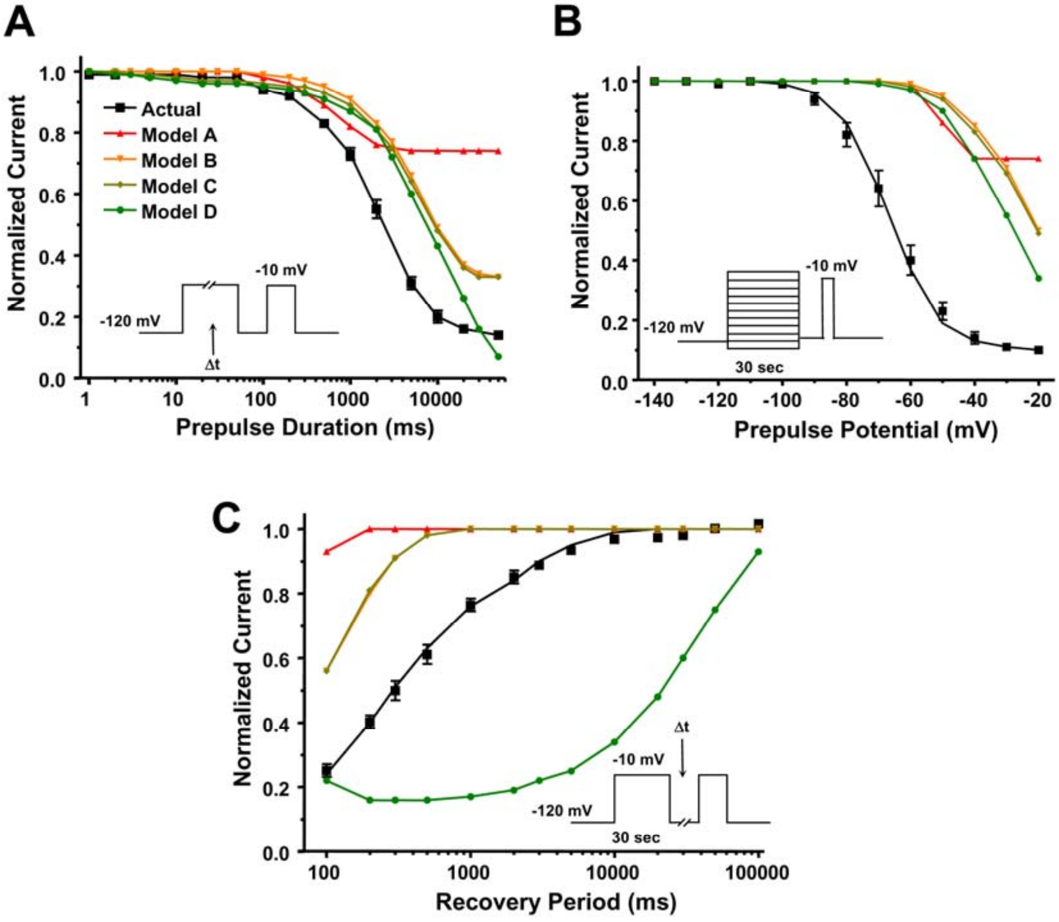

Figure 11. Slow inactivation exhibited by other $\mathrm{Na_V}$1.1 models. Comparison of the slow inactivation exhibited by heterologously expressed WT-$\mathrm{Na_V}$1.1 (black symbols) and previously reported $\mathrm{Na_V}$1.1 computational models (colored symbols). **(A)** Time dependent entry into slow inactivation was examined using a two-pulse protocol consisting of a variable length inactivation pulse to –10 mV followed by a test pulse at –10 mV. Effects of fast inactivation were minimized using a 50 ms inter-pulse to –120 mV to relieve fast inactivation. **(B)** Voltage dependent entry into slow inactivation was examined using a two-pulse protocol consisting of a 30 sec conditioning pulse at various potentials followed by a test pulse at –10 mV. Effects of fast inactivation were minimized using a 50 ms inter-pulse to –120 mV to relieve fast inactivation. **(C)** Time dependent recovery from slow inactivation was examined using a two-pulse protocol consisting of a 30 sec inactivation pulse to –10 mV followed by a variable length inter-pulse to –120 mV and a test pulse to –10 mV.

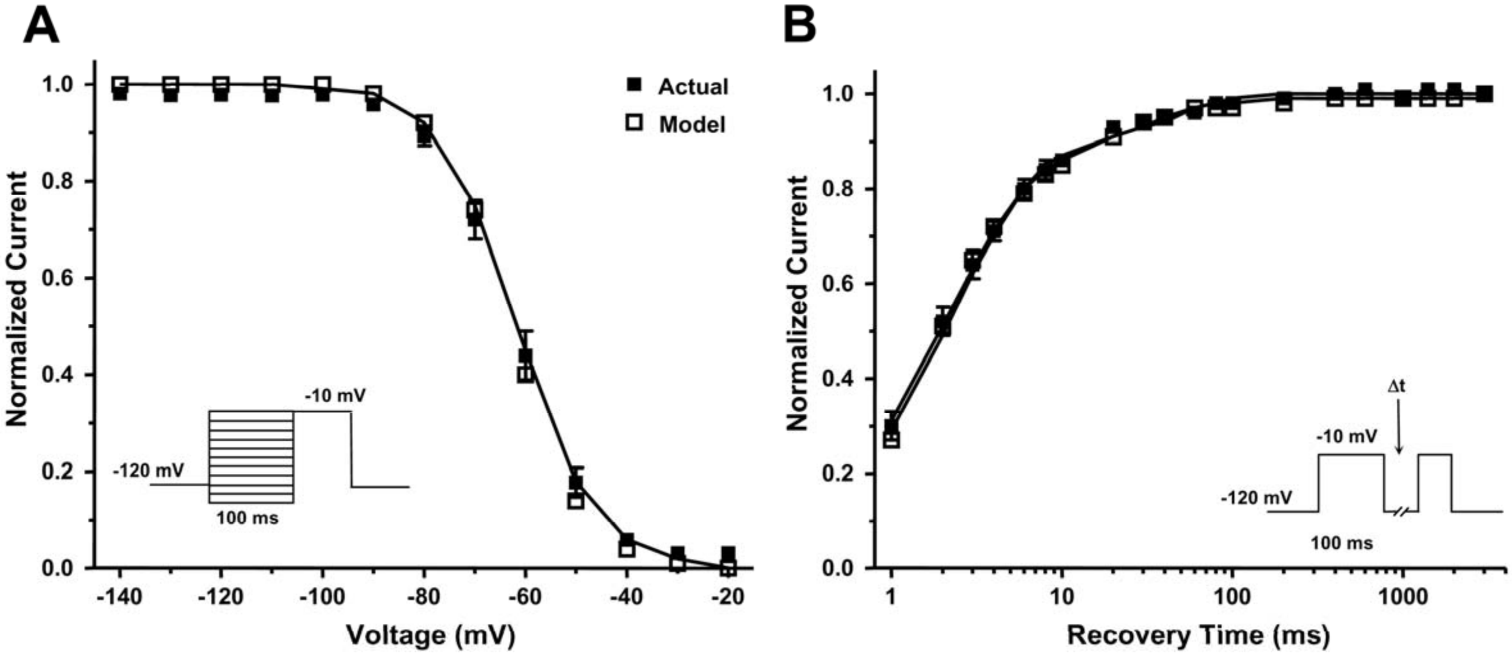

Figure 12. Analysis of simulated WT-Na$_V$1.1 fast inactivation. The WT-Na$_V$1.1 model (open symbols) reproduces the fast inactivation characteristics of channels heterologously expressed in tsA201 cells (*n* = 14, filled symbols). **(A)** Voltage-dependent entry into fast inactivation was examined using a two pulse protocol consisting of a 100 ms conditioning pulse at various potentials followed by a test pulse at –10 mV. **(B)** Time-dependent recovery from fast inactivation was examined using a two pulse protocol consisting of a 100 ms inactivation pulse at –10 mV followed by a variable length return to –120 mV and a second test pulse to –10 mV. Data were fit using either a Boltzmann **(A)** or two exponential **(B)** equation; fit parameters are provided in Table 6.

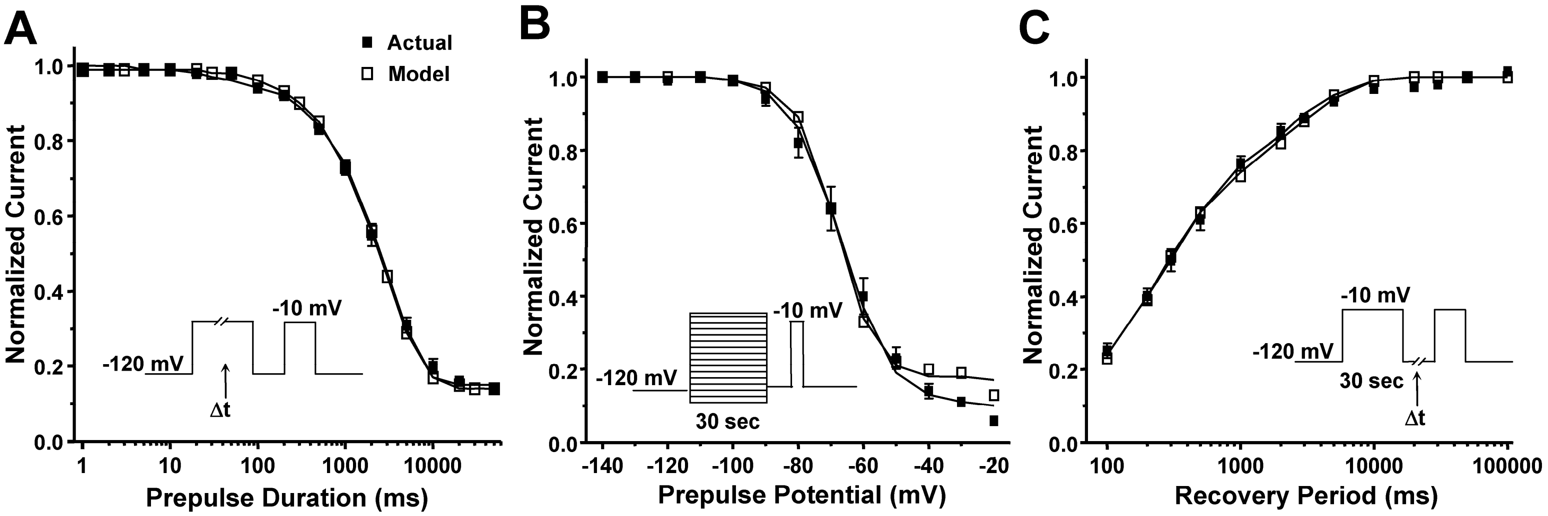

Figure 13. Analysis of simulated WT-Na$_V$1.1 slow inactivation. The WT-Na$_V$1.1 model (open symbols) reproduces the slow inactivation characteristics of heterologously expressed channels (*n* = 11, filled symbols). **(A)** Time-dependent entry into slow inactivation was examined using a two-pulse protocol consisting of a variable length inactivation pulse to –10 mV followed by a test pulse at –10 mV. Effects of fast inactivation were minimized using a 50 ms inter-pulse step to –120 mV to relieve fast inactivation. **(B)** Voltage-dependent entry into slow inactivation was examined using a two-pulse protocol consisting of a 30 sec conditioning pulse at various potentials followed by a test pulse at –10 mV. Effects of fast inactivation were minimized using a 50 ms inter-pulse step to –120 mV to relieve fast inactivation. **(C)** Time-dependent recovery from slow inactivation was examined using a two pulse protocol consisting of a 30 sec inactivation pulse to –10 mV followed by a variable length inter-pulse step to –120 mV and a test pulse to –10 mV. Data were fit using either a two exponential **(A and C)** or Boltzmann **(B)** equation; fit parameters are provided in Table 8.

Table 8. Slow inactivation parameters for $Na_V1.1$ models

		Onset of slow inactivation§				Voltage dependence of slow inactivation				Recovery from slow inactivation§		
		τ_1 (ms)	τ_2 (ms)	I_r	*n*	$V_{1/2}$ (mV)	k (mV)	I_r	*n*	τ_1 (ms)	τ_2 (ms)	*n*
Actual	**WT-$Na_V1.1$**	30 ± 7 (3 ± 1%)	3029 ± 283 (83 ± 1%)	14 ± 1	14	-66.7 ± 2.0	7.8 ± 0.2	10 ± 1	11	238 ± 16 (65 ± 3%)	2487 ± 240 (35 ± 3%)	11
Model	**WT-$Na_V1.1$**	30 (1 %)	2793 (84 %)	15		-68.5	6.2	17		225 (63 %)	2647 (37 %)	
Model	**R1648H**	30 (1 %)	3112 (83 %)	16		-68.6	6.1	18		221 (63 %)	2650 (37 %)	

§values in parentheses represent amplitude.

dependence compared to actual WT-$Na_V1.1$. In addition, simulated WT-$Na_V1.1$ recovered from slow inactivation with the same biphasic time-dependence of actual WT-$Na_V1.1$ (Figure 13C).

Modeling increased persistent current

Beginning with the model for WT-$Na_V1.1$, we constructed a computational model for the GEFS+ mutant R1648H. The major biophysical defect exhibited by R1648H is an increased persistent current resulting from increased probability of late single channel openings (Lossin et al., 2002; Rhodes et al., 2004; Vanoye et al., 2006). We were able to generate this biophysical phenotype by destabilizing the fast inactivated state ***FØL*** within the WT-$Na_V1.1$ Markov model (Figure 4). Increasing the rate constant for the transition from ***FØL*** to ***FØ*** (β_6, Table 5) allowed a small fraction of channels to transiently re-enter the open state ***O*** and generate the increased persistent current (Figure 14A, inset). No other changes, such as additional states, were needed to generate this aberrant channel activity.

Figure 14A illustrates whole-cell current traces for the models WT-$Na_V1.1$ and R1648H in response to a voltage step to –10 mV from a holding potential of –120 mV. R1648H exhibits a significant persistent current beginning 10 ms after the voltage step. The persistent current predicted between 190-200 ms after the voltage step for our R1648H model was 1.8 % of peak current compared to 0.3 % for the WT-$Na_V1.1$ model. Figure 14B illustrates that the persistent current generated by both models (open bars) corresponds well with the persistent current measured for heterologously expressed WT-$Na_V1.1$ (filled bar, 0.3 ± 0.1 % of peak, n = 9) and R1648H (filled bar, 1.8 ± 0.3 % of peak, n = 6) (Rhodes et al., 2004).

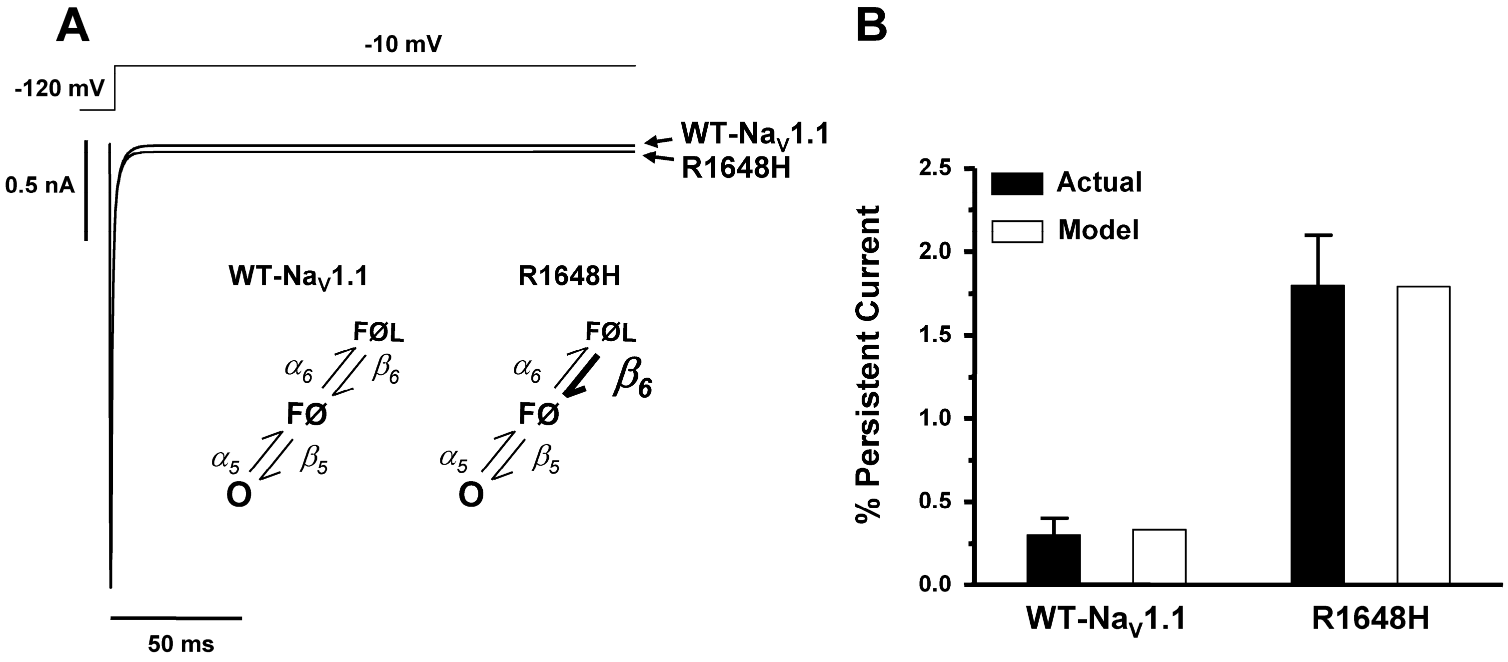

Figure 14. Computational model of GEFS+ mutant R1648H. (A) The model for R1648H was constructed by destabilizing the fast inactivated state ***FØL*** (6-fold increase in β_6, inset). Whole-cell current simulations of R1648H reveal increased persistent sodium current compared to simulated WT-Na$_V$1.1. **(B)** Levels of simulated persistent current for models WT-Na$_V$1.1 (open bar, 0.3 % of peak current) and R1648H (open bar, 1.8 % of peak current) replicate the average persistent current empirically measured for heterologously expressed WT-Na$_V$1.1 (filled bar, 0.3 ± 0.1 % of peak current, *n* = 9) and R1648H (filled bar, 1.8 ± 0.3 % of peak current, *n* = 6). Persistent current was measured during the final 10 ms of a 200 ms voltage step to –10 mV.

Complete characterization of simulated R1648H activation, fast inactivation and slow inactivation was performed as described for the WT-Na_V1.1 model. There was no difference between R1648H and WT-Na_V1.1 (Tables 6-8) in agreement with the original study of this mutant (Lossin et al., 2002). Both computational models accurately reproduce the biophysical parameters that were measured for each channel. Using our simulation environment, previously reported Na_V1.1 models predicted persistent current levels that varied widely between 0.6 and 2.3% of peak current (Figure 15).

Simulated R1648H exhibits late channel openings

The computational models for WT-Na_V1.1 and R1648H were generated using experimentally recorded Na_V1.1 whole-cell data as a calibration standard to tune the voltage-dependent rate equations (Table 5). We next tested whether our models could reproduce the single channel properties observed for WT-Na_V1.1 and R1648H (Vanoye et al., 2006). We used the stochastic single channel simulator in NEURON to test the single channel characteristics of model WT-Na_V1.1 and model R1648H in response to voltage steps to 0 mV. Figures 16A and 16B illustrate 5 consecutive voltage step simulations for models WT-Na_V1.1 and R1648H, respectively. The mean open time determined for simulated WT-Na_V1.1 was 0.29 ± 0.02 ms (n = 3) compared to 0.30 ± 0.02 ms (n = 3) for that generated by the R1648H model. These open times compare well with the open times measured for heterologously expressed WT-Na_V1.1 (0.25 ± 0.03 ms, n = 4) and R1648H (0.23 ± 0.02 ms, n = 5) (Vanoye et al., 2006).

Model R1648H exhibits an increase in late single channel openings (>10 ms after voltage step) compared to WT-Na_V1.1. Averaging 200 consecutive simulations reveals that WT-Na_V1.1 exhibits a low level of late single channel activity (Figure 16C). In contrast, model R1648H opens late in many simulations (Figure 16D). Figures 16E and 16F illustrate the open probability (P_o) diary for the same 200 consecutive simulations of

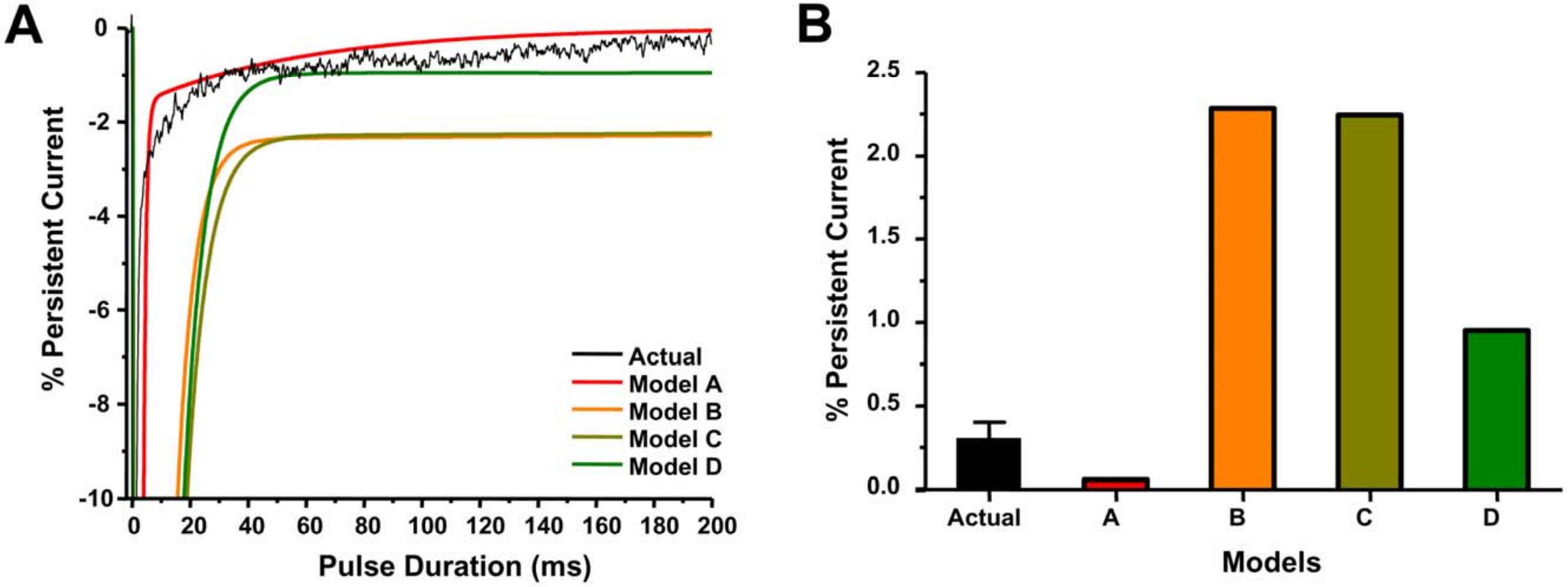

Figure 15. Persistent current exhibited by other Na$_V$1.1 models. (A) Whole-cell simulations of previously reported Na$_V$1.1 models (colored lines) reveal wide variation in levels of persistent current compared to heterologously expressed WT-Na$_V$1.1 (black line). Representative currents generated in response to a 200 ms voltage step to –10 mV and normalized to peak current amplitude. **(B)** The persistent current generated by previously reported Na$_V$1.1 models varied between 0.06 and 2.28 % of peak. Persistent current measurements were made during the final 10 ms of a 200 ms voltage step.

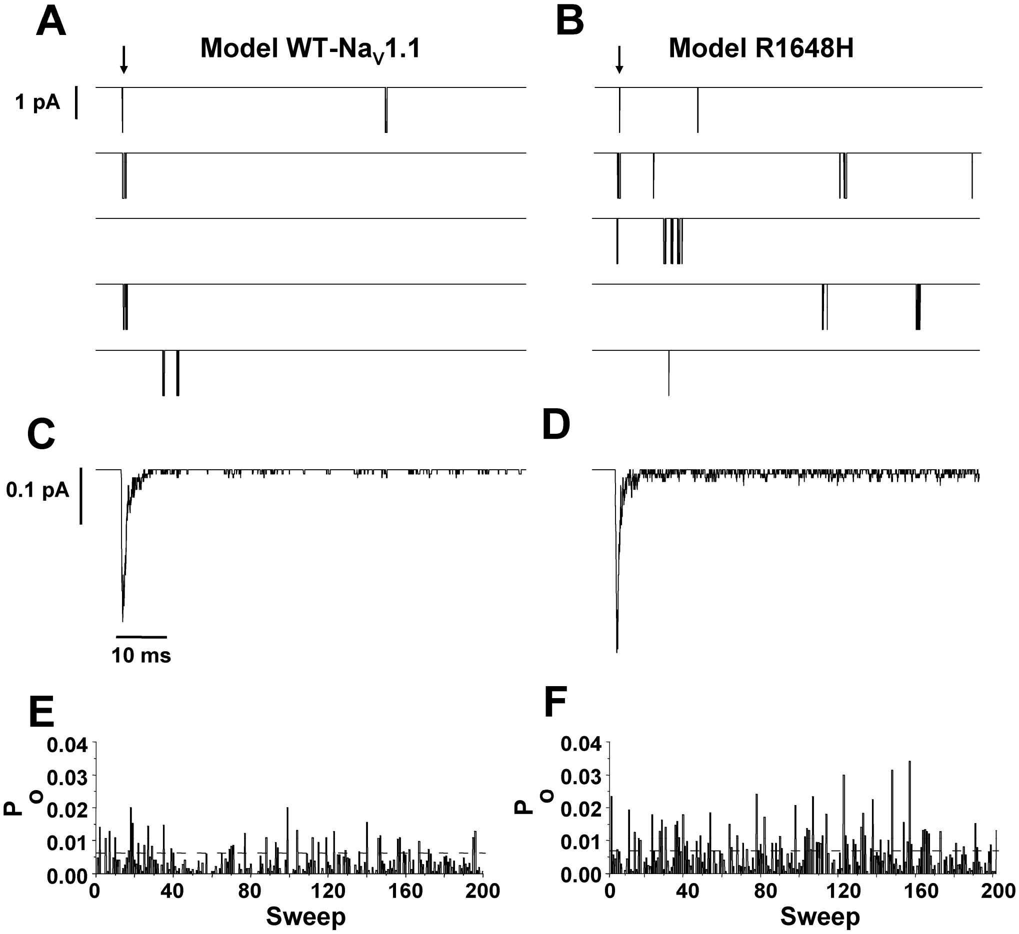

Figure 16. Late channel openings underlie model R1648H persistent current. (A-B) Five consecutive single channel simulations for WT-Na$_V$1.1 and R1648H, respectively. Downward deflections represent channel openings and arrows indicate onset of voltage step from –120 to –10 mV. **(C-D)** Representative ensemble average of 200 consecutive simulations using WT-Na$_V$1.1 and R1648H models, respectively. **(E-F)** Open probability (P_o) diary for each of the 200 simulations for WT-Na$_V$1.1 and R1648H, respectively. P_o calculated 0-80 ms following voltage step.

model WT-$Na_V1.1$ and R1648H. The average probability of late channel opening (P_o 20-100 ms) for model R1648H (0.0036 ± 0.0002, n = 3) was 6-fold greater than simulated WT-$Na_V1.1$ (0.0006 ± 0.0002, n = 3, students t-test, $P < 0.0001$). These results are very similar to the 7.4-fold increase in late P_o measured for heterologously expressed R1648H compared to WT-$Na_V1.1$ (Vanoye et al., 2006).

These data demonstrate that the whole-cell persistent current generated by model R1648H (Figure 14) results from an increase in late single-channel openings as a direct result of destabilizing the fast inactivation locked state (***FØL***). Based on these findings, we propose that selective impairment of the “latching” step of fast inactivation is responsible for the increased persistent current observed for this GEFS+ mutant. It is not yet understood how the R1648H mutation impair the “latching” step of fast inactivation, but the mutation may disrupt the conformation such that the proximal C-terminus is unable stabilize the fast inactivated state.

Discussion

Computational modeling is an effective experimental approach to explore alterations in ion channel behavior that result from disease-associated mutations. Here we describe the construction of ion channel models for WT-$Na_V1.1$ and R1648H that are based on previously recorded $Na_V1.1$ whole-cell experimental data. We fully characterized each model to ensure biophysical accuracy. Moreover, our models provide novel insight into WT-$Na_V1.1$ open state inactivation and define a previously unrecognized molecular mechanism to explain increased persistent current exhibited by a GEFS+ mutant.

Comparison of $Na_V1.1$ models

Previous attempts to generate computational models for WT-$Na_V1.1$ have been based on either HH-style differential equations or Markov chains (Barela et al., 2006; Clancy and Kass, 2004; Spampanato et al., 2004b; Spampanato et al., 2004a). We initially sought to modify an existing WT-$Na_V1.1$ model to fit our experimentally recorded $Na_V1.1$ activity. Each previously reported WT-$Na_V1.1$ model was reconstituted and the resulting whole-cell currents were compared to heterologously expressed human $Na_V1.1$ co-expressed with both human β_1 and β_2 accessory subunits in human tsA201 cells (Figures 6D, 7, 9-11, and 15). Although each previously reported WT-$Na_V1.1$ model reproduced certain $Na_V1.1$ activities, a rigorous characterization of the currently available models revealed that none were able to fully replicate the behavior of the channel (Figures 6D, 7, 9-11, and 15). This may reflect the source of data used during the construction and calibration of each model. The models sharing the HH-equation architecture were calibrated using currents recorded from *Xenopus laevis* oocytes co-expressing rat *Scn1a* and only β_1. In contrast, the previously reported $Na_V1.1$ Markov model was constructed using human $Na_V1.1$ data.

We chose to extend the efforts of Clancy and Kass (Clancy and Kass, 2004) to generate a Markov chain model for $Na_V1.1$ that reproduces all the experimentally recorded whole-cell properties of the heterologously expressed channels. A Markov design provides the parameter flexibility necessary to calibrate the rate equations to fit our experimental data. The major alterations to the previous model include the addition of a two-step open state inactivation pathway and a second layer of slow inactivated states. All rate equations were modified to reproduce the previously recorded activity of heterologously expressed human $Na_V1.1$.

The computational models we developed for WT-Na$_V$1.1 and R1648H generated whole-cell currents that are highly similar to the experimentally recorded data (Figures 5-6) (Lossin et al., 2002; Rhodes et al., 2004; Rhodes et al., 2005; Vanoye et al., 2006). Channel current was voltage-dependent, inward and transient. Characterization of the whole-cell currents revealed the proper biophysical parameters for the peak current amplitude (Figure 8A), time course of activation (Figure 8B), voltage-dependence of activation (Figure 8C) and biphasic whole-cell current inactivation (Figure 8D). Moreover, the model WT-Na$_V$1.1 and model R1648H reproduced the fast and slow inactivation processes for each channel, respectively. Specifically, the models exhibited virtually the same voltage-dependence of fast inactivation (Figure 12A), time-dependent recovery from fast inactivation (Figure 12B), time-dependent entry into slow inactivation (Figure 13A), voltage-dependence of slow inactivation (Figure 13B) and time-dependent recovery from slow inactivation (Figure 13C) as experimentally determined channel properties. This comprehensive characterization confirms that the models WT-Na$_V$1.1 and R1648H exhibit the proper biophysical parameters necessary to accurately emulate the heterologously expressed channel.

Open state inactivation is a two-step process

Our Na$_V$1.1 model incorporates a two-step pathway for open state inactivation (Figures 4 and 5). This scheme was necessary to reproduce the biphasic decay of the Na$_V$1.1 whole-cell current (Figure 5) (Lossin et al., 2002; Rhodes et al., 2004; Rhodes et al., 2005; Vanoye et al., 2006; Lossin et al., 2003). The cardiac voltage-gated sodium channel (*SCN5A*, Na$_V$1.5) also exhibits a two-component whole-cell current decay (Makita et al., 2000; Wang et al., 1996; Wang et al., 2000). Recent experiments have revealed Na$_V$1.5 inactivation to be a multiple step process resulting from pore occlusion by the DIII-DIV inactivation loop followed by inactivation gate stabilization by a second structure encoded in the proximal C-terminal tail (Cormier et al., 2002; Cormier et al., 2002; Glaaser et al., 2006; Motoike et al., 2004). The sodium channel C-terminal tail also influences the rate of fast inactivation. In experiments involving $Na_V1.5/Na_V1.2$ chimeras, the rate of whole-cell current inactivation was determined primarily by the C-terminal tail (Mantegazza et al., 2001).

Although the C-terminus of $Na_V1.1$ has not been directly linked to inactivation, a high homology exists between the neuronal isoforms *SCN1A* and *SCN2A* (~87%) as well as the cardiac *SCN5A* (~60%) (Plummer and Meisler, 1999; Catterall et al., 2005). Our $Na_V1.1$ models predict that similar to $Na_V1.5$ and $Na_V1.2$, a second molecular interaction is important for the stabilization of the inactivation gate. This stabilization could result from the $Na_V1.1$ C-terminus as has been proposed for $Na_V1.5$ (Cormier et al., 2002; Mantegazza et al., 2001; Glaaser et al., 2006; Motoike et al., 2004). However, models alone cannot implicate structural interactions. The stabilization of inactivation may rely on additional channel regions or other associated proteins, such as the accessory β subunits.

It is worth noting that the biphasic open state inactivation proposed here for $Na_V1.1$ (Figure 5B) should not be confused with (or compared to) the two-phase recovery from fast and slow inactivation (Figures 12B and 13C). Extensive biophysical characterization of $Na_V1.1$ as well as other voltage-gated sodium channels has demonstrated that inactivated channels do reopen during the recovery process (Kuo et al., 2006). Thus, recovery from inactivation is distinct from entry into inactivation. The mechanism(s) underlying the biphasic recovery from inactivation have not been completely explored.

Novel mechanism for increased persistent current

The persistent current model R1648H was constructed by altering a single rate constant in the WT-$Na_V1.1$ model. The fast inactivated state ***FØL*** was destabilized by increasing the rate constant β_6. This modification allows a small number of channels to re-enter the open state and generate the characteristic persistent current recorded for this GEFS+ mutant. Figure 14 illustrates that model R1648H exhibits whole-cell persistent current that is comparable to the increased persistent current actually measured for this mutant (Rhodes et al., 2004). In agreement with actual observations, this abnormal activity results from model R1648H exhibiting an increase in late channel openings (Figure 16) and not bursting behavior (Vanoye et al., 2006).

It is worth noting that the R1648H model did not generate P_o values as large as those actually reported for R1648H (Vanoye et al., 2006). The large open probability for R1648H (0.1 - 0.3) observed for a subset of voltage sweeps partially reflects a second prolonged open time (Vanoye et al., 2006). Although the models for WT-$Na_V1.1$ and R1648H accurately reproduce the $Na_V1.1$ whole-cell biophysical activity, future versions of the models may need to include a second open state with a longer dwell time to improve the simulated single-channel behavior. Nevertheless, our models have accurate whole-cell sodium current properties to begin neuronal simulations investigating mechanisms of R1648H epileptogenesis.

The model for R1648H predicts a novel mechanism for the persistent current generated by this GEFS+ mutant. We were able to replicate the increased persistent current exhibited by R1648H by altering a single rate constant (β_6) in the WT-$Na_V1.1$ model. This implies that introducing a histidine at position 1648 within the S4 segment of DIV (R1648H) inhibits the secondary stabilization of fast inactivation. Experimental investigation will be necessary to confirm and characterize these theoretical predictions for open state inactivation.

Our models of WT-Na$_V$1.1 and R1648H generate whole-cell currents that very accurately recapitulate the currents measured for heterologously expressed channels (Figure 6). This feature of our models will be highly valuable when constructing neuronal simulations. It is well accepted that proper *in vivo* excitability results from the integrated activity of a collection of ion conductances. Simulating accurate channel behavior is vital for engineering the next generation of neuronal excitability models.

CHAPTER III

IMPAIRED NA$_V$1.2 FUNCTION AND REDUCED CELL SURFACE EXPRESSION IN BENIGN FAMILIAL NEONATAL-INFANTILE SEIZURES

Introduction

Voltage-gated sodium channels are responsible for the initiation and propagation of action potentials in excitable tissues. These heteromultimeric complexes are comprised of a large (~260 kDa) pore-forming α subunit and smaller (~30 kDa) β accessory subunits. The α subunit is comprised of four homologous domains (DI-DIV) and exhibits significant homology to voltage-gated potassium and calcium channels. Recent structural studies have shown functional voltage-sensing and central pore subdomains within the predicted four-fold pseudo-symmetrical DI-DIV arrangement (Figures 3 and 17A) (Catterall, 2000). Abnormal biophysical activity caused by mutations within channel subdomains is a common theme in inherited channelopathies, and epilepsy in particular.

Mutations in three neuronal voltage-gated sodium channel genes (*SCN1A, SCN2A, and SCN1B*) have been associated with a genetic predisposition to epilepsy (Meisler and Kearney, 2005; Harkin et al., 2007). Specifically, most mutations in *SCN2A*, encoding the pore-forming subunit of Na$_V$1.2, have been identified in cases of benign familial neonatal-infantile seizures (BFNIS) (Heron et al., 2002; Berkovic et al., 2004; Herlenius et al., 2007) (Figure 17A). This epileptic syndrome is characterized by the onset of afebrile generalized seizures at an early age and spontaneous remission within the first year of life. The onset of symptoms in BFNIS, typically between 2 days and 3.5 months, overlaps that of benign familial neonatal convulsions (BFNC) and benign familial infantile seizures (BFIS) (Kaplan and Lacey, 1983). BFNC caused by mutations in *KCNQ2* and *KCNQ3* potassium channel genes has an earlier age of onset (Singh et al., 1998; Charlier et al., 1998). BFIS shares some clinical features with BFNIS, but has a later onset (after three months) and can be associated with mutations in *SCN2A*, *ATP1A2*, as well as other unidentified genes (Striano et al., 2006a). Seizures associated with BFNIS respond well to anticonvulsants and spontaneously remit within the first year of life without long term neurological sequelae. BFNIS exhibits autosomal dominant inheritance with a high degree of penetrance (Berkovic et al., 2004).

Mutations in $Na_V1.2$ have been infrequently associated with more severe forms of epilepsy. A missense *SCN2A* mutation was identified in a generalized epilepsy with febrile seizures plus (GEFS+) patient (Sugawara et al., 2001) and a truncation mutation was identified in a patient exhibiting features of severe myoclonic epilepsy of infancy (SMEI) (Kamiya et al., 2004). These two mutations appear to cause severe defects in channel activity (Sugawara et al., 2001; Kamiya et al., 2004). However, the relationships among specific mutations, channel dysfunction and corresponding clinical phenotype are not well defined for benign *SCN2A*-associated epilepsies, like BFNIS.

To date, eight *SCN2A* mutations have been associated with BFNIS (Figure 17A) (Heron et al., 2002; Berkovic et al., 2004; Herlenius et al., 2007). The BFNIS mutations affect different regions of the protein structure and affect highly conserved residues (Figures 17A and 32). Four of the BFNIS mutations have been studied previously by overexpressing the α subunit alone in either rat cortical neurons or HEK293T cells (Scalmani et al., 2006; Xu et al., 2007b). Here we present the functional characterization of three BFNIS mutations (R1319Q, L1330F and L1563V) using a recombinant human $Na_V1.2$ expressed with the accessory subunits, $h\beta_1$ and $h\beta_2$, in an effort to better define functional defects that may be unique to BFNIS. We found that these mutations had mixed effects on channel activity predicting either loss (R1319Q, L1330F) or gain

(L1563V) of function. Unexpectedly, all three BFNIS mutations exhibited substantially lower levels of protein expression at the cell surface compared to the wild type channel suggesting that reduced sodium channel density may contribute to the pathophysiology of this inherited epilepsy.

Materials and Methods

Mutagenesis of human $Na_V1.2$ cDNA

Full-length human $Na_V1.2$ cDNA was obtained as a generous gift from M. Montal (Ahmed et al., 1992). The ORF was subcloned into the mammalian expression plasmid pCMV-Script, the 5' UTR was removed to improve expression, and two cloning errors (G334D and R1744G) were corrected (see Chapter Three for details). PCR site-directed mutagenesis was used to engineer individual mutations into pCMV-$Na_V1.2$ using a previously described method (primer sequences provided in Table 16) (Lossin et al., 2002; Lossin et al., 2003; Rhodes et al., 2004; Ohmori et al., 2006). Three BFNIS-associated mutations were constructed using codon usage typical of human tissues. Multiple attempts to construct other BFNIS-associated mutations were unsuccessful. Due to the tendency of neuronal voltage-gated sodium channel cDNAs to spontaneously mutate within bacterial culture, we propagated clones in Max Efficiency Stbl2 host cells (Invitrogen Corporation, Carlsbad, CA) at 30 °C, and the entire ORF of each construct was completely sequenced to exclude polymerase errors and inadvertent mutations.

Heterologous expression of $Na_V1.2$

Recombinant $Na_V1.2$ was heterologously coexpressed in human tsA201 cells (HEK293 derivative stably transfected with SV40 large T antigen) with the human β_1 and β_2 voltage-gated sodium channel accessory subunits similar to our previous method of

$Na_V1.1$ expression (Lossin et al., 2002; Lossin et al., 2003; Rhodes et al., 2004; Ohmori et al., 2006). Cells were grown in Dulbecco's Modified Eagle's Medium (Invitrogen Corp., Carlsbad, CA) supplemented with 10% fetal bovine serum (Atlanta Biologicals, Norcross, GA), L-glutamine (2 mM) and penicillin-streptomycin (50 units/ml and 50 µg/ml, respectively) in a humidified, 5% CO_2 atmosphere at 37°C. Only low passage number (< 15) cells were used. Expression of $Na_V1.2$, β_1 and β_2 was achieved by transient cotransfection using Superfect (Qiagen Inc., Valencia, CA, U.S.A.) (5 µg of DNA was transfected at a plasmid mass ratio of 10:1:1 for α_2:β_1:β_2). The human β_1 and β_2 cDNAs were expressed from plasmids that contained separate coding sequences of the fluorescent proteins eGFP (hβ_1-IRES2-eGFP) or DsRed (hβ_2-IRES2-DsRed2) preceded by an internal ribosome entry site (IRES). Cells were plated on glass coverslips and only cells successfully transfected with β_1 and β_2 were used for electrophysiological studies. Unless otherwise noted, all reagents were purchased from Sigma Aldrich (Sigma, St Louis, MO, U.S.A.).

Electrophysiology and data analysis

Whole-cell voltage-clamp recordings were used to characterize the functional properties of wild-type (WT) and mutant sodium channels, as described previously (Lossin et al., 2002; Lossin et al., 2003; Rhodes et al., 2004; Ohmori et al., 2006). Sodium channel currents were recorded at room temperature, 48 to 72 hrs after transfection. Patch pipettes were fabricated from borosilicate glass (Warner Instrument Co., Hamden, CT, U.S.A) by a multistage P-97 Flaming-Brown micropipette puller (Sutter Instruments Co., San Rafael, CA, U.S.A.) and fire-polished by using a microforge (MF 830, Narashige, Japan). Pipette resistance was between 1.0 and 2.0 MΩ. The pipette solution consisted of (in mM) 110 CsF, 10 NaF, 20 CsCl, 2 EGTA, 10 HEPES, with a pH of 7.35 and osmolarity of 310 mOsmol/kg. The bath solution contained in (mM): 145 NaCl, 4 KCl, 1.8 $CaCl_2$, 1 $MgCl_2$, 10 HEPES, with a pH of 7.35 and osmolarity of 310 mOsmol/kg. The osmolarity was adjusted with sucrose. The bath solution was continuously exchanged by a gravity-driven perfusion system. The reference electrode consisted of a 2% agar bridge with composition similar to the bath solution. Cells were allowed to stabilize for 15 min after establishment of the whole-cell configuration before current was measured. Cells exhibiting peak current amplitudes < -0.6 nA were excluded from analysis of biophysical properties to avoid contamination of recordings by a low amplitude (< -0.1 nA) endogenous sodium current that is sometimes present in tsA201 cells. Cells exhibiting peak current amplitudes > -6 nA were also generally excluded from analysis to ensure accurate voltage control. Whole-cell capacitance and access resistance were determined by integrating capacitive transients in response to voltage steps from −120 to −110 mV filtered at 10 kHz. Series resistance was compensated 90-95% to assure that the command potential was reached in less than 100 μs with a voltage error ≤ 2 mV. Leak currents were subtracted by using an online P/4 procedure. All data were low-pass Bessel filtered at 5 kHz and digitized at 50 kHz.

Specific voltage-clamp protocols assessing channel activation, voltage dependence of fast inactivation, and recovery from a 100 ms inactivating prepulse (recovery from fast inactivation) were used as described previously (Lossin et al., 2002; Lossin et al., 2003; Rhodes et al., 2004; Ohmori et al., 2006) and described by figure insets. All voltage-clamp protocols utilized a holding potential of –120 mV and a 60 sec interpulse at the holding potential between sequential protocols. Voltage steps (20 ms) to between –80 to +60 mV in 10 mV increments were used to create a family of voltage-gated inward sodium current traces. The peak current was normalized for cell capacitance and plotted against voltage to generate peak current density-voltage relationships. Conductance (G_{Na}) was calculated as $G_{Na} = I/(V - E_{rev})$ where I is the measured peak current, V is the test voltage, and E_{rev} is the calculated sodium reversal potential. To provide a quantitative evaluation of the voltage dependence of activation, normalized *G-V* curves were fit with a Boltzmann function, $G/G_{max} = (1 + \exp[(V - V_{1/2})/k])^{-1}$, where $V_{1/2}$ is the curve midpoint indicating the voltage at which half of the channels are activated and k is a slope factor corresponding with voltage sensitivity of the channel. The time to peak current and 10 – 90% rise time were quantified for the –30 to +30 mV range using the same voltage-clamp protocol described above. Together these parameters define the magnitude of depolarization needed for channel opening. Voltage dependence of fast inactivation was assessed by 100 ms prepulses to between –160 to –10 mV in 10 mV increments followed by a 20 ms test pulse to –10 mV. The normalized current is plotted against the voltage and the data were fit with Boltzmann functions to determine the voltage for half-maximal inactivation ($V_{1/2}$) and a slope factor (k). Voltage dependence of fast inactivation provides information about the level of depolarization necessary for the channel to enter fast inactivation under steady-state conditions including the physiological range of potentials. Recovery from fast inactivation was determined using a two-pulse protocol. A 100 ms prepulse to –10 mV was followed by a variable amount of time for channel recovery and a 20 ms test pulse to –10 mV. The peak current from the test pulse was normalized to the peak current from the prepulse and plotted against the recovery period. Data were fit with the two exponential function, $I/I_{max} = A_1 \times [1 - \exp(-t/\tau_1)] + A_2 \times [1 - \exp(-t/\tau_2)]$, where τ_1 and τ_2 denote time constants (fast and slow components, respectively), and A_1 and A_2 represent the fast and slow fractional amplitudes. Time dependent recovery from inactivation provides information about how rapidly the channels can be available for a subsequent depolarization stimulus. A second recovery from fast inactivation protocol utilized a 5 ms prepulse to -10 mV followed by a variable amount of time for channel recovery and a 20 ms test pulse to -10 mV. The peak current from the test pulse was normalized to the peak current from the prepulse and plotted against the recovery period. Data were fit with the two exponential function, $I/I_{max} = A_1 \times [1 - \exp(-t/\tau_1)] + A_2 \times [1 - \exp(-t/\tau_2)]$, where τ_1 and τ_2 denote time constants (fast and slow components, respectively), and A_1 and A_2 represent the fast and slow fractional amplitudes. This recovery from fast inactivation protocol was used to see whether a shorter prepulse alters channel availability to a subsequent depolarizing stimulus.

Inactivation of the whole-cell sodium current was evaluated by fitting the decay phase of the current with the two exponential function, $I/I_{max} = A_1 \times \exp(-t/\tau_1) + A_2 \times \exp(-t/\tau_2)$, where τ_1 and τ_2 denote time constants (fast and slow components, respectively), A_1 and A_2 represent the fast and slow fractional amplitudes. For use-dependence studies, cells were stimulated with depolarizing pulse trains (100 pulses, 5 ms, 0 mV) at the indicated frequencies. A recovery interval (15 sec, −120 mV) followed each pulse train. Currents were normalized to the peak current recorded in response to the first pulse in each frequency train. Persistent current was evaluated during the final 10 ms of a 200 ms depolarization to −10 mV and expressed as a percentage of peak current following digital subtraction of currents recorded in the presence and absence of 10 μM tetrodotoxin (TTX). To prevent potential experimenter bias, persistent current experiments and analysis were performed blinded to genotype.

Slow inactivation was examined by paired-pulse protocols in which the response to a 4 ms test pulse to -10 mV was measured before (P1) and after (P2) variable conditioning protocols. Current measured during P2 was then normalized to the maximal current measured during P1. In detail, for onset of slow inactivation, the conditioning comprised voltage steps to -10 mV lasting from 1 ms to 100 sec, followed by a 50 ms recovery from fast inactivation at -120 mV. Conditioning for steady-state slow inactivation consisted of a 30 sec step to voltages between -140 and -10 mV and a 50 ms fast inactivation recovery at -120 mV. Conditioning for recovery from slow inactivation experiments used a 30 sec pulse to -10 mV, followed by recovery periods ranging from 100 ms to 100 sec. P1 pulses were repeated before each change of condition to minimize offset from run-down. In all cases, sufficient recovery time at -120 mV was allotted between different conditions to avoid accumulation of slow inactivation (determined in preliminary experiments; data not shown). Recordings with noticeable changes in P1 amplitude during the course of the experiment were discarded. Data from onset of slow inactivation experiments were plotted versus the length of the conditioning pulse and fitted to the two-exponential decay function, $I/I_{max} = A_1 \times \exp(-t/\tau_1) + A_2 \times \exp(-t/\tau_2) + y_0$ where τ_1 and τ_2 denote time constants (fast and slow components, respectively), A_1 and A_2 represent the fast and slow fractional amplitudes and y_0 represents the fraction of the channels that remains active. Steady-state slow inactivation data were fitted with the Boltzmann function, $I/I_{max} = ((1 - y_0) / (1 + \exp((x-V_{1/2}) / k)) + y_0$, where $V_{1/2}$ is the voltage at which half-maximal slow inactivation occurs, k is the slope factor of the fit, and y_0 is the fraction of the channels that remain active. Recovery from slow inactivation was fitted with the two-exponential function, $I/I_{max} = A_1 \times (1- e\hat{} -x/\tau_1) + A_2 \times (1-e\hat{} -x/\tau_2) + y_0$, where A_1 refers to the fraction of the channels recovering with τ_1, A_2 refers to the fraction of the channels recovering with τ_2, and y_0 is the fraction of the channels that remain active.

Results are presented as mean ± SEM. Statistical comparisons were made in reference to WT-Na_V1.2 by using the unpaired Student's *t* test. Chi-square analysis was used to determine significance level for expression efficiency of mutant alleles compared to WT-Na_V1.2. One-way ANOVA analysis with a Newman-Keuls Multiple Comparison post-test was performed to determine significance for peak whole-cell inward sodium current. Data analysis was performed using Clampfit 9.2 (Axon Instruments, Union City, CA, U.S.A), Excel 2002 (Microsoft, Seattle, WA, U.S.A.), GraphPad Prism 4.0

(GraphPad Software Inc., San Diego, CA), and OriginPro 7.0 (OriginLab, Northampton, MA, U.S.A) software.

Cell Surface Biotinylation

Cell surface biotinylation was performed as described previously (Kahlig et al., 2004; Kahlig et al., 2006a; Carvelli et al., 2002; Daws et al., 2002), with minor modifications for $Na_V1.2$ detection. Wild-type $Na_V1.2$, R1319Q, L1330F, and L1563V were epitope tagged with a triple FLAG tag on the C-terminus to increase detection sensitivity. Cells transfected with WT-$Na_V1.2$ or mutant $Na_V1.2$, β_1, and β_2 as described above were washed twice with 4 ^{o}C PBS, then cell surface proteins were labeled with the cell membrane impermeant biotinylating reagent, Sulfo-NHS-Biotin (Pierce Biotechnology, Rockford, IL), for 1 hr. The reaction was quenched with 100 mM glycine. Cells were then lysed with RIPA buffer (150 mM NaCl, 50 mM Tris-base, 1% IGEPAL CA-630, 0.5% Na Deoxycholate, 0.1 % SDS, pH 7.5) supplemented with Complete Mini Protease Inhibitor Cocktail Tabs (Roche Applied Science, Indianapolis, IN). Scraped lysates were centrifuged at 16,000 x g for 30 min at 4 ^{o}C. Biotinylated proteins in the supernatant were recovered by incubation (2 hrs at 4 ^{o}C) with High Capacity Streptavidin Agarose beads (Pierce Biotechnology, Rockford, IL) followed by centrifugation. The beads were extensively washed with RIPA buffer and biotinylated proteins eluted with 2X Laemmli Sample Buffer containing fresh 5% β-mercaptoethanol. Proteins were separated using SDS-polyacrylamide (7.5%) gel electrophoresis and transferred to polyvinylidene difluoride membranes. Membranes were incubated at room temperature for two hours in 5% milk. $Na_V1.2$ was detected with primary antibodies directed against the FLAG epitope (mouse, anti-FLAG M2, 1:15000, Sigma). The quantity of loaded protein in each lane was determined using a primary antibody directed against the endogenous protein transferrin (mouse, anti-human transferrin receptor, 1:10000 for total protein and 1:2500 for biotinylated protein, Zymed, Carlsbad, CA). Immunoreactive bands were visualized using horseradish peroxidase-conjugated secondary antibody (goat anti-mouse, 1:30000 for total protein and 1:10000 for biotinylated proteins, Santa Cruz Biotechnology, Santa Cruz, CA), directed against the primary antibody, ECL Plus (GE Healthcare, Buckinghamshire, UK) incubation and Hypersensitive ECL film detection. Protein band densitometry was performed using ImageJ software (NIH, Bethesda, MD). To control for protein loading, each $Na_V1.2$ band was normalized to the amount of endogenously expressed transferrin detected for each experimental condition. One-way ANOVA analysis with a Newman-Keuls Multiple Comparison post-test was performed to determine significance for cell surface biotinylation experiments.

Results

We functionally characterized three BFNIS mutations (R1319Q, L1330F, and L1563V) using a recombinant human $Na_V1.2$ co-expressed with the human β_1 and β_2 subunits in cultured cells (tsA201) of human origin. The three missense mutations have been reported previously; L1330F and L1563V by Heron et al. (Heron et al., 2002) and R1319Q by Berkovic et al. (Berkovic et al., 2004). Figure 17A illustrates the approximate position of each mutation within the predicted $Na_V1.2$ two-dimensional topology.

<u>BFNIS mutations cause reduced inward sodium current</u>

All three mutations (R1319Q, L1330F, and L1563V) generated functional sodium channels when transiently expressed in tsA201 cells. Figure 17B illustrates representative whole-cell currents evoked by a series of depolarizing test potentials in cells transiently expressing wild-type $Na_V1.2$ (WT-$Na_V1.2$), R1319Q, L1330F, or L1563V, while Figure 18A presents the corresponding peak current density-voltage relationships. The percentage of tested cells exhibiting quantifiable sodium currents (defined as peak

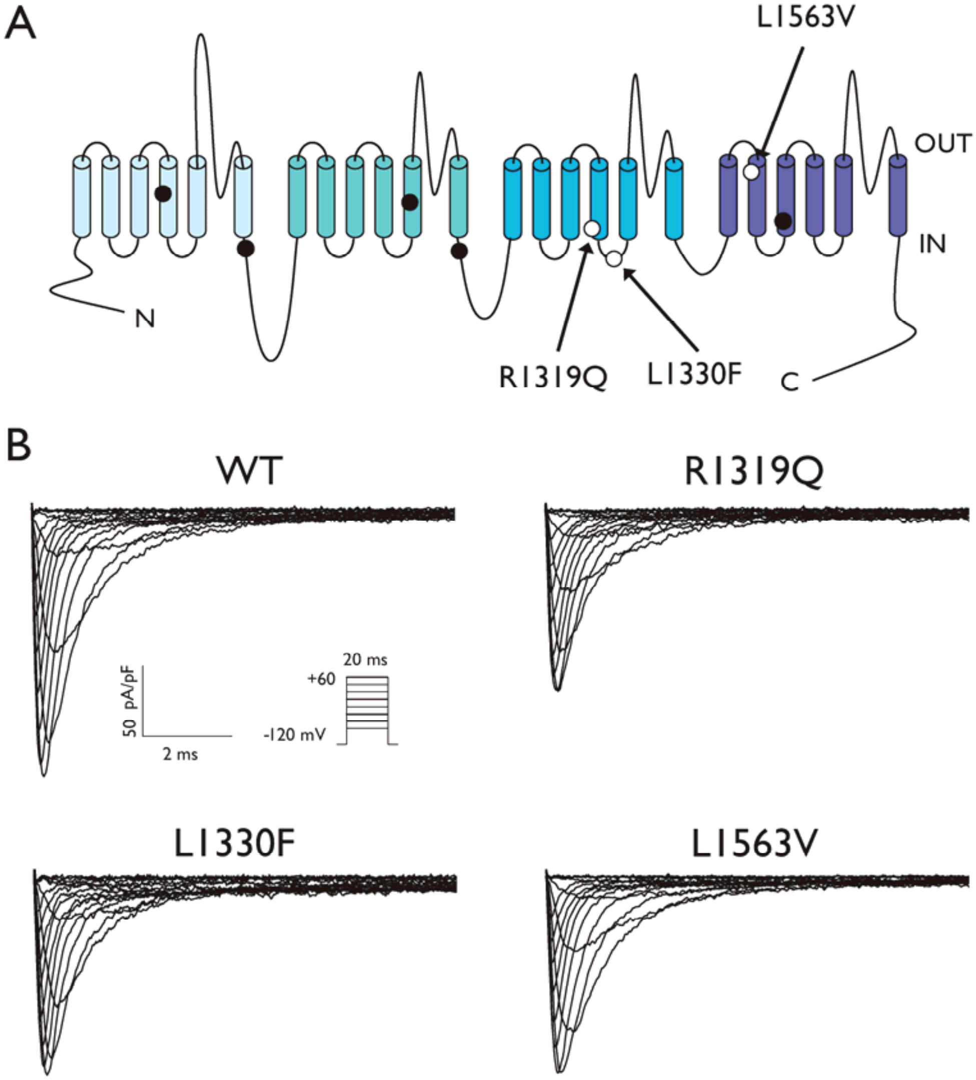

Figure 17. Representative WT-Na$_V$1.2 and mutant Na$_V$1.2 whole-cell sodium currents. (A) Predicted transmembrane topology of Na$_V$1.2 showing the location of BFNIS mutations as circles (open circles represent mutations characterized in this study). **(B)** Sodium currents recorded from tsA201 cells co-expressing the indicated Na$_V$1.2 allele with the β_1 and β_2 accessory subunits. Currents were activated by voltage steps to between –80 and +60 mV from a holding potential of −120 mV (see pulse protocol inset).

current ≥ -0.6 nA) was significantly lower for R1319Q and L1563V as compared to WT-Na$_V$1.2 channels (WT-Na$_V$1.2, 66%, n = 174; R1319Q, 41%, n = 161, $p < 0.001$; L1563V, 45%, n = 115, $p < 0.01$). In this analysis, L1330F expression was not significantly different than WT-Na$_V$1.2 (61%, n = 149). However, when we examined the inward current from all tested cells, thus removing the selection bias for high Na$_V$1.2 expression, the data revealed that all three BFNIS mutants displayed significantly lower peak current amplitudes compared to WT-Na$_V$1.2. Wild-type channels exhibited a mean peak current of −1.96 nA (n = 174), compared to −0.81 nA for R1319Q (n = 161; $p < 0.001$), −1.52 nA for L1330F (n = 149; $p < 0.05$), and −1.12 nA for L1563V (n = 115; $p < 0.001$). Subsequent experiments assessing the kinetics and voltage dependences of activation and inactivation as well as the time course of recovery from inactivation utilized cells with peak inward sodium current ≥ -0.6 nA. In the following subsections, specific biophysical properties of the three mutant channels are presented individually.

L1563V exhibits impaired inactivation

The BFNIS mutant L1563V affects a highly conserved residue within the S2 transmembrane helix of the 4th domain (DIV/S2, Figure 17A and 32). Activation properties (voltage dependence of activation, time to peak current, 10 – 90% rise time of activation) of L1563V were not significantly different than WT-Na$_V$1.2 channels (Figures 18B, 19B, and Tables 9 and 10). However, L1563V appeared to exhibit slower whole-cell current decay (Figure 17B). To quantify the time course of inactivation to enable statistical comparisons between WT- Na$_V$1.2 and L1563V, the whole-cell current decay was fitted with a two-exponential equation and the time constant with the dominant amplitude (τ_1) was plotted against the test potential for L1563V and WT-Na$_V$1.2 (Figure 19A, fit parameters for all mutants provided in Table 11). For cells expressing L1563V we observed significantly larger time constants for inactivation during voltage steps between −10 and 10 mV suggesting impaired fast inactivation. In addition, the voltage dependence of fast inactivation following an inactivating prepulse was significantly shifted in the depolarizing direction for L1563V suggesting that this mutant resists entry into the fast inactivated state (Figure 20A and Table 9). Furthermore, L1563V exhibited an accelerated recovery from fast inactivation indicated by a significantly smaller fast time constant (τ_1) (Figure 20B and Table 9). These data illustrate that L1563V has impaired fast inactivation.

R1319Q has mixed activation and inactivation defects

The R1319Q mutation neutralizes a highly conserved arginine residue in the S4 voltage-sensing segment of domain 3 (Figures 17A and 32). This mutant exhibited a small but significant increase in the slower time constant for inactivation (τ_2) only at −30 mV (Table 11), but otherwise had inactivation kinetics that were not significantly different than WT-$Na_V1.2$ channels. Voltage dependence of fast inactivation for R1319Q was also not significantly different from WT-$Na_V1.2$ (Figure 20A and Table 9), but R1319Q did exhibit a significant difference in recovery from fast inactivation (τ_1) compared to WT-$Na_V1.2$ (Figure 20B and Table 9). We observed a significantly greater time to peak current over the –10 to +20 mV range (Table 10) for R1319Q channels as well as a significantly increased 10-90 % rise time of activation compared to WT-$Na_V1.2$ (Figure 19B). These findings demonstrated slower activation of this mutant. Further evidence for a defect in activation was reflected by a conductance-voltage relationship that was significantly shifted in the depolarizing direction for R1319Q as compared to WT-$Na_V1.2$ (Figure 18B, Table 9). The slope factor (k) also exhibited a significant difference suggesting less steep voltage dependence for R1319Q compared to WT-$Na_V1.2$. These

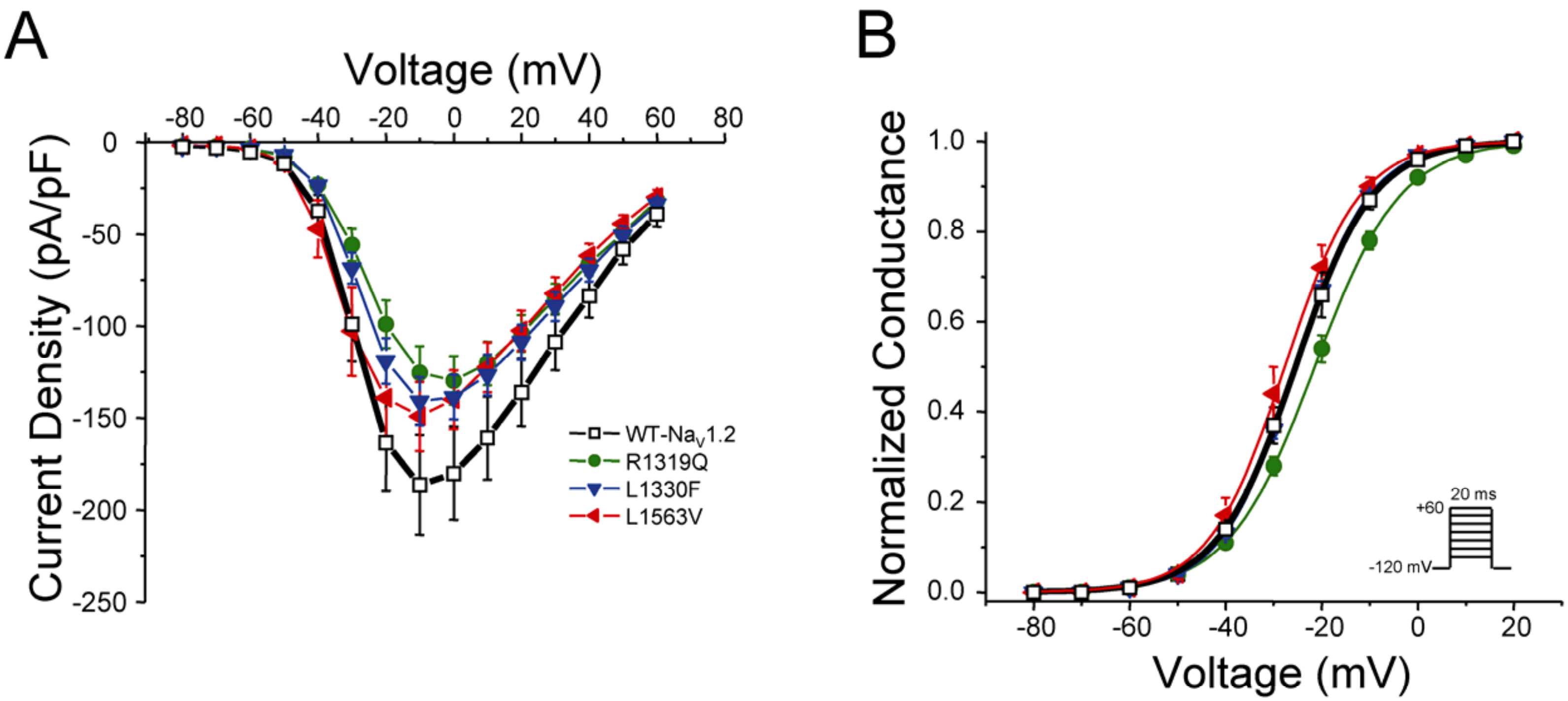

Figure 18. Activation properties of wild-type and mutant Na$_V$1.2. Biophysical properties of human WT-Na$_V$1.2, R1319Q, L1330F, and L1563V expressed in human tsA201 cells. **(A)** Peak current density elicited by test pulses to various potentials and normalized to cell capacitance. **(B)** Voltage dependence of channel activation measured during voltage steps to between –80 and +20 mV. R1319Q displayed a significant depolarizing shift in activation compared to WT-Na$_V$1.2. Pulse protocols are shown as panel insets and fit parameters are provided in Table 9.

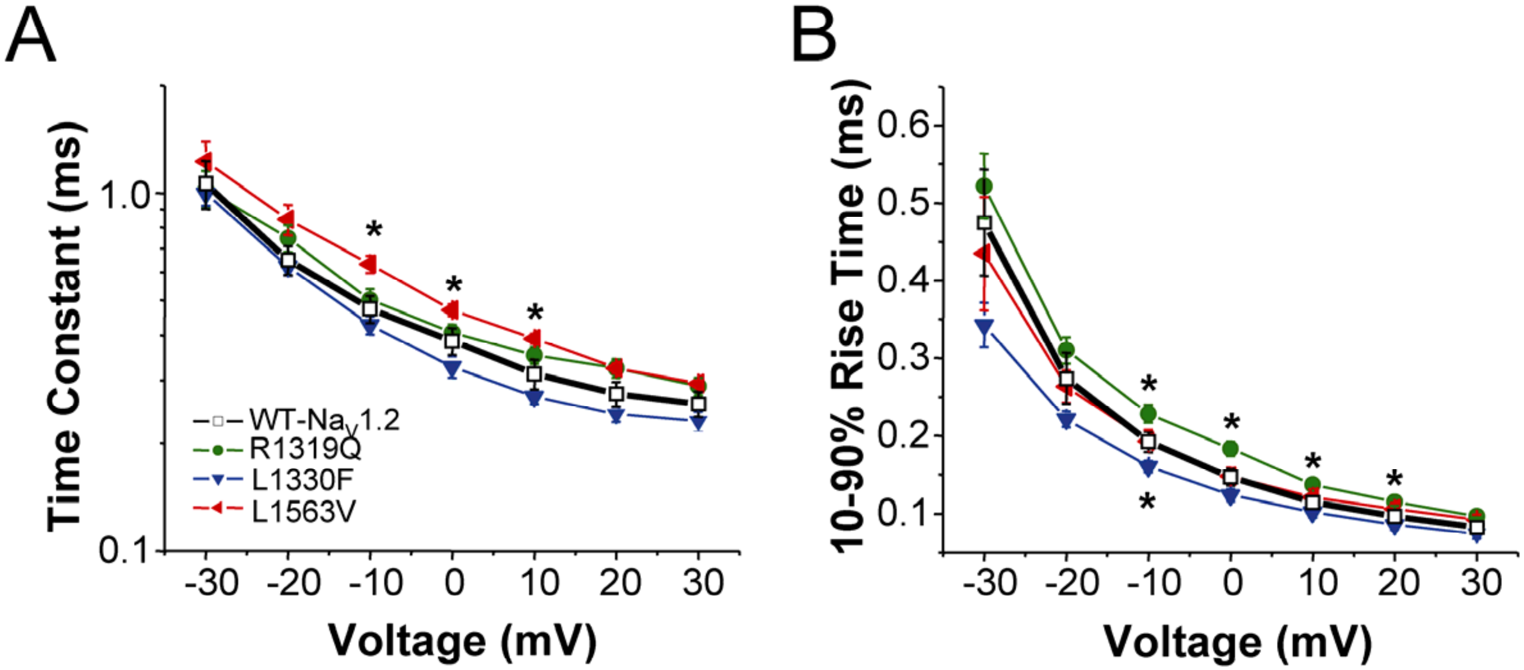

Figure 19. Inactivation and activation kinetics for wild-type and mutant Na$_V$1.2. (A) Fast inactivation time constants for WT-Na$_V$1.2 and BFNIS-associated mutants plotted against test potential. Fast time constants were significantly larger for L1563V (between –10 to + 10 mV, $p < 0.05$) compared to WT-Na$_V$1.2 channels. Fit parameters for all mutants are provided in Table 11. **(B)** Activation kinetics assessed by 10 – 90% rise time plotted against test potential for WT-Na$_V$1.2 and BFNIS-associated mutants. The rise time was significantly longer for R1319Q over the –10 to +20 mV range ($p < 0.05$) and significantly shorter for L1330F at –10 mV ($p < 0.05$) compared to WT-Na$_V$1.2.

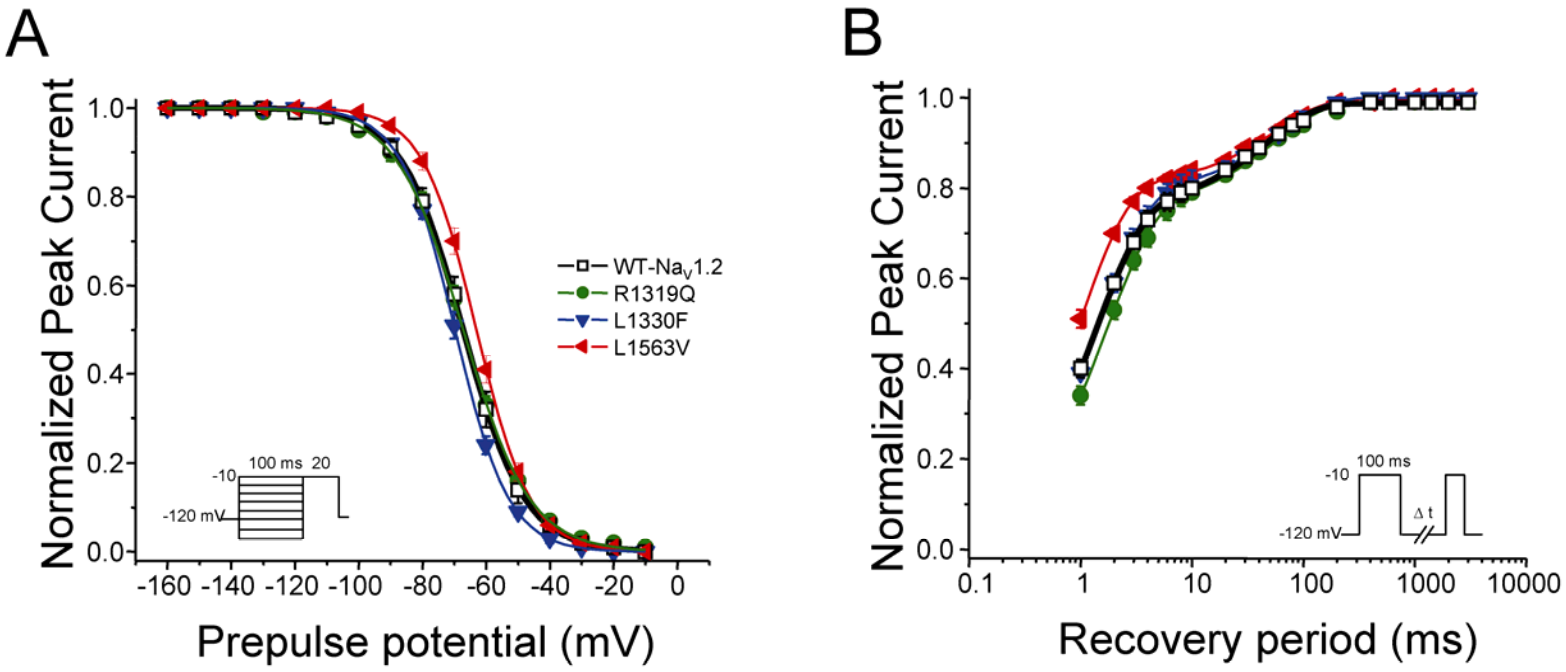

Figure 20. Fast inactivation of wild-type and mutant Na$_V$1.2. (A) Voltage dependence of fast inactivation assessed in response to inactivating prepulses to between –160 and –10 mV. L1563V displayed a significant depolarizing shift in the voltage dependence of fast inactivation compared to WT-Na$_V$1.2. **(B)** Time dependent recovery from fast inactivation assessed following an inactivating prepulse (100 ms at –10 mV). Significant defects in the recovery were observed for both R1319Q (delayed recovery) and L1563V (accelerated recovery). Pulse protocols are shown as panel insets and fit parameters are provided in Table 9.

Table 9. Biophysical parameters of $Na_V1.2$ BFNIS mutations

	Voltage dependence of activation			Voltage dependence of fast inactivation			Recovery from 100 ms inactivating prepulse		
	$V_{1/2}$ (mV)	*k* (mV)	*n*	$V_{1/2}$ (mV)	*k* (mV)	*n*	τ_1 (ms)§	τ_2 (ms)§	*n*
WT-$Na_V1.2$	-25.3 ± 1.4	7.5 ± 0.4	14	-67.4 ± 1.7	9.1 ± 0.8	14	1.4 ± 0.1 (75 ± 2%)	53.6 ± 6.9 (24 ± 2%)	16
R1319Q	-21.4 ± 0.9*	8.6 ± 0.2*	15	-67.1 ± 1.0	10.4 ± 0.9	16	1.7 ± 0.1* (74 ± 2%)	69.8 ± 13.0 (25 ± 2%)	15
L1330F	-25.5 ± 0.7	7.5 ± 0.2	15	-69.7 ± 1.0	8.2 ± 0.4	18	1.5 ± 0.1 (79 ± 2%)	65.5 ± 7.4 (21 ± 2%)	16
L1563V	-27.4 ± 1.8	6.5 ± 0.3	16	-62.9 ± 1.1*	8.1 ± 0.3	16	1.0 ± 0.1*** (80 ± 1%)*	63.6 ± 8.3 (19 ± 1%)*	16

Values significantly different from WT are indicated as follows *$p < 0.05$, ***$p < 0.001$.

§ values in parentheses are amplitude.

Table 10. Time to peak current for BFNIS mutations

	WT-Na$_V$1.2	**R1319Q**	**L1330F**	**L1563V**
-30 mV	0.79 ± 0.06 *n* = 14	0.90 ± 0.04 *n* = 15	0.72 ± 0.05 *n* = 15	0.85 ± 0.08 *n* = 16
-20 mV	0.56 ± 0.04 *n* = 14	0.65 ± 0.04 *n* = 15	0.51 ± 0.03 *n* = 15	0.61 ± 0.05 *n* = 16
-10 mV	0.44 ± 0.02 *n* = 14	0.52 ± 0.02** *n* = 15	0.40 ± 0.02 *n* = 15	0.48 ± 0.03 *n* = 16
0 mV	0.37 ± 0.02 *n* = 14	0.43 ± 0.01* *n* = 15	0.34 ± 0.02 *n* = 15	0.40 ± 0.02 *n* = 16
10 mV	0.33 ± 0.01 *n* = 14	0.36 ± 0.01* *n* = 15	0.29 ± 0.01** *n* = 15	0.34 ± 0.02 *n* = 16
20 mV	0.28 ± 0.01 *n* = 14	0.32 ± 0.01** *n* = 15	0.27 ± 0.01 *n* = 15	0.31 ± 0.02 *n* = 16
30 mV	0.26 ± 0.01 *n* = 14	0.28 ± 0.01 *n* = 15	0.25 ± 0.01 *n* = 15	0.29 ± 0.02 *n* = 16

For statistical differences from WT-Na$_V$1.2 $*p < 0.05$, $**p < 0.01$.

Table 11. Whole-cell current inactivation time constants for BFNIS mutations

	Fast Component§				Slow Component§			
	WT-Na$_V$1.2	**R1319Q**	**L1330F**	**L1563V**	**WT-Na$_V$1.2**	**R1319Q**	**L1330F**	**L1563V**
-30 mV	1.06 ± 0.16 (81 ± 9%)	1.03 ± 0.12 (81 ± 6%)	1.00 ± 0.08 (90 ± 3%)	1.22 ± 0.17 (81 ± 6%)	4.3 ± 0.2 (19 ± 9%)	5.4 ± 0.2* (20 ± 1%)	6.4 ± 0.9* (11 ± 3%)	4.8 ± 0.9 (19 ± 5%)
-20 mV	0.65 ±0.06 (91 ± 2%)	0.75 ± 0.06 (90 ± 3%)	0.62 ± 0.03 (95 ± 1%)	0.84 ± 0.08 (90 ± 1%)	3.6 ± 0.3 (9 ± 3%)	3.7 ± 0.6 (10 ± 3%)	5.1 ± 0.7 (5 ± 0.4%)	4.3 ± 0.5 (10 ± 1%)
-10 mV	0.47 ± 0.04 (93 ± 1%)	0.50 ± 0.04 (93 ± 1%)	0.43 ± 0.02 (96 ± 1%)	0.63 ± 0.04* (95 ± 1%)	3.3 ± 0.3 (7 ± 1%)	4.0 ± 0.5 (7 ± 1%)	5.0 ± 0.5* (4 ± 1%)	4.1 ± 0.4 (5 ± 1%)
0 mV	0.39 ± 0.03 (94 ± 1%)	0.41 ± 0.02 (94 ± 1%)	0.33 ± 0.02 (96 ± 1%)	0.47 ± 0.02* (94 ± 2%)	3.3 ± 0.5 (6 ± 1%)	4.0 ± 0.5 (6 ± 1%)	4.1 ± 0.6 (4 ± 1%)	3.6 ± 0.5 (6 ± 2%)
10 mV	0.31 ± 0.03 (94 ± 1%)	0.35 ± 0.02 (93 ± 1%)	0.27 ± 0.01 (95 ± 2%)	0.39 ± 0.01* (95 ± 1%)	3.0 ± 0.4 (6 ± 1%)	3.2 ± 0.7 (7 ± 1%)	3.9 ± 0.4* (5 ± 2%)	3.6 ± 0.6 (5 ± 1%)
20 mV	0.27 ± 0.02 (93 ± 2%)	0.32 ± 0.02 (92 ± 0.4%)	0.24 ± 0.01 (94 ± 3%)	0.32 ± 0.01 (95 ± 1%)	3.0 ± 0.4 (7 ± 2%)	2.7 ± 0.1 (7 ± 0.4%)	3.7 ± 0.4 (6 ± 3%)	3.9 ± 0.5 (5 ± 1%)
30 mV	0.26 ± 0.02 (93 ± 1%)	0.29 ± 0.02 (89 ± 2%)	0.23 ± 0.01 (94 ± 3%)	0.29 ± 0.01 (93 ± 1%)	2.4 ± 0.2 (7 ± 1%)	2.6 ± 0.1 (10 ± 2%)	3.9 ± 0.4 (6 ± 3%)	3.0 ± 0.5 (7 ± 1%)

Values significantly different from WT-Na$_V$1.2 are indicated as follows *$p < 0.05$. § values in parentheses are amplitude.

differences are consistent with neutralization of an S4 positive charge important for voltage sensing (Stühmer et al., 1989). Our data suggest that the R1319Q mutation alters both inactivation and activation in a manner that predicts a net decrease in channel activity.

L1330F exhibits enhanced use-dependent behavior

The L1330F mutation affects the short intracellular S4-S5 linker connecting the voltage-sensing and central-pore regions of DIII (Figures 17A and 32) (Long et al., 2005; Heron et al., 2002). Comparison of inactivation kinetics between WT-Na_V1.2 and L1330F revealed significant differences in the time constant representing the minor (slow) component of inactivation but only at a few test voltages (Table 11). There were no statistical differences between L1330F and WT-Na_V1.2 channels in the voltage dependence of activation, voltage dependence of fast inactivation, and recovery from fast inactivation (Figures 18, 20, and Table 9). L1330F displayed minor differences in the 10-90% rise time and time to peak current compared to WT-Na_V1.2 (Figure 19B and Table 10).

In the absence of major gating abnormalities for L1330F, we utilized a voltage clamp protocol consisting of a train of depolarizing steps at varying frequencies to test for differences in use-dependent channel behavior. L1330F exhibited a significantly enhanced use-dependent loss of channel availability compared to WT-Na_V1.2 over a large range of frequencies (22 to 133 Hz; Figure 21A). By contrast, the other two mutations we studied exhibited no significant differences in channel availability during the same pulse protocol (Figure 21A). The enhanced use-dependent loss of channel availability for L1330F was evident within the first several pulses as illustrated in Figure 21B for pulsing frequencies of 22, 85, and 133 Hz. These data predict that L1330F will have a net reduction in channel function during rapid stimulation.

The enhanced use-dependent channel availability exhibited by L1330F was not predicted by the individual activation and fast inactivation parameters described above. Recovery from fast inactivation is thought to influence use-dependent channel availability by affecting how quickly the channels are ready for subsequent depolarization as in the pulse train experiments. We performed an alternative recovery from fast inactivation protocol that used a 5 ms prepulse instead of 100 ms because this would more closely simulate the protocol for testing use-dependent channel behavior. L1330Fand WT-Na$_V$1.2 were not statistically different in the recovery from a 5 ms prepulse (Figure 22). We next looked at slow inactivation properties to see if this could explain the difference in use-dependent channel availability since slow inactivation is known to regulate availability of channels at steady-state. We looked at the onset, voltage dependence, and recovery from slow inactivation of WT-Na$_V$1.2 and L1330F. There were no statistical differences between L1330F and Na$_V$1.2 in any of these slow inactivation properties (Figure 23 and Table 12).

Absence of increased persistent current in BFNIS mutations

We previously observed that several Na$_V$1.1 mutations associated with various genetic epilepsy syndromes cause significantly increased persistent current (Lossin et al., 2002; Rhodes et al., 2004; Rhodes et al., 2005; Ohmori et al., 2006). However, none of the BFNIS mutants we studied exhibited this biophysical phenotype as compared to WT-Na$_V$1.2 channels (magnitude of persistent current as percentage of peak current amplitude: WT-Na$_V$1.2: 1.64 ± 0.35%, *n* = 10; R1319Q: 1.74 ± 0.24%, *n* = 9; L1330F: 1.51 ± 0.14%, *n* = 7; L1563V: 1.23 ± 0.39%, *n* = 7). This finding suggests that increased persistent current is not a common biophysical hallmark of Na$_V$1.2 mutations associated with BFNIS.

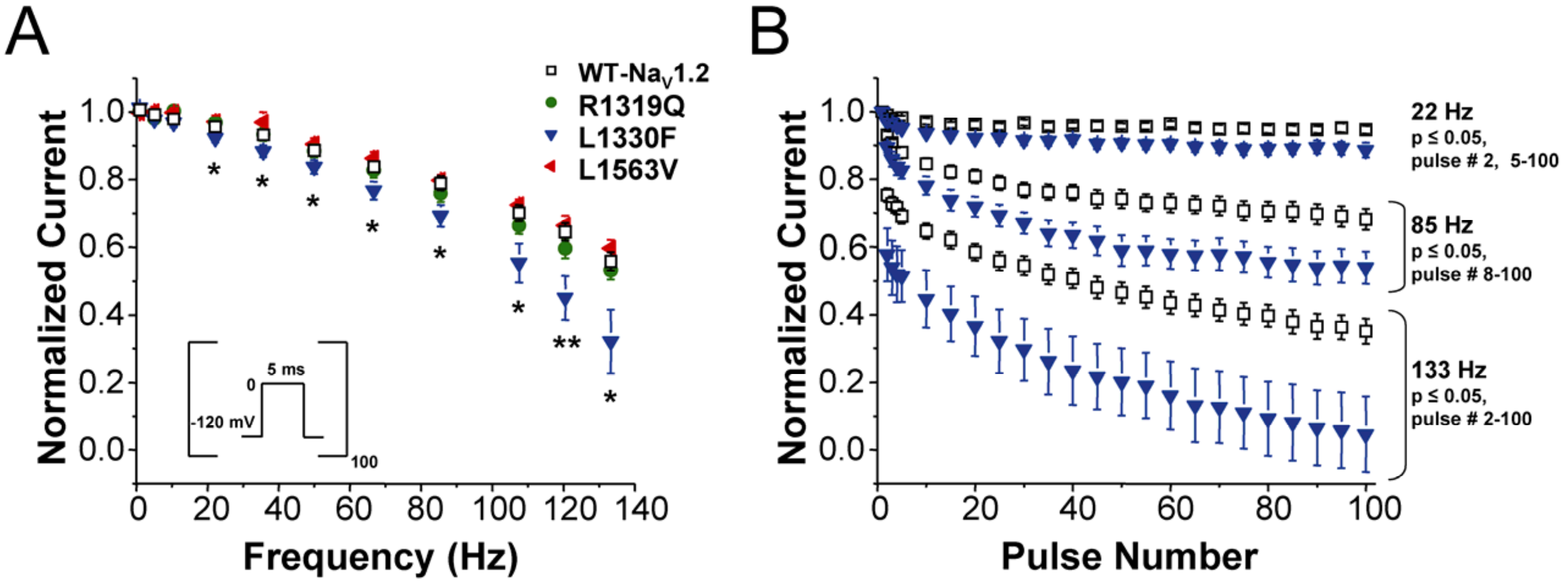

Figure 21. Use-dependent behavior of wild-type and mutant Na$_V$1.2. The response of Na$_V$1.2 alleles to repetitive depolarization (use-dependence of channel behavior) was measured by stimulating cells with voltage step pulse trains (100 pulses, 5 ms, 0 mV) from a holding potential of –120 mV at the indicated frequencies (see inset in panel A). **(A)** Residual peak current amplitude of the 25th pulse for WT-Na$_V$1.2, R1319Q, L1330F and L1563V plotted against pulse frequency. Fewer L1330F channels were available for activation in response to the 25th pulse compared to WT-Na$_V$1.2 for the stimulation frequencies of between 22 and 133 Hz (*, $p < 0.05$; **, $p < 0.01$). **(B)** Normalized peak current measured in response to a voltage step train at frequencies of 22, 85, and 133 Hz. L1330F displays significantly decreased residual current for pulses 2 and 5 to 100 for 22 Hz, pulses 8 to 100 for 85 Hz, and pulses 2 to 100 for 133 Hz ($p \leq 0.05$).

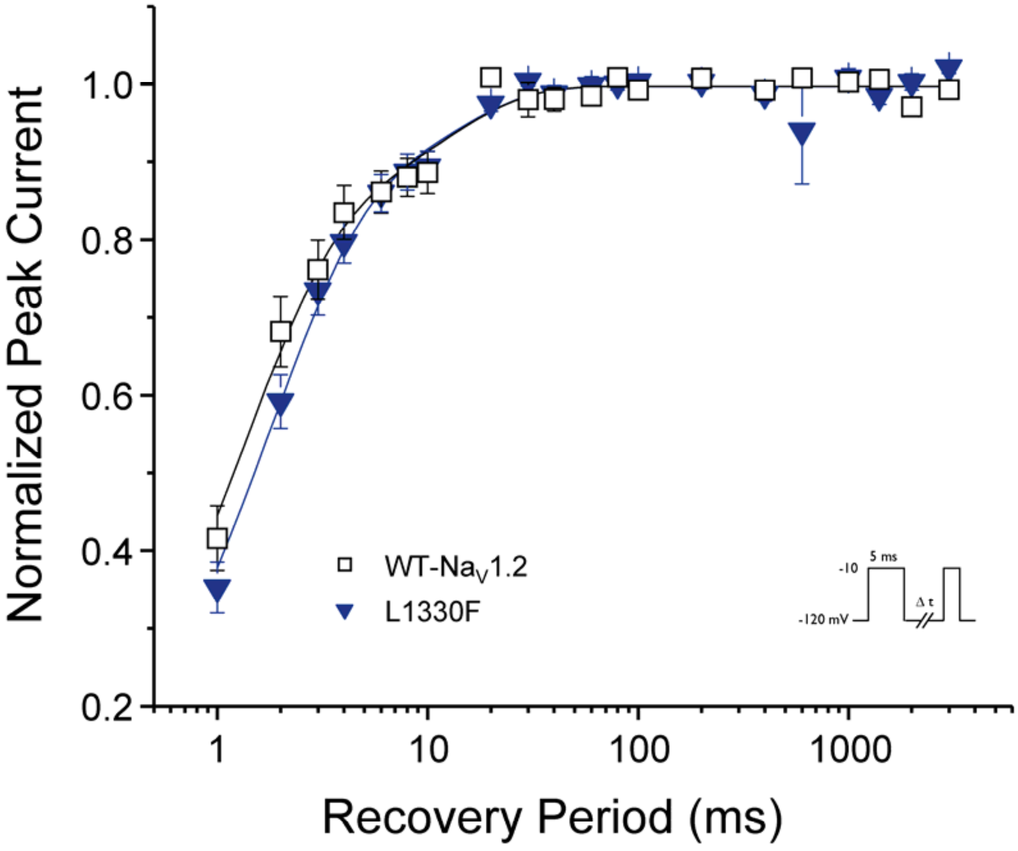

Figure 22. Recovery from a 5 ms inactivating prepulse. Time dependent recovery from fast inactivation assessed following an inactivating prepulse (5 ms at –10 mV) with pulse protocol shown as inset. L1330F displays no differences compared to WT-Na$_V$1.2 in recovery from a short prepulse. The WT-Na$_V$1.2 recovered with a τ_1 of 1.4 ± 0.2 for 81 ± 4% and a τ_2 of 18.8 ± 5.3 for 19 ± 4% of channels (*n* = 7). The L1330F mutant recovered with a τ_1 of 1.8 ± 0.2 for 84 ± 4% and a τ_2 of 21.5 ± 6.7 for 16 ± 4% of channels (*n* = 8).

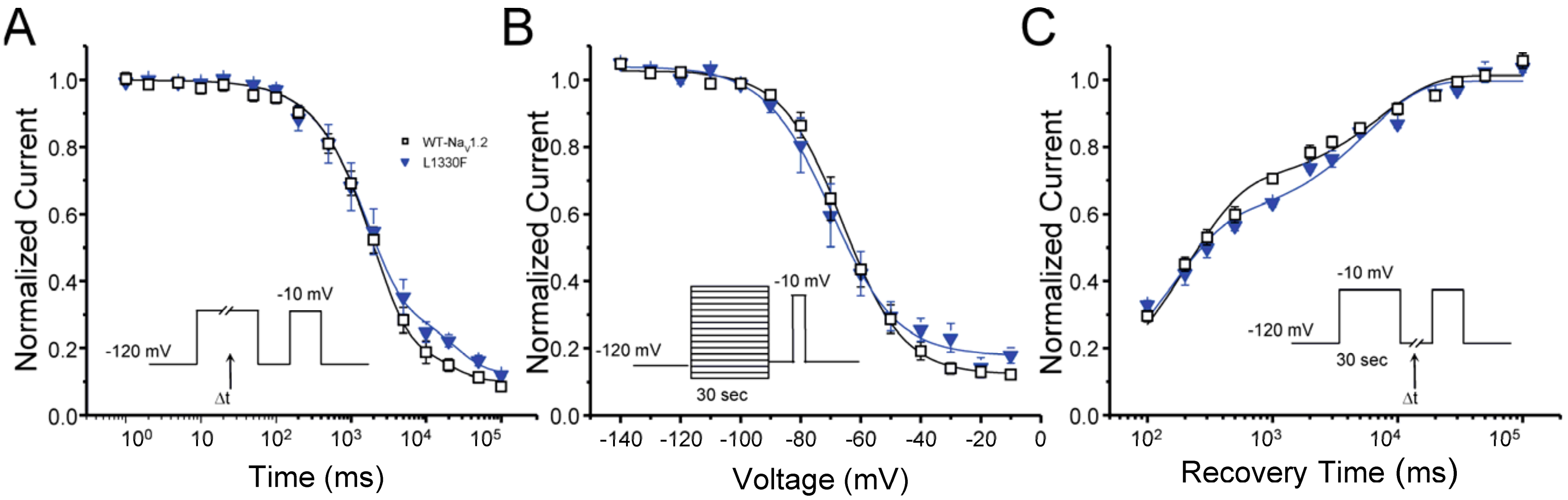

Figure 23. Slow inactivation properties of WT-Na$_V$1.2 are not different than L1330F. (A) Time-dependent entry into slow inactivation was examined using a two-pulse protocol consisting of a variable length inactivation pulse to –10 mV followed by a test pulse at –10 mV. Effects of fast inactivation were minimized using a 50 ms inter-pulse to –120 mV to relieve fast inactivation. **(B)** Voltage-dependent entry into slow inactivation was examined using a two-pulse protocol consisting of a 30 sec conditioning pulse at various potentials followed by a test pulse at –10 mV. Effects of fast inactivation were minimized using a 50 ms inter-pulse to –120 mV to relieve fast inactivation. **(C)** Time-dependent recovery from slow inactivation was examined using a two-pulse protocol consisting of a 30 sec inactivation pulse to –10 mV followed by a variable length inter-pulse to –120 mV and a test pulse to –10 mV. All fit parameters in Table 12 and voltage protocols are shown as figure insets.

Table 12. Slow inactivation parameters of WT-Na$_V$1.2 and L1330F

	Onset of slow inactivation			Voltage dependence of slow inactivation				Recovery from slow inactivation		
	τ_1(ms)§	τ_2 (ms)§	n	$V_{1/2}$ (mV)	k (mV)	I_R	n	τ_1(ms)§	τ_2 (ms)§	n
WT-Na$_V$1.2	2064 ± 277 (73 ± 3%)	21105 ± 7838 (18 ± 2%)	6	-65.3 ± 2.5	8.7 ± 0.4	13 ± 1%	6	194 ± 20 (66 ± 3%)	6307 ± 814 (34 ± 3%)	5
L1330F	2160 ± 374 (66 ± 2)	36671 ± 11495 (23 ± 2)	6	-68.3 ± 3.4	8.1 ± 0.9	19 ± 3%	6	166 ± 32 (59 ± 2%)	6517 ± 825 (41 ± 2%)	5

§ values in parentheses are amplitude.

BFNIS mutants exhibit reduced cell surface expression

All three BFNIS mutations exhibited significantly smaller mean whole-cell peak current levels as compared to WT-Na$_V$1.2. We tested the hypothesis that these mutations affected the level of protein at the plasma membrane by using cell surface biotinylation. Figure 24A illustrates that each BFNIS mutant exhibits lower cell surface expression compared to WT-Na$_V$1.2. Quantification of total cellular proteins levels showed no significant differences for any of the mutants compared with WT-Na$_V$1.2 (Figure 24B). By contrast, quantification of cell surface Na$_V$1.2 protein expression from four independent experiments (Figure 24C) demonstrated that, compared to WT-Na$_V$1.2, each mutant exhibits a substantial reduction in cell surface expression: 79% for R1319Q ($p < 0.001$), 47% for L1330F ($p < 0.01$), and 61% for L1563V ($p < 0.01$; $n = 4$). Reduced Na$_V$1.2 cell surface expression is a novel finding and this predicts a lower number of channels available for generating inward current, a potentially important factor in BFNIS pathogenesis.

Discussion

Elucidation of the molecular basis for brain sodium channelopathies and establishment of genotype-phenotype correlations may shed light on epileptogenesis and help conceptualize new treatment strategies. In this chapter, we examined the properties of three BFNIS mutations (R1319Q, L1330F, and L1563V) using the human Na$_V$1.2 α-subunit coexpressed with human β_1 and β_2 subunits. Although the clinical characteristics of patients with each of these mutations were similar (Heron et al., 2002; Berkovic et al., 2004), our findings indicate that Na$_V$1.2 mutations may exhibit a range of functional abnormalities as well as reduced cell surface expression signifying the complex molecular mechanisms underlying this inherited epilepsy.

Figure 24. Reduced cell surface protein expression of BFNIS mutants. Cell surface expression of WT and the three BFNIS mutations was measured using cell surface biotinylation. Endogenous transferrin levels were measured as a gel loading control. **(A)** Representative experiment illustrating total (top) and cell surface (bottom) $\mathrm{Na_V}$1.2 protein detected with anti-FLAG antibody. $\mathrm{Na_V}$1.2 immunoreactive bands were normalized to the amount of an endogenous protein (transferrin) detected in each experimental lane (below $\mathrm{Na_V}$1.2 detection). The first lane was isolated from cells transfected with untagged WT-$\mathrm{Na_V}$1.2. Lanes 2 – 5 are the FLAG tagged $\mathrm{Na_V}$1.2 constructs ($\mathrm{WT_{FLAG}}$, $\mathrm{R1319Q_{FLAG}}$, $\mathrm{L1330F_{FLAG}}$, $\mathrm{L1563V_{FLAG}}$, respectively). Lane 6 was isolated from untransfected tsA201 cells (mock). All three BFNIS mutations exhibited decreased cell surface $\mathrm{Na_V}$1.2 protein expression. **(B)** Quantification of four independent experiments demonstrated that each BFNIS mutant exhibits total protein expression similar to WT-$\mathrm{Na_V}$1.2 **(C)** Quantification of four independent experiments demonstrated that each BFNIS mutant exhibits a significantly lower level of cell surface channel expression: R1319Q is 21% of WT-$\mathrm{Na_V}$1.2 (***, $p < 0.001$), L1330F is 53% of WT-$\mathrm{Na_V}$1.2 (**, $p < 0.01$) and L1563V is 39% of WT-$\mathrm{Na_V}$1.2 (**, $p < 0.01$) ($n = 4$ for WT-$\mathrm{Na_V}$1.2, R1319Q, L1330F, and L1563V). The biotinylated and total $\mathrm{Na_V}$1.2 bands were normalized to the corresponding transferrin band and the ratio of the normalized biotinylated to total are shown for WT-$\mathrm{Na_V}$1.2, R1319Q, L1330F and L1563V.

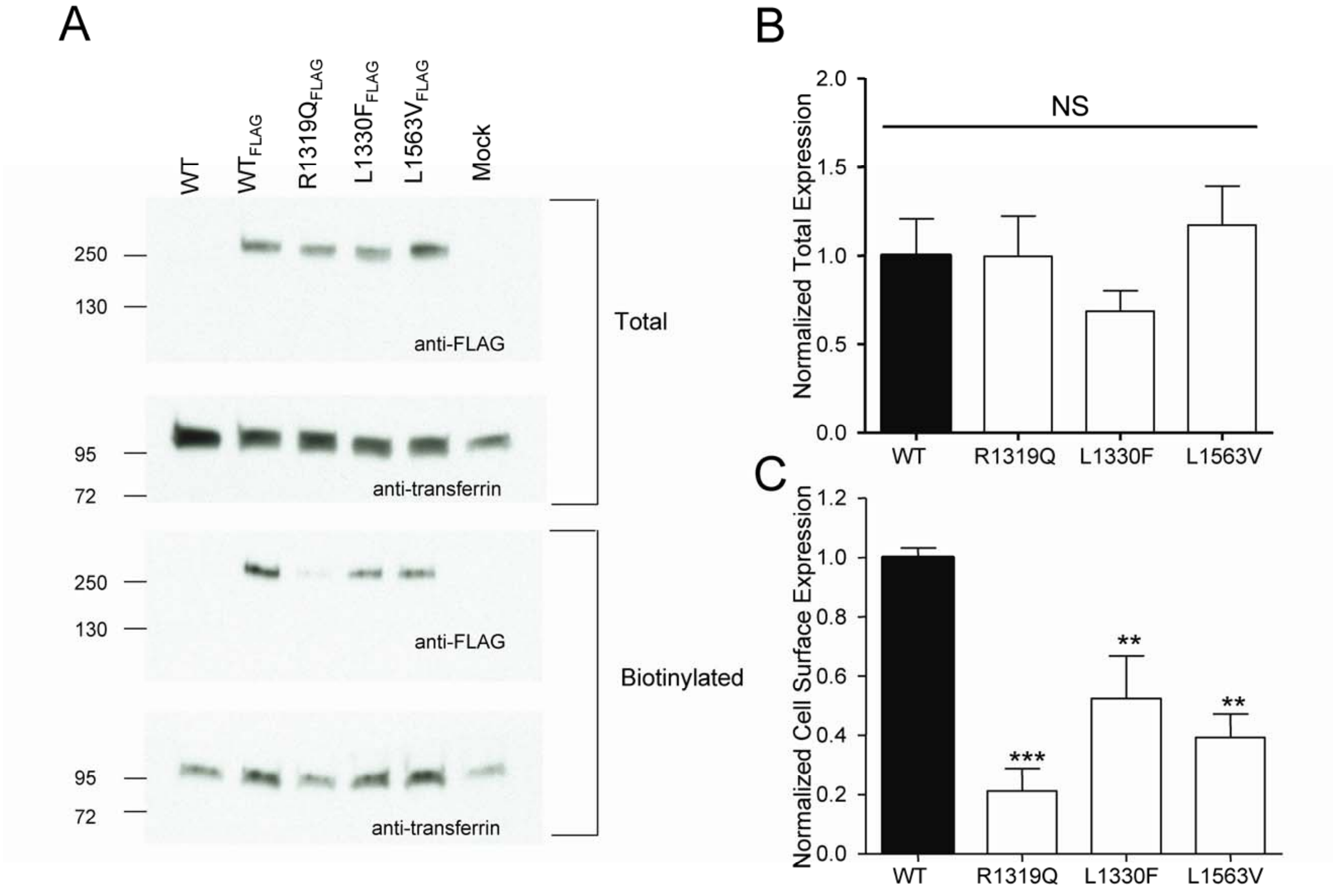
A
WT
WT_{FLAG}
$R1319Q_{FLAG}$
$L1330F_{FLAG}$
$L1563V_{FLAG}$
Mock
250
130
anti-FLAG
95
72
anti-transferrin
Total
250
130
anti-FLAG
Biotinylated
95
72
anti-transferrin
B
Normalized Total Expression
2.0
1.5
1.0
0.5
0.0
NS
WT
R1319Q
L1330F
L1563V
C
Normalized Cell Surface Expression
1.2
1.0
0.8
0.6
0.4
0.2
0.0
***
**
**
WT
R1319Q
L1330F
L1563V

In this study we examined the biophysical properties of wild-type and BFNIS mutant $Na_V1.2$. The R1319Q mutation caused a more positive and less steep voltage dependence of activation, slower activation, and delayed recovery from fast inactivation (Figures 18B, 19B, 20B and Tables 9, 10). These biophysical features predict a loss of channel function. L1330F decreased channel availability in response to repetitive stimulation over a large range of frequencies that may also indicate a loss of channel function (Figure 21). The L1563V mutation impaired fast inactivation, caused a positive shift in the voltage dependence of fast inactivation and displayed accelerated recovery from fast inactivation (Figures 19A, 20 and Tables 9, 11). The functional characteristics of L1563V predict a net gain of channel function. Previous studies have examined expression of voltage-gated sodium channel subunits in brain regions, but few studies convincingly show what neurons highly express $Na_V1.2$. Recent studies using mouse models of SMEI caused by haploinsufficiency of the highly homologous α isoform, $Na_V1.1$ preferentially affected inhibitory interneurons (Yu et al., 2006; Ogiwara et al., 2007). We predict that mutations correlated with a predicted loss of function, R1319Q and L1330F, might preferentially affect inhibitory interneurons while the L1563V mutation might exert its overall gain of function in excitatory neurons. This may help to explain how seemingly divergent biophysical effects may give rise to the same epilepsy syndrome although the exact mechanism for preferentially affecting one functional class of neurons is unknown. In general, these various and subtle biophysical effects probably contribute to the pathogenesis of BFNIS but may not represent the entire story.

In addition to the functional defects conferred by BFNIS mutations, we observed that cells expressing mutant channels exhibited lower peak current levels compared to WT-$Na_V1.2$. Further, all three BFNIS mutants exhibited between 47 and 79% lower cell surface expression of channel protein compared to WT-$Na_V1.2$ in tsA201 cells (Figure 24), and the relative magnitude of the reduction was concordant with mean whole-cell peak current levels. For example, R1319Q exhibited the largest decrease in mean whole-cell peak current as well as the lowest number of cells passing minimum current threshold, and this mutation exhibited the greatest decrement in cell surface expression. By contrast, L1330F had only a moderate reduction in both current amplitudes and cell surface expression. This finding suggests that reduced sodium channel density may be an important factor in the pathogenesis of BFNIS. Many potential mechanisms for decreased protein expression exist including reduced mRNA stability (Wada et al., 2004; Yanagita et al., 2003) and increased protein turnover rate (Gallagher et al., 2007). Previous studies of sodium channel mutations have suggested a role of altered temporal or spatial channel expression in promoting abnormal excitability (Wada, 2006; Waxman, 2007; Yu et al., 2006).

SCN2A encodes $Na_V1.2$, a voltage-gated sodium channel pore forming α-subunit expressed abundantly in the adult central nervous system. Knockout mice deficient in $Na_V1.2$ die perinatally from neuronal apoptosis and hypoxia, suggesting that expression is crucial for early postnatal, but not embryonic development (Planells-Cases et al., 2000). Early in development, $Na_V1.2$ is highly expressed in regions destined to become nodes of Ranvier, and is developmentally replaced by $Na_V1.6$ in adult rat brains (Kaplan et al., 2001). $Na_V1.2$ is also enriched at axon initial segments in developing neurons (Boiko et al., 2003; Garrido et al., 2003b; Garrido et al., 2003a). In the adult brain, unmyelinated axons throughout the rostral central nervous system, including the cortex and hippocampus, have high $Na_V1.2$ expression (Westenbroek et al., 1989; Westenbroek et al., 1992). Clusters of $Na_V1.2$ at nodes and the axon initial segments contribute to determining axonal firing frequency and action potential propagation (Carras et al., 1992; Boiko et al., 2003). Abnormal $Na_V1.2$ function may disrupt the physiological role of this channel in controlling excitability and underlie pathogenesis of genetic epilepsy syndromes. We speculate that the observed temporal transition of

$Na_V1.2$ to $Na_V1.6$ (Salzer, 2002) may also be affected by abnormal $Na_V1.2$ expression or activity.

The three BFNIS mutations presented in our study have been previously analyzed using cultured rat cortical neurons transfected with rat $Na_V1.2$ (Scalmani et al., 2006). Differences in functional properties of the mutant channels between our study and that performed in rat neurons may be explained by species differences of the cDNAs, or experimental limitations (e.g., uncertain voltage control) of the on-cell macropatch recording configuration applied to cultured neurons in that study. In addition, without a selective blocker of $Na_V1.2$, it is technically difficult to assign kinetic properties to $Na_V1.2$ expressed within the background of other voltage-gated sodium channels (Cummins et al., 2001; Herzog et al., 2001; Rush et al., 2005) especially if the mutant channels are expressed at very low levels as we have demonstrated. In our study, we used human $Na_V1.2$ coexpressed with the human β_1 and β_2 accessory subunits in cultured non-neuronal human cells. We further recorded $Na_V1.2$ activity using the whole-cell configuration of the patch-clamp allowing that enables more precise voltage and ionic control. This well established expression and recording approach uniquely permits the isolation and primary characterization of mutant human $Na_V1.2$ channels associated with BFNIS.

Another previous study proposed that the L1563V mutation preferentially affects a putative neonatal isoform of $Na_V1.2$ (Xu et al., 2007b). Although, a preferential functional impact of a mutation on a developmentally regulated splice variant provides an intriguing explanation for the abatement of seizures during late infancy in BFNIS, this should be considered speculative because the temporal regulation of this splicing event is not fully defined (Sarao et al., 1991; Kasai et al., 2001; Raymond et al., 2004; Tate et al., 2005). Further, this previous study characterized $Na_V1.2$ in the absence of β subunits that are known modulators of neuronal sodium channel gating properties (Isom et al., 1994; Catterall, 2000; Catterall et al., 2005), and this limits an accurate correlation with native channels. The absence of β subunits may help to explain why the previous study did not observe significant effects of the L1563V mutation on the same $Na_V1.2$ splice variant that we used (Xu et al., 2007b).

Aberrant trafficking of the mutant proteins to the plasma membrane, possibly because of mis-folding or altered interactions with chaperone proteins including β-subunits, is the most plausible explanation for the findings described in this chapter (Hirose, 2006). However, the mechanism of decreased cell surface expression for each of the BFNIS missense mutations was not determined. Because tsA201 cells are not neuronal in origin, future studies in neurons may help confirm our findings and aid in elucidating the cellular mechanism of altered excitability in BFNIS. Further, it will be interesting to determine $Na_V1.2$ expression levels when WT-$Na_V1.2$ and BFNIS mutants are cotransfected because this would represent the heterozygous state and may account for the autosomal dominant inheritance of the disease. We speculate that reduction of cell surface expression is the predominant effect of these mutations and that loss of $Na_V1.2$ expression on inhibitory interneurons may underlie BFNIS. We also speculate that $Na_V1.2$ expression on interneurons is dynamically regulated with high expression early in life and decreased expression later in life explaining the spontaneous seizure remission within the first year of life.

In summary, we have demonstrated that three *SCN2A* mutations associated with BFNIS cause subtle and divergent biophysical defects in $Na_V1.2$, but also impair cell surface expression. A greater understanding of the exact composition of sodium channel complexes *in vivo* and their targeting to different subcellular localizations will be required to fully understand how these defects cause BFNIS. Future studies will also need to account for the developmentally regulated role of $Na_V1.2$ in neuronal excitability and how this relates to the early seizure remittance seen in BFNIS. Animal models with genetically engineered $Na_V1.2$ mutations may help elucidate the physiological contribution of this isoform and further explain the pathogenesis of BFNIS.

CHAPTER IV

INCREASED NA$_V$1.1 FUNCTION IN MESIAL TEMPORAL LOBE EPILEPSY

Introduction

Temporal lobe epilepsy (TLE) is one of the most common and severe forms of partial epilepsy. TLE and antecedent febrile seizures (FS) have a controversial relationship. Antecedent FS has been found in 25% of TLE patients (Hamati-Haddad and Abou-Khalil, 1998) and 50-80% of refractory TLE patients (French et al., 1993; Baulac et al., 2004). The hypothesis was put forth that prolonged or complex FS (FS+) in childhood could damage the hippocampus causing hippocampal sclerosis (HS) and eventually lead to refractory temporal lobe seizures, most commonly affecting the mesial temporal lobe (Maher and McLachlan, 1995; Baulac et al., 2004). HS and mesial temporal sclerosis can be determined from MRI studies by visualizing hippocampal atrophy or hyperintensities. Alternatively HS can be seen pathologically as neuronal loss in the CA1, CA3, and hilar regions of the hippocampus with pronounced astrogliosis (Maurer-Morelli et al., 2006). To date there has been no conclusive prospective study to show a causal relationship between complex FS, TLE, and HS.

Initially TLE was primarily considered an acquired disorder and little was known about its inheritance (Baulac et al., 2001b). Sporadic TLE may affect either the mesial or lateral regions of the temporal lobe and has been associated with polymorphisms in several genes including interleukin-1β, prodynorphin, a prion protein gene, and the GABA$_B$ receptor 1 gene (Baulac et al., 2004). Familial forms of lateral TLE that are not linked to FS have been associated with leucine-rich, glioma inactivated 1 (*LGI1*) (Baulac et al., 2004; Wang and Lu, 2008).

Several studies have examined the genetics of TLE in families with FS resulting in several different candidate loci or genes. One study of a French family with FS and subsequent TLE without hippocampal abnormalities on MRI showed digenic inheritance of particular haplotypes on 18qter and 1q25-q31 (Baulac et al., 2001b). Another family with FS and childhood absence epilepsy (CAE) had one member with febrile seizures plus (FS+) who developed pharmacoresistant TLE. FS+ are FS that persist beyond six years of age or FS in combination with afebrile seizures. In this study, a region of 3p and a possible modifier locus on 18p were implicated in the epilepsy phenotype because all FS patients who developed epilepsy shared both haplotypes (Nabbout et al., 2007).

A mutation in a well conserved *SCN1A* residue, M145T, was isolated in a family with FS (Mantegazza et al., 2005). Three of the family members also developed TLE and two of these patients also had HS via MRI studies (Colosimo et al., 2007). Genetic analyses were also performed on families with generalized epilepsy with febrile seizures plus (GEFS+). One large GEFS+ family had several members who had subsequent epilepsy including individuals who had TLE. A combination of pedigree analysis and gene sequencing showed autosomal dominant inheritance of the *SCN1A* mutation, K1270T, in all affected family members and one asymptomatic individual (Abou-Khalil et al., 2001). Another study of several GEFS+ families found several patients who developed TLE with the *SCN1B* mutation C121W (Scheffer et al., 2007). These findings suggest that mutations in voltage-gated sodium channel subunits, either α or β, can lead to TLE.

Our collaborators screened brain tissue resected from mesial TLE (MTLE) patients for mutations in the voltage-gated sodium channel genes *SCN1A*, *SCN2A*, and *SCN3A*. A novel mutation in *SCN1A*, N211S, was identified by Jennifer A. Kearney, Sarah K. Bergren, James O. McNamara, and Miriam H. Meisler (unpublished observations). We functionally characterized the mutant and found that it caused an increase in function.

Materials and Methods

Subjects and mutation detection

46 patients with MTLE were diagnosed according to the criteria of the Commission on Classification and Terminology of the ILAE (1989). DNA was extracted from resected brain tissue by proteinase-K digestion, followed by phenol:chloroform extraction and ethanol precipitation. The 26 coding exons of *SCN1A, SCN2A* and *SCN3A* were amplified individually from genomic DNA and analyzed by conformation sensitive gel electrophoresis. PCR products containing variants were gel purified and sequenced on an ABI Model 3730 automated sequencer in the University of Michigan DNA Sequencing Core. NINDS Neurologically Normal Caucasian Control Panels (Coriell NDPT006 and NDPT009; $n = 184$) and a panel of 111 subjects who were > 60 years of age without personal or family history of neurological disease (Rainier et al., 2006) were screened for N211S by PCR-RFLP analysis, based on an alternative BsrDI restriction site.

Mutagenesis of human $Na_V1.1$ cDNA

The full-length human $Na_V1.1$ cDNA was previously cloned into the mammalian expression plasmid pCMV-Script. PCR site-directed mutagenesis was used to engineer individual mutations into pCMV-$Na_V1.1$ using a previously described method (Lossin et al., 2002; Lossin et al., 2003; Rhodes et al., 2004; Ohmori et al., 2006). The mesial temporal lobe epilepsy-associated mutation, N211S, was constructed using codon usage typical of human tissues. Due to the tendency of neuronal voltage-gated sodium channel cDNAs to spontaneously mutate within bacterial culture, we propagated clones in Max Efficiency Stbl2 host cells (Invitrogen Corporation, Carlsbad, CA) at 30 °C, and the entire ORF of each construct was completely sequenced to exclude polymerase errors and inadvertent mutations. Two recombinant clones of the mutation were evaluated functionally.

Heterologous expression of $Na_V1.1$

Recombinant $Na_V1.1$ was heterologously coexpressed in human tsA201 cells (HEK293 derivative stably transfected with SV40 large T antigen) with the human β_1 and β_2 voltage-gated sodium channel accessory subunits similar to our previous method of $Na_V1.1$ expression (Lossin et al., 2002; Lossin et al., 2003; Rhodes et al., 2004; Ohmori et al., 2006). Cells were grown in Dulbecco's Modified Eagle's Medium (DMEM) (Invitrogen Corp., Carlsbad, CA) supplemented with 10% fetal bovine serum (Atlanta Biologicals, Norcross, GA), L-glutamine (2 mM) and penicillin-streptomycin (50 units/ml and 50 µg/ml, respectively) in a humidified, 5% CO_2 atmosphere at 37°C. Only low passage number (< 15) cells were used. Expression of $Na_V1.1$, β_1 and β_2 was achieved by transient transfection using Fugene 6 (Roche Applied Science, Indianapolis, IN) (5 µg of DNA was transfected at a plasmid mass ratio of 10:1:1 for α_2:β_1:β_2). The human β_1 and β_2 cDNAs were expressed from plasmids that contained separate coding sequences of the marker genes CD8 (pCD8-IRES-hβ_1) or the fluorescent protein GFP (pGFP-IRES-hβ_2) preceded by an internal ribosome entry site (IRES). Transfected cells were dissociated by brief exposure to Trypsin/EDTA, resuspended in supplemented DMEM medium and allowed to recover for 30 min at 37 °C at 5% CO_2. CD8 antibody-covered microbeads (Dynabeads M-450 CD8, Dynal, Norway) suspended in 150 µl DMEM were added to the cell suspension and gently shaken. Only cells positive for CD8 antigen and GFP fluorescence indicative of hβ_1 and hβ_2 expression were used for electrophysiological analysis. Unless otherwise noted, all reagents were purchased from Sigma Aldrich (Sigma, St Louis, MO).

Electrophysiology and data analysis

Whole-cell voltage-clamp recordings were used to characterize the functional properties of WT and mutant sodium channels, as described previously (Lossin et al., 2002; Lossin et al., 2003; Rhodes et al., 2004; Ohmori et al., 2006). Sodium channel currents were recorded at room temperature, 24 to 48 hr after transfection. Patch pipettes were fabricated from borosilicate glass (Warner Instrument Co., Hamden, CT) by a multistage P-97 Flaming-Brown micropipette puller (Sutter Instruments Co., San Rafael, CA) and fire-polished by using a microforge (MF 830, Narashige, Japan). Pipette resistance was between 1.0 and 2.0 MΩ. The pipette solution consisted of (in mM) 110 CsF, 10 NaF, 20 CsCl, 2 EGTA, 10 HEPES, with a pH of 7.35 and osmolarity of 310 mOsmol/kg. The bath solution contained in (mM): 145 NaCl, 4 KCl, 1.8 $CaCl_2$, 1 $MgCl_2$, 10 HEPES, with a pH of 7.35 and osmolarity of 310 mOsmol/kg. The osmolarity was adjusted with sucrose. The bath solution was continuously exchanged by a gravity-driven perfusion system. The reference electrode consisted of a 2% agar bridge with composition similar to the bath solution. Cells were allowed to stabilize for 15 min after establishment of the whole-cell configuration before current was measured. Cells exhibiting peak current amplitudes < -0.6 nA were excluded from analysis of biophysical properties to avoid contamination of recordings by low amplitude (< -0.1 nA) endogenous sodium current that is sometimes present in tsA201 cells. Cells exhibiting peak current amplitudes > -6 nA were also generally excluded from analysis to ensure accurate voltage control. Whole-cell capacitance and access resistance were determined by integrating capacitive transients in response to voltage steps from −120 to −110 mV filtered at 10 kHz. Series resistance was compensated 90-95% to assure that the command potential was reached in less than 100 μs with a voltage error < 2 mV. Leak currents were subtracted by using an online P/4 procedure. All data were low-pass Bessel filtered at 5 kHz and digitized at 50 kHz.

Specific voltage-clamp protocols assessing channel activation, voltage dependence of fast inactivation, and recovery from a 100 ms inactivating prepulse (recovery from fast inactivation) were used as described previously (Lossin et al., 2002; Lossin et al., 2003; Rhodes et al., 2004; Ohmori et al., 2006) and described by figure insets. All voltage-clamp protocols utilized a holding potential of –120 mV and a 60 sec interpulse at the holding potential between sequential protocols. Voltage steps (20 ms) to between –80 to +60 mV in 10 mV increments were used to create a family of voltage-gated inward sodium current traces. The peak current was normalized for cell capacitance and plotted against voltage to generate peak current density-voltage relationships. Conductance (G_{Na}) was calculated as $G_{Na} = I/(V - E_{rev})$ where I is the measured peak current, V is the test voltage, and E_{rev} is the calculated sodium reversal potential. To provide a quantitative evaluation of the voltage dependence of activation, normalized *G-V* curves were fit with a Boltzmann function, $G/G_{max} = (1 + \exp[(V - V_{1/2})/k])^{-1}$, where $V_{1/2}$ is the curve midpoint indicating the voltage at which half of the channels are activated and k is a slope factor corresponding with voltage sensitivity of the channel. The time to peak current and 10 – 90% rise time were quantified for the –30 to +30 mV range using the same voltage-clamp protocol described above. Together these parameters define the magnitude of depolarization needed for channel opening. Voltage dependence of fast inactivation was assessed by 100 ms prepulses to between –140 to –10 mV in 10 mV increments followed by a 20 ms test pulse to –10 mV. The normalized current is plotted against the voltage and the data were fit with Boltzmann functions to determine the voltage for half-maximal inactivation ($V_{1/2}$) and a slope factor (k). Voltage dependence of fast inactivation provides information about the level of depolarization necessary for the channel to enter fast inactivation under steady-state conditions including the physiological range of potentials. Recovery from fast inactivation was determined using a two-pulse protocol. A 100 ms prepulse to –10 mV was followed by a variable amount of time for channel recovery and a 20 ms test pulse to –10 mV. The peak current from the test pulse was normalized to the peak current from the prepulse and plotted against the recovery period. Data were fit with the two exponential function, $I/I_{max} = A_1 \times [1 - \exp(-t/\tau_1)] + A_2 \times [1 - \exp(-t/\tau_2)]$, where τ_1 and τ_2 denote time constants (fast and slow components, respectively), and A_1 and A_2 represent the fast and slow fractional amplitudes. Time dependent recovery from inactivation provides information about how rapidly the channels can be available for a subsequent depolarization stimulus.

Inactivation of the whole-cell sodium current was evaluated by fitting the decay phase of the current with the two exponential function, $I/I_{max} = A_1 \times \exp(-t/\tau_1) + A_2 \times \exp(-t/\tau_2)$, where τ_1 and τ_2 denote time constants (fast and slow components, respectively), A_1 and A_2 represent the fast and slow fractional amplitudes. For studies of use-dependent channel availability, cells were stimulated with depolarizing pulse trains of 200 pulses to 0 mV for 5 ms each at the indicated frequencies. A recovery interval of 15 sec at −120 mV followed the pulse train at each frequency. Currents were normalized to the peak current recorded in response to the first pulse in each frequency train. Persistent current was evaluated during the final 10 ms of a 200 ms depolarization to −10 mV and expressed as a percentage of peak current following digital subtraction of currents recorded in the presence and absence of 10 μM tetrodotoxin (TTX). To prevent potential experimenter bias, persistent current experiments and analysis were performed blinded to genotype.

Cell Surface Biotinylation

Cell surface biotinylation was performed as described previously (Kahlig et al., 2004; Kahlig et al., 2006a; Carvelli et al., 2002; Daws et al., 2002), with minor modifications for $Na_V1.1$ detection. Wild-type $Na_V1.1$ and N211S were epitope tagged with a triple FLAG tag on the C-terminus to increase detection sensitivity. Cells transfected with WT-$Na_V1.1$ or N211S, β_1, and β_2 as described above were washed twice with 4 ^oC PBS, then cell surface proteins were labeled with the cell membrane impermeant biotinylating reagent, Sulfo-NHS-Biotin (Pierce Biotechnology, Rockford, IL), for 1 hr. The reaction was quenched with 100 mM glycine. Cells were then lysed with RIPA buffer (150 mM NaCl, 50 mM Tris-base, 1% IGEPAL CA-630, 0.5% Na Deoxycholate, 0.1 % SDS, pH 7.5) supplemented with Complete Mini Protease Inhibitor Cocktail Tabs (Roche Applied Science, Indianapolis, IN). Scraped lysates were centrifuged at 16,000 x g for 30 min at 4 ^oC. Biotinylated proteins in the supernatant were recovered by incubation (2 hrs at 4 ^oC) with High Capacity Streptavidin Agarose beads (Pierce Biotechnology, Rockford, IL) followed by centrifugation. The beads were extensively washed with RIPA buffer and biotinylated proteins eluted with 2X Laemmli Sample Buffer containing fresh 5% β-mercaptoethanol. Proteins were separated using SDS-polyacrylamide (7.5%) gel electrophoresis and transferred to polyvinylidene difluoride membranes. Membranes were incubated at room temperature for two hrs in 5% milk. $Na_V1.1$ was detected with primary antibodies directed against the FLAG epitope (mouse, anti-FLAG M2, 1:15000, Sigma). The quantity of loaded protein in each lane was determined using a primary antibody directed against the endogenous protein transferrin (mouse, anti-human transferrin receptor, 1:10000 for total protein and 1:2500 for biotinylated protein, Zymed, Carlsbad, CA). Immunoreactive bands were visualized using horseradish peroxidase-conjugated secondary antibody (goat anti-mouse, 1:30000 for total protein and 1:10000 for biotinylated proteins, Santa Cruz Biotechnology, Santa

Cruz, CA), directed against the primary antibody, ECL Plus (GE Healthcare, Buckinghamshire, UK) incubation and Hypersensitive ECL film detection. Protein band densitometry was performed using ImageJ software (NIH, Bethesda, MD). To control for protein loading, each $Na_V1.1$ band was normalized to the amount of endogenously expressed transferrin detected for each experimental condition. One-way ANOVA analysis with a Newman-Keuls Multiple Comparison post-test was performed to determine significance for cell surface biotinylation experiments.

Results

Sequence analysis

46 patients underwent surgical resection of mesial temporal lobe following a diagnosis of intractable MTLE. Our collaborators, Kearney et al. isolated genomic DNA from the brain tissue and the coding exons of three sodium channel genes, *SCN1A*, *SCN2A*, and *SCN3A*, were sequenced. One sample had an A632G nucleotide substitution in the coding region of exon 5 in *SCN1A*. This substitution alters a highly conserved asparagine for a serine residue at position 211 (N211S) (Figure 25). The N211S mutation was confirmed to affect a residue in exon 5A and not the alternatively spliced exon 5N. The heterozygote frequency was 0.02 (n = 46) with a minor allele frequency of 0.01 (n = 92) in the MTLE samples. In control samples the heterozygote frequency was 0 (n = 295) and the minor allele frequency was 0 (n = 590).

N211S causes increased inward sodium current

We functionally characterized the mesial temporal lobe epilepsy-associated mutation (N211S) using a recombinant human $Na_V1.1$ co-expressed with the human β_1 and β_2 subunits in cultured cells (tsA201) of human origin. N211S is a novel missense

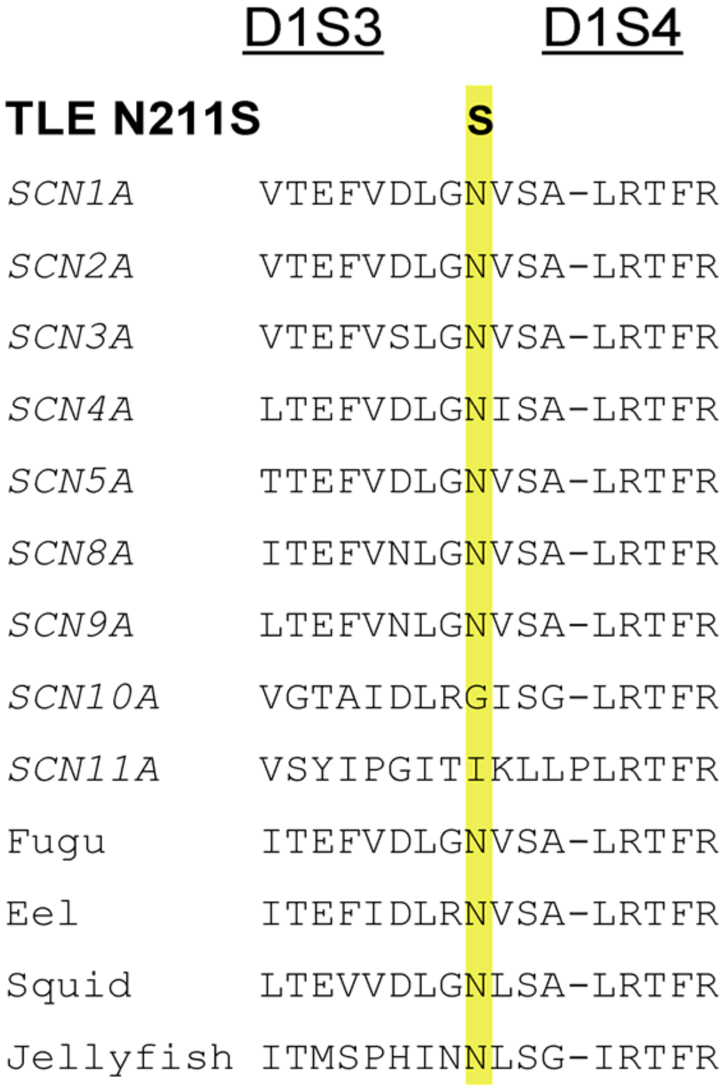

```
                 D1S3      D1S4
TLE N211S                 S
SCN1A       VTEFVDLGNVSA-LRTFR
SCN2A       VTEFVDLGNVSA-LRTFR
SCN3A       VTEFVSLGNVSA-LRTFR
SCN4A       LTEFVDLGNISA-LRTFR
SCN5A       TTEFVDLGNVSA-LRTFR
SCN8A       ITEFVNLGNVSA-LRTFR
SCN9A       LTEFVNLGNVSA-LRTFR
SCN10A      VGTAIDLRGISG-LRTFR
SCN11A      VSYIPGITIKLLPLRTFR
Fugu        ITEFVDLGNVSA-LRTFR
Eel         ITEFIDLRNVSA-LRTFR
Squid       LTEVVDLGNLSA-LRTFR
Jellyfish   ITMSPHINNLSG-IRTFR
```

Figure 25. Evolutionary conservation of N211S. Alignment of amino acid sequences of *SCN1A* region containing DI S3-S4 linker with N211S. The residue is highlighted in yellow and shows a high level of conservation across other human voltage-gated sodium channels and across species.

mutation identified by our collaborators. N211S disrupts a residue in the extracellular linker between S3-S4 of Domain I. Figure 26A illustrates the approximate position of N211S within the predicted $Na_V1.1$ two-dimensional topology.

N211S generated functional voltage-gated sodium channels when transiently expressed in tsA201 cells with the auxiliary $h\beta_1$ and $h\beta_2$ subunits. Figure 26B illustrates representative whole-cell currents evoked by a series of depolarizing test potentials in cells transiently expressing wild-type $Na_V1.1$ (WT-$Na_V1.1$) or N211S (shown as protocol inset Figure 26B). Cells transfected with N211S displayed a significant increase in the peak inward sodium current over a large range of test voltage potentials. The corresponding peak current density-voltage relationships are presented in Figure 27A. After normalizing for cell capacitance, N211S caused a significant increase in current density ($p \leq 0.05$) over the -20 to +50 mV voltage range compared to WT-$Na_V1.1$ (Figure 27A).

N211S exhibits normal gating behaviors

Activation properties were determined from the family of voltage steps to between -80 to +60 mV from a holding potential of -120 mV (Figure 26B). Activation kinetics were examined by measuring the time to peak current and 10 – 90% rise time for activation for the -30 to +30 mV range. N211S did not display differences in activation kinetics compared to WT-$Na_V1.1$ (Table 13). Additionally the voltage dependence of activation was not significantly different between N211S and WT-$Na_V1.1$ channels (Figures 27B and Table 14).

N211S does not exhibit altered whole-cell current decay compared to WT-$Na_V1.1$ when the data was fitted with a two-exponential equation (fit parameters provided in Table 15). The voltage dependence of fast inactivation following an inactivating prepulse was similar for WT-$Na_V1.1$ and N211S (Fig. 28A and Table 14). Furthermore, N211S

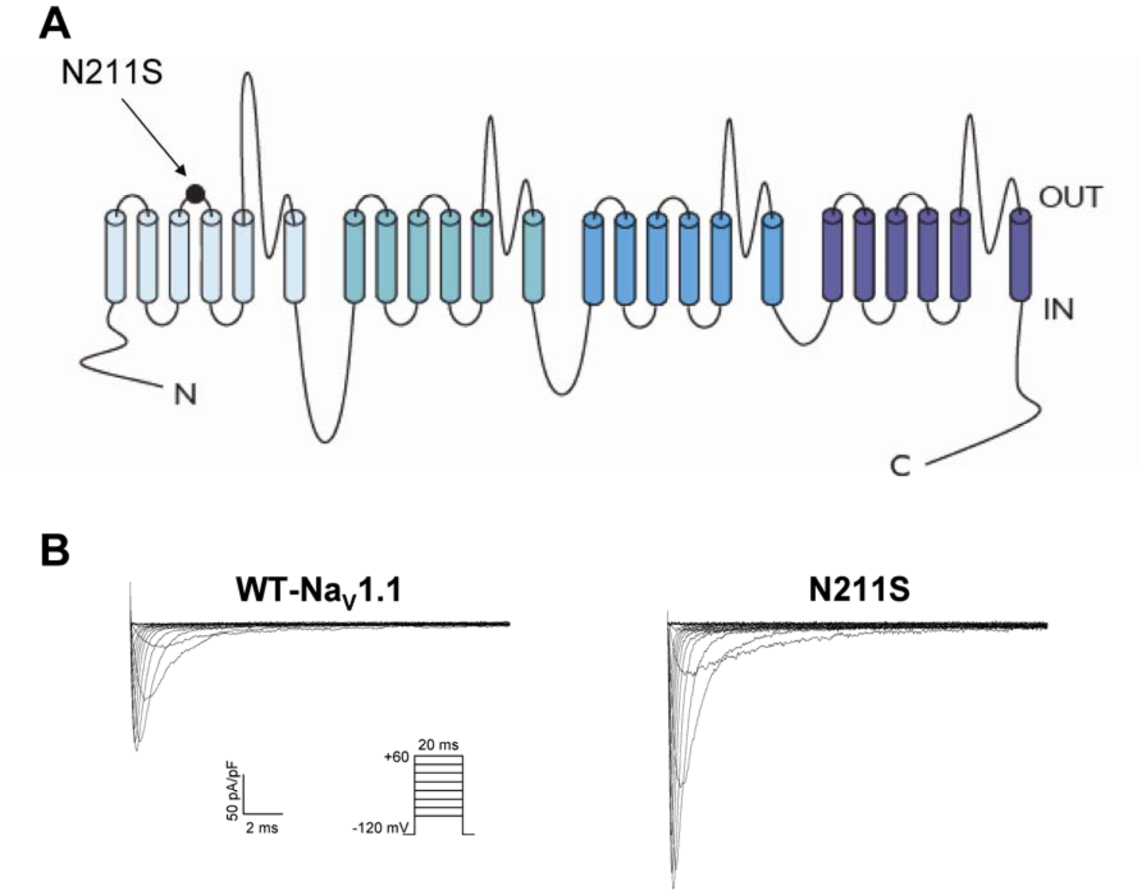

Figure 26. Representative WT-Na$_V$1.1 and N211S whole-cell sodium currents. (A) Predicted transmembrane topology of Na$_V$1.1 showing the location of novel MTLE mutation N211S as a filled circle. **(B)** Sodium currents recorded from tsA201 cells coexpressing the indicated Na$_V$1.1 allele with the hβ$_1$ and hβ$_2$ accessory subunits. Currents were activated by voltage steps to between –80 and +60 mV from a holding potential of −120 mV (see pulse protocol shown as panel inset).

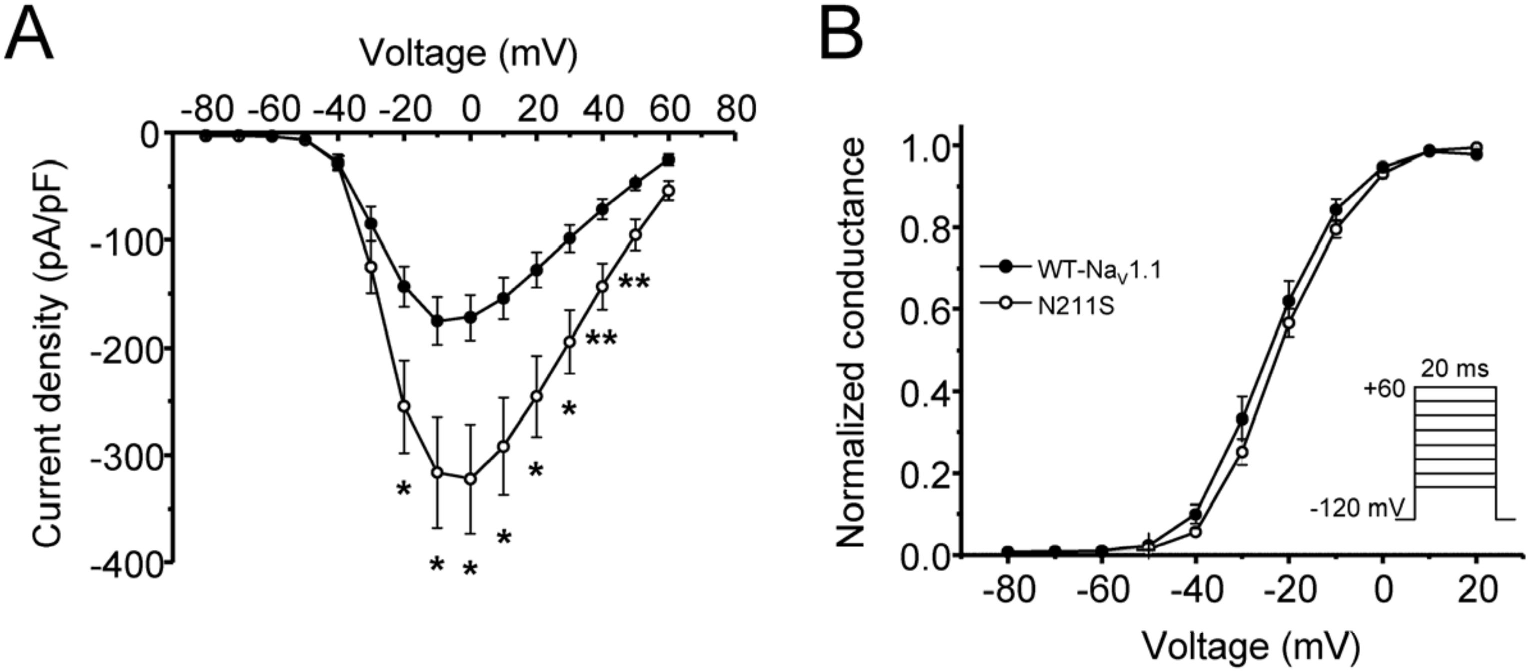

Figure 27. Voltage dependence of activation for WT-Na$_V$1.1 and N211S. (A) Peak current density elicited by test pulses to various potentials and normalized to cell capacitance. N211S exhibits increased peak current density compared to WT-Na$_V$1.1 for the -20 to +50 mV range (*$p < 0.05$, **$p < 0.01$). **(B)** Voltage dependence of channel activation measured during voltage steps to between –80 and +20 mV. N211S does not exhibit altered voltage dependence of activation compared to WT-Na$_V$1.1. Pulse protocol is shown as a panel inset and fit parameters are provided in Table 14.

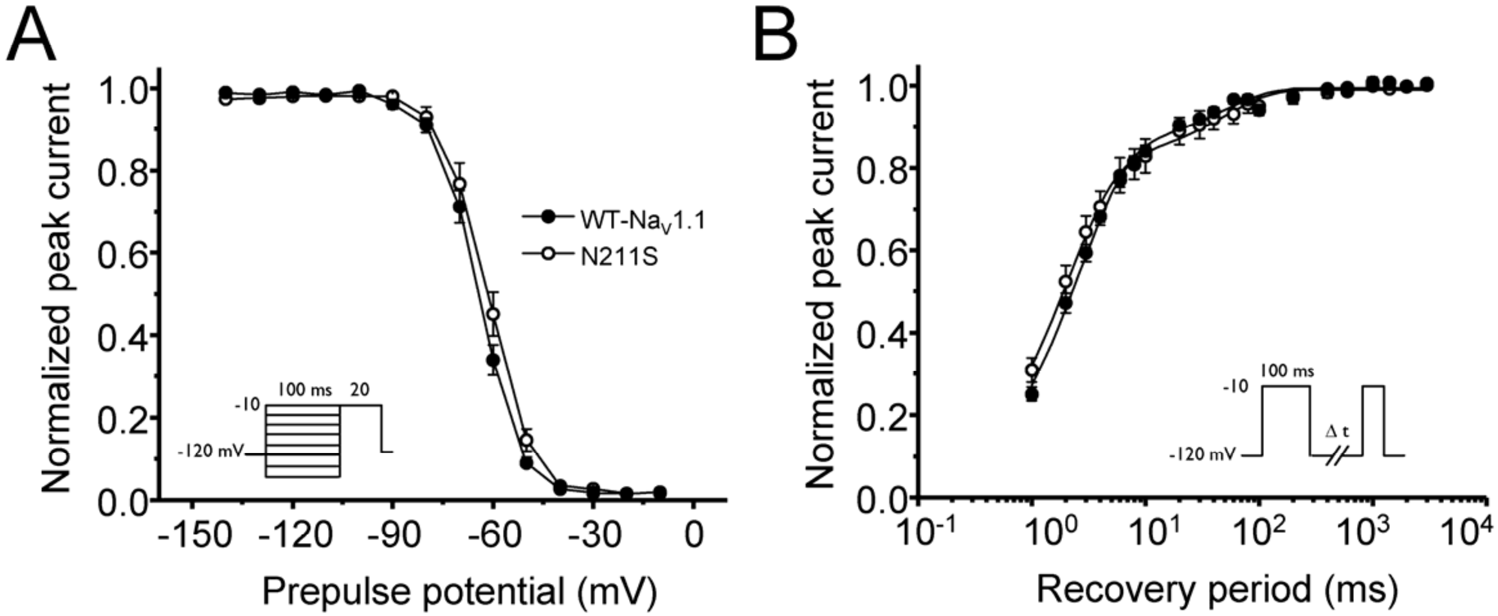

Figure 28. Fast inactivation properties of WT-Na$_V$1.1 and N211S. (A) Voltage dependence of fast inactivation assessed in response to inactivating prepulses to between –140 and –10 mV. N211S displayed similar voltage dependence of fast inactivation compared to WT. **(B)** Time dependent recovery from fast inactivation assessed following an inactivating prepulse (100 ms at –10 mV). No significant defects in the recovery in fast inactivation were found for N211S. Pulse protocols are shown as panel insets and fit parameters are provided in Table 14.

Table 13. Activation kinetics of WT-Na$_V$1.1 and N211S

	10 – 90% Rise Time		Time to Peak Current	
	WT-Na$_V$1.1	**N211S**	**WT-Na$_V$1.1**	**N211S**
-30 mV	0.60 ± 0.09 (*n* = 11)	0.56 ± 0.05 (*n* = 13)	1.05 ± 0.10 (*n* = 11)	0.98 ± 0.07 (*n* = 13)
-20 mV	0.30 ± 0.02 (*n* = 11)	0.32 ± 0.02 (*n* = 13)	0.65 ± 0.04 (*n* = 11)	0.67 ± 0.04 (*n* = 13)
-10 mV	0.21 ± 0.01 (*n* = 11)	0.20 ± 0.01 (*n* = 13)	0.46 ± 0.02 (*n* = 11)	0.47 ± 0.02 (*n* = 13)
0 mV	0.15 ± 0.01 (*n* = 11)	0.15 ± 0.01 (*n* = 13)	0.36 ± 0.01 (*n* = 11)	0.37 ± 0.01 (*n* = 13)
10 mV	0.12 ± 0.01 (*n* = 11)	0.12 ± 0.01 (*n* = 13)	0.31 ± 0.01 (*n* = 11)	0.31 ± 0.01 (*n* = 13)
20 mV	0.09 ± 0.01 (*n* = 11)	0.10 ± 0.01 (*n* = 13)	0.27 ± 0.01 (*n* = 11)	0.27 ± 0.01 (*n* = 13)
30 mV	0.07 ± 0.01 (*n* =11)	0.08 ± 0.01 (*n* = 13)	0.25 ± 0.01 (*n* = 11)	0.24 ± 0.01 (*n* = 13)

Table 14. Biophysical parameters of WT-Na_V1.1 and N211S

	Voltage dependence of activation			Voltage dependence of fast inactivation			Recovery from 100 ms inactivating prepulse		
	$V_{1/2}$ (mV)	k (mV)	n	$V_{1/2}$ (mV)	k (mV)	n	τ_1 (ms)§	τ_2 (ms)§	
WT-Na_V1.1	-23.8 ± 1.7	7.2 ± 0.2	11	-64.1 ± 1.2	6.2 ± 0.1	9	2.6 ± 0.2 (84 ± 1%)	48.5 ± 7.7 (16 ± 1%)	10
N211S	-21.5 ± 1.1	7.36 ± 0.2	13	-61.2 ± 1.6	6.0 ± 0.1	13	2.3 ± 0.3 (80 ± 3%)	50.1 ± 15.0 (19 ± 3%)	13

§ values in parentheses are amplitude.

Table 15. Whole-cell current inactivation time constants for WT-Na$_V$1.1 and N211S

	Fast Component§		Slow Component§	
	WT-Na$_V$1.1	**N211S**	**WT-Na$_V$1.1**	**N211S**
-30 mV	1.50 ± 0.22 (65 ± 11%)	1.82 ± 0.29 (77 ± 9%)	17.69 ± 7.55 (39 ± 11%)	12.39 ± 3.25 (23 ± 10%)
-20 mV	0.88 ± 0.07 (96 ± 1%)	0.96 ± 0.11 (95 ± 2%)	3.76 ± 3.22 (4 ± 1%)	7.87 ± 3.01 (4 ± 2%)
-10 mV	0.49 ± 0.02 (96 ± 1%)	0.52 ± 0.03 (95 ± 1%)	7.71 ± 1.44 (4 ± 1%)	4.26 ± 0.37 (4 ± 1%)
0 mV	0.35 ± 0.02 (95 ± 2%)	0.35 ± 0.01 (95 ± 1%)	4.82 ± 1.24 (4 ± 1%)	3.57 ± 0.46 (4 ± 1%)
10 mV	0.30 ± 0.01 (95 ± 1%)	0.28 ± 0.01 (95 ± 1%)	3.27 ± 0.39 (4 ± 1%)	2.92 ± 0.30 (4 ± 1%)
20 mV	0.25 ± 0.01 (94 ± 1%)	0.23 ± 0.01 (93 ± 1%)	3.78 ± 0.71 (6 ± 1%)	2.13 ± 0.27 (6 ± 1%)
30 mV	0.25 ± 0.02 (95 ± 2%)	0.21 ± 0.01 (94 ± 1%)	4.13 ± 0.66 (6 ± 2%)	1.94 ± 0.20 (6 ± 1%)

§ values in parentheses are amplitude. For WT-Na$_V$1.1, *n* = 11 and for N211S, *n* = 13.

recovered from fast inactivation similarly to WT-Na$_V$1.1 (Figures 28B and Table 14). These data illustrate that N211S has kinetic and voltage dependent behaviors similar to WT-Na$_V$1.1.

In the absence of major gating abnormalities for N211S, we utilized a voltage protocol consisting of a train of depolarizing steps at varying frequencies to test for differences in use-dependent channel behavior. N211S exhibited use-dependent loss of channel availability similar to WT-Na$_V$1.1 over a large range of frequencies (1 to 140 Hz; Figure 29A). No significant differences in channel availability during the pulse protocol were visible over 200 pulses (Figure 29B). These data predict that N211S and Na$_V$1.1 will behave similarly during rapid stimulation.

Absence of increased persistent current in the N211S mutation

We previously observed that several Na$_V$1.1 mutations associated with various genetic epilepsy syndromes cause significantly increased persistent current (Lossin et al., 2002; Rhodes et al., 2004; Rhodes et al., 2005; Ohmori et al., 2006). However, the N211S mutant did not exhibit an increased persistent current as compared to WT channels (magnitude of persistent current as percentage of peak current amplitude: WT: 1.64 ± 0.35%, n = 10; N211S: 1.74 ± 0.24%, n = 9). This finding suggests that increased persistent current is not a common biophysical hallmark of Na$_V$1.1 mutations associated with MTLE.

N211S exhibits normal cell surface expression

N211S exhibited significantly larger mean whole-cell peak current levels compared to WT-Na$_V$1.1. No other biophysical parameters we assayed were significantly different between N211S and WT-Na$_V$1.1. We tested the hypothesis that N211S increases the level of protein in the plasma membrane by performing cell surface

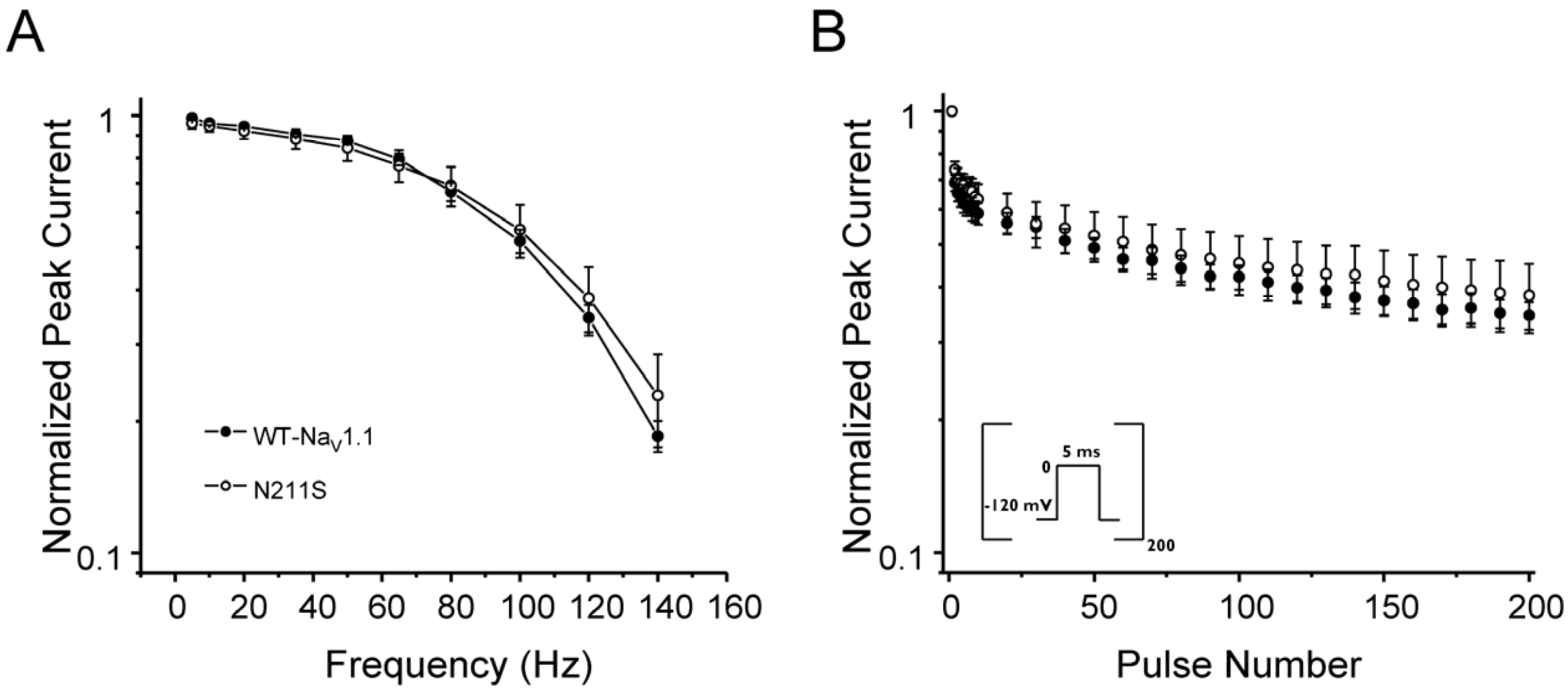

Figure 29. Use-dependent channel behavior of a MTLE mutant. The response of WT-Na$_V$1.1 and N211S to repetitive depolarization (use-dependent channel behavior) was measured by stimulating cells with voltage step pulse trains (200 pulses, 5 ms, 0 mV) from a holding potential of –120 mV at the indicated frequencies (see pulse protocol inset in panel B). **(A)** Residual peak current amplitude of the 200th pulse for WT-Na$_V$1.1 (*n* = 9) and N211S (*n* = 11) plotted against pulse frequency. **(B)** Normalized peak current measured in response to a voltage step train at a frequency of 120 Hz. N211S has similar use-dependent channel behavior to WT-Na$_V$1.1.

biotinylation. Figure 30A illustrates that WT-Na$_V$1.1 and N211S exhibited similar total and cell surface expression. Quantification of cell surface Na$_V$1.1 protein expression from four independent experiments (Fig. 30B, C) demonstrated that N211S does not significantly increase total protein (70% for N211S; n = 4) or cell surface expression compared to WT-Na$_V$1.1 (120% for N211S; n = 4). Surprisingly the two-fold increase in mean peak current density is not due to an alteration of the cell surface expression of N211S compared to WT-Na$_V$1.1. This suggests that N211S would differ from WT-Na$_V$1.1 in single channel properties of single channel conductance or open channel probability.

Discussion

Elucidation of the molecular basis for brain sodium channelopathies and establishment of genotype-phenotype correlations may shed light on epileptogenesis and help conceptualize new treatment strategies. Our collaborators identified a novel mutation in Na$_V$1.1 from brain tissue resected from a case of intractable MTLE. We then examined the functional properties of the MTLE mutation (N211S) using the human Na$_V$1.1 α-subunit coexpressed with human β_1 and β_2 subunits.

Unfortunately we do not have access to the medical history and family history for the patient with the novel N211S mutation. We can hypothesize that the patient had antecedent FS like the previously reported 50 – 80% of intractable MTLE patients (French et al., 1993; Baulac et al., 2004). We can also hypothesize that the *SCN1A* mutation may be carried by other family members who have diverse epilepsy phenotypes (Abou-Khalil et al., 2001; Mantegazza et al., 2005; Colosimo et al., 2007). Another consideration is that N211S may be a benign variant that was present but not the primary cause of MTLE in the patient. N211S was not present in control samples, but it may be present in the general population at a low frequency. Screening more MTLE patients and control samples can help determine if N211S is a disease-causing mutation

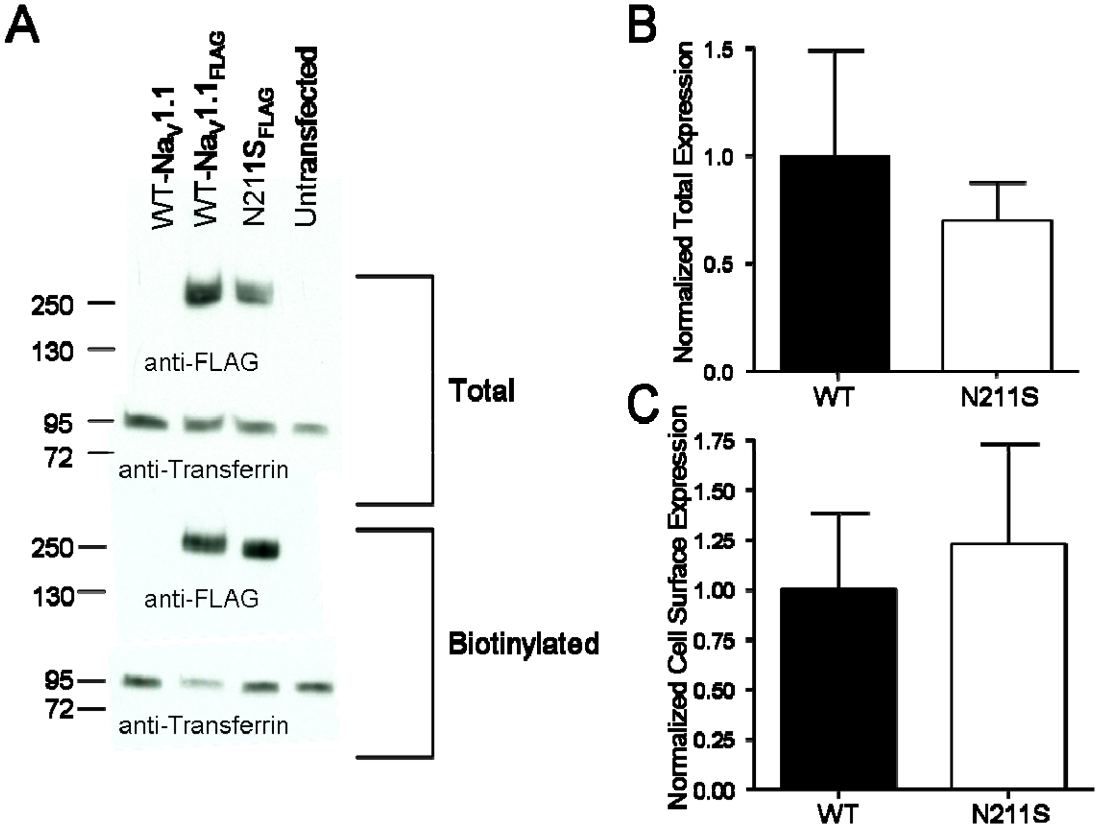

Figure 30. Cell surface protein expression of WT-Na$_V$1.1 and N211S. Cell surface expression of WT-Na$_V$1.1 and N211S was measured using cell surface biotinylation. Endogenous transferrin levels were measured as a gel loading control. **(A)** Representative experiment illustrating total (top) and cell surface (bottom) Na$_V$1.1 protein detected with anti-FLAG antibody. Na$_V$1.1 immunoreactive bands were normalized to the amount of an endogenous protein (transferrin) detected in each experimental lane (below Na$_V$1.1 detection). The first lane was isolated from cells transfected with untagged WT-Na$_V$1.1. Lane 2 is WT-Na$_V$1.1$_{FLAG}$, lane 3 is N211S$_{FLAG}$ and lane 4 was isolated from untransfected tsA201 cells (mock). **(B)** Quantification of four independent experiments demonstrated that total protein levels are similar for WT-Na$_V$1.1 and N211S. **(C)** Quantification of four independent experiments demonstrated that cell surface expression levels are similar for WT-Na$_V$1.1 and N211S. The biotinylated and total Na$_V$1.1 bands were normalized to the corresponding transferrin band and the ratio of the normalized biotinylated to total are shown for WT-Na$_V$1.1 and N211S.

or rare benign variant. Also functional data that supports a mechanism for N211S causing MTLE would help demarcate N211S as a mutation.

In this chapter, we examined the biophysical properties of WT-$Na_V1.1$ and MTLE mutant N211S. In comparison to WT-$Na_V1.1$, N211S did not alter voltage dependence or kinetics of activation, whole-cell current, fast inactivation, use-dependent channel behavior, or persistent sodium current (Figures 27B – 29, and Tables 13 – 15). The N211S mutation caused an increase of approximately two-fold in the current density-voltage relationship (Figures 26B, 27A). The large increase in current density exhibited by N211S is in opposition with a previous report about a *SCN1A* mutation found in a family with febrile seizures and TLE (Mantegazza et al., 2005; Colosimo et al., 2007). Thus, our finding was novel and unexpected and exemplifies the complexity of determining how biophysical function relates to the epilepsy phenotype.

We next sought to understand why the N211S mutation increased current density. We hypothesized that the increased current density might be due to an increase in the number of channels at the cell surface. To address this, we performed cell surface biotinylation. N211S had similar total and cell surface $Na_V1.1$ protein expression (Figure 30). Future experiments will need to utilize single channel analysis to look at open channel probability and single channel conductance to determine what property confers increased current density. To date only one study has examined the function of epilepsy associated mutations in $Na_V1.1$. This study found that one mutation did not alter single channel properties and the other mutation, R1648H, caused an increase in late channel openings (Vanoye et al., 2006). Any single channel defects caused by N211S would be novel and increase understanding of the role $Na_V1.1$ plays in TLE pathogenesis.

The N211S mutation also disrupts a predicted N-linked glycosylation sequence. Glycosylation of voltage-gated sodium channels confers isoform specific and developmental alterations of voltage dependent and kinetic properties (Bennett, 2002;

Stocker and Bennett, 2006). Determining whether N211S is disrupting glycosylation *in vivo* is a difficult experiment, but it would be informative to know whether the functional impact of the mutation is partly due to disruption of the N-linked glycosylation sequence.

Originally thought to be an acquired disorder, TLE is now recognized to have genetic risk factors. Several families with other epilepsy syndromes such as FS, GEFS+ or CAE have family members who develop TLE (Colosimo et al., 2007; Nabbout et al., 2007). One *SCN1B* mutation that is linked to GEFS+ was also found in several TLE patients (Scheffer et al., 2007). Two earlier studies found *SCN1A* mutations in TLE patients (Abou-Khalil et al., 2001; Colosimo et al., 2007) making identification of N211S an independent confirmation that $Na_V1.1$ dysfunction can predispose or cause TLE.

In summary, we characterized a novel *SCN1A* mutation identified in brain tissue samples isolated from a patient with intractable MTLE. N211S disrupts a highly conserved residue located in the extracellular linker between S3-S4 of Domain I (Figure 25, 26A). The mutation causes an increase in current density (Figure 26B and 27A) without an alteration of voltage dependent and kinetic properties (Figures 27B – 29, and Tables 13 – 15) or number of channels at the cell surface (Figure 30). Future studies in neurons or the use of animal models may aid in elucidating the link between sodium channel mutation and MTLE.

CHAPTER V

SUMMARY AND FUTURE DIRECTIONS

Summary

Epilepsy is a common neurological disorder affecting an estimated 2.7 million people in the United States (Centers for Disease Control). Inherited forms of epilepsy comprise a relatively small percentage of cases. In recent years, defects in several different genes have been associated with Mendelian forms of epilepsy. Genes involved in epilepsy are most commonly components of ion channels including voltage-gated sodium and potassium channels, $GABA_A$ receptors, and acetylcholine receptors. Other commonly mutated proteins are related to neuronal maturation and migration like *LGI1*. The category of ion channels most commonly mutated among genetic epilepsy syndromes is voltage-gated sodium channels.

This thesis research characterized voltage-gated sodium channel mutations associated with different forms of genetic epilepsy. In an attempt to better understand mechanisms underlying epilepsy, we utilized several model systems. In Chapter Two, we used computational modeling to investigate WT-Na_V1.1 and a GEFS+ mutation. Chapters Three and Four and Appendix A used heterologous expression of mutant neuronal voltage-gated sodium channels in tsA201 cells for biophysical and biochemical studies. Finally in Appendix B, we described our experiments using a transgenic mouse model of epilepsy for electrophysiological and biochemical experiments.

Chapter Two described using computational modeling to investigate function of WT-Na_V1.1. We used actual data acquired from heterologous expression in tsA201 cells to develop a Markov model of WT-Na_V1.1. A novel aspect to our WT-Na_V1.1 model was introduction of a biphasic open state inactivation process. The open channel transitions to an unstable inactivated state before entering a “latched” or more stable inactivated state. Our model was able to replicate activation, fast inactivation, slow inactivation, persistent current and single channel properties of WT-Na$_V$1.1. We then created a model for the GEFS+ mutation, R1648H. To create R1648H, we increased the rate constant from the stabilized fast inactivated state back to the unstable inactivated state. Altering just one rate constant was able to maintain the whole-cell properties including the increased persistent current and at the increased late channel openings at the single channel level that are seen when R1648H was patch clamped in heterologous expression systems.

Chapters Three and Appendix A investigated the role BFNIS-Na$_V$1.2 mutations. In Appendix A, we described setting up the conditions for the heterologous expression system used in subsequent chapters. We first constructed a human WT-Na$_V$1.2 for functional expression and then used site-directed mutagenesis to create three BFNIS mutations (R1319Q, L1330F, and L1563V). We established the optimal conditions for transfection and whole-cell patch clamp experiments for the subsequent experiments described in Chapter Three.

Chapter Three described the functional characterization of three BFNIS alleles. We found that R1319Q caused a depolarizing shift in the voltage dependence of activation, slower activation kinetics, and a slightly delayed recovery from fast inactivation. The L1330F allele caused enhanced use-dependent channel behavior compared to WT-Na$_V$1.2. The L1563V mutation slowed whole-cell current decay, depolarized voltage dependence of fast inactivation, and accelerated recovery from fast inactivation. All three mutations caused a decrease in mean inward peak current compared to WT-Na$_V$1.2. We used cell surface biotinylation to examine the hypothesis that decreased mean inward peak current resulted from fewer channels at the cell surface. We found that all three mutations decreased cell surface expression by between 47 and 79%. The decreased cell surface expression was a novel finding in BFNIS and probably represents a more pathophysiologically relevant deficit than the subtle biophysical defects exhibited by each mutation.

Chapter Four characterized a novel *SCN1A* mutation from brain tissue resected from a MTLE patient identified by our collaborators. The mutation, N211S, disrupts a highly conserved amino acid in the S3-S4 extracellular linker in DI that is part of a predicted N-linked glycosylation site. We used a heterologous expression system to functionally characterize N211S under conditions similar to those established in Appendix A. We found that N211S exhibited a large increase in current density compared to WT-Na$_V$1.1. No other voltage dependent or gating properties we measured were altered. Additionally N211S did not lead to altered use-dependent channel behavior or increased persistent current. We performed cell surface biotinylation to explore the hypothesis that the increased current density was the result of increased number of channels at the cell surface. We did not find significant alterations in the expression of N211S at the cell surface.

In Appendix B, we discussed our initial experiments using transgenic mice carrying a *Scn2a* mutation (GAL879-881QQQ) that caused impairments in inactivation and increased persistent current. Transgenic mice from the congenic C57BL/6J background (B6.Q54) have low seizure susceptibility, whereas mice that are F1 from C67BL/6J crossed to SJL/J (F1.Q54) have a much more severe seizure phenotype. We hypothesized that genetic modifiers may directly influence voltage-gated sodium channel function and account for the differing seizure susceptibilities between the B6.Q54 and F1.Q54. We performed whole-cell patch clamp recordings from acutely dissociated hippocampal neurons from WT littermate mice. We established several conditions for recording voltage-gated sodium channel current. Once we had optimized aspects of the dissection and electrophysiological recordings, we performed whole-cell patch clamp studies on acutely dissociated hippocampal neurons from both B6.Q54 and F1.Q54. We obtained several recordings, but have not made a final determination whether the two background strains have significant differences in voltage dependent or kinetic properties of voltage-gated sodium channels. Preliminarily, the two strains may have some voltage dependent differences that may contribute to altered excitability. We found that B6.Q54 neurons displayed persistent sodium current despite the low seizure threshold. We also sought to determine whether background strain influenced protein expression levels of the transgene by performing western blot analysis of membrane preparations from whole brain. Although we could specifically detect the transgene protein in mice from both background strains, determining differences in the transgene expression level were beyond the level of our detection.

Implications for pathophysiology of epilepsy

The GEFS+ mutation *SCN1A*-R1648H disrupts a highly conserved arginine residue in the S4 of DIV. Generally, mutations in S4 segments are predicted to cause defective channel activation but mutations specifically in DIV of sodium channels have been demonstrated to disrupt inactivation as the primary consequence (Chahine et al., 1994; Ji et al., 1996; Cha et al., 1999). The processes of activation and fast inactivation are coupled and define the biexponential whole-cell inactivation curve. The Markov chain models of WT-$Na_V1.1$ and R1648H predicted that $Na_V1.1$ undergoes fast inactivation in a two step manner. Destabilizing the reverse transition from the stable fast inactivated state to the unstable fast inactivated state was able to increase late channel openings on the single channel level and increase persistent current at the whole-cell level as is seen for R1648H when recorded at the patch clamp setup. This suggests that R1648H has a defect in stabilization of the fast inactivation gate. Although fast inactivation is known to be critical for limiting the amount of sodium ions that enter the cell following depolarization, the way that defective fast inactivation results in epilepsy is not understood. Experiments need to be done to see how the R1648H mutation alters the conformation of the sodium channel to impair fast inactivation. This would then have broader implications for understanding the mechanism of increased persistent current exhibited by some other sodium channel mutations.

We speculate that persistent sodium current from epilepsy mutations including R1648H cause an aberrant membrane depolarization that may lead to neuronal firing in the absence of strong depolarizing stimuli. Aberrant neuronal firing would offset the regulation of normal brain excitability and could lead to epilepsy. Enhanced understanding of the role persistent current plays in regulating neuronal firing may aid in better therapeutic options for specific epilepsy patients as discussed below.

Each of the BFNIS mutations exhibited subtle biophysical defects. R1319Q altered activation and L1330F exhibited enhanced use-dependent channel behavior predicting a loss of channel function for both of these mutations. The L1563V mutation exhibited impaired inactivation predicting a gain of channel function. One explanation for these divergent biophysical effects resulting in similar epilepsy phenotypes could be that R1319Q and L1330F preferentially affect excitatory neurons while L1563V preferentially affects inhibitory neurons. The mechanism for each mutation having a predominant effect on a different functional class of neurons is not understood.

A recent mouse model of SMEI showed that haploinsufficiency of $Na_V1.1$ selectively reduced current density in inhibitory interneurons (Yu et al., 2006). Decreased sodium current density may underlie BFNIS if loss of $Na_V1.2$ primarily affects inhibitory interneurons reducing the negative feedback on excitatory neurons as in the SMEI mouse model. Perhaps $Na_V1.2$ expression is high in inhibitory neurons early in life and expressed at lower levels within the first year of life which may explain the early onset of seizures followed by spontaneous seizure remittance.

Decreased current density resulting from reduced mutant sodium channel cell surface expression appears important to the pathogenesis of BFNIS. Missense BFNIS mutations may result in misfolded proteins that cause disturbances in sodium channel membrane expression. Many potential mechanisms for decreased cell surface protein expression exist including decreased stability of mRNA, decreased delivery to the membrane, increased internalization, and altered interactions with chaperone proteins like β-subunits (Yanagita et al., 2003; Wada et al., 2004; Gallagher et al., 2007; Hirose, 2006). Future studies will need to examine how the BFNIS missense mutations cause impaired protein trafficking and cell surface expression as discussed below.

The MTLE $Na_V1.1$ mutation, N211S, displayed increased current density without an increase in cell surface expression. Increased sodium current density is a novel biophysical finding in an epilepsy-associated mutation. We can speculate that the increased current density of N211S is due to either increased single channel conductance or increased open channel probability. Gain of $Na_V1.1$ function would be predicted to increase sodium current. To result in epilepsy, we speculate that N211S increases neuronal sodium current of excitatory neurons. This is in contrast to the finding that loss of $Na_V1.1$ results in decreased sodium currents in hippocampal interneurons but does not affect sodium current from hippocampal excitatory neurons (Yu et al., 2006). One thing that may account for our predicted defect is that increased $Na_V1.1$ function may result in decreased expression and sodium current through other sodium channel α isoforms.

Many cases of TLE also present with damage to the temporal lobe including hippocampal sclerosis or mesial temporal lobe sclerosis. It is unclear whether physical damage to the temporal lobe precedes epilepsy. Perhaps increased sodium current as exhibited by N211S predisposes to neuronal injury in the temporal lobe which ultimately results in epilepsy. Studying the N211S mutation may contribute to our understanding of what causes temporal lobe epilepsy and identify novel therapeutic options.

Implications for treatment of epilepsy

Although one main goal of this research is to better understand mechanisms underlying epilepsy, another major goal is to aid in identification of novel treatment options for epilepsy. In the future, patients will be diagnosed with a particular epilepsy syndrome and treated with a pharmaceutical agent to target their specific problem. We hope that increased understanding of the biophysical defects or trafficking defects may enable development of better therapeutic agents.

R1648H is a GEFS+ mutation that exhibits increased persistent current. Therapeutic agents that specifically target the persistent sodium current are under development and may be the proper treatment option for patients with the R1648H mutation. Ranolazine specifically blocks persistent sodium current in the cardiac sodium channel, $Na_V1.5$. Ranolazine has been used successfully to alleviate the frequency and severity of anginal attacks (Hale et al., 2008). Although no selective persistent sodium channel blocker has been used in patients with epilepsy, we predict that agents like ranolazine may have a large therapeutic benefit in patients where the primary defect is increased persistent sodium current.

Many epilepsy mutations exhibit decreased sodium current. The BFNIS mutations we characterized had decreased sodium current and reduced channel cell surface expression. Attempts have been made to rescue sodium current density by interactions with the proteins like the β subunits, low temperature incubation, and incubation with sodium channel blockers. For example, the GEFS+ mutation M1841T exhibits decreased sodium current density that can be partially restored by a 24 hr preincubation with phenytoin (Rusconi et al., 2007). Although this mutant channel exhibits sodium channel attributes similar to that of WT-Na$_V$1.1, when expression at the surface is increased the mutant channel may not behave similarly to WT. For example, a long QT syndrome mutation in Na$_V$1.5, L1825P, can be partially rescued by incubation with cisapride. The mutant channels rescued to the cell surface exhibit increased persistent current (Liu et al., 2005). Therapeutic agents that restore cell surface channel expression should be pursued with caution to ensure that the rescued mutant channels have no underlying biophysical defects. Unexpected channel dysfunction after restoring membrane expression would decrease the benefit of these drugs or cause a worsening of the disease phenotype.

Future directions

Determine effects of epilepsy mutations using sodium channel Markov models

Now that we have established a Markov model of WT-Na$_V$1.1 and R1648H that accurately generate sodium channel behavior. The Na$_V$1.1 channel models can be taken from the single compartment environment we used in Chapter Two and insert the models into neuronal simulation environments. We would want to further examine the two step open state inactivation in a neuronal environment. Experiments investigating how excitability parameters including action potential threshold, width, and duration differ between the WT-Na$_V$1.1 and R1648H models could yield informative data about how R1648H causes GEFS+. We would like to use the R1648H model to do *in silico* pharmacology experiments to find ideal therapeutics targeting persistent sodium current. The WT-Na$_V$1.1 model can also be a starting point for other well characterized Na$_V$1.1 mutations with biophysical phenotypes that differ from that of R1648H. A few potentially interesting mutations to investigate would include the SMEI mutation R1648C, the GEFS+ mutation D1866Y, and the ICEGTC mutant V983A. The WT-Na$_V$1.1 model could help to generate other sodium channel models including $Na_V1.2$ and $Na_V1.3$ implicated in other genetic epilepsy syndromes.

Determine source of reduced BFNIS mutant channel cell surface expression

We found subtle biophysical defects in each of the three BFNIS mutations we characterized in Chapter Three. In a heterologous expression system, it would be interesting to examine the sodium current in response to an action potential voltage waveform for each mutant in comparison to WT-$Na_V1.2$. Similar to the use-dependent channel behavior experiments, this would be another way to see the cumulative functional impact of the biophysical defects. BFNIS is a developmentally regulated epilepsy syndrome, and it would be informative to examine how seizure remittance occurs within the first year of life. Experiments following coexpression of WT-$Na_V1.2$ and the BFNIS mutants may elucidate the mechanism of autosomal dominant inheritance for this disorder. Another interesting direction for this project would be examining function of the BFNIS mutations in cells of neuronal origin. In neurons the expression and trafficking of mutant channels may be different than in tsA201 cells. Additionally in neurons, the biophysical properties may be affected by endogenous proteins thereby displaying defects that were not observed in tsA201 cells.

We would like to determine why there are fewer mutant channels on the cell surface. Experiments examining channel turnover rates and subcellular distribution of channels may be informative. First we would want to determine where in the cells the channels reside because the total expression levels for the BFNIS mutants were not different than WT-$Na_V1.2$. We could use subcellular fractionation by centrifugation with a density gradient and then examine $Na_V1.2$ in each of the fractions using western blot analysis. Alternatively we could perform immunohistochemistry using fluorescent immunostaining to see colocalization of $Na_V1.2$ and subcellular structures with confocal microscopy. To study turnover of the sodium channels, we could first inhibit internalization with high sucrose and see if this restores cell surface expression of BFNIS mutant channels. We could also block internalization of the sodium channel with dominant-negative dynamin or a cholesterol-depleting drug to block clathrin or caveoli-mediated internalization. Both experiments should be performed because the mechanism responsible for $Na_V1.2$ internalization is unknown. This would help determine if the BFNIS mutant channels are removed from the plasma membrane more than WT-$Na_V1.2$. We would also want to examine whether the BFNIS mutants have altered interactions with the β subunits, proteins known to regulate expression and localization of α subunits. $Na_V1.1$ mutations associated with GEFS+ including M1841T and D1866Y have been shown to have decreased interaction with the β_1 subunit. All of the above experiments collectively would help determine why BFNIS mutant $Na_V1.2$ has reduced cell surface expression. Experiments described above would aid in understanding the pathophysiology of BFNIS and elucidate potential mechanisms for treatment.

Define single channel properties of MTLE mutation N211S

The N211S mutation significantly increased current density without alteration of cell surface expression as described in Chapter Four. The next step to examining the increased current density would be single channel analysis. N211S likely has altered open channel probability or single channel conductance compared to WT-$Na_V1.1$. Defects in either of these properties would be novel mechanisms of sodium channel mutations causing epilepsy. Similar to above, it would be interesting to examine N211S in neurons and determine if increased current density is the only alteration in function. The role of increased sodium current on temporal lobe damage as in hippocampal sclerosis should also be examined.

Determine sodium channel properties of *Scn2a* Q54 neurons

We optimized dissection and electrophysiological conditions for examining neurons from B6.Q54 and F1.Q54 neurons. Preliminary experiments described in Appendix B revealed that B6.Q54 neurons have a significant level of persistent current. We need to determine if F1.Q54 neurons also display similar levels of persistent current. The whole-cell patch clamp recordings need to be repeated to observe differences between the two background strains and potential effects of genetic modifiers. If we find that the background strains have similar voltage-gated sodium current, then we would predict that the genetic modifiers do not directly affect the voltage-gated sodium channels. We would then want to perform whole-cell voltage clamp experiments examining potassium current. We would want to conduct current clamp experiments to determine resting membrane potential, input-output relationships, and action potential characteristics. Another avenue for conducting these experiments would be to isolate embryonic cultures and maintain the cultures for approximately three weeks before conducting current clamp experiments. These experiments would decrease the difficulties of space clamp and high voltage error seen in voltage clamp of neurons isolated from P21 animals, but would require verification of transgene expression. The biochemical analysis of membrane preparations from B6.Q54 and F1.Q54 neurons could be optimized more to detect differences in transgene expression. Another interesting experiment would be to determine the amount of overexpression of the transgene compared to the endogenous $Na_V1.2$ protein to see if this contributes to the differing seizure susceptibilities between the two background strains.

Computational modeling of epilepsy mutations

Computational modeling can be an informative way to increase understanding of previous observations or to predict the impact of perturbations to an established system.

The earliest models of voltage-gated sodium channel function utilized a Hodgkin-Huxley (HH) type channel. The HH type of gating approximates voltage-gated sodium channel function but differs in many substantial ways. To more accurately replicate channel behavior, more complex models including Markov chains have been used. To date, computational models of several different ion channels have been created.

Now that increasingly complicated ion channel models have been created, they can be used in combination with complex cellular environments including various functional classes of neurons from several brain regions (e.g. pyramidal neuron from area CA3 of the hippocampus). The expression level of the channels and test responses to various stimuli can be controlled. Additionally ion channels can be inserted into singular neurons or into neuronal networks ranging from two to hundreds of neurons. One large caveat to using computational modeling is that the user has control over many parameters that may not have biological data to suggest appropriate values. Caution should be exercised when interpreting what the model predicts especially if all assumptions used to set parameters are not known. Even with these drawbacks, computational modeling has enormous potential to supply mechanisms of abnormal excitability and will be increasingly utilized in the future to determine avenues for new research and explain complicated biological data.

Novel epilepsy-associated sodium channel mutations

To date, mutations in many genes have been linked to epilepsy. Over 300 mutations in sodium channels have been associated with several forms of inherited epilepsy. Initially mutations in a sodium channel β subunit, *SCN1B*, were found in GEFS+ patients. Subsequently, several mutations in *SCN1A* and one mutation in *SCN2A* were also identified in GEFS+ patients. Now mutations in *SCN1A* also have been found in patients with SMEI, ICEGTC, MTLE, IS, FS, and cryptogenic epilepsy syndromes. Mutations in *SCN2A* have been associated with BFNIS most commonly, but have also been linked to BFIS and SMEI. Recently mutations in *SCN3A* were identified in cryptogenic pediatric partial epilepsy.

As screening candidate genes in patients with epilepsy becomes more common, mutations are identified with increasing rapidity. Although heterologous expression of epilepsy-associated mutations has been the most rapid source of functional data, it has been difficult to acquire the data rapidly enough to keep up with the identification of mutations. Interpretation of functional characterizations from heterologous systems has also not been straightforward. Mutations identified in patients with the same epilepsy syndrome often have different biophysical phenotypes and how these various deficits sum to a similar pathophysiology is not well understood. Some studies that only assessed standard whole-cell properties including voltage dependence and kinetics of gating would benefit from examining slow inactivation, use-dependent channel behavior, persistent current, responses to action potential waveforms, and other experiments that may mimic physiological inputs. Additionally performing single channel analysis to find single channel conductance and channel open probability may also provide useful information for mechanisms underlying epilepsy pathogenesis. Future experiments will need to determine new methods for interpreting data from heterologous expression studies and explain the seizure remittance seen in some inherited epilepsy syndromes. One major goal of this type of research is to understand the biophysical defect well enough to develop a therapeutic strategy for patients with that particular disease-causing mutation. One example of this might be the use of a persistent sodium current blocker for the treatement of GEFS+ in a patient with the R1648H mutation as discussed above.

Another consideration for studies using a heterologous expression model is trafficking of the proteins. Initially this model system was used to characterize biophysical functions and any alterations in current density were not further explored.

Other disease-causing mutations in non-neuronal voltage-gated sodium channels and epilepsy-associated mutations in non-sodium channels have been shown to have defective protein trafficking. Recently studies have been expanded to examine cell surface expression and protein trafficking especially in the presence of alterations in current density. It would be interesting to examine the protein expression and trafficking of biophysically nonfunctional mutations in *SCN1A* that are frequently associated with SMEI. It is likely that future experiments will further refine the use of heterologous expression systems for examination of protein trafficking and would also look at the modulation and regulation by auxiliary subunits or other interacting proteins.

A few heterologous expression studies have not been performed in immortalized cell lines such as tsA201 or CHO-K1 cells; instead the studies utilize acutely dissociated cells such as neurons for studying epilepsy-associated mutations. The acutely dissociated neurons are then transfected with WT and mutant cDNAs. Although this approach may be an improvement over cells of non-neuronal origin, there are still many considerations for interpreting this data. The first obstacle is that acutely dissociated neurons are difficult to transfect and result in low transfection efficiency making this difficult for biochemical experiments. The second consideration is that overexpression of a particular cDNA would overwhelm the endogenous interacting proteins. This potentially means that the overexpressed protein may not be trafficked correctly or undergo normal regulatory mechanisms which can confound interpretations of functional data. Another difficulty is distinguishing the overexpressed protein from the endogenous ones. In some cases, knockout or knockdown of the endogenous protein can aid in characterization of the transfected allele. If knockout or knockdown is not possible, an epitope tag or a point mutation that confers different pharmacological properties can be used to distinguish between the different alleles. One other issue will be determining what brain region or neuron type is of interest and importance to study. It is also possible that instead of using acutely dissociated neurons, that heterologous expression of sodium channel proteins in primary neuronal culture preparations may be a less heterogenous system to utilize. Heterologous expression of mutant proteins in acutely dissociated cells or in primary neuronal culture preparations will continue to be refined and provide some novel directions for the study of disease causing mutations.

Animal models of epilepsy

Although there are several species that have been used for animal models of epilepsy, the most commonly used animal is the mouse. Transgenic mouse lines have provided sources for *in vivo* data but are now being replaced by knockout and targeted insertion models. The downside for transgenic mice is that the transgene is randomly integrated into the genome with differing copy numbers in each line. The knockout or targeted insertion models are ideal since they maintain the original chromosomal location and in the case of targeted insertion models maintain a total of two copies in the genome. A few lines are conditional targeted insertions where exposure to a chemical is required for activation of the inserted gene. Much progress has been made in the technology of creating better mouse models of disease.

The initial mouse models of epilepsy included non-disease associated mutations and random mutations found in inbred strains. These models are able to replicate some epilepsy phenotypes and may provide information about some unexpected proteins important in the pathogenesis of epilepsy. Newer models have centered on known disease-causing mutations with the goal of understanding the more severe genetic epilepsy syndromes. Animal models will provide the best behavioral and physiological data to understand mechanisms of disease. The animal models can also be used to test novel therapeutic regimens in the hope of developing better clinical treatment strategies, A few drawbacks of animal models include the time and money involved in developing and maintaining large mouse colonies. Now that so many epilepsy mutations have been discovered, there needs to be a lot of thought put into determining which animal models can provide answers unattainable by earlier models or other experimental designs. Another difficulty is determining how to conduct physiological experiments because there are almost endless possibilities. Despite these few disadvantages, eventually animal models will provide answers to the questions that the model systems discussed above will not be able to satisfy.

APPENDIX A

HETEROLOGOUS EXPRESSION AND ELECTROPHYSIOLOGY OF HUMAN $Na_V1.2$

Introduction

Voltage-gated sodium channel mutations have been linked to many heritable diseases. Mutations in the cardiac isoform, *SCN5A*, which encodes the protein $Na_V1.5$ have been associated with congential long QT syndrome, Brugada Syndrome, sick sinus syndrome, and sudden infant death syndrome (Wang et al., 1995; Bezzina et al., 1999; Benson et al., 2003; Wedekind et al., 2001). Mutations in the skeletal muscle isoform, *SCN4A*, which encodes the protein $Na_V1.4$ have been associated with paramyotonia congenita, and forms of periodic paralysis (Ebers et al., 1991; Bulman et al., 1999). The sodium channel $Na_V1.7$ is encoded by the gene *SCN9A* and is highly expressed in the peripheral nervous system. Mutations in *SCN9A* are found in cases of primary erythermalgia and congenital insensitivity to pain (Yang et al., 2004; Cox et al., 2006). Brain sodium channel mutations result in a wide variety of inherited epilepsy syndromes and were more recently discovered to cause familial hemiplegic migraine (FHM) (Wallace et al., 1998; Escayg et al., 2000b; Claes et al., 2001; Sugawara et al., 2001; Heron et al., 2002; Fujiwara et al., 2003; Kamiya et al., 2004; Dichgans et al., 2005; Vanmolkot et al., 2007). My dissertation research has focused on mutations in *SCN1A* and *SCN2A*, the $Na_V1.1$ and $Na_V1.2$ proteins respectively, associated with generalized epilepsy with febrile seizures plus (GEFS+), mesial temporal lobe epilepsy (MTLE), and benign familial neonatal-infantile seizures (BFNIS).

Experimental strategy

Most of the information gathered on the functional impact of these channelopathy-associated voltage-gated sodium channel mutants has come from heterologous expression systems. The mutations are created in either human or rat cDNA and then overexpressed in tsA201 or CHO-K1 cells. Since neuronal voltage-gated sodium channels frequently spontaneously recombine, our laboratory has developed strategies to perform the molecular biology in human cDNAs. These strategies are described below for constructing the wild-type (WT) $Na_V1.2$ and for making the BFNIS-associated *SCN2A* mutations. The methods below were previously employed in our laboratory to acquire data for WT-$Na_V1.1$ and R1648H to create the Markov models discussed previously in Chapter Two as part of Specific Aim I. The methods described here were also important for Specific Aim II experiments Chapters Three and Four.

Materials and Methods

Construction of pCMV-*SCN2A*

We received a clone of human *SCN2A* in the pSVK3 (Pharmacia Biotech, Sweden) vector as a gift from Mauricio Montal (Ahmed et al., 1992). We moved *SCN2A* to the pCMV-Script (Stratagene, La Jolla, CA) vector to improve expression. I did the molecular biology with the help of Kim Greene for one step. We used a forward primer introducing a NotI restriction site upstream of the start codon and a reverse primer that matched the *SCN2A* sequence downstream of an ApaLI (primer sequences in Table 16). The PCR fragment was purified and restriction digested with NotI and ApaLI (all enzymes from New England Biolabs, Ipswich, MA). We deleted most of the 3' UTR by cutting with XhoI positioned 220 base pairs (bp) after the stop codon. The main *SCN2A* fragment, vector fragment, and the digested PCR product were gel purified. The three

Table 16. Primer sequences for construction of pCMV-*SCN2A* and BFNIS mutations

	Forward Primer	**Reverse Primer**
SCN2A **5’ end**	GACTGCTACACTACGTACGCGGCCGCCATGGCACAGTCAGTGCTGGTA	TCCCGTAAAAATGTGAAATCT
G334D Outer Primers	CGTCAGATCCGCTAGCTATT	TAAAGGTTTTCCCAGAAGTC
G334D Mutagenic Primers	ATTTTTTAGAGGGGCAAAATGATGCTCTGCTTTGTGGCAACAG	CTGTTGCCACAAAGCAGAGCATCATTTTGCCCCTCTAAAAAAT
R1744G Outer Primers	CTTTGGCAACAGCATGATCT	TCATACGAGGGTGGAGACGT
R1744G Mutagenic Primers	CCTGGAAGCTCAGTTAAAGGAGACTGTGGGAACCCAT	ATGGGTTCCCACAGTCTCCTTTAACTGAGCTTCCAGG
R1319Q Outer Primer	AGATAGTGGAGCACAATTGG	TCCAGGGTGATCTTTGTCAG
R1319Q Mutagenic Primers	CACTGAGAGCTTTGTCCCAGTTCGAAGGAATGAGGGCTGTTGTAAATGCT	AGCATTTACAACAGCCCTCATTCCTTCGAACTGGGACAAAGCTCTCAGTG
L1330F Outer Primers	AAAGCCTTTGTTAGGAAGCA	GAGAGATCAGTTTCAGCACAC
L1330F Mutagenic Primers	TGAGGGCTGTTGTAAATGCATTTTTAGGAGCCATTCCATCTAT	ATAGATGGAATGGCTCCTAAAAATGCATTTACAACAGCCCTCA
L1563V Outer Primers	GTTGATTCACGAAATGTAGA	TCCCAAACCTCATAGAACAT
L1563V Mutagenic Primers	GTCAAGAAATGACAAACATTGTGTACTGGATCAATCTGGTGTTTATTGTTCTG	ACACCAGATTGATCCAGTACACAATGTTTGTCATTTCTTGAC

pieces were ligated together using T4 DNA Ligase. The ligation was incubated overnight at room temperature before transforming MAX Efficiency Stbl2 competent cells (Invitrogen Corp., Carlsbad, CA). Derived from JM109 cells, Stbl2 cells are specialized for cloning unstable inserts like the brain sodium channels. When neuronal sodium channels are transformed into other competent cells, frequent recombination events occur throughout the open reading frame (ORF). The cultures were grown at 30 °C for four or five days, the optimal conditions for Stbl2 cells. The purified cDNA was sequenced to check for errors in the 5' and 3' cloning sites and the ORF of *SCN2A*.

Once we transferred *SCN2A* to the pCMV-Script vector, we corrected two cloning errors in the original pSVK3-SCN2A vector. The two errors were G334D and R1744G that are G1001A and A5230G at the nucleotide level. We used a two-round or double overlap PCR strategy (Figure 31). The first round of PCR used a pair of outer primers and mutagenic primers to create two initial fragments. The forward outer primer was paired with the reverse mutagenic primer and vice versa. The second round of PCR annealed the two purified first round products during the first few cycles before the outer primers were added to amplify the whole target sequence which is then purified. The sequences of primers are shown in Table 16. The G334D substitution was subcloned into *SCN2A* with the NotI restriction site nine nucleotides upstream of the start codon and the BssSI restriction site at nucleotide position 416. The R1744G mutation was subcloned into *SCN2A* with the NheI site at nucleotide position 4481 and the EcoRI site at nucleotide position 5192.

Each PCR and vector fragment was restriction digested and gel purified. The fragments were ligated together using T4 DNA Ligase. The ligation was transformed into MAX Efficiency Stbl2 competent cells and grown at 30°C for about four days. The purified DNA was digested with multiple restriction enzymes and sequenced fully to

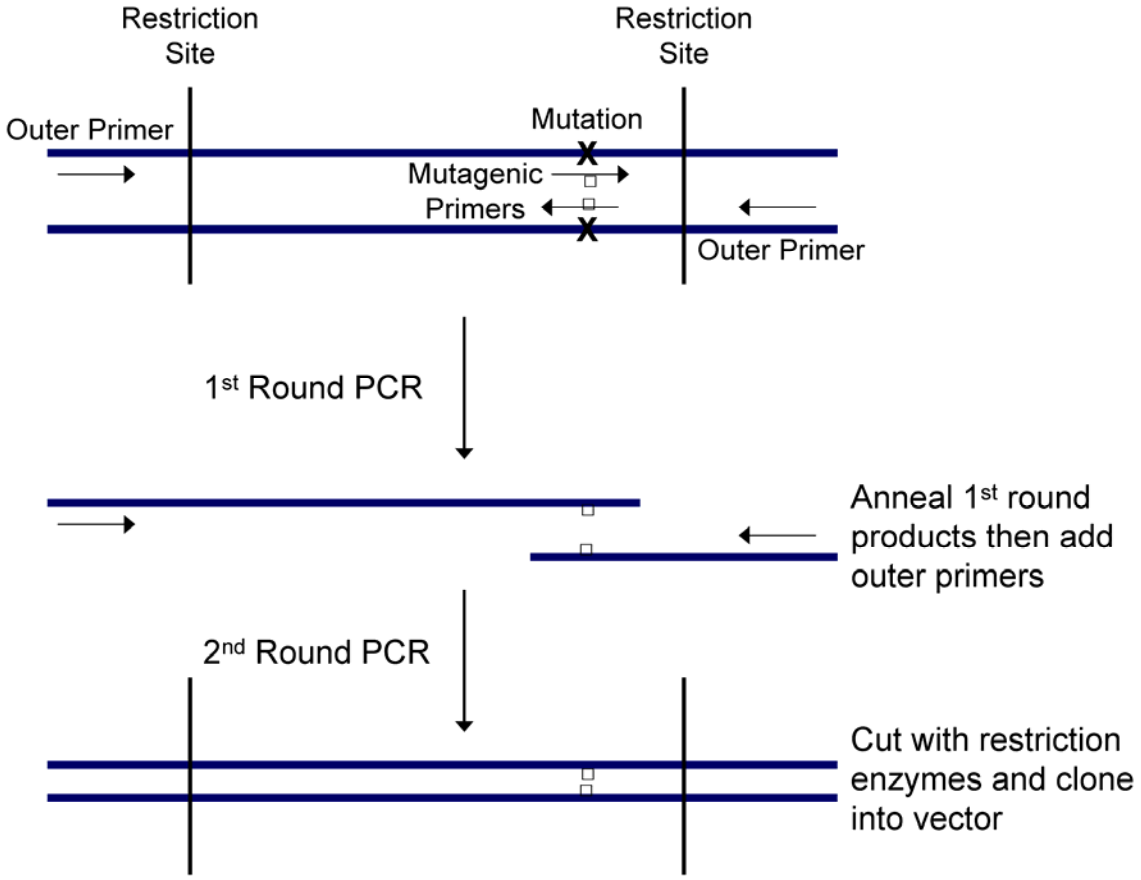

Figure 31. Schematic of double overlap PCR. The top section shows the double stranded DNA separated to show the location of primer binding sites and the target mutation. The first round PCR pairs the forward outer primer with the reverse mutagenic primer and the forward mutagenic primer with the reverse outer primer. The first round of PCR thus results in two products that have corrected the mutation. The second round of PCR requires a few cycles to anneal the purified two first round products before addition of both outer primers. Once the final corrected product is made, the DNA can be cut with restriction enzymes for cloning into a vector.

exclude inadvertent mutations. Correct fully sequenced clones were then used in experiments as wild-type $Na_V1.2$, WT-$Na_V1.2$, or for subsequent mutagenesis.

Construction of BFNIS mutants

We next attempted to construct the mutations reported in the literature associated with BFNIS (Figure 17A) (Heron et al., 2002; Berkovic et al., 2004). After construction of three BFNIS mutations (R1319Q, L1330F, and L1563V) were completed, several unsuccessful attempts using multiple strategies were made to construct three others (R223Q, V892I, and L1003I). Subsequently another report came out with two other BFNIS mutations (Herlenius et al., 2007) that we never attempted to construct.

The R1319Q mutation results from a G3956A nucleotide substitution. R1319Q disrupts a highly conserved internal arginine in the S4 transmembrane segment of Domain III (DIII) (Figures 17A and 32A). The primers used to construct R1319Q and the other BFNIS mutations are listed in Table 16. All mutants were constructed using the double overlap PCR strategy schematized in Figure 31. R1319Q was cloned into pCMV-*SCN2A* using the BlpI site at position 3656 and the NheI restriction site at position 5156. The L1330F mutation results from a C3988T nucleotide substitution. L1330F is a highly conserved residue in the S4-S5 intracellular linker of DIII (Figures 17A and 32B). L1330F was subcloned into pCMV-*SCN2A* with the BglII site at position 3128 and the PshAI restriction site at position 4659. Finally, the L1563V mutation results from a C4687G transversion. This mutation disrupts a highly conserved residue in the S2 transmembrane segment of Domain IV (DIV) (Figures 17A and 32C). L1563V was subcloned into pCMV-*SCN2A* with the BsrGI restriction site at position 4339 and the BsgI site at 5356. PCR fragments were restriction digested and gel purified. Similar to above, the PCR and vector fragments were ligated with T4 DNA Ligase and transformed into MAX Efficiency Stbl2 cells and grown at 30 °C for four days. Each of BFNIS

Figure 32. Sequence alignment for BFNIS mutants. (A) The evolutionary conservation of R1319Q and surrounding amino acids is shown for human voltage-gated sodium channels and channels in other species. The yellow box highlights the residue of interest. The R1319Q mutation is shown to affect a residue near the intracellular face of S4. **(B)** The evolutionary conservation of L1330F and surrounding amino acids is shown for human voltage-gated sodium channels and orthologs. The yellow box highlights the residue of interest. The L1330F mutation affects a residue in the intracellular S4-S5 linker. **(C)** The evolutionary conservation of L1563V and surrounding amino acids is shown for human voltage-gated sodium channels and channels in other species. The yellow box highlights the residue of interest. The L1563V mutation disrupts a highly conserved residue close to the extracellular face of S2.

A

S4 **S4-S5 Linker**

BFNIS R1319Q	**Q**
h*SCN2A*	LRPLRALSRFEGMRAVV
h*SCN1A*	LRPLRALSRFEGMRVVV
h*SCN3A*	LRPLRALSRFEGMRVVV
h*SCN4A*	LRPLRALSRFEGMRVVV
h*SCN5A*	LRPLRALSRFEGMRVVV
h*SCN7A*	LRPLRVLS**Q**FERMKVVV
h*SCN8A*	LRPLRALSRFEGMRVVV
h*SCN9A*	LRPLRALSRFEGMRVVV
h*SCN10A*	LRPLRALSRFEGMRVVV
h*SCN11A*	LRPLRALS**Q**FEGMKVVV
Rat	LRPLRALSRFEGMRVVV
Mouse	LRPLRALSRFEGMRVVV
Dog	LRPLRALSRFEGMRVVV
Fugu	LRPLRALSRFEGMRVVV
Zebrafish	FRPLRALSRFDGMRVVV
Honeybee	LRPLRAMSRMQGMRVVV
Mosquito	LRPLRAMSRMQGMRVVV

B

S4-S5 Linker

BFNIS L1330F	**F**
h*SCN2A*	GMRAVVNALLGAIPSIM
h*SCN1A*	GMRVVVNALLGAIPSIM
h*SCN3A*	GMRVVVNALVGAIPSIM
h*SCN4A*	GMRVVVNALLGAIPSIM
h*SCN5A*	GMRVVVNALVGAIPSIM
h*SCN7A*	RMKVVVRALIKTTLPTL
h*SCN8A*	GMRVVVNALVGAIPSIM
h*SCN9A*	GMRVVVNALIGAIPSIM
h*SCN10A*	GMRVVVDALVGAIPSIM
h*SCN11A*	GMKVVVNALIGAIPAIL
Rat	GMRVVVNALLGAIPSIM
Mouse	GMRVVVNALVGAIPSIM
Dog	GMRVVVNALLGAIPSIM
Fugu	GMRVVVNALLGAIPSIF
Zebrafish	GMRVVVNALLGAIPSIM
Honeybee	GMRVVVNALVQAIPSIF
Mosquito	GMRVVVNALVQAIPSIF

C

S2

BFNIS L1563V	**V**
h*SCN2A*	QSQEMTNILYWINLVFI
h*SCN1A*	QSEYVTTILSRINLVFI
h*SCN3A*	QGKYMTLVLSRINLVFI
h*SCN4A*	QSQLKVDILYNINMIFI
h*SCN5A*	QSPEKINILAKINLLFV
h*SCN7A*	QSLQMSIALYWINSIFV
h*SCN8A*	QSKQMENILYWINLVFV
h*SCN9A*	QSQHMTEVLYWINVVFI
h*SCN10A*	QSEEKTKILGKINQFFV
h*SCN11A*	QPKAMKSILDHLNWVFV
Rat	QSQEMTNILYWINLVFI
Mouse	QSKQMENILYWINLVFV
Dog	QSQEMTNILYWINLVFI
Fugu	QSEKMKNTLNYINVVFI
Zebrafish	QSIEMTRALYWINVIFI
Honeybee	QTQTFSDVLDYLNMIFI
Mosquito	QSETFSAVLDYLNMIFI

constructs required screening of between 48 and 210 clones to find two independent clones without mutations to be utilized for electrophysiological and biochemical experiments.

Results

Optimization of heterologous expression system

To begin our heterologous expression studies of $Na_V1.2$, we used the conditions previously established in our laboratory for the related $Na_V1.1$ studies (Lossin et al., 2002; Lossin et al., 2003; Rhodes et al., 2004; Ohmori et al., 2006). Briefly, we selected the tsA201 cell line, a derivative of human embryonic kidney, HEK293, stably expressing the SV40 large T antigen. The tsA201 cell line has low endogenous voltage-gated sodium current (< -100 pA in non-transfected tsA201 cells) and high vector expression (data not shown). We used a minimum threshold of -600 pA to ensure that any low endogenous sodium current would not significantly alter voltage dependent or kinetic properties of our $Na_V1.2$ constructs. We discarded cells with sodium current greater than -6 nA to ensure adequate voltage control. A range of -600 pA to -6 nA is within the range reported in the literature for whole-cell voltage-gated sodium current from acutely isolated hippocampal neurons.

Amount of DNA transfected

Previously, about 4 μg of the pore-forming α subunit was transfected in combination with β subunits. We performed preliminary experiments to determine what amount of $Na_V1.2$ cDNA should be transfected and whether it should be cotransfected with $h\beta_1$ and $h\beta_2$. We transiently transfected 1, 2, or 4 μg of WT-$Na_V1.2$ into tsA201 cells.

We cotransfected vectors containing either eGFP or both hβ_1-IRES2-eGFP and hβ_2-IRES2-DsRed2 to keep a mass ratio of 10 α:1 eGFP or 10 α: 1 β_1: 1 β_2.

For cells transfected with 1 µg of WT-Na$_V$1.2 and eGFP, only 36% had current greater than the minimum threshold of -600 pA (*n* = 14). Similarly, cells transfected with 2 µg of WT-Na$_V$1.2 and eGFP had 19% of cells with current greater than the minimum threshold (*n* = 16). Conversely, cells transfected with 4 µg of WT-Na$_V$1.2 and eGFP had 50% of cells pass the minimum threshold (*n* = 10). When we examined the three conditions in the presence of the hβ_1 and hβ_2 subunits, 25% of cells transfected with 1 µg, 22% of cells transfected with 2 µg, and 83% of cells transfected with 4 µg of WT-Na$_V$1.2 had current that passed the minimum threshold (*n* ≥ 10 for each group). The current density-voltage relationships for the three different transfection amounts with cotransfection of either eGFP or the β subunits are shown in Figure 19.

Amount of transfection reagent

Previous studies in our laboratory had used 36 µl of Superfect (Qiagen, Valencia, CA) with 4-5 µg of cDNA. We performed the above experiments with a standard 36 µl of Superfect. We also performed experiments on cells transfected with 4.5 µg of cDNA and 72 µl of Superfect or 2.25 µg of cDNA and 18 µl of Superfect. Increasing the Superfect:DNA ratio by doubling the amount of cDNA and Superfect to 72 µl resulted in 17% of cells passing the minimum threshold of -600 pA (*n* = 6). Keeping the Superfect:DNA ratio the same by halving the amount of each resulted in 25% of cells passing minimum threshold (*n* = 16). The experiments using between 1 and 4 µg of Na$_V$1.2 cDNA transfected, cotransfected with either eGFP or the β subunits (Figure 33), and three transfection reagent ratios set up 4 µg Na$_V$1.2, 0.5 µg hβ_1, and 0.5 µg hβ_2 with 36 µl of Superfect as our standard transfection conditions for all future experiments (Figure 34).

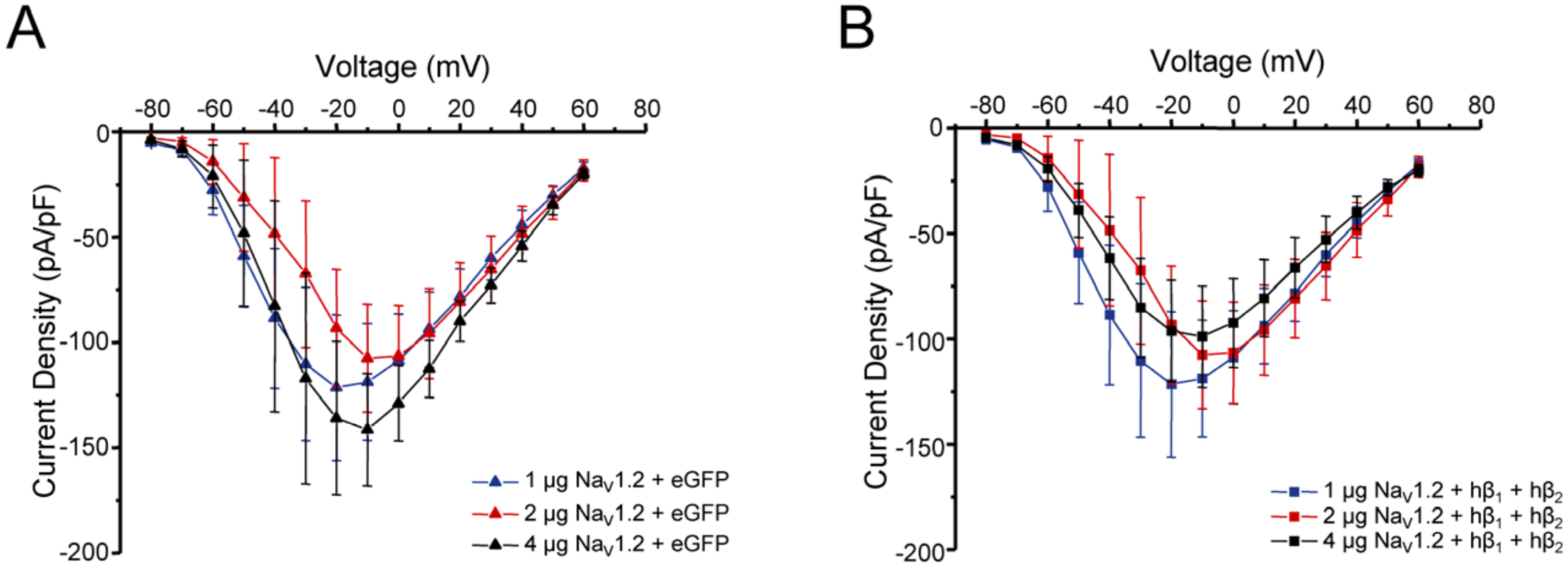

Figure 33. Effect of amount of DNA transfected. (A) Current density-voltage relationship for cells cotransfected with three different amounts of Na$_V$1.2 cDNA and eGFP. **(B)** Current density-voltage relationship from cells with three different amounts of Na$_V$1.2 cDNA cotransfected with hβ$_1$ and hβ$_2$. We chose to use 4 μg of Na$_V$1.2 cotransfected with both β subunits for subsequent experiments. (n ≥ 4 for each condition).

Figure 34. Heterologous expression system. Here is a schematic diagram showing pertinent features of the heterologous expression system we employed for the electrophysiological experiments. This chapter describes several experiments to find optimal conditions for the heterologous expression system. We cotransfected 4.0 µg pCMV-*SCN2A* with 0.5 µg phβ_1-IRES2-eGFP and 0.5 µg phβ_2-IRES2-DsRed2. We used 36 µl of Superfect in combination with our cDNAs to transfect tsA201 cells. We performed our whole-cell patch clamp experiments 48 to 72 hrs post transfection. Our inverted microscope for patch clamp experiments has a set of epifluoresence filters that allow us to detect cells that are expressing the eGFP and DsRed2 fluorophores. Cells that are expressing both fluorophores appear yellow and are presumed to have been successfully transfected with all three plasmids.

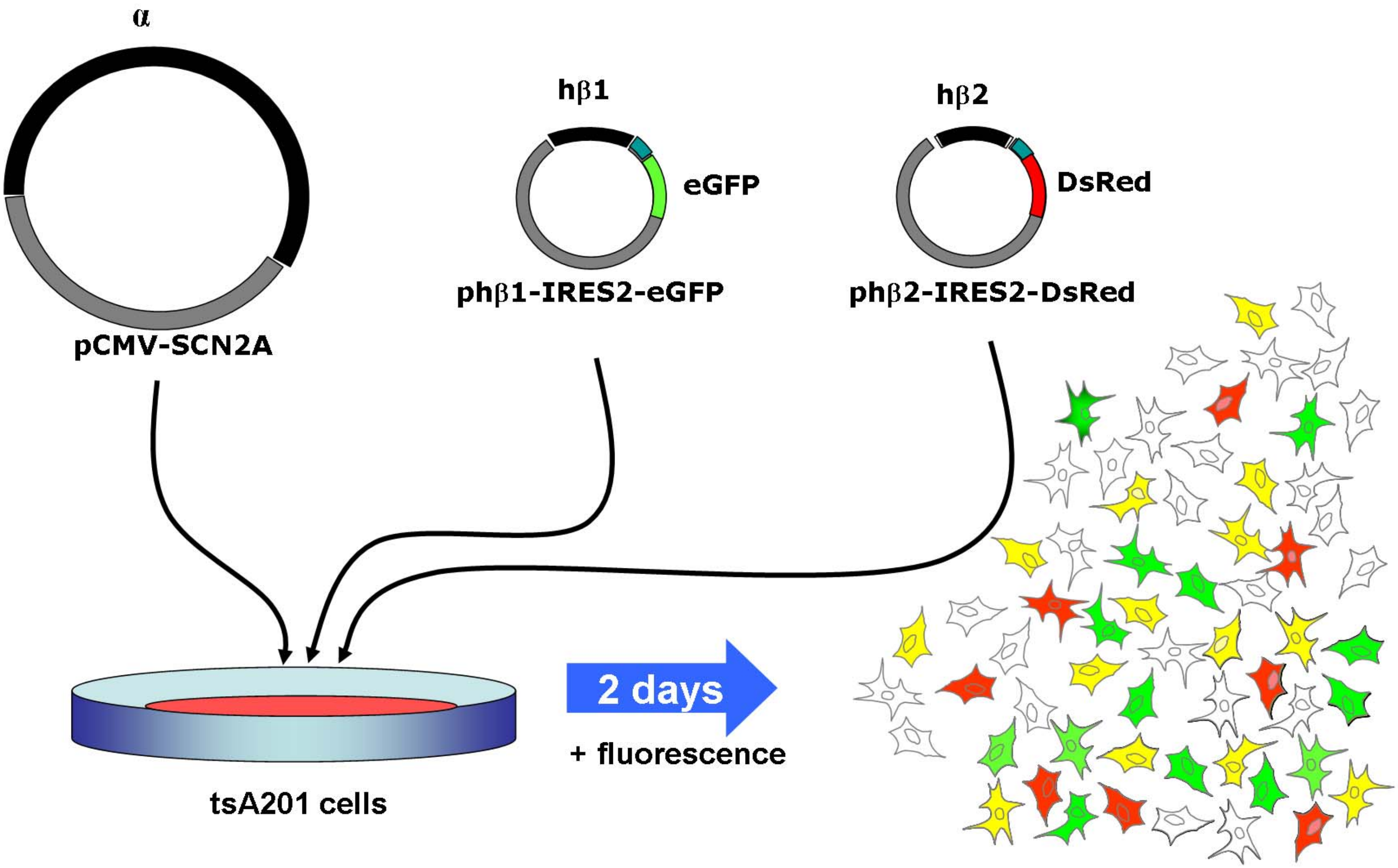
α
hβ1
hβ2
eGFP
DsRed
pCMV-SCN2A
phβ1-IRES2-eGFP
phβ2-IRES2-DsRed
tsA201 cells
2 days
+ fluorescence

Cell line comparison

Our laboratory had previously used tsA201 cells to characterize $Na_V1.1$ (Lossin et al., 2002; Lossin et al., 2003; Rhodes et al., 2004; Rhodes et al., 2005; Ohmori et al., 2006; Kamiya et al., 2004). Previous studies of $Na_V1.2$ used CHO-K1 and HEK293 cells (Ahmed et al., 1992). We performed some preliminary experiments with $Na_V1.2$, $h\beta_1$, and $h\beta_2$ cotransfected into tsA201 and CHO-K1 cells (Figure 35). We also found that currents from tsA201 cells were larger than CHO-K1 cells (Figure 35). We decided to perform all subsequent experiments in tsA201 cells using the amount of cDNA and transfection reagent described above (Figure 34).

Optimization of whole-cell patch clamp conditions

Time after transfection

We next sought to determine how long after transfecting cells we should perform electrophysiological experiments. Previous studies from our laboratory with the highly homologous $Na_V1.1$ protein were conducted 24 to 48 hrs after transfection (Lossin et al., 2002; Lossin et al., 2003; Rhodes et al., 2004; Rhodes et al., 2005; Ohmori et al., 2006). We decided to see whether the optimum time to do experiments would be 24, 48, 72, or 96 hrs after transfection. At each of these time points we performed whole-cell patch clamp experiments to see what percentage of cells had current greater than the minimum threshold of -600 pA. At 24 hrs, there were many fewer cells that appeared yellow (denoting presence of both $h\beta_1$ and $h\beta_2$) or red (denoting presence of $h\beta_2$). This was likely caused by the slower time course of DsRed2 maturation compared to other fluorophores and that it appears green early in maturation before turning red (Verkhusha et al., 2004). When we patched yellow cells 24 hrs post transfection, only 15% of cells passed our current threshold. The 48 and 72 hr time points had 44% and 63% of cells pass threshold respectively. Only 8% of cells at 96 hrs after transfection had current

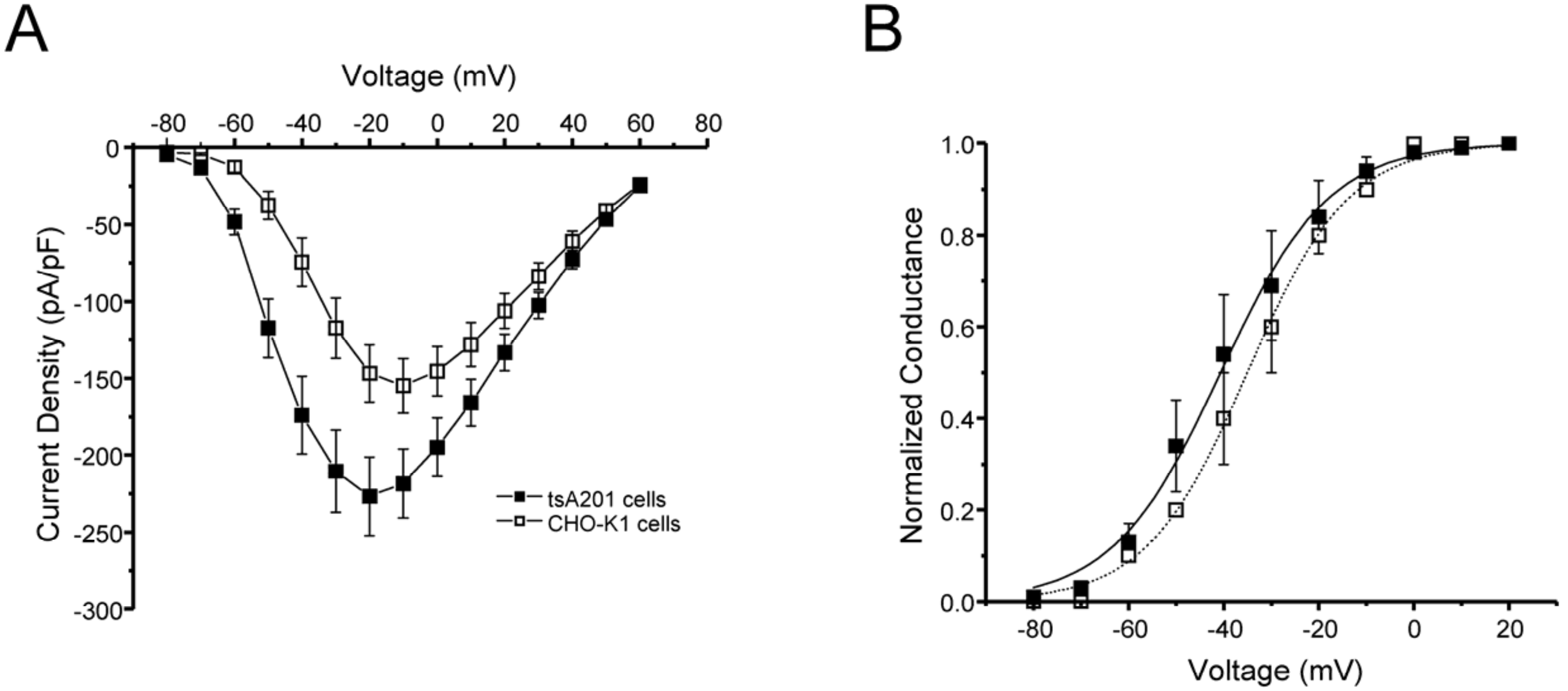

Figure 35. Comparison of WT-Na$_V$1.2 in two cell lines. (A) Current density-voltage relationship for cells that transiently expressed WT-Na$_V$1.2 with β$_1$ and β$_2$ in tsA201 and CHO-K1 cells. The current density is significantly larger over the -80 to -10 mV voltage range for tsA201 cells compared to CHO-K1 cells ($p \leq 0.05$). **(B)** The voltage dependence of activation curves are similar for WT-Na$_V$1.2 in tsA201 and CHO-K1 cells. The $V_{1/2}$ for activation was -40.6 ± 0.7 mV for tsA201 cells and -35.0 ± 0.5 for CHO-K1 cells. The k for activation was 11.4 ± 0.6 for tsA201 cells (*n* = and 18) 10.6 ± 0.5 for CHO-K1 cells (*n* = 15).

greater than our threshold (n = 12 - 16 for each time point). We chose to continue experiments only within 48 to 72 hrs post transfection (Figure 34).

Time after establishing whole-cell configuration

We next wanted to determine how long after establishing the whole-cell configuration the electrophysiological recordings should be performed. Previous studies of $Na_V1.1$ began experiments ten minutes after establishing the whole-cell configuration. Because initial experiments with $Na_V1.2$ showed high variability, we decided to perform a time course by running a family of 20 ms voltage steps to between -80 and 60 mV from a holding potential of -120 mV. We then converted the peak currents at each test potential to normalized conductances and fitted the data with a Boltzmann equation to look at the voltage dependence of activation. We did recordings in two minute increments beginning just after establishing the whole-cell configuration and ending at 30 minutes. In Figure 36, we show two representative time points, 10 and 20 minutes, to illustrate that we observed a time-dependent hyperpolarizing shift in the voltage dependence of activation, similar to that previously observed for $Na_V1.1$ (Vanoye et al., 2006). We decided to do all subsequent experiments 15 min after establishing the whole-cell configuration to allow for equilibration of the internal pipette solution, stabilization of variability, and to decrease the length of all experiments.

Holding potential

In preliminary experiments, we found a high amount of variability in recordings and saw that the voltage dependence of fast inactivation data was inconsistently affected by the most negative potentials (-120 to -140 mV) we examined (data not shown). We had been using a holding potential of -120 mV and decided to see if a holding potential of -150 mV might improve either of these parameters. We performed

Figure 36. Effect of holding potential and time course. (A) The current density-voltage relationships for WT-Na$_V$1.2 from a holding potential of -120 or -150 mV at 10 and 20 minutes after establishing the whole-cell configuration. **(B)** Voltage dependence of activation for WT-Na$_V$1.2 from a holding potential of -120 and -150 mV at 10 and 20 minutes after establishing the whole-cell configuration. The V$_{1/2}$ for 10 minutes from -120 mV is -32.3 ± 4.1, 10 minutes from -150 mV is -30.7 ± 4.2, 20 minutes from -120 mV is -38.6 ± 3.3, and 20 minutes from -150 mV is -36.4 ± 3.5. The k for voltage dependence of activation for 10 minutes from -120 mV is 8.0 ± 0.5, 10 minutes from -150 mV is 8.2 ± 0.5, 20 minutes from -120 mV is 8.2 ± 0.4, and 20 minutes from -150 mV is 8.8 ± 0.4. (n = 7-9 for each condition).

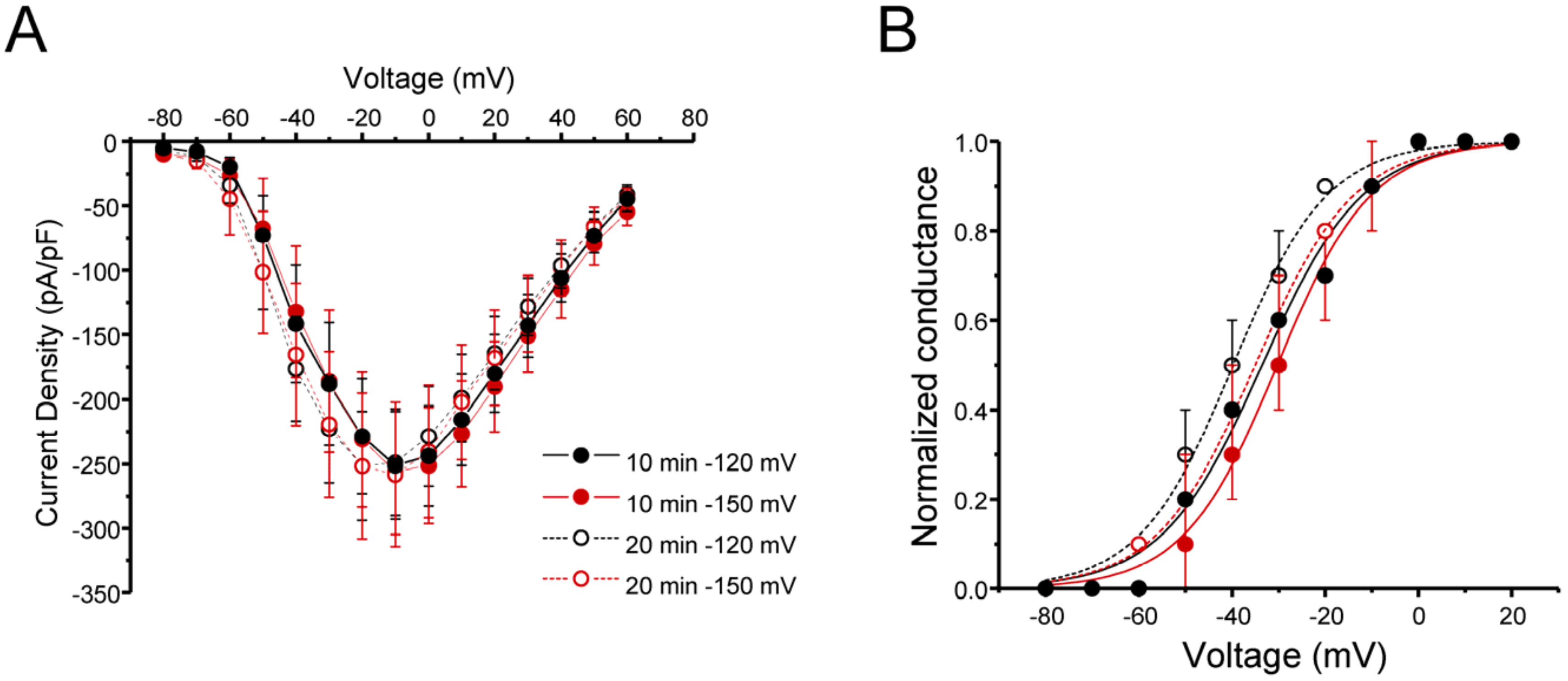
A
Voltage (mV)
-80
-60
-40
-20
0
20
40
60
80
0
-50
-100
-150
-200
-250
-300
-350
Current Density (pA/pF)
10 min -120 mV
10 min -150 mV
20 min -120 mV
20 min -150 mV
B
1.0
0.8
0.6
0.4
0.2
0.0
Normalized conductance
-80
-60
-40
-20
0
20
Voltage (mV)

these experiments concurrently with the above experiments on amount of time after establishing the whole-cell configuration. In Figure 36, current density-voltage relationships and voltage dependence of activation are shown for 10 and 20 min after establishing whole-cell configuration from holding potentials of both -120 and -150 mV. We found that the holding potential of -150 mV did not decrease variability but did increase the difficulty of the experiments since cells were not as stable when held at such a hyperpolarized potential (Figure 36). We subsequently used -120 mV for a holding potential and began our recordings 15 min after establishing the whole-cell configuration between 48 and 72 hrs post transfection.

Discussion

Heterologous expression systems have been a fundamental tool for understanding the functional impact of disease-causing mutations. Electrophysiological experiments in a heterologous expression system can provide rapid functional data about disease-causing mutations. In particular for the neuronal voltage-gated sodium channels, $Na_V1.1$ and $Na_V1.2$, epilepsy-associated mutations have been investigated using whole-cell patch clamp of tsA201 or CHO-K1 cells.

In this appendix, we described the construction of a human *SCN2A* cDNA and specific methods employed for construction of BFNIS associated $Na_V1.2$ mutations for electrophysiological study. We then conducted a series of preliminary experiments to optimize our heterologous expression system to achieve a high level of $Na_V1.2$ expression conducive for functional testing. We also conducted a series of preliminary experiments to optimize our electrophysiological recordings. From these experiments, we were able to establish baseline conditions to perform functional characterizations of WT-$Na_V1.2$ and three BFNIS mutants (R1319Q, L1330F, and L1563V). These studies will increase our understanding of mechanisms underlying neuronal excitability disorders including benign monogenic epilepsies.

APPENDIX B

CHARACTERIZATION OF NEURONAL SODIUM CHANNELS FROM MUTANT *Scn2a* TRANSGENIC MICE WITH DIFFERING SEIZURE SUSCEPTIBILITY

Introduction

Animal models allow for investigation of mechanisms underlying epilepsy in a more physiological setting than heterologous expression studies. The early animal models of epilepsy involved seizure induction in animals by administration of chemicals like pilocarpine or pentylenetetrazole (PTZ) or by electrical stimulation as in kindling protocols. Alternatively, spontaneous mutations in inbred mouse and rat strains, like slow-wave epilepsy (*swe*) or stargazer (*stg*), have resulted in a variety of epilepsy phenotypes. More recent animal models of epilepsy are the result of genetically altering animals through knockout or transgenic expression of specific genes (Frankel, 1999; Bertram, 2007).

Early investigations of voltage-gated sodium channels created substitutions in different regions of the predicted channel topology to determine functional domains. The substitutions were then characterized in a heterologous expression system. One mutation that increased persistent current and impaired whole-cell current inactivation in *Xenopus* oocytes was the GAL879-881QQQ mutation located in the S4-S5 intracellular linker of DII of rat *Scn2a* (Smith and Goldin, 1997). This is a region of the sodium channel now implicated in fast inactivation by interacting with the fast inactivation gate.

Prior to the identification of epilepsy-associated mutations in neuronal voltage-gated sodium channels, the GAL879-881QQQ mutation in rat *Scn2a* was introduced as a transgene into mice. The transgene was driven by the neuronal specific enolase (NSE) promoter and contains a FLAG epitope in close proximity to the ATG of *Scn2a* (Figure

46A). The original characterization was of transgenic mice (Q54) with a mixed background comprised mostly of C57BL/6J and (12-25%) SJL/J (Table 4). The Q54 mice had spontaneous seizures originating in the hippocampus around two months, one month after increased persistent current could be observed in acutely isolated hippocampal neurons (Kearney et al., 2001).

The Q54 mice were then bred onto a congenic C57BL/6J background (B6.Q54) where a significant decrease in the number of seizures, the number of mice with seizures, and seizure severity were observed compared to the mice from a mixed background (Bergren et al., 2005). A forward cross with the SJL/J line was performed resulting in F1.Q54 mice that are 50% C57BL/6J and 50% SJL/J. The F1.Q54 mice had a significantly higher incidence of seizures, increased seizure severity, and a shorter lifespan compared to the B6.Q54 mice. A genome wide scan identified two loci (modifiers of epilepsy, MOE1 and MOE2) that could account for the majority of the difference in seizure susceptibility between the two backgrounds (Bergren et al., 2005).

Although genetic modifiers modulate the seizure susceptibility in these mice, it is unknown whether the modifiers modulate the voltage-gated sodium channels directly or modulate a different protein such as another ion channel or cytoskeletal protein. We hypothesized that the difference in seizure susceptibility was due to the genetic modifier directly affecting the function of the sodium channel transgene. We sought to determine the effect of the modifier on the sodium channel using two different methods: electrophysiology and biochemistry. The electrophysiological experiments were performed on acutely isolated hippocampal neurons and the biochemical experiments were performed on membrane preparations isolated from whole mouse brain. Below we describe steps to optimize these experiments and results from our preliminary characterization of brain sodium channels from the two Q54 mouse lines (B6.Q54 and F1.Q54) with differing seizure susceptibility.

Materials and methods

Preparation of neuronal cultures

Mice aged between postnatal (P) day P21 and P23 were deeply anesthetized with isoflurane (MINRAD Inc., Orchard Park, NY). The animals were decapitated with surgical scissors (unless otherwise noted, all surgical tools were from Fine Science Tools Inc., Foster City, CA) and the heads were soaked in a beaker of 70% ethanol. The dissection was performed in less than 30 minutes from the point of decapitation to getting the tissue in trypsin to increase cell viability as determined by counting cells with trypan blue (Invitrogen Corp., Carlsbad, CA) staining. The skin and skull were cut along midline using small angled scissors. Curved forceps were used to remove the overlying skull. The brain was removed and put into 4 ml of ice cold sterile filtered dissection solution with 0.2% penicillin/streptomycin (in mM): 145 NaCl, 3 KCl, 10 HEPES, 5.6 glucose, pH of 7.3 or Hanks' balanced salt solution (HBSS) (product number H9394, Sigma. St. Louis, MO). This was repeated for each mouse. Then one brain at a time was put on a fresh piece of grade number 1 Whatman filter paper (VWR International, West Chester, PA) and the cerebellum was removed. Then the brain was hemisected, and one hemisphere was put into a 35 mm petri dish with 4 ml of fresh ice cold sterile filtered dissection solution until ready for hippocampal dissection.

The other hemisphere was oriented with the cortex towards the filter paper and the midbrain facing up. The midbrain was removed using one hippocampus tool while the underlying hippocampus and cortex was protected with another hippocampus tool. The brain was reoriented so the anterior part was facing up. The hippocampus was removed with the rounded edge of the hippocampus tool and placed into a new 35 mm dish with 4 ml of fresh ice cold sterile filtered dissection solution. This was repeated until each hippocampus was removed. One hippocampus at a time was cut into two or three pieces while in the dissection solution using a #20 scalpel blade (Roboz Surgical Instrument Co., Gaithersburg, MD). The piece of hippocampus was put on a fresh piece of Whatman filter paper with the cut face down and was kept moist with dissecting solution. The convex surface, presumed to be mostly CA1 region, under a dissecting microscope (Carl Zeiss Microimaging, Inc., Thornwood, NY) was removed and put into a new 35 mm dish with 4 ml of fresh ice cold sterile filtered dissection solution. This was repeated until all pieces of CA1 were in one dish.

Next the CA1 tissue was trypsinized by combining 5 ml of ice cold dissection solution with 3 mg of Trypsin (Research Products International Corp., Mt. Prospect, IL) and sterile filtering directly into a new 35 mm dish. The pieces of CA1 were transferred using a sterile transfer pipette into the trypsin. The tissue was digested at room temperature using room air for 30 min. The dish was swirled every 10 min to ensure even distribution of trypsin to the CA1 tissue. After the trypsin digest was complete, the tissue was transferred to a dish with 5 mL dissection solution and swirled for 30 sec. This was repeated in three more times for a total of four washes each time using a new sterile transfer pipette.

After thoroughly washing the trypsinized tissue, a sterile transfer pipette was used to move just the CA1 pieces to a 15 ml conical tube containing plating media (84% Neurobasal-A, 8% F-12, 8% FBS, 0.2% penicillin/streptomycin, 0.08 mM L-glutamine). The volume of plating media depended upon the number of animals and size of tissue digested. The least volume ever used was 1 ml (for one mouse only) and the maximum was 3 ml (when three or four mice were used). Typically the dissection was performed on two mice of the same genotype and the tissue was triturated in 2 ml. The trituration was performed with a long Pasteur pipette that was lightly fire polished at the tip just prior to use. The tissue was triturated about 40 times or until the plating media was quite cloudy and small tissue pieces. When the tissue was triturated 20 times, the cell count was too low and if the tissue was triturated > 80 times, the cell count increased but the cell viability decreased. The contents of the 15 ml conical tube (both media and remaining chunks of tissue) were passed through a 40 µm cell strainer (BD Biosciences, San Jose, CA) into a sterile 50 mL conical tube. From this tube, 25 µl were put into a sterile 1.5 ml tube with 25 µl of Trypan blue stain to count live and dead cells. The remaining cell suspension was plated in 250-275 µl volumes in the center glass coverslip of poly-d-lysine coated 35 mm dishes (MatTek Corp., Ashland, MA). The dishes were put in a 37 °C incubator humidified with 5% CO_2 for two hours. The dish was then washed with 1 ml of media (either plating media as described above or maintenance media containing 98% Neurobasal-A, 2% B-27 supplement, and 0.2% penicillin/streptomycin). The media was aspirated and then 2 ml of fresh plating or maintenance media were added to each dish. The dishes were then returned to the incubator until they were used for whole-cell patch clamp studies. If the dishes were maintained in the incubator longer than 48 hrs, then 1 ml of the media was aspirated and replaced with 1 ml fresh media.

Electrophysiological recording

Whole-cell voltage-clamp recordings were used to characterize the functional properties of voltage-gated sodium channels, as described previously with some small modifications (Lossin et al., 2002; Lossin et al., 2003; Rhodes et al., 2004; Ohmori et al., 2006). Sodium channel currents were recorded at room temperature, 1 to 75 hrs after neuron plating. We identified isolated neurons with phase bright membranes and no blebbing that appeared somewhat pyramidal in morphology (branching level depended upon time after dissection as seen in Figure 38). Neurons were photographed using a Moticam 3000 camera and Motic Images Advanced 3.2 software (Motic, Richmond, British Columbia, Canada) to document cell morphology. After obtaining the whole-cell configuration, another picture was taken and one last picture at the end of the recording to document changes in morphology over the course of the experiment.

Patch pipettes were fabricated from custom 8520 patch glass (Warner Instrument Co., Hamden, CT) using a multistage P-97 Flaming-Brown micropipette puller (Sutter Instruments Co., San Rafael, CA) and fire-polished by using a microforge (MF 830, Narashige, Japan). Pipette resistance was between 1.4 and 4.0 MΩ (but ideally between 2.0 and 2.5 MΩ). The pipette solution consisted of (in mM) 140 CsF, 10 NaCl, 1 EGTA, 10 HEPES, with a pH of 7.3. The bath solution was comprised of in (mM): 140 NaCl, 3 KCl, 1 $CaCl_2$, 1 $MgCl_2$, 10 HEPES, with a pH of 7.3. The dish of neurons was rinsed three times with freshly filtered extracellular bath solution and then filled with 2 ml of freshly filtered extracellular bath solution. Each dish was allowed to equilibrate for 10 min prior to the first recording and was discarded within 90 min of adding the extracellular solution. The reference electrode consisted of a 2% agar bridge with composition similar to the bath solution. Cells were allowed to stabilize for 10 min after establishment of the whole-cell configuration before current was measured. Cells exhibiting peak current amplitudes < -0.5 nA were excluded from analysis of biophysical properties to avoid contamination of noise in recordings and high levels of current at holding potential (leak current). Whole-cell capacitance and access resistance were determined by integrating capacitive transients in response to voltage steps from −100 to −110 mV filtered at 10 kHz. Series resistance was compensated 90-95%. Leak currents were subtracted by using an online P/4 procedure. All data were low-pass Bessel filtered at 5 kHz and digitized at 50 kHz.

Specific voltage-clamp protocols assessing channel activation and voltage dependence of fast inactivation were used as described previously with small modifications (Lossin et al., 2002; Lossin et al., 2003; Rhodes et al., 2004; Ohmori et al., 2006) and illustrated as panel insets in the figures. All voltage-clamp protocols utilized a holding potential of –100 mV and a 60 sec interpulse at the holding potential between sequential protocols. The holding potential was -100 mV to prevent channels from opening or inactivating between test pulses but was not more hyperpolarized because that destabilized the neurons. Voltage steps (20 ms) to between –80 to +60 mV in 5 mV increments were used to create a family of voltage-gated inward sodium current traces. The peak current was normalized for cell capacitance and plotted against voltage to generate peak current density-voltage relationships. Conductance (G_{Na}) was calculated as $G_{Na} = I/(V - E_{rev})$ where I is the measured peak current, V is the test voltage, and E_{rev} is the calculated sodium reversal potential. To provide a quantitative evaluation of the voltage dependence of activation, normalized G-V curves were fit with a Boltzmann function, $G/G_{max} = (1 + \exp[(V - V_{1/2})/k])^{-1}$, where $V_{1/2}$ is the curve midpoint indicating the voltage at which half of the channels are activated and k is a slope factor corresponding with voltage sensitivity of the channel. These parameters define the magnitude of depolarization needed for channel opening. Voltage dependence of fast inactivation was assessed by 100 ms prepulses to between –140 to –10 mV in 10 mV increments followed by a 20 ms test pulse to –10 mV. The normalized current is plotted against the voltage and the data were fit with Boltzmann functions to determine the voltage for half-maximal inactivation ($V_{1/2}$) and a slope factor (k). Voltage dependence of fast inactivation provides information about the level of depolarization necessary for the channel to enter fast inactivation under steady-state conditions including the physiological range of potentials. When a neuron was stable, persistent current was evaluated during the final 10 ms of a 200 ms depolarization to −10 mV and expressed as a percentage of peak current following digital subtraction of currents recorded in the presence and absence of 10 µM tetrodotoxin (TTX).

Results are presented as mean ± SEM unless otherwise noted. Data analysis was performed using Clampfit 9.2 (Axon Instruments, Union City, CA), Excel 2002

(Microsoft, Seattle, WA), GraphPad Prism 4.0 (GraphPad Software Inc., San Diego, CA), and OriginPro 7.0 (OriginLab, Northampton, MA) software.

Membrane preparations

For biochemical experiments from transgenic mice, we performed membrane isolations from whole brain as previously described with a few modifications (Hartshorne and Catterall, 1984). As described above, young mice (P21-P23) were deeply anesthetized with isoflurane and rapidly decapitated. The brain was dissected, weighed, and put in an ice cold Dounce homogenizer. Solution 1 comprised of 0.32 M sucrose and 5 mM Tris/HCl with a pH of 7.4 was sterile filtered and supplemented with complete protease inhibitor cocktail tabs, EDTA free (Roche Applied Science, Indianapolis, IN). Ice cold solution 1 (10 ml per gram of brain tissue) was added to the Dounce homogenizers and the brains were homogenized with 10 strokes. The homogenate was transferred to round bottom 14 ml falcon tubes and centrifuged at 700 x g for 10 min. The supernatant was saved and the pellet was resuspended in ice cold solution 1 supplemented with protease inhibitors at 6.6 ml per gram of original tissue. The new homogenate was centrifuged in 14 ml falcon tubes at 700 x g for 10 min. The supernatant was combined with the previous supernatant in an Oak Ridge tube and the pellets were discarded. The supernatants were spun at 27,000 x g for 40 min. The supernatant was discarded. The pellet was resuspended in solution 2 in a volume of 16.6 ml per gram of original tissue to cause osmotic lysis of cells in the homogenate. Solution 2 is comprised of 5 mM Tris/HCl with a pH of 8.2 and 1 mM EDTA supplemented with the protease inhibitors described above. The suspension was incubated on ice for 15 min and then homogenized for 4 strokes with the Dounce homogenizer. The homogenate was then spun at 27,000 x g for 40 min. The supernatant was discarded. The pellet was resuspended in solution 3 supplemented with protease inhibitors at a volume of 2 ml per gram of tissue. Solution 3 contained 200 mM KCl, 10 mM HEPES, adjusted with 1 M Tris-base to pH 7.5. The concentration of each membrane preparation was determined using the BCA protein assay kit (Pierce Biotechnology, Rockford, IL).

The samples (25 µg of each as determined by the BCA assay) were mixed with 2X Laemmli Sample Buffer containing fresh 5% β-mercaptoethanol. The samples were incubated at 65 °C for 20 min prior to being separated using SDS-polyacrylamide (7.5%) gel electrophoresis and transfer to polyvinylidene difluoride membranes. Membranes were incubated at room temperature for two hours in 5% milk. The transgene was detected with primary antibodies directed against the FLAG epitope (mouse, anti-FLAG M2, 1:15000, Sigma). Immunoreactive bands were visualized using horseradish peroxidase-conjugated secondary antibody (goat anti-mouse, 1:100000, Santa Cruz Biotechnology, Santa Cruz, CA), directed against the primary antibody, Super Signal West Femto Maximum Sensitivity Substrate (Pierce Biotechnology, Rockford, IL) incubation and Hypersensitive film detection.

Results

We optimized several conditions for recording from acutely isolated CA1 hippocampal neurons. We used optimized conditions to record from neurons expressing the GAL879-881QQQ transgene in the B6.Q54 and F1.Q54 background strains to look for differences in sodium current. We also used western blot analysis of membrane preparations from whole brains to examine transgene expression of both background strains.

Cell plating

We began by performing hippocampal dissections on wild-type (WT) mice to optimize methods. We plated isolated neurons on 35 mm Corning dishes that were uncoated, but the neurons would not adhere well. We next tried coating the dishes with poly-l-ornithine (PLO) in a borate buffer (0. 5 mg PLO per ml of buffer), but this proved difficult to standardize. We then used pre-coated dishes coated with collagen or poly-d-lysine coating on a glass coverslip in the middle of the plastic dish from MatTek Corporation (Ashland, MA). We found that the MatTek dishes with the poly-d-lysine coating worked best and used them for subsequent experiments (including the majority of the experiments described below).

We plated 250 µl of cell suspension in the center of the dish and filled the other 2 ml of media within 10 minutes. The original plating method resulted in glial proliferation and a large amount of debris remaining on the dish. We found that performing the trituration in plating media and plating 250-275 µl in the center of the dish allowing 2 hrs for settling time and adherence was optimal (1 hr was too short for adherence and 3.5 – 4 hrs was too long to remove most of the debris). After 2 hrs, 1 ml of maintenance media was used to wash the dish and then 2 ml of maintenance media were added to the dish. If the dishes were maintained longer than 48 hrs, then 1 ml of media was removed and replaced with 1 ml of fresh maintenance media. All dishes were used within 72 hrs of neuron plating.

Optimization of pipettes

During our initial recordings, we noticed that the opening of the pipette was too large and resulted in most of the neuron being drawn up into the pipette. This could be seen visually through the microscope or by measuring the capacitance of the neuron. We started performing whole-cell recordings using thin wall borosilicate glass we had previously used for our heterologous expression studies with pipette resistances of between 1.0 and 2.0 MΩ. We tried to increase the resistance and decrease the size of the pipette opening, but were unsuccessful in making the tip small enough. We tried four different types of glass before settling on a custom patch glass from Warner Instruments with a resistance of between 2.0 and 4.0 MΩ as the optimal condition for all subsequent experiments.

Time after dissection

Based upon the literature, we began electrophysiological experiments 1 hr after plating neurons. At early time points after dissection, we saw either no or very small (≤ -200 pA) inward voltage dependent currents (Figure 37A). We slowly lengthened the time between dissection and electrophysiological experiments. Prior to the Moticam 3000 installation, we successfully obtained a recording from one WT neuron approximately 7 hrs after dissection (Figure 37B). Other than the one recording presented in Figure 37B, no other neurons patched less than 48 hrs post dissection had inward voltage-dependent current > -500 pA. Another difficulty with recording 1 to 24 hrs after plating was the spherical shape of the neurons that makes morphological identification of neurons difficult (Figure 38A). We found that after 48 hrs the morphology was no longer spherical and by 72 hrs there was extensive branching of the neurons (Figure 38B). Although we initially planned to record from CA1 pyramidal neurons, we decided to record from any healthy neurons because the NSE promoter used to drive the *Scn2a* transgene (Figure 46A) is expressed in all neurons. We recorded from neurons that had phase bright membranes without blebbing, and that had at least one intact process.

Properties of B6.Q54 neurons

After setting optimal conditions by using WT mice, we recorded from neurons isolated from B6.Q54 mice, the mice with the less severe seizure phenotype. We had difficulty discerning neuronal type by morphology, but chose neurons that looked healthy

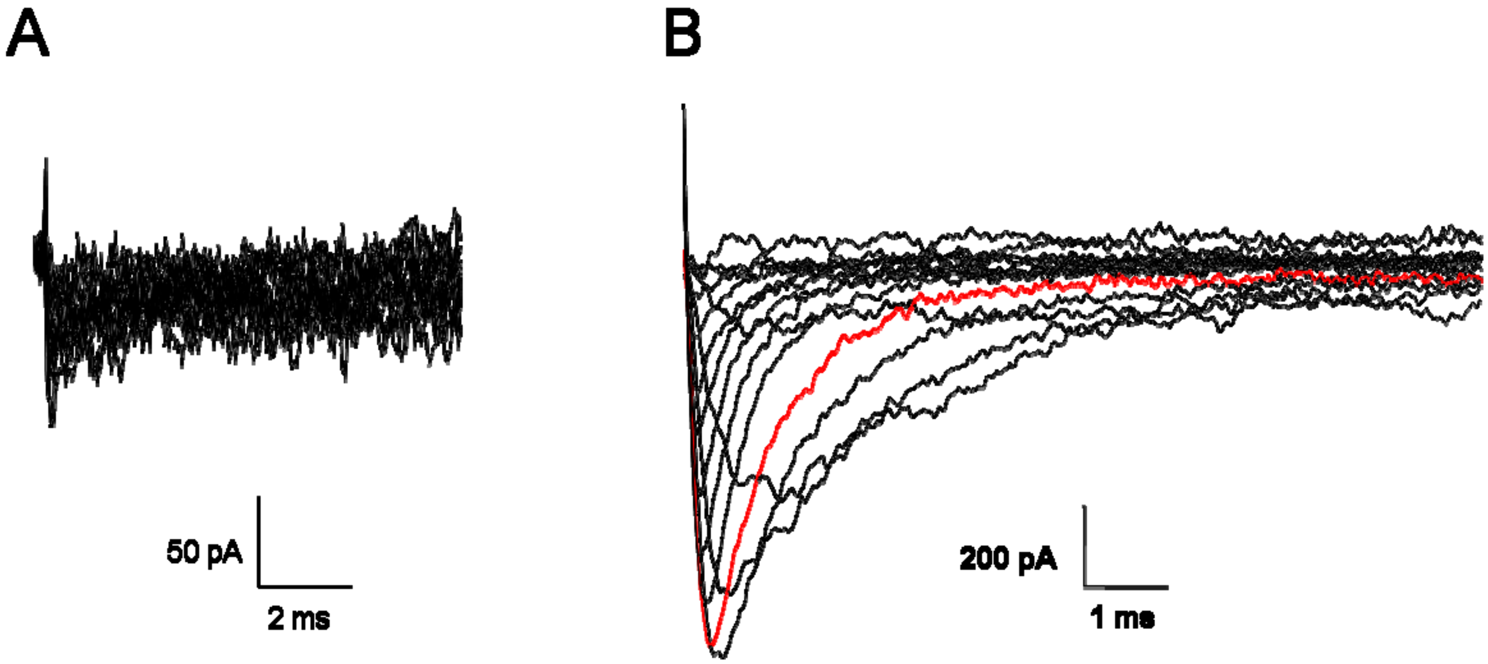

Figure 37. Representative whole-cell traces from WT neurons. (A) Typical recording from initial experiments when most of the neuron was drawn up into the pipette. The capacitance of this cell was 2 pF. **(B)** Best recording from a WT neuron collected 7 hrs post dissection. The neuron had a capacitance of 5.6 pF and a maximum inward peak current of -1.0 nA. The red trace indicates the step to -10 mV.

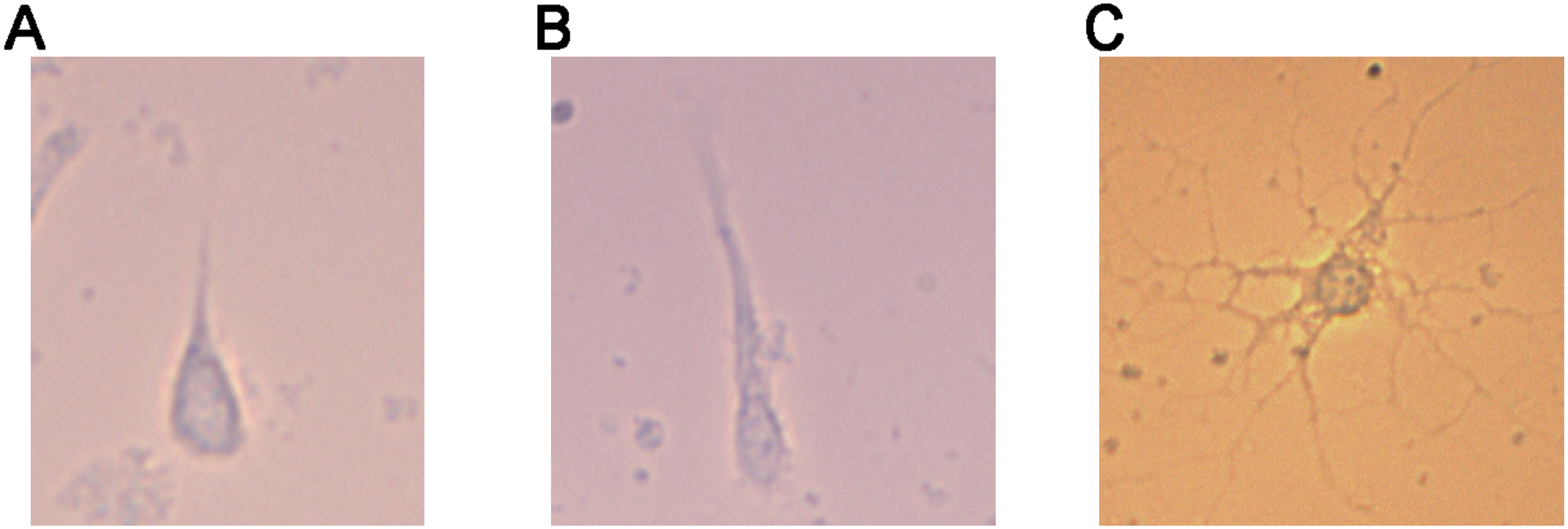

Figure 38. Representative neuronal morphologies. (A) Picture of a neuron about 20 hrs post dissection. The neuron had no voltage-gated inward current but highlights the rounded nature of neurons less than 48 hrs post dissection. **(B)** Picture of a neuron about 48 hrs after dissection which still has very little branching. The peak inward current was -100 pA. **(C)** Picture of a neuron 67 hrs post dissection showing extensive branching of processes. The neuron had a peak inward current of -300 pA.

and had at least one intact process. We obtained recordings of voltage-gated sodium channel currents from four B6.Q54 neurons that each had current ≥ -900 pA (Figures 39 – 41). Representative traces are shown for each neuron in Figures 39C and 41. Based on earlier experiments, we used a holding potential of -100 mV to limit channel inactivation and maximize membrane potential stability. We ran standard protocols to look at current density-voltage relationships, voltage dependence of activation and fast inactivation (Figures 42, 43A and Table 17). For two of the neurons we also examined persistent current by recording a 200 ms test pulse in the absence and presence of TTX (Figure 43B and Table 17). Both B6.Q54 neurons examined had persistent current with a mean of 4.4 % of peak current.

Properties of F1.Q54 neurons

Since fewer F1.Q54 animals were available and there were time constraints, we performed fewer experiments on neurons isolated from F1.Q54 mice. We were only able to obtain recordings from one neuron (Figure 44A). The representative trace for this neuron is shown in Figure 44B. We examined the current density-voltage relationship and voltage dependences of activation and fast inactivation (Figure 45 and Table 17). More studies need to be performed before any conclusions can be drawn.

Transgene protein expression levels

We performed western blot analysis on membrane preparations from whole mouse brain of B6.Q54, F1.Q54, or WT littermates. The transgene contains a singleFLAG epitope at the N terminus of *Scn2a* (Figure 46A) (Kearney et al., 2001). We addressed the question of whether the transgene was expressed at different levels in

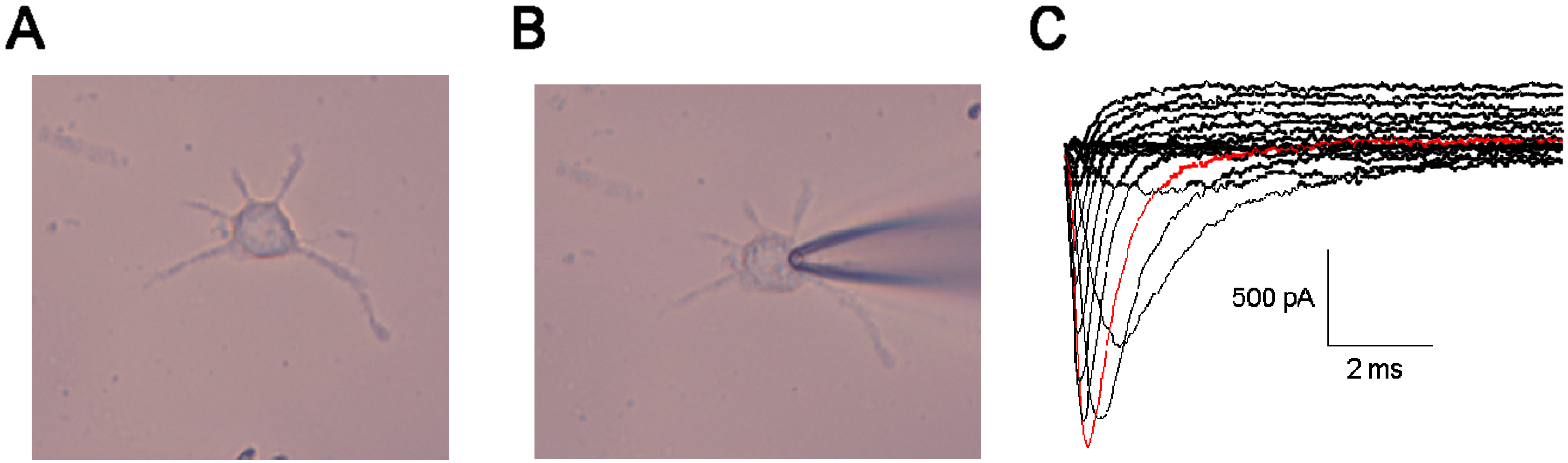

Figure 39. B6.Q54 neuron. (A) A picture of a B6.Q54 neuron 48.5 hrs after dissection. **(B)** Picture of the same B6.Q54 neuron with pipette sealed onto neuron. **(C)** Representative trace from this neuron with the red line indicating the step to -10 mV. The capacitance of this neuron was 21 pF and the maximum peak current was -1.55 nA. The current density-voltage relationship and other biophysical parameters are presented in Figures 42 and 43.

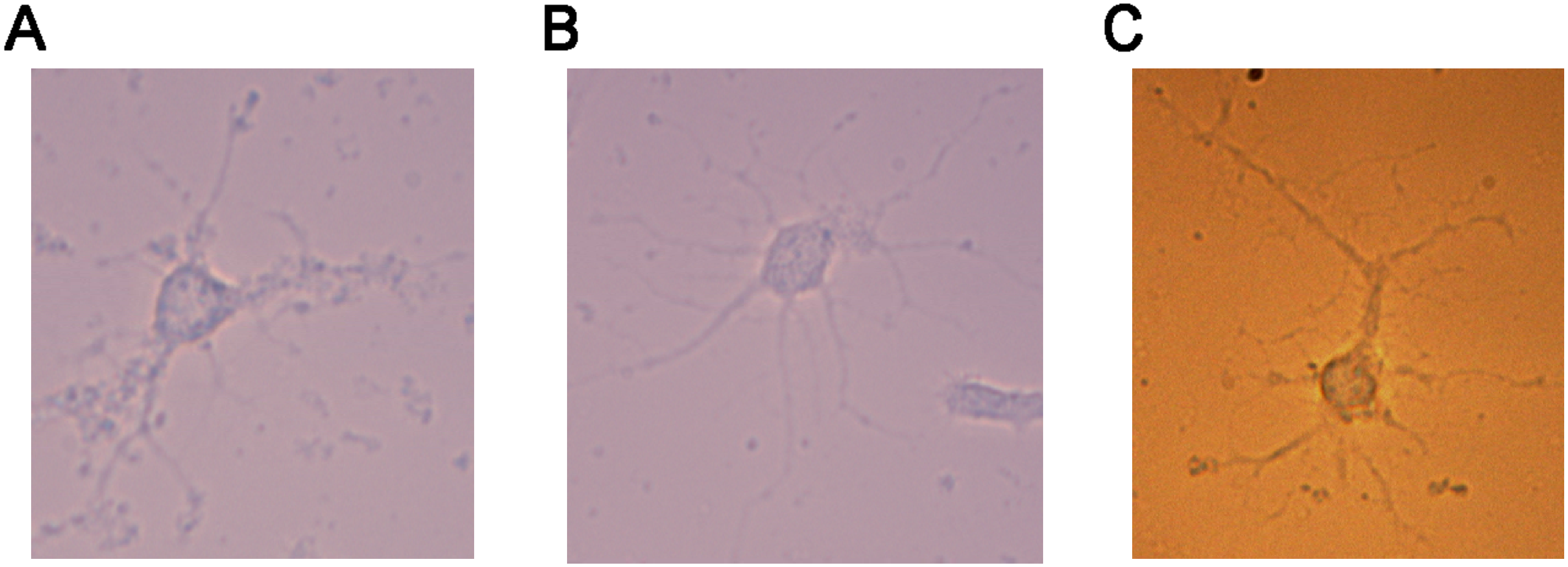

Figure 40. Pictures of B6.Q54 neurons. (A) Picture of a B6.Q54 neuron 70 hrs after dissection. The capacitance of the neuron was 18 pF and the maximum peak inward current was -2.0 nA. **(B)** Picture of a B6.Q54 neuron 71 hrs after dissection. This neuron had a capacitance of 21 pF and a maximum peak inward current of -900 pA. **(C)** Picture of a B6.Q54 neuron 69 hrs post dissection with a capacitance of 39 pF and a maximum peak inward current of -1.2 nA. The representative traces for each of these neurons are shown in Figure 41. The biophysical parameters of these neurons are shown in Figures 42 and 43.

Figure 41. Representative whole-cell traces from B6.Q54 neurons. Representative traces in response to 20 ms voltage steps from a holding potential of -100 mV to between -80 and +60 mV. The red line indicates the step to -10 mV. The scale bars are as shown for each panel. **(A)** Representative trace for neuron in Figure 40A with a peak current of -2.0 nA and a capacitance of 18 pF. **(B)** Representative trace for neuron in Figure 40B that has a capacitance of 21 pF with a peak current of -900 pA. **(C)** Representative trace for neuron in Figure 40C. This neuron had a capacitance of 39 pF and a peak current of -1.2 nA.

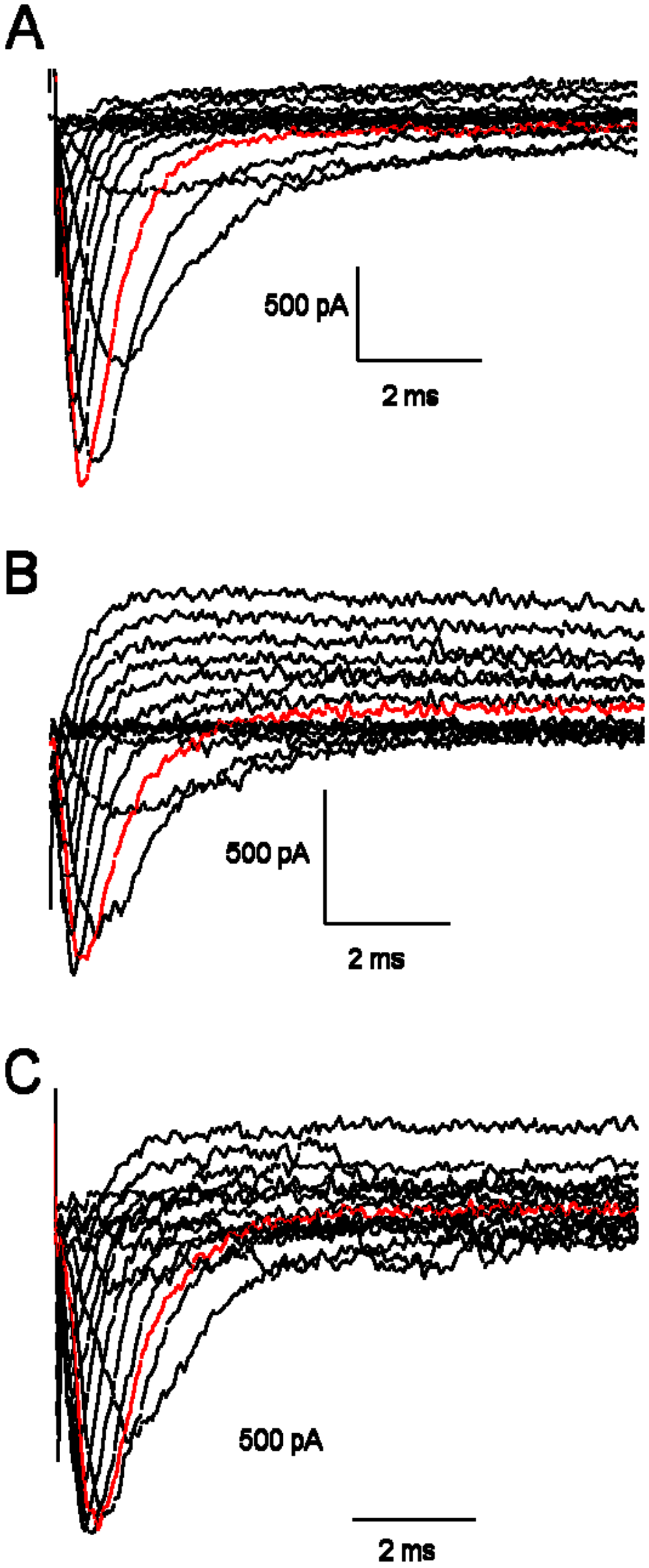
A
500 pA
2 ms
B
500 pA
2 ms
C
500 pA
2 ms

Figure 42. Activation properties of B6.Q54 neurons. (A) Current density-voltage relationship for B6.Q54 neurons (*n* = 4, pictures of neurons and representative traces shown in Figures 39 – 41). **(B)** The normalized conductance-voltage curve shows the voltage dependence of activation for B6.Q54 neurons (*n* = 4 as described above). The fit parameters are shown in Table 17 and the voltage protocol is shown as panel inset.

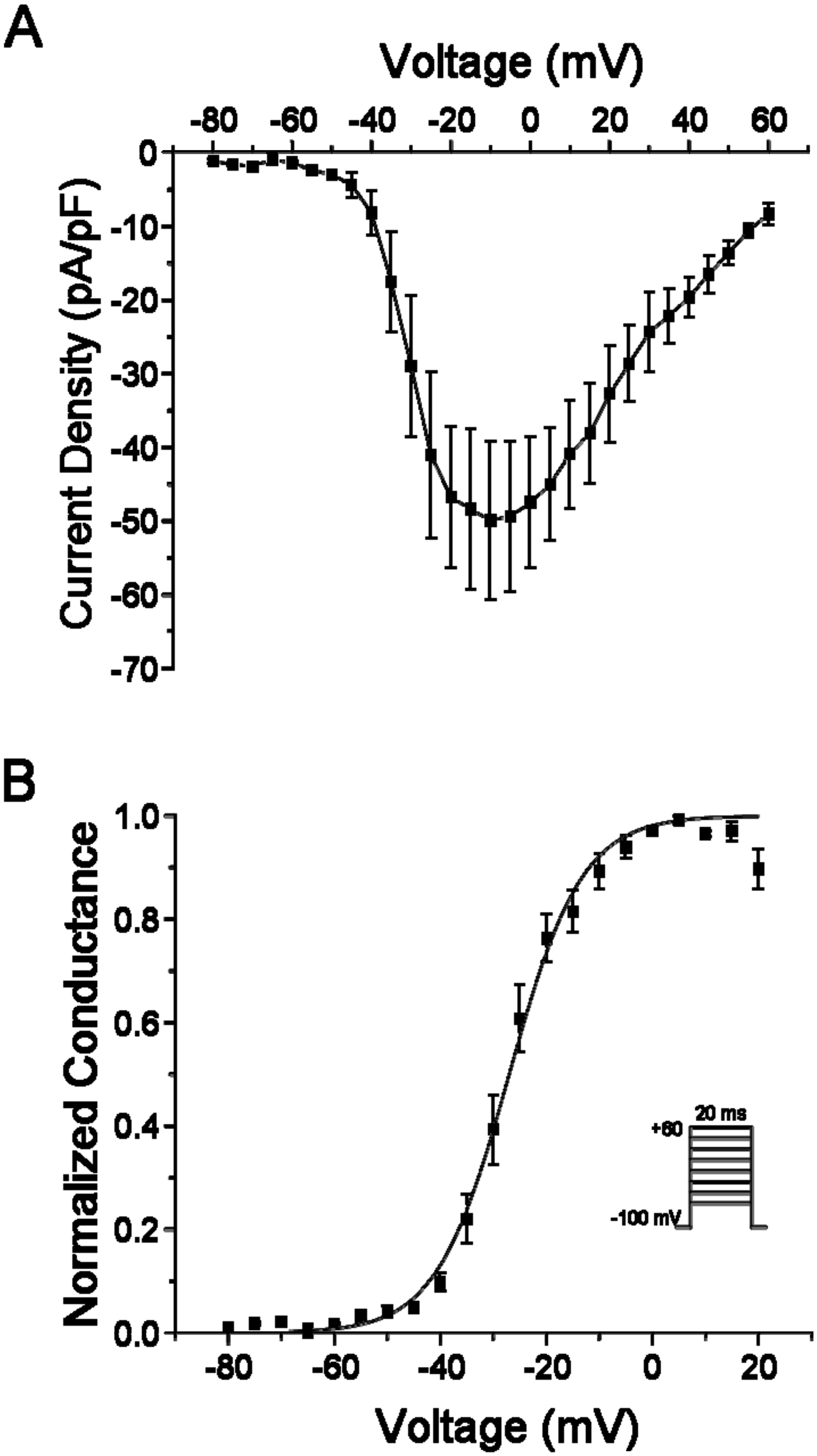
A
Voltage (mV)
-80
-60
-40
-20
0
20
40
60
Current Density (pA/pF)
0
-10
-20
-30
-40
-50
-60
-70
B
Normalized Conductance
1.0
0.8
0.6
0.4
0.2
0.0
20 ms
+60
-100 mV
-80
-60
-40
-20
0
20
Voltage (mV)

Figure 43. Fast inactivation and persistent current of B6.Q54 neurons. (A) Voltage dependence of fast inactivation for B6.Q54 neurons (*n* =4). The fit parameters are shown in Table 17 and the voltage protocol is shown as panel inset. **(B)** Persistent current properties of B6.Q54 neurons (*n* = 2, neurons in Figures 39 and 40A). The TTX sensitive current is shown as a percentage of peak current over the 200 ms pulse duration. The mean persistent current is shown in Table 17.

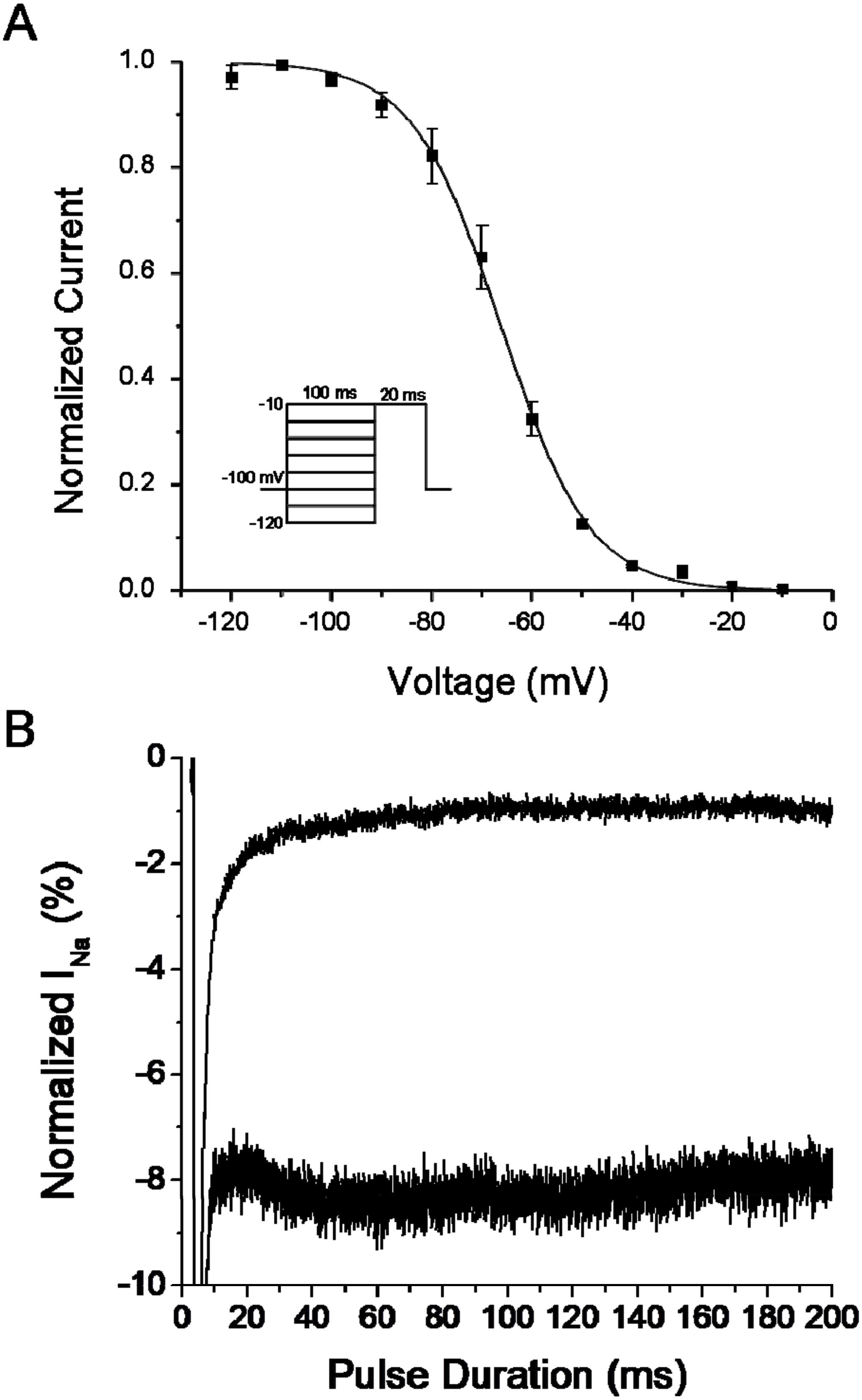
A
1.0
0.8
0.6
0.4
0.2
0.0
Normalized Current
-120
-100
-80
-60
-40
-20
0
Voltage (mV)
100 ms
20 ms
-10
-100 mV
-120
B
0
-2
-4
-6
-8
-10
Normalized I_{Na} (%)
0
20
40
60
80
100
120
140
160
180
200
Pulse Duration (ms)

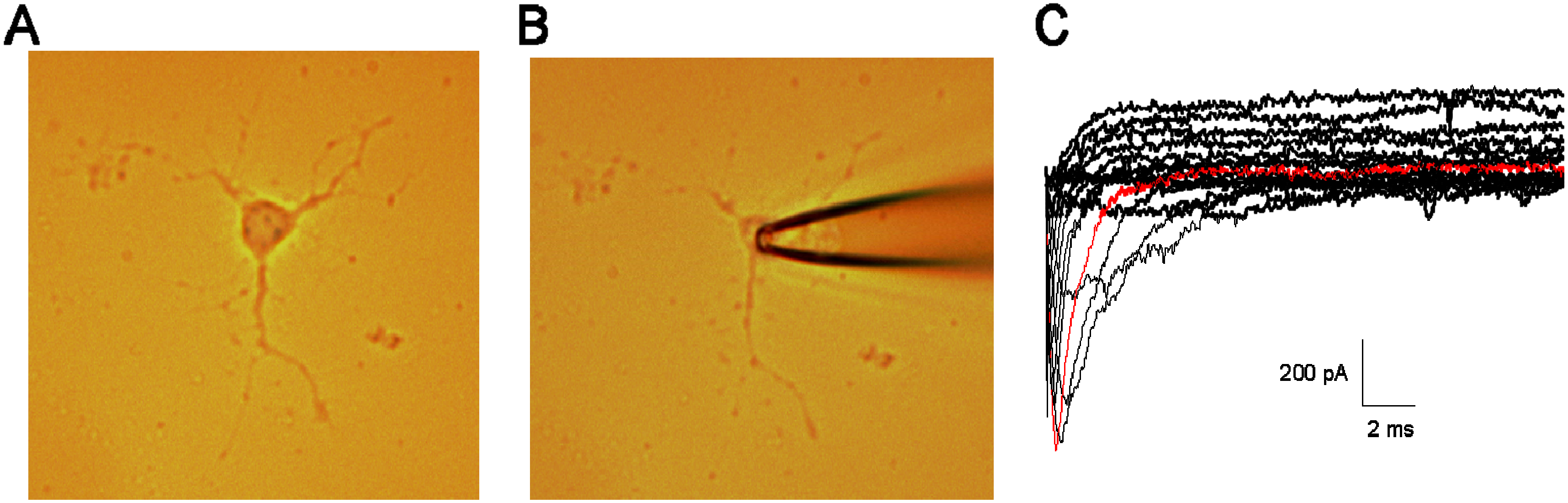

Figure 44. F1.Q54 neuron. (A)) A picture of one F1.Q54 neuron 45 hrs after dissection. **(B)** Picture of the same F1.Q54 neuron with pipette sealed onto neuron. **(C)** Representative trace from this neuron with the red line indicating the step to -10 mV. The capacitance of this neuron was 15 pF and the maximum peak current was -850 pA. The current density-voltage relationship and other biophysical parameters are presented in Figure 45.

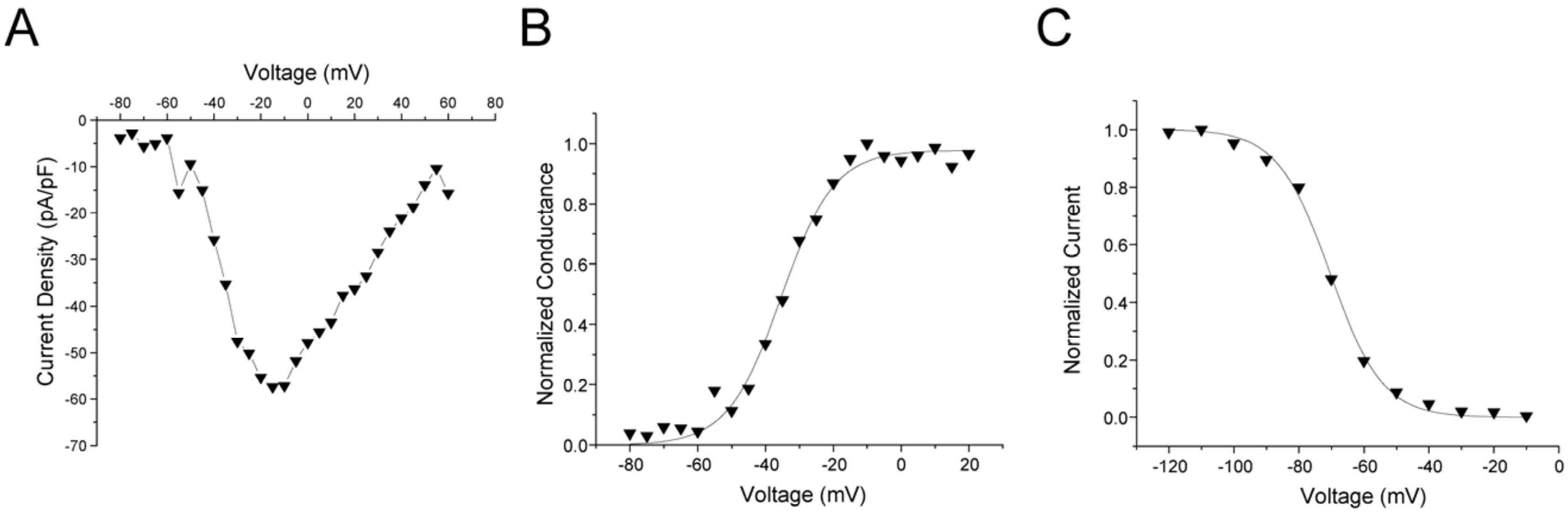

Figure 45. Biophysical parameters for F1.Q54. (A) Current density-voltage relationship for the F1.Q54 neuron depicted in Figure 44. **(B)** Voltage dependence of activation for the neuron in Figure 44. **(C)** Voltage dependence of fast inactivation for F1.Q54 neuron. The fit parameters are shown in Table 17 and the voltage protocols were the same as the inset in Figure 42B and 43A.

Table 17. Biophysical parameters of B6.Q54 and F1.Q54 neurons

	Voltage dependence of activation			Voltage dependence of fast inactivation			Persistent Current	
	$V_{1/2}$ (mV)	*k* (mV)	*n*	$V_{1/2}$ (mV)	*k* (mV)	*n*	*Mean (% of peak)*	*n*
B6.Q54	-26.9 ± 1.7	6.6 ± 0.4	4	-66.4 ± 1.8	8.6 ± 0.8	4	4.4 ± 3.5	2
F1.Q54	-34.9	8.3	1	-70.4	8.1	1		

two strains of mice. We were able to detect the transgene in membrane preparations isolated from B6.Q54 and F1.Q54 (Figure 46B). The transgene was specifically detected because the WT littermate lacked a signal at the same molecular weight (Figure 46B).

Discussion

In this appendix, we described our attempts to record from acutely isolated neurons and study transgene expression levels from two transgenic mouse lines with differing seizure susceptibility. These studies were preliminary and need to be repeated but provided the infrastructure in the laboratory and setup optimal conditions for conducting these and future experiments.

We found that B6.Q54 neurons have a current density-voltage relationship, voltage dependence of activation and fast inactivation similar to those reported in the literature (Figures 42, 43A). The recordings from F1.Q54 also appear similar to those reported in the literature (Figure 45) and to those from B6.Q54 (Figures 42, 43A). Based on the data we have collected, there seems to be a preliminary difference in the voltage-gated sodium currents generated from neurons isolated from Q54 transgenic mice from the two background strains. The voltage dependences of activation and fast inactivation for the F1.Q54 neuron were both hyperpolarized in comparison to B6.Q54. If this holds true with increased replicates, then this may suggest that the modifier is altering the sodium channel directly. Increased persistent current was previously seen in the neurons isolated from Q54 animals of mixed background (Kearney et al., 2001). We examined the neurons isolated from B6.Q54 mice and found increased persistent current with a mean of 4.4% (Figure 43B) instead of the previously observed 2% of peak current (Kearney et al., 2001). Although more experiments need to be performed, the presence of increased persistent current in the mice with less severe seizures suggests

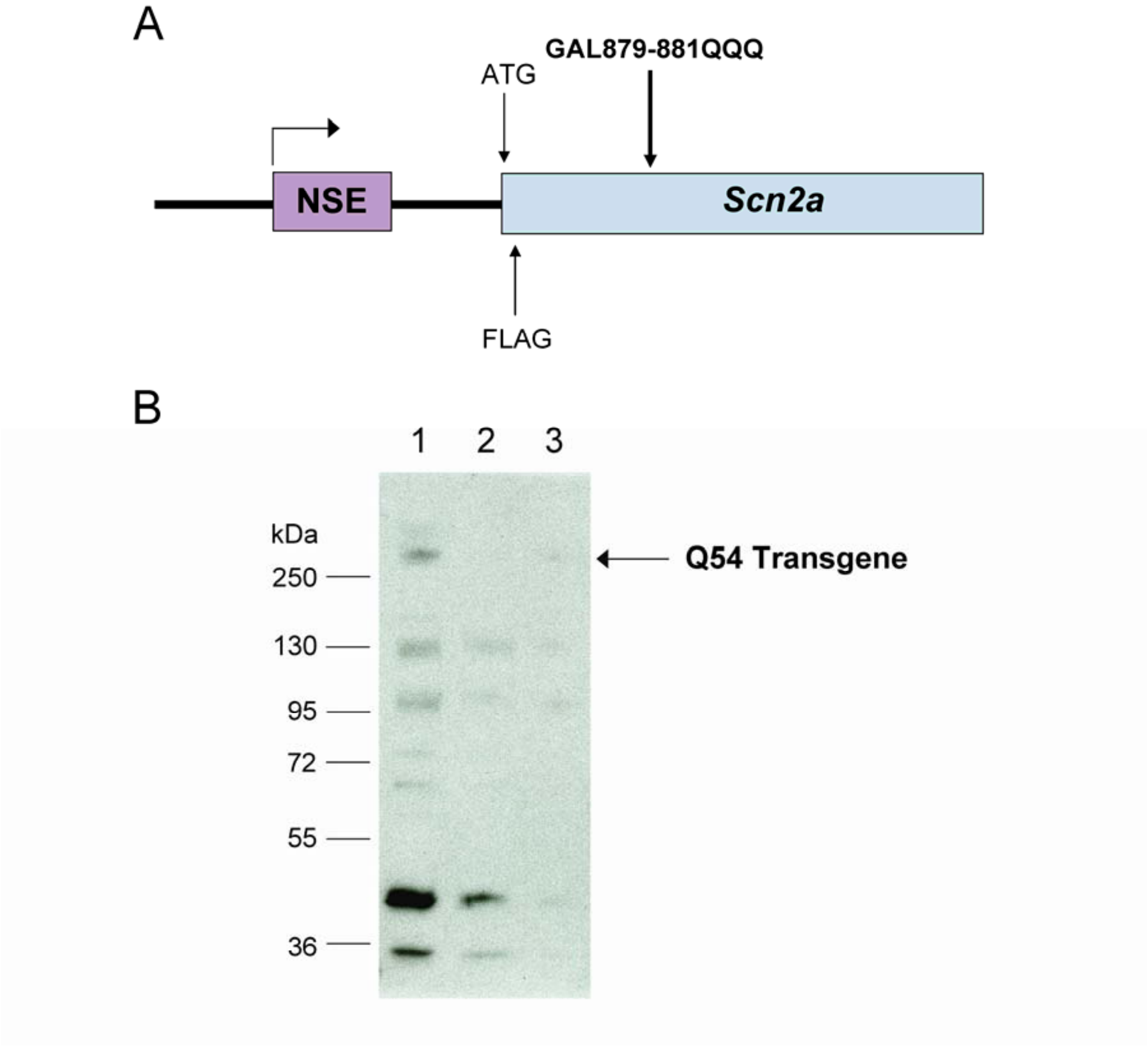

Figure 46. Transgene expression in B6.Q54 and F1.Q54 animals. (A) Schematic diagram showing the structure of the Q54 transgene. Key features include the NSE promoter, start site (ATG) for *Scn2a*, FLAG epitope, and *Scn2a* coding sequence. **(B)** Representative western blot analysis of membrane preparations probed with anti-FLAG antibody to examine transgene levels. Lane 1 was isolated from B6.Q54, lane 2 from a WT littermate control mouse, and lane 3 is isolated from F1.Q54. The arrows indicate transgene detection at ~260 kDa molecular weight.

that the genetic modifiers are not affecting the persistent sodium current caused directly by the mutant sodium channel. After confirmation of elevated persistent current and a more thorough examination of voltage dependent properties in neurons isolated from F1.Q54 mice, voltage clamp recordings isolating potassium current or current clamp recordings would aid in determining how the genetic modifiers are altering neuronal excitability.

We performed western blot analysis to determine if the mutant *Scn2a* transgene was expressed at different levels in the two background strains. The western blot analysis of the membrane preparations from the whole brain of B6.Q54 and F1.Q54 revealed no differences in the transgene expression (Figure 46B). Our detection may not be sensitive enough to pick up differences in the protein expression at this point, but perhaps more optimization could reveal differences. The protein samples were loaded based on concentration estimates from performing the BCA assay. The samples are probably not equally loaded as seen by nonspecific bands at lower molecular weights (Figure 46B). Future experiments need to load more equivalent amounts of each protein sample. We would also be interested to examine the transgene to endogenous $Na_V1.2$ expression ratio and see if the ratio differs between the two background strains. The data from these two experiments are another way to determine if the genetic modifiers directly modulate the sodium channel transgene.

Ultimately animal models will help investigate defects in neuronal excitability in ways that other model systems cannot address. For example, animal models allow us to test physiological questions that cannot be assessed through *in vitro* studies. Though the findings presented in this chapter are preliminary results, they demonstrate avenues for further investigation with regards to genetic modifiers that may contribute to better understanding phenotypic variability in genetic forms of epilepsy. Animal models, including the Q54 animals used in above experiments, can be useful tools for testing new therapeutic agents as treatment options for specific forms of epilepsy.

REFERENCES

(1989) Proposal for revised classification of epilepsies and epileptic syndromes. Commission on Classification and Terminology of the International League Against Epilepsy. Epilepsia 30:389-399.

Abou-Khalil B, Ge Q, Desai R, Ryther R, Bazyk A, Bailey R, Haines JL, Sutcliffe JS, George AL, Jr. (2001) Partial and generalized epilepsy with febrile seizures plus and a novel *SCN1A* mutation. Neurology 57:2265-2272.

Ahmed CM, Ware DH, Lee SC, Patten CD, Ferrer-Montiel AV, Schinder AF, McPherson JD, Wagner-McPherson CB, Wasmuth JJ, Evans GA, Montal M (1992) Primary structure, chromosomal localization, and functional expression of a voltage-gated sodium channel from human brain. Proc Natl Acad Sci U S A 89:8220-8224.

Alekov A, Rahman MM, Mitrovic N, Lehmann-Horn F, Lerche H (2000) A sodium channel mutation causing epilepsy in man exhibits subtle defects in fast inactivation and activation in vitro. J Physiol 529 Pt 3:533-539.

Audenaert D, Claes L, Ceulemans B, Lofgren A, Van BC, De JP (2003) A deletion in *SCN1B* is associated with febrile seizures and early-onset absence epilepsy. Neurology 61:854-856.

Baranauskas G, Martina M (2006) Sodium currents activate without a Hodgkin-and-Huxley-type delay in central mammalian neurons. J Neurosci 26:671-684.

Barela AJ, Waddy SP, Lickfett JG, Hunter J, Anido A, Helmers SL, Goldin AL, Escayg A (2006) An epilepsy mutation in the sodium channel *SCN1A* that decreases channel excitability. J Neurosci 26:2714-2723.

Baulac S, Gourfinkel-An I, Nabbout R, Huberfeld G, Serratosa J, LeGuern E, Baulac M (2004) Fever, genes, and epilepsy. Lancet Neurol 3:421-430.

Baulac S, Gourfinkel-An I, Picard F, Rosenberg-Bourgin M, Prud'homme JF, Baulac M, Brice A, LeGuern E (1999) A second locus for familial generalized epilepsy with febrile seizures plus maps to chromosome 2q21-q33. Am J Hum Genet 65:1078-1085.

Baulac S, Huberfeld G, Gourfinkel-An I, Mitropoulou G, Beranger A, Prud'homme JF, Baulac M, Brice A, Bruzzone R, LeGuern E (2001a) First genetic evidence of $GABA_A$ receptor dysfunction in epilepsy: a mutation in the gamma2-subunit gene. Nat Genet 28:46-48.

Baulac S, Picard F, Herman A, Feingold J, Genin E, Hirsch E, Prud'homme JF, Baulac M, Brice A, LeGuern E (2001b) Evidence for digenic inheritance in a family with both febrile convulsions and temporal lobe epilepsy implicating chromosomes 18qter and 1q25-q31. Ann Neurol 49:786-792.

Beaussart M, Loiseau P (1969) Hereditary factors in a random population of 5200 epileptics. Epilepsia 10:55-63.

Bennett ES (2002) Isoform-specific effects of sialic acid on voltage-dependent Na^+ channel gating: functional sialic acids are localized to the S5-S6 loop of domain I. J Physiol 538:675-690.

Benson DW, Wang DW, Dyment M, Knilans TK, Fish FA, Strieper MJ, Rhodes TH, George AL, Jr. (2003) Congenital sick sinus syndrome caused by recessive mutations in the cardiac sodium channel gene (*SCN5A*). J Clin Invest 112:1019-1028.

Bergren SK, Chen S, Galecki A, Kearney JA (2005) Genetic modifiers affecting severity of epilepsy caused by mutation of sodium channel *Scn2a*. Mamm Genome 16:683-690.

Berkovic SF, Heron SE, Giordano L, Marini C, Guerrini R, Kaplan RE, Gambardella A, Steinlein OK, Grinton BE, Dean JT, Bordo L, Hodgson BL, Yamamoto T, Mulley JC, Zara F, Scheffer IE (2004) Benign familial neonatal-infantile seizures: characterization of a new sodium channelopathy. Ann Neurol 55:550-557.

Berkovic SF, Howell RA, Hay DA, Hopper JL (1998) Epilepsies in twins: genetics of the major epilepsy syndromes. Ann Neurol 43:435-445.

Berkovic SF, Mulley JC, Scheffer IE, Petrou S (2006) Human epilepsies: interaction of genetic and acquired factors. Trends Neurosci 29:391-397.

Berkovic SF, Scheffer IE (1997) Genetics of human partial epilepsy. Curr Opin Neurol 10:110-114.

Bertram E (2007) The relevance of kindling for human epilepsy. Epilepsia 48 Suppl 2:65-74.

Bezzina C, Veldkamp MW, van Den Berg MP, Postma AV, Rook MB, Viersma JW, van L, I, Tan-Sindhunata G, Bink-Boelkens MT, van Der Hout AH, Mannens MM, Wilde AA (1999) A single Na^+ channel mutation causing both long-QT and Brugada syndromes. Circ Res 85:1206-1213.

Bianchi A, Viaggi S, Chiossi E (2003) Family study of epilepsy in first degree relatives: data from the Italian Episcreen Study. Seizure 12:203-210.

Boiko T, Van WA, Caldwell JH, Levinson SR, Trimmer JS, Matthews G (2003) Functional specialization of the axon initial segment by isoform-specific sodium channel targeting. J Neurosci 23:2306-2313.

Bulman DE, Scoggan KA, van O, Nicolle MW, Hahn AF, Tollar LL, Ebers GC (1999) A novel sodium channel mutation in a family with hypokalemic periodic paralysis. Neurology 53:1932-1936.

Carras PL, Coleman PA, Miller RF (1992) Site of action potential initiation in amphibian retinal ganglion cells. J Neurophysiol 67:292-304.

Carvelli L, Moron JA, Kahlig KM, Ferrer JV, Sen N, Lechleiter JD, Leeb-Lundberg LM, Merrill G, Lafer EM, Ballou LM, Shippenberg TS, Javitch JA, Lin RZ, Galli A (2002) PI 3-kinase regulation of dopamine uptake. J Neurochem 81:859-869.

Catterall WA (1999) Molecular properties of brain sodium channels: an important target for anticonvulsant drugs. Adv Neurol 79:441-456.

Catterall WA (2000) From ionic currents to molecular mechanisms: the structure and function of voltage-gated sodium channels. Neuron 26:13-25.

Catterall WA, Goldin AL, Waxman SG (2005) International Union of Pharmacology. XLVII. Nomenclature and structure-function relationships of voltage-gated sodium channels. Pharmacol Rev 57:397-409.

Cha A, Ruben PC, George AL, Jr., Fujimoto E, Bezanilla F (1999) Voltage sensors in domains III and IV, but not I and II, are immobilized by Na^+ channel fast inactivation. Neuron 22:73-87.

Chahine M, George AL, Jr., Zhou M, Ji S, Sun W, Barchi RL, Horn R (1994) Sodium channel mutations in paramyotonia congenita uncouple inactivation from activation. Neuron 12:281-294.

Charlier C, Singh NA, Ryan SG, Lewis TB, Reus BE, Leach RJ, Leppert M (1998) A pore mutation in a novel KQT-like potassium channel gene in an idiopathic epilepsy family. Nat Genet 18:53-55.

Chen C, Bharucha V, Chen Y, Westenbroek RE, Brown A, Malhotra JD, Jones D, Avery C, Gillespie PJ, III, Kazen-Gillespie KA, Kazarinova-Noyes K, Shrager P, Saunders TL, Macdonald RL, Ransom BR, Scheuer T, Catterall WA, Isom LL (2002) Reduced sodium channel density, altered voltage dependence of inactivation, and increased susceptibility to seizures in mice lacking sodium channel β2-subunits. Proc Natl Acad Sci U S A 99:17072-17077.

Chen C, Dickendesher TL, Oyama F, Miyazaki H, Nukina N, Isom LL (2007) Floxed allele for conditional inactivation of the voltage-gated sodium channel β1 subunit *Scn1b*. Genesis 45:547-553.

Chen C, Westenbroek RE, Xu X, Edwards CA, Sorenson DR, Chen Y, McEwen DP, O'Malley HA, Bharucha V, Meadows LS, Knudsen GA, Vilaythong A, Noebels JL, Saunders TL, Scheuer T, Shrager P, Catterall WA, Isom LL (2004) Mice lacking sodium channel β1 subunits display defects in neuronal excitability, sodium channel expression, and nodal architecture. J Neurosci 24:4030-4042.

Chen Y, Lu J, Pan H, Zhang Y, Wu H, Xu K, Liu X, Jiang Y, Bao X, Yao Z, Ding K, Lo WH, Qiang B, Chan P, Shen Y, Wu X (2003) Association between genetic variation of *CACNA1H* and childhood absence epilepsy. Ann Neurol 54:239-243.

Chioza B, Wilkie H, Nashef L, Blower J, McCormick D, Sham P, Asherson P, Makoff AJ (2001) Association between the α_{1a} calcium channel gene *CACNA1A* and idiopathic generalized epilepsy. Neurology 56:1245-1246.

Claes L, Del-Favero J, Ceulemans B, Lagae L, Van BC, De JP (2001) De novo mutations in the sodium-channel gene *SCN1A* cause severe myoclonic epilepsy of infancy. Am J Hum Genet 68:1327-1332.

Clancy CE, Kass RS (2003) Pharmacogenomics in the treatment of epilepsy. Pharmacogenomics 4:747-751.

Clancy CE, Kass RS (2004) Theoretical investigation of the neuronal Na^+ channel *SCN1A*: abnormal gating and epilepsy. Biophys J 86:2606-2614.

Clancy CE, Rudy Y (1999) Linking a genetic defect to its cellular phenotype in a cardiac arrhythmia. Nature 400:566-569.

Clancy CE, Rudy Y (2002) Na^+ channel mutation that causes both Brugada and long-QT syndrome phenotypes: a simulation study of mechanism. Circulation 105:1208-1213.

Colosimo E, Gambardella A, Mantegazza M, Labate A, Rusconi R, Schiavon E, Annesi F, Cassulini RR, Carrideo S, Chifari R, Canevini MP, Canger R, Franceschetti S, Annesi G, Wanke E, Quattrone A (2007) Electroclinical Features of a Family with Simple Febrile Seizures and Temporal Lobe Epilepsy Associated with *SCN1A* Loss-of-Function Mutation. Epilepsia.

Colquhoun D, Dowsland KA, Beato M, Plested AJ (2004) How to impose microscopic reversibility in complex reaction mechanisms. Biophys J 86:3510-3518.

Cormier JW, Rivolta I, Tateyama M, Yang AS, Kass RS (2002) Secondary structure of the human cardiac Na^+ channel C terminus: evidence for a role of helical structures in modulation of channel inactivation. J Biol Chem 277:9233-9241.

Cossette P, Liu L, Brisebois K, Dong H, Lortie A, Vanasse M, Saint-Hilaire JM, Carmant L, Verner A, Lu WY, Wang YT, Rouleau GA (2002) Mutation of *GABRA1* in an autosomal dominant form of juvenile myoclonic epilepsy. Nat Genet 31:184-189.

Cox JJ, Reimann F, Nicholas AK, Thornton G, Roberts E, Springell K, Karbani G, Jafri H, Mannan J, Raashid Y, Al-Gazali L, Hamamy H, Valente EM, Gorman S, Williams R, McHale DP, Wood JN, Gribble FM, Woods CG (2006) An *SCN9A* channelopathy causes congenital inability to experience pain. Nature 444:894-898.

Cummins TR, Aglieco F, Renganathan M, Herzog RI, Dib-Hajj SD, Waxman SG (2001) $Na_V1.3$ sodium channels: rapid repriming and slow closed-state inactivation display quantitative differences after expression in a mammalian cell line and in spinal sensory neurons. J Neurosci 21:5952-5961.

Daws LC, Callaghan PD, Moron JA, Kahlig KM, Shippenberg TS, Javitch JA, Galli A (2002) Cocaine increases dopamine uptake and cell surface expression of dopamine transporters. Biochem Biophys Res Commun 290:1545-1550.

De FM, Becchetti A, Patrignani A, Annesi G, Gambardella A, Quattrone A, Ballabio A, Wanke E, Casari G (2000) The nicotinic receptor $\beta 2$ subunit is mutant in nocturnal frontal lobe epilepsy. Nat Genet 26:275-276.

Dibbens LM, Feng HJ, Richards MC, Harkin LA, Hodgson BL, Scott D, Jenkins M, Petrou S, Sutherland GR, Scheffer IE, Berkovic SF, Macdonald RL, Mulley JC (2004) *GABRD* encoding a protein for extra- or peri-synaptic $GABA_A$ receptors is a susceptibility locus for generalized epilepsies. Hum Mol Genet 13:1315-1319.

Dichgans M, Freilinger T, Eckstein G, Babini E, Lorenz-Depiereux B, Biskup S, Ferrari MD, Herzog J, Van den Maagdenberg AM, Pusch M, Strom TM (2005) Mutation in the neuronal voltage-gated sodium channel *SCN1A* in familial hemiplegic migraine. Lancet 366:371-377.

Ebers GC, George AL, Barchi RL, Ting-Passador SS, Kallen RG, Lathrop GM, Beckmann JS, Hahn AF, Brown WF, Campbell RD, . (1991) Paramyotonia congenita and hyperkalemic periodic paralysis are linked to the adult muscle sodium channel gene. Ann Neurol 30:810-816.

Escayg A, De WM, Lee DD, Bichet D, Wolf P, Mayer T, Johnston J, Baloh R, Sander T, Meisler MH (2000a) Coding and noncoding variation of the human calcium-channel β4-subunit gene *CACNB4* in patients with idiopathic generalized epilepsy and episodic ataxia. Am J Hum Genet 66:1531-1539.

Escayg A, MacDonald BT, Meisler MH, Baulac S, Huberfeld G, An-Gourfinkel I, Brice A, LeGuern E, Moulard B, Chaigne D, Buresi C, Malafosse A (2000b) Mutations of *SCN1A*, encoding a neuronal sodium channel, in two families with GEFS+2. Nat Genet 24:343-345.

Featherstone DE, Richmond JE, Ruben PC (1996) Interaction between fast and slow inactivation in Skm1 sodium channels. Biophys J 71:3098-3109.

Finkelstein A, Peskin CS (1984) Some unexpected consequences of a simple physical mechanism for voltage-dependent gating in biological membranes. Biophys J 46:549-558.

Fong GC, Shah PU, Gee MN, Serratosa JM, Castroviejo IP, Khan S, Ravat SH, Mani J, Huang Y, Zhao HZ, Medina MT, Treiman LJ, Pineda G, gado-Escueta AV (1998) Childhood absence epilepsy with tonic-clonic seizures and electroencephalogram 3-4-Hz spike and multispike-slow wave complexes: linkage to chromosome 8q24. Am J Hum Genet 63:1117-1129.

Frankel WN (1999) Detecting genes in new and old mouse models for epilepsy: a prospectus through the magnifying glass. Epilepsy Res 36:97-110.

French JA, Williamson PD, Thadani VM, Darcey TM, Mattson RH, Spencer SS, Spencer DD (1993) Characteristics of medial temporal lobe epilepsy: I. Results of history and physical examination. Ann Neurol 34:774-780.

Fujiwara T, Sugawara T, Mazaki-Miyazaki E, Takahashi Y, Fukushima K, Watanabe M, Hara K, Morikawa T, Yagi K, Yamakawa K, Inoue Y (2003) Mutations of sodium channel alpha subunit type 1 (*SCN1A*) in intractable childhood epilepsies with frequent generalized tonic-clonic seizures. Brain 126:531-546.

Fukuma G, Oguni H, Shirasaka Y, Watanabe K, Miyajima T, Yasumoto S, Ohfu M, Inoue T, Watanachai A, Kira R, Matsuo M, Muranaka H, Sofue F, Zhang B, Kaneko S, Mitsudome A, Hirose S (2004) Mutations of neuronal voltage-gated Na^+ channel α1 subunit gene *SCN1A* in core severe myoclonic epilepsy in infancy (SMEI) and in borderline SMEI (SMEB). Epilepsia 45:140-148.

Gallagher MJ, Ding L, Maheshwari A, Macdonald RL (2007) The GABA$_A$ receptor α1 subunit epilepsy mutation A322D inhibits transmembrane helix formation and causes proteasomal degradation. Proc Natl Acad Sci U S A 104:12999-13004.

Gargus JJ, Tournay A (2007) Novel mutation confirms seizure locus *SCN1A* is also familial hemiplegic migraine locus FHM3. Pediatr Neurol 37:407-410.

Garrido JJ, Fernandes F, Moussif A, Fache MP, Giraud P, Dargent B (2003a) Dynamic compartmentalization of the voltage-gated sodium channels in axons. Biol Cell 95:437-445.

Garrido JJ, Giraud P, Carlier E, Fernandes F, Moussif A, Fache MP, Debanne D, Dargent B (2003b) A targeting motif involved in sodium channel clustering at the axonal initial segment. Science 300:2091-2094.

Gautron S, Dos SG, Pinto-Henrique D, Koulakoff A, Gros F, Berwald-Netter Y (1992) The glial voltage-gated sodium channel: cell- and tissue-specific mRNA expression. Proc Natl Acad Sci U S A 89:7272-7276.

George AL, Jr. (2004) Molecular basis of inherited epilepsy. Arch Neurol 61:473-478.

George AL, Jr. (2005) Inherited disorders of voltage-gated sodium channels. J Clin Invest 115:1990-1999.

George AL, Jr., Knittle TJ, Tamkun MM (1992) Molecular cloning of an atypical voltage-gated sodium channel expressed in human heart and uterus: evidence for a distinct gene family. Proc Natl Acad Sci U S A 89:4893-4897.

Glaaser IW, Bankston JR, Liu H, Tateyama M, Kass RS (2006) A carboxyl-terminal hydrophobic interface is critical to sodium channel function. Relevance to inherited disorders. J Biol Chem 281:24015-24023.

Gong B, Rhodes KJ, Bekele-Arcuri Z, Trimmer JS (1999) Type I and type II Na$^+$ channel α-subunit polypeptides exhibit distinct spatial and temporal patterning, and association with auxiliary subunits in rat brain. J Comp Neurol 412:342-352.

Gurnett CA, Hedera P (2007) New ideas in epilepsy genetics: novel epilepsy genes, copy number alterations, and gene regulation. Arch Neurol 64:324-328.

Hale SL, Shryock JC, Belardinelli L, Sweeney M, Kloner RA (2008) Late sodium current inhibition as a new cardioprotective approach. J Mol Cell Cardiol 44:954-967.

Hamati-Haddad A, Abou-Khalil B (1998) Epilepsy diagnosis and localization in patients with antecedent childhood febrile convulsions. Neurology 50:917-922.

Hanlon MR, Wallace BA (2002) Structure and function of voltage-dependent ion channel regulatory β subunits. Biochemistry 41:2886-2894.

Harkin LA, et al. (2007) The spectrum of *SCN1A*-related infantile epileptic encephalopathies. Brain 130:843-852.

Hartshorne RP, Catterall WA (1984) The sodium channel from rat brain. Purification and subunit composition. J Biol Chem 259:1667-1675.

Haug K, et al. (2003) Mutations in *CLCN2* encoding a voltage-gated chloride channel are associated with idiopathic generalized epilepsies. Nat Genet 33:527-532.

Helbig I, Scheffer IE, Mulley JC, Berkovic SF (2008) Navigating the channels and beyond: unravelling the genetics of the epilepsies. Lancet Neurol 7:231-245.

Herlenius E, Heron SE, Grinton BE, Keay D, Scheffer IE, Mulley JC, Berkovic SF (2007) *SCN2A* Mutations and Benign Familial Neonatal-Infantile Seizures: The Phenotypic Spectrum. Epilepsia 48:1138-1142.

Heron SE, Crossland KM, Andermann E, Phillips HA, Hall AJ, Bleasel A, Shevell M, Mercho S, Seni MH, Guiot MC, Mulley JC, Berkovic SF, Scheffer IE (2002) Sodium-channel defects in benign familial neonatal-infantile seizures. Lancet 360:851-852.

Herzog RI, Cummins TR, Waxman SG (2001) Persistent TTX-resistant Na^+ current affects resting potential and response to depolarization in simulated spinal sensory neurons. J Neurophysiol 86:1351-1364.

Hille B (2001) Ion channels of excitable membranes. Sunderland, MA Sinauer.

Hines ML, Carnevale NT (2001) NEURON: a tool for neuroscientists. Neuroscientist 7:123-135.

Hirose S (2006) A new paradigm of channelopathy in epilepsy syndromes: intracellular trafficking abnormality of channel molecules. Epilepsy Res 70 Suppl 1:S206-S217.

Hodgkin AL, Huxley AF (1952a) A quantitative description of membrane current and its application to conduction and excitation in nerve. J Physiol 117:500-544.

Hodgkin AL, Huxley AF (1952b) Currents carried by sodium and potassium ions through the membrane of the giant axon of Loligo. J Physiol 116:449-472.

Hodgkin AL, Huxley AF (1952c) The components of membrane conductance in the giant axon of Loligo. J Physiol 116:473-496.

Hodgkin AL, Huxley AF (1952d) The dual effect of membrane potential on sodium conductance in the giant axon of Loligo. J Physiol 116:497-506.

Holland KD, Kearney JA, Glauser TA, Buck G, Keddache M, Blankston JR, Glaaser IW, Kass RS, Meisler MH (2008) Mutation of sodium channel *SCN3A* in a patient with cryptogenic pediatric partial epilepsy. Neurosci Lett 433:65-70.

Horn R, Vandenberg CA (1984) Statistical properties of single sodium channels. J Gen Physiol 84:505-534.

Irvine LA, Jafri MS, Winslow RL (1999) Cardiac sodium channel Markov model with temperature dependence and recovery from inactivation. Biophys J 76:1868-1885.

Isom LL, De Jongh KS, Catterall WA (1994) Auxiliary subunits of voltage-gated ion channels. Neuron 12:1183-1194.

Isom LL, De Jongh KS, Patton DE, Reber BF, Offord J, Charbonneau H, Walsh K, Goldin AL, Catterall WA (1992) Primary structure and functional expression of the β1 subunit of the rat brain sodium channel. Science 256:839-842.

Isom LL, Ragsdale DS, De Jongh KS, Westenbroek RE, Reber BF, Scheuer T, Catterall WA (1995) Structure and function of the β2 subunit of brain sodium channels, a transmembrane glycoprotein with a CAM motif. Cell 83:433-442.

Ji S, George AL, Jr., Horn R, Barchi RL (1996) Paramyotonia congenita mutations reveal different roles for segments S3 and S4 of domain D4 in hSkM1 sodium channel gating. J Gen Physiol 107:183-194.

Kahlig KM, Javitch JA, Galli A (2004) Amphetamine regulation of dopamine transport. Combined measurements of transporter currents and transporter imaging support the endocytosis of an active carrier. J Biol Chem 279:8966-8975.

Kahlig KM, Lute BJ, Wei Y, Loland CJ, Gether U, Javitch JA, Galli A (2006a) Regulation of dopamine transporter trafficking by intracellular amphetamine. Mol Pharmacol 70:542-548.

Kahlig KM, Misra SN, George AL, Jr. (2006b) Impaired inactivation gate stabilization predicts increased persistent current for an epilepsy-associated *SCN1A* mutation. J Neurosci 26:10958-10966.

Kalachikov S, Evgrafov O, Ross B, Winawer M, Barker-Cummings C, Martinelli BF, Choi C, Morozov P, Das K, Teplitskaya E, Yu A, Cayanis E, Penchaszadeh G, Kottmann AH, Pedley TA, Hauser WA, Ottman R, Gilliam TC (2002) Mutations in *LGI1* cause autosomal-dominant partial epilepsy with auditory features. Nat Genet 30:335-341.

Kamiya K, Kaneda M, Sugawara T, Mazaki E, Okamura N, Montal M, Makita N, Tanaka M, Fukushima K, Fujiwara T, Inoue Y, Yamakawa K (2004) A nonsense mutation of the sodium channel gene *SCN2A* in a patient with intractable epilepsy and mental decline. J Neurosci 24:2690-2698.

Kananura C, Haug K, Sander T, Runge U, Gu W, Hallmann K, Rebstock J, Heils A, Steinlein OK (2002) A splice-site mutation in *GABRG2* associated with childhood absence epilepsy and febrile convulsions. Arch Neurol 59:1137-1141.

Kaplan MR, Cho MH, Ullian EM, Isom LL, Levinson SR, Barres BA (2001) Differential control of clustering of the sodium channels $Na_V1.2$ and $Na_V1.6$ at developing CNS nodes of Ranvier. Neuron 30:105-119.

Kaplan RE, Lacey DJ (1983) Benign familial neonatal-infantile seizures. Am J Med Genet 16:595-599.

Kasai N, Fukushima K, Ueki Y, Prasad S, Nosakowski J, Sugata K, Sugata A, Nishizaki K, Meyer NC, Smith RJ (2001) Genomic structures of *SCN2A* and *SCN3A* - candidate genes for deafness at the DFNA16 locus. Gene 264:113-122.

Kazen-Gillespie KA, Ragsdale DS, D'Andrea MR, Mattei LN, Rogers KE, Isom LL (2000) Cloning, localization, and functional expression of sodium channel β1A subunits. J Biol Chem 275:1079-1088.

Kearney JA, Plummer NW, Smith MR, Kapur J, Cummins TR, Waxman SG, Goldin AL, Meisler MH (2001) A gain-of-function mutation in the sodium channel gene *Scn2a* results in seizures and behavioral abnormalities. Neuroscience 102:307-317.

Kjeldsen MJ, Corey LA, Christensen K, Friis ML (2003) Epileptic seizures and syndromes in twins: the importance of genetic factors. Epilepsy Res 55:137-146.

Klugbauer N, Lacinova L, Flockerzi V, Hofmann F (1995) Structure and functional expression of a new member of the tetrodotoxin-sensitive voltage-activated sodium channel family from human neuroendocrine cells. EMBO J 14:1084-1090.

Kuhn FJ, Greeff NG (1999) Movement of voltage sensor S4 in domain 4 is tightly coupled to sodium channel fast inactivation and gating charge immobilization. J Gen Physiol 114:167-183.

Kuo JJ, Lee RH, Zhang L, Heckman CJ (2006) Essential role of the persistent sodium current in spike initiation during slowly rising inputs in mouse spinal neurones. J Physiol 574:819-834.

Lauger P (1995) Conformational transitions of ion channels. In: Single-channel recording (Sakmann B, Neher E, eds). pp 651-662. New York: Plenum.

Lennox WG (1951) The heredity of epilepsy as told by relatives and twins. J Am Med Assoc 146:529-536.

Liu K, Yang T, Viswanathan PC, Roden DM (2005) New mechanism contributing to drug-induced arrhythmia: rescue of a misprocessed LQT3 mutant. Circulation 112:3239-3246.

Long SB, Campbell EB, Mackinnon R (2005) Voltage sensor of K_V1.2: structural basis of electromechanical coupling. Science 309:903-908.

Lossin C, Rhodes TH, Desai RR, Vanoye CG, Wang D, Carniciu S, Devinsky O, George AL, Jr. (2003) Epilepsy-associated dysfunction in the voltage-gated neuronal sodium channel *SCN1A*. J Neurosci 23:11289-11295.

Lossin C, Wang DW, Rhodes TH, Vanoye CG, George AL, Jr. (2002) Molecular basis of an inherited epilepsy. Neuron 34:877-884.

Macdonald RL, Gallagher MJ, Feng HJ, Kang J (2004) $GABA_A$ receptor epilepsy mutations. Biochem Pharmacol 68:1497-1506.

Macdonald RL, Greenfield LJ, Jr. (1997) Mechanisms of action of new antiepileptic drugs. Curr Opin Neurol 10:121-128.

Maher J, McLachlan RS (1995) Febrile convulsions. Is seizure duration the most important predictor of temporal lobe epilepsy? Brain 118 (Pt 6):1521-1528.

Makita N, Shirai N, Wang DW, Sasaki K, George AL, Jr., Kanno M, Kitabatake A (2000) Cardiac Na^+ channel dysfunction in Brugada syndrome is aggravated by β_1-subunit. Circulation 101:54-60.

Malhotra JD, Kazen-Gillespie K, Hortsch M, Isom LL (2000) Sodium channel β subunits mediate homophilic cell adhesion and recruit ankyrin to points of cell-cell contact. J Biol Chem 275:11383-11388.

Maljevic S, Krampfl K, Cobilanschi J, Tilgen N, Beyer S, Weber YG, Schlesinger F, Ursu D, Melzer W, Cossette P, Bufler J, Lerche H, Heils A (2006) A mutation in the $GABA_A$ receptor α_1-subunit is associated with absence epilepsy. Ann Neurol 59:983-987.

Mantegazza M, Gambardella A, Rusconi R, Schiavon E, Annesi F, Cassulini RR, Labate A, Carrideo S, Chifari R, Canevini MP, Canger R, Franceschetti S, Annesi G, Wanke E, Quattrone A (2005) Identification of an $Na_V1.1$ sodium channel (*SCN1A*) loss-of-function mutation associated with familial simple febrile seizures. Proc Natl Acad Sci U S A 102:18177-18182.

Mantegazza M, Yu FH, Catterall WA, Scheuer T (2001) Role of the C-terminal domain in inactivation of brain and cardiac sodium channels. Proc Natl Acad Sci U S A 98:15348-15353.

Marini C, Harkin LA, Wallace RH, Mulley JC, Scheffer IE, Berkovic SF (2003) Childhood absence epilepsy and febrile seizures: a family with a $GABA_A$ receptor mutation. Brain 126:230-240.

Maurer-Morelli CV, Secolin R, Marchesini RB, Santos NF, Kobayashi E, Cendes F, Lopes-Cendes I (2006) The *SCN2A* gene is not a likely candidate for familial mesial temporal lobe epilepsy. Epilepsy Res 71:233-236.

McEwen DP, Meadows LS, Chen C, Thyagarajan V, Isom LL (2004) Sodium channel $\beta1$ subunit-mediated modulation of $Na_V1.2$ currents and cell surface density is dependent on interactions with contactin and ankyrin. J Biol Chem 279:16044-16049.

Meadows LS, Malhotra J, Loukas A, Thyagarajan V, Kazen-Gillespie KA, Koopman MC, Kriegler S, Isom LL, Ragsdale DS (2002) Functional and biochemical analysis of a sodium channel $\beta1$ subunit mutation responsible for generalized epilepsy with febrile seizures plus type 1. J Neurosci 22:10699-10709.

Meisler MH, Kearney JA (2005) Sodium channel mutations in epilepsy and other neurological disorders. J Clin Invest 115:2010-2017.

Morante-Redolat JM, et al. (2002) Mutations in the *LGI1/Epitempin* gene on 10q24 cause autosomal dominant lateral temporal epilepsy. Hum Mol Genet 11:1119-1128.

Morgan K, Stevens EB, Shah B, Cox PJ, Dixon AK, Lee K, Pinnock RD, Hughes J, Richardson PJ, Mizuguchi K, Jackson AP (2000) $\beta3$: an additional auxiliary subunit of the voltage-sensitive sodium channel that modulates channel gating with distinct kinetics. Proc Natl Acad Sci U S A 97:2308-2313.

Motoike HK, Liu H, Glaaser IW, Yang AS, Tateyama M, Kass RS (2004) The Na^+ channel inactivation gate is a molecular complex: a novel role of the COOH-terminal domain. J Gen Physiol 123:155-165.

Mulley JC, Scheffer IE, Petrou S, Dibbens LM, Berkovic SF, Harkin LA (2005) *SCN1A* mutations and epilepsy. Hum Mutat 25:535-542.

Nabbout R, Baulac S, Desguerre I, Bahi-Buisson N, Chiron C, Ruberg M, Dulac O, LeGuern E (2007) New locus for febrile seizures with absence epilepsy on 3p and a possible modifier gene on 18p. Neurology 68:1374-1381.

Nakayama J, Arinami T (2006) Molecular genetics of febrile seizures. Epilepsy Res 70 Suppl 1:S190-S198.

Nakayama J, Fu YH, Clark AM, Nakahara S, Hamano K, Iwasaki N, Matsui A, Arinami T, Ptacek LJ (2002) A nonsense mutation of the *MASS1* gene in a family with febrile and afebrile seizures. Ann Neurol 52:654-657.

Naundorf B, Wolf F, Volgushev M (2006) Unique features of action potential initiation in cortical neurons. Nature 440:1060-1063.

Noda M, Ikeda T, Kayano T, Suzuki H, Takeshima H, Kurasaki M, Takahashi H, Numa S (1986) Existence of distinct sodium channel messenger RNAs in rat brain. Nature 320:188-192.

Ogiwara I, Miyamoto H, Morita N, Atapour N, Mazaki E, Inoue I, Takeuchi T, Itohara S, Yanagawa Y, Obata K, Furuichi T, Hensch TK, Yamakawa K (2007) $Na_V1.1$ localizes to axons of parvalbumin-positive inhibitory interneurons: a circuit basis for epileptic seizures in mice carrying an *Scn1a* gene mutation. J Neurosci 27:5903-5914.

Ohmori I, Kahlig KM, Rhodes TH, Wang DW, George AL, Jr. (2006) Nonfunctional *SCN1A* is common in severe myoclonic epilepsy of infancy. Epilepsia 47:1636-1642.

Osaka H, Ogiwara I, Mazaki E, Okamura N, Yamashita S, Iai M, Yamada M, Kurosawa K, Iwamoto H, Yasui-Furukori N, Kaneko S, Fujiwara T, Inoue Y, Yamakawa K (2007) Patients with a sodium channel $\alpha1$ gene mutation show wide phenotypic variation. Epilepsy Res 75:46-51.

Patlak J (1991) Molecular kinetics of voltage-dependent Na^+ channels. Physiol Rev 71:1047-1080.

Phillips HA, Scheffer IE, Berkovic SF, Hollway GE, Sutherland GR, Mulley JC (1995) Localization of a gene for autosomal dominant nocturnal frontal lobe epilepsy to chromosome 20q 13.2. Nat Genet 10:117-118.

Planells-Cases R, Caprini M, Zhang J, Rockenstein EM, Rivera RR, Murre C, Masliah E, Montal M (2000) Neuronal death and perinatal lethality in voltage-gated sodium channel α_{II}-deficient mice. Biophys J 78:2878-2891.

Plummer NW, Meisler MH (1999) Evolution and diversity of mammalian sodium channel genes. Genomics 57:323-331.

Ragsdale DS, Avoli M (1998) Sodium channels as molecular targets for antiepileptic drugs. Brain Res Brain Res Rev 26:16-28.

Rainier S, Sher C, Reish O, Thomas D, Fink JK (2006) De novo occurrence of novel SPG3A/atlastin mutation presenting as cerebral palsy. Arch Neurol 63:445-447.

Raymond CK, Castle J, Garrett-Engele P, Armour CD, Kan Z, Tsinoremas N, Johnson JM (2004) Expression of alternatively spliced sodium channel α-subunit genes. Unique splicing patterns are observed in dorsal root ganglia. J Biol Chem 279:46234-46241.

Rhodes TH, Lossin C, Vanoye CG, Wang DW, George AL, Jr. (2004) Noninactivating voltage-gated sodium channels in severe myoclonic epilepsy of infancy. Proc Natl Acad Sci U S A 101:11147-11152.

Rhodes TH, Vanoye CG, Ohmori I, Ogiwara I, Yamakawa K, George AL, Jr. (2005) Sodium channel dysfunction in intractable childhood epilepsy with generalized tonic-clonic seizures. J Physiol 569:433-445.

Richard EA, Miller C (1990) Steady-state coupling of ion-channel conformations to a transmembrane ion gradient. Science 247:1208-1210.

Rothberg BS, Magleby KL (2001) Testing for detailed balance (microscopic reversibility in ion channel gating. Biophys J 80:3025-3026.

Ruben PC, Starkus JG, Rayner MD (1992) Steady-state availability of sodium channels. Interactions between activation and slow inactivation. Biophys J 61:941-955.

Rusconi R, Scalmani P, Cassulini RR, Giunti G, Gambardella A, Franceschetti S, Annesi G, Wanke E, Mantegazza M (2007) Modulatory proteins can rescue a trafficking defective epileptogenic $Na_V1.1$ Na^+ channel mutant. J Neurosci 27:11037-11046.

Rush AM, Dib-Hajj SD, Waxman SG (2005) Electrophysiological properties of two axonal sodium channels, $Na_V1.2$ and $Na_V1.6$, expressed in mouse spinal sensory neurones. J Physiol 564:803-815.

Salzer JL (2002) Nodes of Ranvier come of age. Trends Neurosci 25:2-5.

Sarao R, Gupta SK, Auld VJ, Dunn RJ (1991) Developmentally regulated alternative RNA splicing of rat brain sodium channel mRNAs. Nucleic Acids Res 19:5673-5679.

Scalmani P, Rusconi R, Armatura E, Zara F, Avanzini G, Franceschetti S, Mantegazza M (2006) Effects in neocortical neurons of mutations of the $Na_V1.2$ Na^+ channel causing benign familial neonatal-infantile seizures. J Neurosci 26:10100-10109.

Scheffer IE, Berkovic SF (1997) Generalized epilepsy with febrile seizures plus. A genetic disorder with heterogeneous clinical phenotypes. Brain 120 (Pt 3):479-490.

Scheffer IE, Harkin LA, Grinton BE, Dibbens LM, Turner SJ, Zielinski MA, Xu R, Jackson G, Adams J, Connellan M, Petrou S, Wellard RM, Briellmann RS, Wallace RH, Mulley JC, Berkovic SF (2007) Temporal lobe epilepsy and GEFS+ phenotypes associated with *SCN1B* mutations. Brain 130:100-109.

Scheffer IE, Wallace R, Mulley JC, Berkovic SF (2001) Clinical and molecular genetics of myoclonic-astatic epilepsy and severe myoclonic epilepsy in infancy (Dravet syndrome). Brain Dev 23:732-735.

Schneggenburger R, Ascher P (1997) Coupling of permeation and gating in an NMDA-channel pore mutant. Neuron 18:167-177.

Schulte U, Thumfart JO, Klocker N, Sailer CA, Bildl W, Biniossek M, Dehn D, Deller T, Eble S, Abbass K, Wangler T, Knaus HG, Fakler B (2006) The epilepsy-linked *Lgi1* protein assembles into presynaptic K_V1 channels and inhibits inactivation by $K_V\beta 1$. Neuron 49:697-706.

Shah BS, Stevens EB, Pinnock RD, Dixon AK, Lee K (2001) Developmental expression of the novel voltage-gated sodium channel auxiliary subunit β3, in rat CNS. J Physiol 534:763-776.

Singh NA, Charlier C, Stauffer D, DuPont BR, Leach RJ, Melis R, Ronen GM, Bjerre I, Quattlebaum T, Murphy JV, McHarg ML, Gagnon D, Rosales TO, Peiffer A, Anderson VE, Leppert M (1998) A novel potassium channel gene, KCNQ2, is mutated in an inherited epilepsy of newborns. Nat Genet 18:25-29.

Singh R, Andermann E, Whitehouse WP, Harvey AS, Keene DL, Seni MH, Crossland KM, Andermann F, Berkovic SF, Scheffer IE (2001) Severe myoclonic epilepsy of infancy: extended spectrum of GEFS+? Epilepsia 42:837-844.

Smith MR, Goldin AL (1997) Interaction between the sodium channel inactivation linker and domain III S4-S5. Biophys J 73:1885-1895.

Spampanato J, Aradi I, Soltesz I, Goldin AL (2004a) Increased neuronal firing in computer simulations of sodium channel mutations that cause generalized epilepsy with febrile seizures plus. J Neurophysiol 91:2040-2050.

Spampanato J, Escayg A, Meisler MH, Goldin AL (2003) Generalized epilepsy with febrile seizures plus type 2 mutation W1204R alters voltage-dependent gating of $Na_V1.1$ sodium channels. Neuroscience 116:37-48.

Spampanato J, Kearney JA, de HG, McEwen DP, Escayg A, Aradi I, MacDonald BT, Levin SI, Soltesz I, Benna P, Montalenti E, Isom LL, Goldin AL, Meisler MH (2004b) A novel epilepsy mutation in the sodium channel *SCN1A* identifies a cytoplasmic domain for β subunit interaction. J Neurosci 24:10022-10034.

Stafstrom CE (2003) *SCN1A* in SMEI, ICEGTC, and GEFS+: Alphabet Soup or Emerging Genotypic-Phenotypic Clarity? Epilepsy Curr 3:219-220.

Steinlein OK, Mulley JC, Propping P, Wallace RH, Phillips HA, Sutherland GR, Scheffer IE, Berkovic SF (1995) A missense mutation in the neuronal nicotinic acetylcholine receptor α4 subunit is associated with autosomal dominant nocturnal frontal lobe epilepsy. Nat Genet 11:201-203.

Stocker PJ, Bennett ES (2006) Differential sialylation modulates voltage-gated Na^+ channel gating throughout the developing myocardium. J Gen Physiol 127:253-265.

Striano P, Bordo L, Lispi ML, Specchio N, Minetti C, Vigevano F, Zara F (2006a) A novel *SCN2A* mutation in family with benign familial infantile seizures. Epilepsia 47:218-220.

Striano P, et al. (2006b) Linkage analysis and disease models in benign familial infantile seizures: a study of 16 families. Epilepsia 47:1029-1034.

Stromme P, Mangelsdorf ME, Shaw MA, Lower KM, Lewis SM, Bruyere H, Lutcherath V, Gedeon AK, Wallace RH, Scheffer IE, Turner G, Partington M, Frints SG, Fryns JP, Sutherland GR, Mulley JC, Gecz J (2002) Mutations in the human ortholog of Aristaless cause X-linked mental retardation and epilepsy. Nat Genet 30:441-445.

Stühmer W, Conti F, Suzuki H, Wang XD, Noda M, Yahagi N, Kubo H, Numa S (1989) Structural parts involved in activation and inactivation of the sodium channel. Nature 339:597-603.

Sugawara T, Mazaki-Miyazaki E, Fukushima K, Shimomura J, Fujiwara T, Hamano S, Inoue Y, Yamakawa K (2002) Frequent mutations of *SCN1A* in severe myoclonic epilepsy in infancy. Neurology 58:1122-1124.

Sugawara T, Tsurubuchi Y, Agarwala KL, Ito M, Fukuma G, Mazaki-Miyazaki E, Nagafuji H, Noda M, Imoto K, Wada K, Mitsudome A, Kaneko S, Montal M, Nagata K, Hirose S, Yamakawa K (2001) A missense mutation of the Na^+ channel α_{II} subunit gene $Na_V1.2$ in a patient with febrile and afebrile seizures causes channel dysfunction. Proc Natl Acad Sci U S A 98:6384-6389.

Sugawara T, Tsurubuchi Y, Fujiwara T, Mazaki-Miyazaki E, Nagata K, Montal M, Inoue Y, Yamakawa K (2003) $Na_V1.1$ channels with mutations of severe myoclonic epilepsy in infancy display attenuated currents. Epilepsy Res 54:201-207.

Tate SK, Depondt C, Sisodiya SM, Cavalleri GL, Schorge S, Soranzo N, Thom M, Sen A, Shorvon SD, Sander JW, Wood NW, Goldstein DB (2005) Genetic predictors of the maximum doses patients receive during clinical use of the anti-epileptic drugs carbamazepine and phenytoin. Proc Natl Acad Sci U S A 102:5507-5512.

The YK, Wagner M, Timmer J (2002) Method-independent effect in testing for detailed balance in ion channel gating. Biophys J 82:2275-2276.

Thomsen LL, Kirchmann M, Bjornsson A, Stefansson H, Jensen RM, Fasquel AC, Petursson H, Stefansson M, Frigge ML, Kong A, Gulcher J, Stefansson K, Olesen J (2007) The genetic spectrum of a population-based sample of familial hemiplegic migraine. Brain 130:346-356.

Trimmer JS, Cooperman SS, Tomiko SA, Zhou JY, Crean SM, Boyle MB, Kallen RG, Sheng ZH, Barchi RL, Sigworth FJ, . (1989) Primary structure and functional expression of a mammalian skeletal muscle sodium channel. Neuron 3:33-49.

Ulbricht W (2005) Sodium channel inactivation: molecular determinants and modulation. Physiol Rev 85:1271-1301.

Vandenberg CA, Horn R (1984) Inactivation viewed through single sodium channels. J Gen Physiol 84:535-564.

Vanmolkot KR, Babini E, De VB, Stam AH, Freilinger T, Terwindt GM, Norris L, Haan J, Frants RR, Ramadan NM, Ferrari MD, Pusch M, Van den Maagdenberg AM, Dichgans M (2007) The novel p.L1649Q mutation in the *SCN1A* epilepsy gene is associated with familial hemiplegic migraine: genetic and functional studies. Mutation in brief #957. Online. Hum Mutat 28:522.

Vanoye CG, Lossin C, Rhodes TH, George AL, Jr. (2006) Single-channel properties of human $Na_V1.1$ and mechanism of channel dysfunction in *SCN1A*-associated epilepsy. J Gen Physiol 127:1-14.

Vassilev P, Scheuer T, Catterall WA (1989) Inhibition of inactivation of single sodium channels by a site-directed antibody. Proc Natl Acad Sci U S A 86:8147-8151.

Vedantham V, Cannon SC (1998) Slow inactivation does not affect movement of the fast inactivation gate in voltage-gated Na^+ channels. J Gen Physiol 111:83-93.

Verkhusha VV, Chudakov DM, Gurskaya NG, Lukyanov S, Lukyanov KA (2004) Common pathway for the red chromophore formation in fluorescent proteins and chromoproteins. Chem Biol 11:845-854.

Vestergaard M, Pedersen CB, Sidenius P, Olsen J, Christensen J (2007) The long-term risk of epilepsy after febrile seizures in susceptible subgroups. Am J Epidemiol 165:911-918.

Vilin YY, Makita N, George AL, Jr., Ruben PC (1999) Structural determinants of slow inactivation in human cardiac and skeletal muscle sodium channels. Biophys J 77:1384-1393.

Wada A (2006) Roles of voltage-dependent sodium channels in neuronal development, pain, and neurodegeneration. J Pharmacol Sci 102:253-268.

Wada A, Yanagita T, Yokoo H, Kobayashi H (2004) Regulation of cell surface expression of voltage-dependent $Na_V1.7$ sodium channels: mRNA stability and posttranscriptional control in adrenal chromaffin cells. Front Biosci 9:1954-1966.

Wallace RH, Hodgson BL, Grinton BE, Gardiner RM, Robinson R, Rodriguez-Casero V, Sadleir L, Morgan J, Harkin LA, Dibbens LM, Yamamoto T, Andermann E, Mulley JC, Berkovic SF, Scheffer IE (2003) Sodium channel α1-subunit mutations in severe myoclonic epilepsy of infancy and infantile spasms. Neurology 61:765-769.

Wallace RH, Marini C, Petrou S, Harkin LA, Bowser DN, Panchal RG, Williams DA, Sutherland GR, Mulley JC, Scheffer IE, Berkovic SF (2001) Mutant $GABA_A$ receptor γ2-subunit in childhood absence epilepsy and febrile seizures. Nat Genet 28:49-52.

Wallace RH, Wang DW, Singh R, Scheffer IE, George AL, Jr., Phillips HA, Saar K, Reis A, Johnson EW, Sutherland GR, Berkovic SF, Mulley JC (1998) Febrile seizures and generalized epilepsy associated with a mutation in the Na^+-channel β1 subunit gene *SCN1B*. Nat Genet 19:366-370.

Wang DW, George AL, Jr., Bennett PB (1996) Comparison of heterologously expressed human cardiac and skeletal muscle sodium channels. Biophys J 70:238-245.

Wang DW, Makita N, Kitabatake A, Balser JR, George AL, Jr. (2000) Enhanced Na^+ channel intermediate inactivation in Brugada syndrome. Circ Res 87:E37-E43.

Wang Q, Shen J, Splawski I, Atkinson D, Li Z, Robinson JL, Moss AJ, Towbin JA, Keating MT (1995) *SCN5A* mutations associated with an inherited cardiac arrhythmia, long QT syndrome. Cell 80:805-811.

Wang X, Lu Y (2008) Genetic etiology of new forms of familial epilepsy. Front Biosci 13:3159-3167.

Waxman SG (2007) Channel, neuronal and clinical function in sodium channelopathies: from genotype to phenotype. Nat Neurosci 10:405-409.

Wedekind H, Smits JP, Schulze-Bahr E, Arnold R, Veldkamp MW, Bajanowski T, Borggrefe M, Brinkmann B, Warnecke I, Funke H, Bhuiyan ZA, Wilde AA, Breithardt G, Haverkamp W (2001) De novo mutation in the *SCN5A* gene associated with early onset of sudden infant death. Circulation 104:1158-1164.

West JW, Patton DE, Scheuer T, Wang Y, Goldin AL, Catterall WA (1992) A cluster of hydrophobic amino acid residues required for fast Na^+-channel inactivation. Proc Natl Acad Sci U S A 89:10910-10914.

Westenbroek RE, Merrick DK, Catterall WA (1989) Differential subcellular localization of the RI and RII Na^+ channel subtypes in central neurons. Neuron 3:695-704.

Westenbroek RE, Noebels JL, Catterall WA (1992) Elevated expression of type II Na^+ channels in hypomyelinated axons of *shiverer* mouse brain. J Neurosci 12:2259-2267.

Whitaker WR, Clare JJ, Emson PC (1999) Differential distribution of voltage-gated sodium channel alpha- and beta-subunits in human brain. Ann N Y Acad Sci 868:88-92.

Whitaker WR, Clare JJ, Powell AJ, Chen YH, Faull RL, Emson PC (2000) Distribution of voltage-gated sodium channel α-subunit and β-subunit mRNAs in human hippocampal formation, cortex, and cerebellum. J Comp Neurol 422:123-139.

Whitaker WR, Faull RL, Waldvogel HJ, Plumpton CJ, Emson PC, Clare JJ (2001) Comparative distribution of voltage-gated sodium channel proteins in human brain. Brain Res Mol Brain Res 88:37-53.

Wyllie DJ, Behe P, Nassar M, Schoepfer R, Colquhoun D (1996) Single-channel currents from recombinant NMDA NR1a/NR2D receptors expressed in Xenopus oocytes. Proc Biol Sci 263:1079-1086.

Xu J, Clancy CE (2008) Ionic mechanisms of endogenous bursting in CA3 hippocampal pyramidal neurons: a model study. PLoS ONE 3:e2056.

Xu R, Thomas EA, Gazina EV, Richards KL, Quick M, Wallace RH, Harkin LA, Heron SE, Berkovic SF, Scheffer IE, Mulley JC, Petrou S (2007a) Generalized epilepsy with febrile seizures plus-associated sodium channel $\beta 1$ subunit mutations severely reduce β subunit-mediated modulation of sodium channel function. Neuroscience 148:164-174.

Xu R, Thomas EA, Jenkins M, Gazina EV, Chiu C, Heron SE, Mulley JC, Scheffer IE, Berkovic SF, Petrou S (2007b) A childhood epilepsy mutation reveals a role for developmentally regulated splicing of a sodium channel. Mol Cell Neurosci 35:292-301.

Yanagita T, Kobayashi H, Uezono Y, Yokoo H, Sugano T, Saitoh T, Minami S, Shiraishi S, Wada A (2003) Destabilization of $Na_V1.7$ sodium channel alpha-subunit mRNA by constitutive phosphorylation of extracellular signal-regulated kinase: negative regulation of steady-state level of cell surface functional sodium channels in adrenal chromaffin cells. Mol Pharmacol 63:1125-1136.

Yang Y, Wang Y, Li S, Xu Z, Li H, Ma L, Fan J, Bu D, Liu B, Fan Z, Wu G, Jin J, Ding B, Zhu X, Shen Y (2004) Mutations in *SCN9A*, encoding a sodium channel alpha subunit, in patients with primary erythermalgia. J Med Genet 41:171-174.

Yu FH, Mantegazza M, Westenbroek RE, Robbins CA, Kalume F, Burton KA, Spain WJ, McKnight GS, Scheuer T, Catterall WA (2006) Reduced sodium current in GABAergic interneurons in a mouse model of severe myoclonic epilepsy in infancy. Nat Neurosci 9:1142-1149.

Yu FH, Westenbroek RE, Silos-Santiago I, McCormick KA, Lawson D, Ge P, Ferriera H, Lilly J, DiStefano PS, Catterall WA, Scheuer T, Curtis R (2003) Sodium channel β4, a new disulfide-linked auxiliary subunit with similarity to β2. J Neurosci 23:7577-7585.

Zucca C, Redaelli F, Epifanio R, Zanotta N, Romeo A, Lodi M, Veggiotti P, Airoldi G, Panzeri C, Romaniello R, De PG, Bonanni P, Cardinali S, Baschirotto C, Martorell L, Borgatti R, Bresolin N, Bassi MT (2008) Cryptogenic epileptic syndromes related to *SCN1A*: twelve novel mutations identified. Arch Neurol 65:489-494.